MICRO-/NANOTECHNOLOGIES TO ENGINEER MICROENVIRONMENTAL CUES FOR REGENERATIVE HEART VALVE THERAPIES

by

Yingfei Xue

B. Eng. in Pharmaceutical Engineering, East China University of Science & Technology, 2012
M.S. in Pharmaceutical Sciences, University of Pittsburgh, 2013

Submitted to the Graduate Faculty of

School of Pharmacy in partial fulfillment

of the requirements for the degree of

Doctor of Philosophy

University of Pittsburgh

2018

UNIVERSITY OF PITTSBURGH

SCHOOL OF PHARMACY

This dissertation was presented

by

Yingfei Xue

It was defended on

July 24th, 2018

and approved by

Song Li, M.D., Ph.D., Professor

Center for Pharmacogenetics, Department of Pharmaceutical Sciences, School of Pharmacy

Julie Phillippi, Ph.D., Assistant Professor

Department of Cardiothoracic Surgery, School of Medicine

Department of Bioengineering, Swanson School of Engineering, University of Pittsburgh

Yadong Wang, Ph.D., McAdam Family Foundation Professor of Cardiac Assist Technology

Meinig School of Biomedical Engineering, Cornell University

Dissertation Advisor: **Shilpa Sant**, Ph.D., Assistant Professor

Department of Pharmaceutical Sciences, School of Pharmacy

Departments of Bioengineering, Swanson School of Engineering, University of Pittsburgh

Dissertation Co-Advisor: **Vinayak Sant**, Ph.D., Assistant Professor

Department of Pharmaceutical Sciences, School of Pharmacy, University of Pittsburgh

MICRO-/NANOTECHNOLOGIES TO ENGINEER MICROENVIRONMENTAL CUES FOR REGENERATIVE HEART VALVE THERAPIES

Yingfei Xue, Ph.D.

University of Pittsburgh, 2018

Scaffold-based regenerative heart valve therapy represents a promising and innovative approach to address the unmet clinical need in treating valvular heart diseases. However, current tissue-engineered heart valve scaffolds often suffer from issues such as architectural and mechanical mismatch to native valve leaflet, thrombogenicity, and calcification tendency. Our overall goal is to provide effective strategies to improve the design of regenerative heart valve therapies by alleviating these common issues. This dissertation summarizes our efforts to develop micro-/nanotechnology-based strategies in mimicking the fibrous architecture and mechanical properties of the native valves while improving the biocompatibility of tissue-engineered scaffolds.

We first synthesized a novel series of polyethylene glycol (PEG) functionalized biodegradable elastomers. With different molar ratios and molecular weights of PEG in the polymer backbone, these biodegradable and biocompatible elastomers possessed widely tunable mechanical properties and desirable degradation mechanism.

We then fabricated PEGylated biodegradable elastomers into fibrous scaffolds by electrospinning. The introduction of PEG into the polymer backbone led to reduced thrombogenicity of the fibrous scaffolds. Moreover, the uniaxial and cyclic mechanical properties of fibrous scaffolds could be tuned to mimic those of the native valve leaflets.

The electrospinning process was further modified to fabricate anisotropic fibrous scaffolds. By modulating polymer formulation, fibrous scaffolds were produced to possess

anisotropic biaxial mechanical properties. The anisotropic nature of scaffold also guided the alignment of human valvular interstitial cells (hVICs) seeded on the scaffolds.

To address the calcification tendency of heart valve substitutes, we developed shape-specific cerium oxide nanoparticles (CNPs), which have unique properties to mitigate oxidative stress. We demonstrated that the oxidative stress exacerbated the calcification in hVICs. We then demonstrated the effectiveness of CNPs in alleviating oxidative stress and preventing calcification in hVICs.

Finally, we combined antioxidant CNPs with anisotropic fibrous scaffolds to obtain nanocomposite scaffolds. These scaffolds possessed antioxidant properties and supported hVIC attachment and proliferation. In an oxidative stress-induced calcification model, hVICs cultured on CNP encapsulated scaffolds displayed reduced calcification tendency.

Collectively, using micro-/nanotechnology-based strategies, we developed novel tissue-engineered heart valve scaffolds with anisotropic mechanical properties and the potential to mitigate the thrombogenicity and calcification frequently observed in current valve replacement therapies.

TABLE OF CONTENTS

LIST OF TABLES

LIST OF FIGURES

PREFACE

“Completing a Ph.D. degree is not a picnic. It requires a committed 5 or 6 years of your life being an apprentice.” When I look back on my last 5 years in the Sant lab at the University of Pittsburgh School of Pharmacy, I am grateful to be surrounded by a group of talented and selfless mentors, collaborators, colleagues, and friends. You all make my Ph.D. study less difficult and more fun. My most sincere and heartfelt gratitude goes to all of you.

This dissertation will not be possible without many people, but most importantly, Drs. Shilpa and Vinayak Sant. There are many reasons that make me feel very grateful to have Drs. Sant as my Ph.D. advisor and co-advisor. Thank you for giving me the freedom to choose my research topic when I first joined the lab; thank you for always encouraging me to jump out of my comfort zone; thank you for the countless time and efforts you spent on my projects from study design, experiment execution, data analysis, manuscript writing, and presentation skills; thank you for always making yourself available to sit down with me and discuss what has gone wrong and how to overcome these difficulties when I encountered obstacles; thank you for connecting me with great collaborators who have benefited my research projects immensely; and thank you for all your personal suggestions for me moving forward in my career development. This list can go on and on and I cannot thank you enough for the enormous efforts you have spent on me. I would like you to know that I am proud to be the first Ph.D. student in the lab and I hope you will be proud of me as well.

I am sincerely grateful to my committee members, Dr. Song Li, Dr. Julie Phillippi, and Dr. Yadong Wang, for your considerable guidance, encouragement, comments, and criticisms on my research. You all have raised me from a freshman in scientific research to a skilled and independent scientist.

I would also like to take this opportunity to thank all my past and current colleagues and friends in Dr. Sant's lab. Special thanks go to Mr. Akhil Patel. Your passion for science, thoughtfulness, hospitality, and humor are just a few of your characteristics that I look up to. We have shared so many wonderful memories inside and outside the lab and you certainly make my Ph.D. study more enjoyable. Special thanks also go to Dr. Manjulata Singh. You are such a dedicated scientist, patient mentor, and agreeable friend. To all other friends in Dr. Sant's laboratory: Shilpaa Mukundan, Jean Liou, Yuzhe Chen, Tatyana Yatsenko, Harini Venkata Krishnan, Piyusha Sane, Vibishan Balasubramanian, Prithivirajan Durairajan, Sameera Sansare, Yohann Pitale, Lavanya Kondiparthi, Supraja Ranganathan, Sricharani rao Balmuri, Vijetha G.V Viju, Vishal Rakshe, Jack Gong, Urmi Chheda and Mrunal Sakharkar. I am grateful to fight along with all of you in the same trench.

Many thanks to our extremely supportive and friendly collaborators: Dr. Julie Phillippi, Ms. Jen Hill, Dr. Cynthia St. Hilaire, Dr. Kartik Balachandran, Mr. Prashanth Ravishankar, Dr. Donna B Stolz, Dr. Tracy Cui, and Dr. Elia Beniash for access to their lab equipment and expert insights.

I would like to express my appreciation to the School of Pharmacy at the University of Pittsburgh. Specifically, to Dr. Patricia Kroboth for leading a wonderful student-oriented research program within the school; to Dr. Barry Gold and Dr. Billy Day for recruiting me to the school in the first place; to Dr. Robert Gibbs, Dr. Paul Johnston, Dr. Lisa Rohan, Dr. Xiangqun

Xie, and Center for Pharmacogenetics for access to various instruments in their labs; to Dr. Maggie Folan, Lori Altenbaugh, and Dolores Hornick for all their administrative help in these past years.

This dissertation is dedicated to my dearest family members, my father Hong, my mother Xiaoxin, my wife Jing, and my daughter Mingyi. I am lucky to always have your unconditioned love, confidence, and support to go through difficult moments in my Ph.D. study. I look forward to sharing with you my career success.

ABBREVIATIONS

α-SMA: alpha smooth muscle actin; APS-co-PEG: poly (1,3-diamino-2-hydroxypropane-co-glycerol sebacate)-co-poly (ethylene glycol); CAT: catalase; CNP: cerium oxide nanoparticle; COL-1: collagen-1; DCFH-DA: 2,7-dichlorodihydrofluorescein diacetate; DPPH: 2,2-diphenyl-1-picrylhydrazyl; DSC: differential scanning calorimetry; ECM: extracellular matrix; EM: elastic modulus; FTIR: Fourier-transform infrared; GPC: gel permeation chromatography; HVTE: heart valve tissue engineering; LR: long rod; mRNA: messenger ribonucleic acid; NMR: nuclear magnetic resonance; OPN: osteopontin; PAV: porcine aortic valve; PCL: polycaprolactone; PEG: polyethylene glycol; PGS: poly(glycerol sebacate); Pi: inorganic phosphate; ROS: reactive oxygen species; RUNX-2: Runt-related transcription factor 2; SEM: scanning electron microscopy; SOD: superoxide dismutase; SR: short rod; UTS: ultimate tensile strength; VIC: valvular interstitial cell; VIM: vimentin;

1.0 INTRODUCTION

[Xue Y, Sant V, Phillippi JA, and Sant S. (2017) Acta Biomaterialia 48. 2–19.]

1.1 VALVULAR HEART DISEASES AND CURRENT TREATMENTS

1.1.1 Current issues in treating valvular heart diseases

Valvular heart diseases represent a major public health issue affecting more than 5 million adults in the US alone [1]. Valvular heart diseases remain a serious concern and economic burden, particularly in pediatric patients with the incidence of 1–2 cardiac valve defects in 1000 births in the US, and 8 in 1000 births globally [2, 3]. Each year, more than 25,000 deaths in the US and 3% of sudden deaths in the European Union are caused by cardiac valve defects [4]. In addition, recent epidemiology has forecasted a dramatic increase in the prevalence of valvular heart disease in the next 50 years due to the increasing aging population [5]. Despite the tremendous interdisciplinary efforts in understanding heart valve pathology, drug/therapy development and clinical healthcare over the past few decades, a substantial unmet clinical need in treating valvular heart diseases remains.

Currently, there is a lack of effective pharmacological treatment specifically for valvular heart diseases while valve repair and replacement stand as the only clinically available treatment

options. Strikingly, almost 70% of the diseased valves are beyond the capability of valve repair and therefore, must be replaced [6]. Indeed, heart valve replacement surgery remains the second most performed procedures among all cardiovascular related surgeries with a total of 300,000 valve replacement performed annually worldwide and a total of 14 billion US dollars in medical costs in the US alone [7]. Currently, the mainstay in valve replacement are mechanical and bioprosthetic valves, both of which suffer from several major drawbacks. Valve replacement by a bioprosthetic valve often lead to rapid ectopic calcification *in vivo* and its tendency towards mechanical failure further shortens its durability [8]. On the other hand, mechanical valve replacements demand long-term anticoagulant therapy and may be subjected to life-threatening hemodynamic failure [9, 10]. More importantly, both valve replacements are not viable and cannot grow with patients [11]. As a result, these valve replacements are likely to require re-operation, often multiple re-operations, especially for pediatric patients [12]. Therefore, there is a pressing and imminent need for developing new treatment options that can mitigate or overcome the problems associated with the current treatments.

1.1.2 Scaffold-based heart valve regenerative therapy

To overcome the drawbacks of current therapies, heart valve tissue engineering (HVTE) has been proposed as a promising strategy for regenerating and/or repairing diseased valve tissue [13-16]. Tissue engineering can enhance the limited self-healing capacity of damaged, malformed, or diseased tissue by guided reconstruction of native extracellular matrix (ECM)-mimetic microenvironment with adequate biomechanical integrity and by providing the necessary biomimetic physical and biological cues [17]. HVTE is of special significance and potential because valvular heart diseases often result in substantial loss of healthy cells as well as

disruption of normal tissue microenvironment that are beyond the repair capacity of native valves [18]. Therefore, biomimetic tissue-engineered heart valve constructs that can deliver cells while providing mechanical support and biological cues to promote valve regeneration are in critical need [19, 20]. Among different components of HVTE, scaffold plays a critical role in directing and guiding the cellular activities towards regeneration. Ideally, a suitable scaffold would mimic the complex hierarchical and anisotropic structure of valve leaflet ECM and withstand the dynamic mechanical environment *in vivo*. Here, we are particularly interested in scaffolds prepared from synthetic elastomers. These scaffolds have been well established and recognized as one of the promising tools to engineer microenvironments mimicking native heart valve ECM [21]. In HVTE, scaffolds made from biodegradable synthetic elastomer offer a wealth of benefits including 1) more controllable material composition and structure than natural materials, thus minimizing the variance between batches [22]; 2) high mechanical compliance and elastic behavior, which enables them to endure the high demand of cyclic stretch and relaxation processes experienced by native valve tissue *in vivo* [23]; 3) low immunogenicity and toxicity because the degradation products are mostly endogenous metabolic molecules [24]; 4) tunable degradation rates that will balance evolving mechanical properties due to gradually degrading matrix and new ECM synthesized by the regenerating tissue [25, 26]; and 5) ease of processability by common material fabrication methods such as molding, spraying, spinning and stereolithography [22]. Therefore, synthetic biodegradable elastomers are especially suitable material candidates for HVTE scaffolds.

In spite of the exponential growth in HVTE research, a mature tissue-engineered heart valve construct made from synthetic biodegradable elastomers has yet to be developed for clinical use [4]. Such slow progress towards clinical translation can be attributed to several

challenges in the field. One important feature responsible for valve function is the complex multiscale hierarchical architecture and tri-layer structure of native valve leaflets. This consists of anisotropic fibrous layers of ventricularis and fibrosa which are instrumental for closing and opening of the leaflets. In addition, middle proteoglycan-rich spongiosa provides shock-absorbing properties. Recapitulation of such intricate structure in synthetic elastomers is still challenging. Many researchers in the materials science as well as tissue engineering field are working towards developing functional heart valves, yet lack of materials with tunable degradation rates and processability to capture fibrous structure with mechanical compliance along with shock-absorbing properties of the middle spongiosa layer are some of the many hurdles to the progress in the field. Inadequacies in creating such a biomimetic construct might contribute to lack of efficacy of tissue-engineered valves. Moreover, the optimal morphological, physical, mechanical and degradation properties of an ideal HVTE construct are not yet understood [27]. This may be due, in part, to the lack of long term *in vivo* efficacy and safety data on the currently available HVTE constructs [27].

Previously, several reviews have summarized the synthesis and properties of biodegradable elastomers used for tissue engineering [22, 23, 28] and their application towards HVTE using different approaches [29-31]. However, how the multiscale hierarchical architecture, mechanical anisotropy, scaffold degradability and biocompatibility of synthetic elastomeric scaffold-based HVTE approaches are associated with HVTE outcome have not been thoroughly reviewed. Hence, based on the most recent studies on synthetic biodegradable elastomers used for HVTE from 2000 to 2016, we emphasize on the discussion of native heart valve microenvironments and various up-and-coming approaches to engineer synthetic elastomers to recreate key features in the heart valve microenvironment such as anisotropic and

hierarchical tri-layered architecture, mechanical anisotropy, biodegradability, and biocompatibility.

1.2 SYNTHETIC BIODEGRADABLE ELASTOMERS

This section introduces and summarizes different types of synthetic biodegradable elastomers that have been explored for HVTE to date. Table 1–4 summarize existing studies on polyurethane (PU)-based elastomers, poly (hydroxyalkanoate) (PHA)-based elastomers, poly (e-caprolactone) (PCL)-based elastomers and poly(glycerol sebacate) (PGS)-based (thermoset) elastomers for HVTE, respectively.

1.2.1 Thermoplastic elastomers

Thermoplastic elastomers, or physically crosslinked elastomers, refer to a category of elastomers whose individual polymer chains are linked to each other by weak inter/intramolecular interactions such as hydrogen bonds and dipole-dipole interactions. The majority of thermoplastic elastomers consist of a rigid domain providing the structural integrity and an amorphous domain, which renders the flexibility. Such elastomers can be melted and remodeled and are therefore widely exploited for tissue-engineered constructs.

a. Polyurethane (PU)-based elastomers

PU polymers include a large class of elastomers with varying chemical structures, physical properties and degradation profiles. Due to their wide property spectrum and facile fabrication methods, PUs are one of the most widely used synthetic polymers for biomedical applications

[32]. PUs share the common polymer backbone structure, which includes an aliphatic or aromatic units coming from the isocyanate monomers and a more complex moiety derived from polyether or polyester monomers. PUs often undergo microphase separation forming a soft segment created by polyester or polyether and a hard segment formed by diisocyanates and chain extenders [26]. Conventionally, PUs have been developed to resist degradation for long term implantation [33]. However, more recently, chemical modifications of PUs have been explored to accelerate their biodegradability so that they can be suitable for applications which require the fast degrading materials. Currently, PU, polycarbonaturethane (PCU) and poly (ester urethane) urea (PEUU) have been used alone or in combination with other materials for HVTE (Table 1).

Table 1. PU-based elastomers used for HVTE studies

Type of PU elastomers	Year (Ref)	Fabrication Method	Scaffold Description	Significant Findings
PCU	2003 [34]	molding	Bi-leaflet structure designed for the mitral valve	Scaffold showed excellent hemodynamic performance and durability with mild calcification in calf model. (*in vivo* study)
PEUU	2006 [35]	Electrospinning on rotating stainless steel mandrel	Fibers with different diameter, porosity and anisotropy	High velocity spun scaffolds exhibited highly anisotropic mechanical properties closely resembling the native pulmonary valve leaflet.
POSS-PCU	2009 [36]	Solvent casting	100, 150 and 200 μm thick films; can be fabricated into valve shape design	POSS–PCU possessed excellent mechanical strength, good surface properties and resistance to platelet adhesion.
PU (not specified)	2012 [37]	PU spraying technique	Randomly oriented PU fiber sheet with a thickness of 0.3 mm; sutured to a Teflon fixation unit	Conditioning of scaffolds in a pulsatile bioreactor may improve the tolerance of cells to shear stress.
PEUU with PEO or PCL	2012 [38]	Electrospinning on rotating stainless steel mandrel	Electrospun scaffold with various fiber densities and mechanical properties	The scaffold morphology and mechanical properties can be tuned by secondary fiber populations and processing parameters.
PEUU	2013 [39]	Electrospinning on rotating stainless steel	Isotropic and anisotropic electrospun scaffold	Based on FE simulation, curvilinear fiber trajectories for tissue-engineered semilunar

		mandrel		valves leaflet resulted in more uniform strain field under physiologic loading.
PU (not specified)	2013 [40]	PU spraying	Randomly oriented PU fiber sheet with a thickness of 0.3 mm; Sutured to a Teflon fixation unit	The biocompatibility of the synthetic scaffold was good. Conditioning in the newly developed bioreactor improved cell adaption to shear stress.
PEUU	2015 [41]	Electrospinning on conical mandrels of varying pitch angles	The angle of fiber alignment varied linearly over scaffold length.	The electrospun constructs exhibited a curvilinear fiber structure and local mechanical properties similar to the native leaflet.

PU: polyurethane; PCU: polycarbonaturethane; PEUU: poly(ester urethane) urea; POSS: polyhedral oligomeric silsesquioxane; PEO: poly(ethylene) oxide; PCL: poly(ε-caprolactone); FE: finite element.

b. Poly(hydroxyalkanoate) (PHA)-based elastomers

PHAs are a class of polyesters formed by hydroxyl-alkanoic acid which share the same structure of HO-R-COOH where R represents alkyl units [42]. In the field of biomaterials, PHAs are one of the oldest elastomers ever discovered and usually refer to those derived from bacterial fermentation under limiting nutrients and excess carbon environment [42, 43]. PHAs are naturally occurring polyesters synthesized by a variety of microorganisms and then isolated for further use. This class of elastomers is generally stronger than PUs and more suitable for work under dynamic conditions such as cardiovascular tissue engineering [28]. Currently, PHA, poly-4-hydroxybutyrate (P4HB), poly-3-hydroxybutyrate (P3HB), polyhydroxyoctanoate (PHOH), poly (3-hydroxybutyrate-co4-hydroxybutyrate) (P3HB-co-4HB) and poly (3-hydroxybutyrate-co-3-hydroxyhexanoate) (PHBHHx) have been used solely or in combination with other materials for HVTE (Table 2).

Table 2. PHA-based elastomers used for HVTE studies

Type of PHA elastomers	Year (Ref)	Fabrication Method	Scaffold Description	Significant Findings
PGA, PHA and P4HB	2000 [44]	Salt leaching	Tri-leaflet heart valve scaffolds; nonwoven mesh of fibers (pore size: 100–300 μm; porosity: 95%).	PHA and P4HB could be molded into the shape of a tri-leaflet heart valve scaffold and showed a considerable amount of cell attachment and ECM formation.
PHA	2000 [45]	Salt leaching	Porous scaffold (pore size: 80–180 μm)	PHAs could be used to fabricate a three-dimensional, biodegradable heart valve scaffold.
PHA	2000 [46]	Salt leaching	Porous scaffold (pore size: 180–240 μm)	PHA scaffold could maintain valve function for 120 days in lambs. (*in vivo* study)
P4HB/PGA composite	2000 [47]	Heat-application welding	P4HB coated PGA mesh	Scaffolds conditioned in biomimetic environment *in vitro* could function satisfactorily *in vivo* up to 5 months. (*in vivo* study)
P4HB/PGA composite	2002 [48]	Heat-application welding	P4HB coated PGA mesh	Scaffold showed good biocompatibility with marrow stromal cells and constructs showed similar morphological and mechanical properties of native heart valve.
P4HB and PHOH	2002 [49]	Porogen leaching	Porous scaffold porosity: 60–80%; pore size: 80–200 μm	Scaffold opened and closed synchronously under sub-physiological and supra-physiological flow conditions.
P4HB-PGA and P4HB-PGA/PLLA composite	2003 [50]	P4HB dip coating	Non-woven PGA/PLLA mesh coated with P4HB	Mechanical stimulation of scaffolds by dynamic flexure resulted in reduced stiffness and induced anisotropic mechanical properties.
P3HB, P4HB and P3HB-co-4HB + Decellularized valve	2004 [51]	Dip-coating of polymer on ECM	Similar surface morphology, texture and microporosity of decellularized	Matrix/polymer hybrid tissue valves had better biological and biomechanical characteristics than decellularized ECM. (*in vivo* study)

			matrix	
P3HB, P4HB and P3HB-co-4HB + decellularized valve	2004 [52]	Dip coating/ impregnation of lyophilized decellularized matrices	Porous scaffold coated with thin polymer layer	Hybrid scaffolds showed excellent biomechanical, hemodynamic, and structural characteristics under systemic load conditions.
P4HB	2006 [53]	Three-dimensional stereolithographic modeling	Porosity of approximately 80% (pore size: 200 to 400 µm)	Seeding of cryopreserved human umbilical cord cells showed excellent growth potential and *in vitro* tissue formation.
P4HB/PGA composite	2006 [54]	P4HB dip coating	Non-woven PGA mesh coated with P4HB; thickness: 1.0 mm	Prenatal fetal progenitors could be used as new cell source for the engineering of living heart valve leaflets.
P4HB/PGA composite	2006 [55]	P4HB dip coating	Non-woven PGA mesh coated with P4HB; thickness: 1.0 mm	The heart valve leaflet fabrication from prenatal umbilical cord–derived progenitor cells was feasible.
PHBHHx coated decellularized valve	2007 [56]	PHBHHx coating	Porous surface with thin polymer layer coating	PHBHHx coating improved mechanical properties, reduced calcification and promoted the repopulation of hybrid valve.
P4HB coated decellularized valve	2008 [57]	Electrospinning	Ultrathin P4HB fibers have magnitude similarity to the fibrils in ECM	The feasibility and improved biomechanical characteristics of a novel hybrid heart valve leaflet scaffold was demonstrated.
Decellularized leaflet coated chitosan/ P4HB	2009 [58]	Electrospinning	Fibers of chitosan/P4HB randomly deposited on the surface of decellularized leaflets.	bFGF loaded hybrid valve leaflets showed increased mechanical properties and good cytocompatibility**.**
P4HB	2009 [59]	Stereolithographic modeling	Scaffold with length and inner diameter compared with the homograft	This technique allowed fabricating custom-made, patient-specific polymeric cardiovascular tissue engineering scaffolds.
P4HB/PGA composite	2009 [60]	P4HB dip coating	Non-woven PGA mesh coated with	A real-time and non-invasive functionality check of tissue-

			P4HB	engineered valves could be used to monitor mechanical properties during tissue culture.
P4HB	2010 [61]	Three-dimensional stereolithographic modeling	Porous scaffolds with porosity of 80% (pore size 200 to 400 μm)	Generation of viable tissue-engineered heart valves based on $CD133^+$ cells derived from umbilical cord blood and P4HB scaffold was successful.
P4HB/PGA composite	2010 [62]	P4HB dip coating	Non-woven PGA mesh coated with P4HB	*In vitro* mechanical conditioning induced the development of native-like tissue architecture.
P4HB/PGA composite	2010 [63] 2011 [64] 2012 [65]	P4HB dip coating	Non-woven PGA mesh coated with P4HB	Proof-of-concept study in combining tissue-engineered scaffold with minimally-invasive valve replacement technology. (*in vivo* study)
P4HB/PGA composite	2012 [66]	P4HB dip coating	Non-woven PGA mesh coated with P4HB	Prenatal in-vitro fabrication and fetal implantation of amniotic fluid stem cell-based heart valves in the ovine fetal model. (*in vivo* study)

PGA: polyglycolide; PHA: polyhydroxyalkanoate; P4HB: poly-4-hydroxybutyrate; PHOH: polyhydroxyoctanoate; PLLA: poly-L-lactide; ECM: extracellular matrix; P3HB: poly-3-hydroxybutyrate; P3HB-co-4HB: poly (3-hydroxybutyrate-co4-hydroxybutyrate); PHBHHx: poly (3-hydroxybutyrate-co-3-hydroxyhexanoate); bFGF: basic fibroblast growth factor

c. Poly(ε-caprolactone) (PCL)-based thermoplastic elastomers

PCL based thermoplastics are also a family of polymers that have been widely applied in biomedical fields [14]. This class of polymers includes PCL, poly(glycolic acid) (PGA), poly(lactic acid) (PLA) and their copolymers. Generally, they have excellent biocompatibility and controlled biodegradation profile, which enable them to be used for the applications in

sutures and drug delivery systems that have been approved by FDA [28]. The synthesis of PCL-based thermoplastics is often accomplished by the ring-opening polymerization of the corresponding acid monomer in the presence of an initiator. Currently, PCL, PGA and PLA have been used alone or in combination with other materials for HVTE (Table 3).

Table 3. PCL-based elastomers used for HVTE studies

Type of PCL based elastomers	Year (Ref)	Fabrication Method	Scaffold Description	Significant Findings
PGA	2000 [67]	N/A	Non-woven scaffold with fiber diameter of 12–15 mm	Pre-coating of polymeric scaffold with autologous human ECM could improve cell attachment.
PCL	2006 [68]	Electrospinning/ Knitting	Electrospun scaffold: fiber diameter: 5–10μm; pore size: 15–20μm; Knitted scaffold: rectangular patch with three leaflets knitted on semilunar pocket	An optimal scaffold could be a combination of the strength of the knitted structure and the cell-filtering ability of the spun structure.
PCL	2006 [69]	Knitting	Knitted patch sutured into a tube and covered with fibrin	This scaffold was mechanically reliable and biocompatible.
PGA/PLLA blend	2006 [70]	N/A	Non-woven 50:50 blend of PGA and PLLA fibers with diameter of 0.012–0.015 mm	Cyclic flexure and laminar flow could synergistically accelerate tissue formation.
PCL	2007 [71]	Electrospinning	Random fibers without beads defect; porosity: 89.13± 2.5%; fiber diameter: 3.11 ± 0.43 μm.	PCL electrospun leaflets showed a correct co-aptation in the diastolic phase during pulse duplicator testing.
PCL	2008 [72]	Electrospinning	Tri-leaflet valve shape fiber; fiber diameter: 4 μm	Leaflets were able to open and close under mechanical/hydraulic conditions.

PGA/PLLA composite	2010 [73]	Manual and machine needle punch	Non-woven fiber sheet	MSCs seeded on the scaffold functioned well at the time of implantation in sheep model, but suffered regurgitation after 6 weeks. (*in vivo* study)
PGA/PLLA blend	2010 [74]	N/A	Non-woven fibrous scaffolds in a functional tri-leaflet valve	Preconditioning of scaffolds in organ level bioreactor resulted in higher tissue formation rate.
PCL	2013 [75]	Electrospinning	Conventional electrospun scaffold	PCL scaffolds were with minimal compaction and without compromising tissue composition and properties.
PEG/PCL composite	2014 [76]	Electrospinning/ molding	Anisotropic PCL scaffold embedded in PEG hydrogel	PCL as an analog to the fibrosa could improve strength and introduce anisotropic mechanical behavior.
PEGDMA-PLA	2014 [77]	Electrospinning	Morphologically similar to native leaflets	Scaffold showed biomechanical properties that resembled the native valve matrix.
PCL	2014 [78]	Jet-spraying	Aligned nanofibers (600 nm); >90% porosity	Scaffolds had anisotropic mechanical properties, which induce cell orientation along with fiber alignment.
PCL/Chitosan composite+ decellularized ECM	2015 [79]	Electrospinning	Nanofibers but with beaded morphology	Scaffolds had superior mechanical properties and enhanced cyto- and haemocompatibility.
PCL	2015 [80]	Electrospinning	Biomimetic circumferentially oriented nanofibers	VICs aligned along the scaffold and showed fibroblast phenotype.
PGA-P4HB or PCL	2016 [81]	Electrospinning	Conventional electrospun scaffold	Slow degrading scaffold were favored over fast-degrading materials in terms of maintaining of their shape, promoting cell proliferation and ECM secretion.

PGA: polyglycolide; PCL: poly(ε-caprolactone); MSCs: mesenchymal stem cells; PLLA: poly-L-lactide; PEG: poly(ethylene glycol); PEGDMA: poly(ethylene glycol) dimethacrylate; VICs: valvular interstitial cells; ECM: extracellular matrix.

1.2.2 Thermoset elastomers

Thermoset elastomers, or chemically crosslinked elastomers, refer to a class of elastomers whose individual polymer chain is linked to others by covalent bonds. The formation of the thermoset elastomers requires at least one of the monomers to have at least three functional groups that can react with other monomers so that polymer chain can grow linearly and also form a network structure. Usually, the synthesis of thermoset elastomers is accomplished in two steps. The first step involves the synthesis of a linear chain pre-polymer with little crosslinking. The second step is the curing process, which results in the crosslinked polymer network structure. Such crosslinking processes are either achieved thermally or via radiation. Once cured, the elastomers cannot be melted and remodeled and will only undergo degradation.

a. Poly(glycerol sebacate) (PGS)

PGS has been the most widely studied thermoset elastomer. PGS was first synthesized in 2002 by the polycondensation reaction of glycerol and sebacic acid [82]. Since then, PGS has been well characterized in terms of its degradation, mechanical and biological properties. Meanwhile, PGS is amenable to multiple fabrication methods and have been proposed for different tissue engineering applications by numerous studies [83]. Table 4 summarizes the studies involving the use of PGS for HVTE.

Table 4. PGS-based elastomers used for HVTE studies

Type of PGS elastomers	Year (Ref)	Fabrication Method	Scaffold Description	Significant Findings
Protein coated PGS	2007 [84]	Salt fusion	Pore size 75 to 150 µm, porosity 90%, thickness 1.0 mm	Scaffold pre-coating with ECM proteins could allow the tuning of cellular behavior by altering ECM production and cell phenotype.
PGS	2013 [85]	Laser ablation	Diamond-shaped pores	Scaffold matched the anisotropy and peak tangent moduli of native bovine aortic heart valve leaflets.
PGS	2013 [86]	Machining-based micromolding	Diamond-shaped pores	Scaffolds with anisotropic stiffness resembling those of native valvular tissues in the low stress–strain ranges.
PGS/PCL	2013 [87]	Electrospinning	Porous electrospun scaffold	VICs were able to remodel the synthetic scaffolds by depositing new matrix proteins and maintaining scaffolds mechanical properties.
PGS/PCL + Hyaluronic acid & Gelatin	2014 [88]	Electrospinning /hydrogel embedding	Fiber-reinforced hydrogel	PGS–PCL scaffolds preserved mechanical properties while hydrogel improved the three-dimensional distribution of VIC.
PGS-PCL	2014 [89]	Electrospinning	Electrospun aligned fibers	Scaffold mechanical property could be tuned to mimic the native heart valve.
PGS-PCL	2014 [90]	Micromolding/ electrospinning/ Layer by layer assembly	Tri-layered structure resembled valve leaflet	Scaffold had tunable anisotropic mechanical properties similar to native heart valves. Scaffolds opened and closed properly in *ex vivo* model.
PGS/PCL	2015 [91]	Electrospinning /hydrogel	Fiber-reinforced hydrogel	COLLAGEN 1 and ELASTIN genes expression were higher in fiber-hydrogel composite scaffolds than

+ Hyaluronic acid & Gelatin		embedding		those of fiber-only and hydrogel-only scaffolds.

PGS: poly(glycerol sebacate); PCL: poly(ε-caprolactone); VICs: valvular interstitial cells; ECM: extracellular matrix

1.2.3 Summary

In summary, tunable biodegradability and excellent mechanical compliance of synthetic biodegradable elastomers have attracted them as materials of choice for soft tissue engineering such as HVTE. Both thermoplastic and thermoset biodegradable elastomers listed above have their own pros and cons. Most of the thermoplastic elastomers are non-toxic with good processability [28]. However, they do suffer from heterogeneous degradation profile, which may lead to unpredictable loss of mechanical integrity during degradation [92]. On the other hand, thermoset elastomers have more controllable degradation kinetics and predicable mechanical stability during degradation [22]. However, they have poor processability compared to thermoplastic elastomers despite some recent efforts on the creation of functional thermoset elastomeric scaffolds by rapid prototyping, micromolding, microablation and electrospinning [83]. In addition, since both classes of elastomers are synthetic materials, they are often considered to have potential foreign body response after implantation [28]. The following sections discuss applications of both classes of elastomers in HVTE and biomimetic strategies to improve their tissue engineering outcomes.

1.3 IMPORTANT SCAFFOLD DESIGN CRITERIA FOR TISSUE-ENGINEERED HEART VALVES

The development of biomimetic tissue-engineered construct has been recognized as one of the central themes in the field of tissue engineering [17, 93]. The principle of ‘‘Form follows Function” has been actively practiced [94, 95]. In particular, for HVTE, it has been acknowledged that cellular activities are instructed by biophysical factors such as anisotropy and multiscale hierarchy in ECM architecture [95-97]. Valve ECM-mimetic scaffolds have shown promising results in multiple *in vitro* and preliminary *in vivo* studies implying that a tissue-engineered heart valve scaffold, which can recapitulate the native valve structure has huge promise to become a functional construct. Here, we identify several key design criteria for the functional biomaterial-based heart valve constructs such as anisotropic architecture, mechanical anisotropy, and biocompatibility.

1.3.1 Scaffold architecture

Scaffold architecture provides the structural support and cues to the cells cultured on it. Moreover, the scaffold architecture can also affect its mechanical properties and degradability. Native valve leaflet ECM has its own macroscopic shape, size and unique fibrillar microarchitecture [98]. Therefore, tissue-engineered scaffold recapitulating these morphological properties holds great promise in guiding valve tissue regeneration [20]. This section discusses how the architecture of biodegradable elastomeric scaffolds has evolved for HVTE application.

a. Natural heart valve tissue architecture

Structurally, adult heart valves consist of three flexible tissue leaflets with a highly complex structure. Cross-section of the valve leaflet is characterized by a tri-layered structure that consists of fibrosa, spongiosa and ventricularis, each of which have their own ECM protein composition and alignment [99]. Fibrosa consists of circumferentially oriented thick collagen bundle structure and provides mechanical strength to the leaflet [100]. Spongiosa is made up of randomly oriented proteoglycans, which acts as a cushion between the fibrosa and ventricularis layers [101]. Ventricularis is composed of radially oriented elastic fibers (mainly elastin), which results in high elasticity in radial direction and enables the proper opening and closing of the valve [101]. Thus, heart valve leaflets possess multiscale hierarchical organization from micro- to macro-scale. Additionally, the circumferentially and radially aligned ECM proteins in fibrosa and ventricularis layers confer anisotropic structural and mechanical properties to heart valve leaflets. These important features of heart valve leaflets pose substantial challenges in recapitulating the valve structural characteristics using conventional tissue engineering scaffolds and motivate the development of new generation biomimetic HVTE scaffold.

b. Mimicry of anisotropic nature of heart valve leaflet

Early studies on polymeric HVTE constructs used randomly oriented fibers or meshes as heart valve prosthesis to match the macroscopic size and shape of valve [44, 45, 47, 48, 67]. These studies demonstrated that scaffolds made from biocompatible materials could support the growth of multiple cell types (vascular cells, myofibroblasts and endothelial cells) and ECM protein secretion with similar inflammatory response level compared to that of human heart valve homografts [40]. However, scaffold architecture design was not taken into consideration.

To match the anisotropic nature of native heart valve leaflets, electrospun poly (ester urethane) urea (PEUU) were produced with aligned fiber network by tuning the rotating mandrel

velocity [102]. The mechanical properties of highly anisotropic fibers closely resembled those of the native pulmonary heart valve leaflet. Based on this elastomeric scaffold leaflet, finite element (FE) simulation was applied to explore the optimal shape and architecture for HVTE, which was accomplished by comparing the deformed shape from computational modeling and *ex vivo* microCT scan of a native ovine valve leaflet [39]. The curvilinear fiber architecture was determined to be the optimal architecture for the valve leaflet with local mechanical properties comparable to those of native heart valve leaflet [41].

Alternatively, hybrid poly(glycerol sebacate)-poly(ε-caprolactone) (PGS-PCL) scaffolds with anisotropic fibrous structure were fabricated by directional electrospinning technique [89]. Primary human valvular interstitial cells (VICs) could attach and align according to the fiber alignment of PGS-PCL scaffolds and actively expressed smooth muscle actin and heart valve ECM proteins such as collagen and vimentin. Similarly, anisotropic nanofibrous PCL scaffold was fabricated by jet-spraying technique [78]. Porous scaffolds supported cell invasion, proliferation and ECM protein deposition. More importantly, the aligned fiber structure was able to instruct cellular alignment and polarization along the fiber orientation [78].

c. Mimicry of anisotropic nature of heart valve leaflet

Besides the anisotropic fibrous structure, the recapitulation of tri-layered valve leaflet with unique ECM fiber alignment in each layer is another challenge for the design and fabrication of elastomeric scaffolds [98]. So far, only a limited number of studies have devised tri-layered scaffolds, with the intention to mimic both structural and mechanical anisotropy of the native valve leaflets. As an example, anisotropic sandwich-like polyethylene glycol (PEG)-PCL hydrogel–fiber composites were developed by embedding PCL fibers within the PEG hydrogel [84]. The alignment of VICs cultured on top of sandwich PEG-PCL scaffolds was guided by the

anisotropy of underlying electrospun PCL fibers. Although the constructs were believed to mimic only fibrosa, this study provided a novel approach of combining hydrogel and fibrous scaffold for HVTE. In another study, a diamond-patterned PGS layer was created by micromolding, which served as the central layer [98]. Then, unidirectionally aligned PGS-PCL fibers were directly electrospun on the PGS layer [98]. These hybrid constructs supported growth of VICs and mesenchymal stem cells (MSCs) and guided their alignment. After 4 weeks of culture, the mechanical properties (stiffness and tensile strength) of the engineered constructs in both circumferential and radial directions were comparable to the native valve tissue and correlated well with the *de novo* ECM protein deposition. To further evaluate the potential of these scaffolds for a leaflet replacement, the authors tested the construct in an *ex vivo* model of leaflet replacement in the pulmonary valve position of isolated fresh pig hearts. Tri-layered scaffolds had adequate systolic performance and complete diastolic co-aptation, which was better than single layered scaffold [98].

1.3.2 Mechanical properties of scaffolds

The mechanical properties of ECM play important roles in determining the cellular behaviors, as shown in cell biology [103], disease pathology [104] as well as tissue regeneration [105]. Since tissue-engineered scaffolds act as temporary ECM substitutes and provide initial support to the seeded/recruited cells, their mechanical properties should ideally be similar to those of the targeted native tissues and/or could be tuned to deliver mechanical cues for tissue repair/regeneration by activating/deactivating cells.

a. Native heart valve leaflet mechanics

Human heart valves are responsible for controlling the continuous unidirectional blood flow into/out from the ventricles. Normally, average human heart beats almost 2 billion times through the life span [106]. Hence, heart valves are subject to highly dynamic mechanical loads such as high pressure (as high as 12 kPa in adults) and shear stress due to blood flow. Uniaxial mechanical testing on porcine leaflet revealed that the valve leaflet had good compliance initially, but eventually became rigid at larger strains [7]. Due to its unique ECM (collagen and elastin) fiber alignment, valve leaflet demonstrated anisotropic mechanical properties in circumferential and radial directions. Uniaxial mechanical testing also revealed that the elastic modulus of the initial loading phase varies between 2 and 10 kPa in the radial direction and 20–100 kPa in the circumferential direction [107]. Biaxial mechanical testing further confirmed that the valve leaflet is highly anisotropic (index of anisotropy: 0.247) [108, 109]. Therefore, ideal HVTE scaffolds should be elastic and strong enough to withstand the dynamic *in vivo* environment without permanent deformation under the influence of repeated stresses. More importantly, HVTE scaffolds should resemble the anisotropic nature of valve leaflet to provide the correct biomechanical cues towards functional valve regeneration [110].

b. Strategies to tune the mechanical properties of HVTE scaffolds

Early studies on synthetic HVTE scaffolds highlighted the importance of mechanical properties to provide tissue support as well as to endure the *in vivo* mechanical environment and the implantation procedure such as suture [44]. However, there is no consensus in the field on the optimal mechanical properties of HVTE scaffolds, for both, as-prepared and during *in vivo* degradation of scaffolds and tissue remodeling. Therefore, it is worthwhile to develop methods that can widely tune the mechanical properties of HVTE scaffolds so that the optimal mechanical properties can be assessed.

One of the methods to tune the mechanical properties of elastomeric scaffold is by modifying the chemical structure of well-established elastomers. Based on the structure of polycarbonate (PCU), Kidane et al. grafted polyhedral oligomeric silsesquioxanes (POSS) segment onto polycarbonate and found that PCU-POSS possessed higher tensile strength, Young's modulus and elongation at break than pure PCU [36]. It was hypothesized that nanoscale POSS segment could form strong intermolecular forces with neighboring molecules and reduce its dipole interaction potential, thus making the polymer stronger.

Amoroso et al. focused on fine tuning the scaffold stiffness by electrospinning PEUU with modified fiber intersection densities [38]. This was achieved by the addition of a secondary polymer strain (non-leachable PCL or leachable poly(ethylene) oxide (PEO)) during electrospinning. The lower bending moduli were achieved with the higher fiber intersection densities within PEUU scaffolds. Interestingly, the incorporation of non-leachable, stiff secondary fiber populations (PCL) led to higher bending moduli while the removal of leachable secondary fiber populations (PEO) resulted in lower bending moduli.

Post-manufacturing modifications have also offered new possibilities to further tune the mechanical properties of elastomeric scaffolds. Tseng et al. modified electrospun PCL scaffolds by protein adsorption, alkali digestion and acrylation, respectively [76]. All three modifications changed the physico-chemical properties of the scaffolds and significantly reduced the elastic modulus compared to the unmodified scaffolds. Additionally, modification by acrylation and protein adsorption also resulted in the change in mechanical anisotropy of electrospun scaffolds.

1.3.3 Biocompatibility of scaffolds

Most current biodegradable scaffolds and their degradation products are non-toxic and can support cell proliferation. However, such scaffolds are still considered as foreign materials to the body. Therefore, synthetic tissue engineering scaffold may suffer from low cell attachment, inflammation and thrombogenicity *in vivo*. Many studies have shown that the physico-chemical properties such as hydrophilicity, surface charge and roughness are crucial for the cell attachment and protein adsorption *in vivo*, which eventually determine the cytocompatibility, level of inflammatory reaction and hemocompatibility [111].

Emerging trend in the tissue engineering field is the departure from the ‘‘bio-inert” scaffolds towards “bio-responsive” and “bio-instructive” scaffolds [112]. In the context of tissue engineering, bio-responsive and bio-instructive materials refer to those, which can respond to the *in vivo* biological environment and provide proper cues towards the tissue regeneration [113]. Various strategies that have been proposed to improve the biocompatibility of elastomeric scaffolds are summarized in this section.

a. Use of decellularized tissue matrix and natural ECM proteins to improve cell attachment and regulate cell behavior

Native derived tissue-engineered constructs such as decellularized tissue matrix have been extensively studied in growing animal model [114], long-term *in vivo* performance [115] and clinical study [116]. Indeed, one of the greatest advantages of using decellularized tissue scaffolds is that they are derived from materials already present inside body and do not usually pose the toxicity problems. Also, they are bioactive with specific protein binding sites and other biochemical signals that may assist in a range of cellular activities including cell attachment and

cell-cell communication [117]. Therefore, it is valuable to incorporate the advantages offered by natural biomaterial into the design of HVTE scaffold.

Surface coating or functionalization of biodegradable elastomers with natural ECM proteins can promote cell attachment onto the hybrid scaffolds and can also regulate *de novo* synthesis of ECM proteins, remodeling, and the inflammatory response [118]. In an effort to engineer cellular behaviors such as *de novo* ECM production and functional cellular phenotypes on tissue-engineered heart valves constructs, porous PGS scaffolds were pre-coated with laminin, fibronectin, fibrin, collagen types I/III, or elastin, respectively [84]. The hybrid scaffolds significantly increased cellularity of the scaffolds and regulated cellular behaviors such as ECM protein production.

b. Reduce thrombogenicity of HVTE scaffold

One common reason of the material failure *in vivo*, especially in artificial heart valves is their high thrombogenicity, which is a serious issue for all constructs in direct contact with the blood [119]. Hence, significant efforts are needed in the field of HVTE to reduce scaffold thrombogenicity. One such chemical modification is the incorporation of a polyethylene glycol (PEG) motif into the chemical structure of elastomers [120, 121]. The fabrication of nanocomposite scaffolds made of elastomers and nanomaterials may also reduce thrombogenicity. For example, Kannan et al. demonstrated that POSS-PCU nanocomposites have lower thrombogenicity than polytetrafluoroethylene (PTFE) and PCU due to the remarkable ability of nanocomposite surface to repel both proteins and platelet offering greater thrombo-resistance [122]. In addition, nanocomposites made of elastomers and carbon nanotubes have also been shown to have antithrombotic property [123, 124]. It was speculated that the improved electrostatic properties, nanostructured topography as well as pure carbon composition could

have contributed to the reduced thrombogenicity [123, 124]. We envision the use of synthetic elastomers will provide new antithrombotic strategy since the chemical structure of synthetic elastomers can be easily modified to obtain novel materials with lower thrombogenicity. The issue of thrombogenicity may also be tackled by the delivery of antithrombotic agents. Heparin–VEGF polyelectrolyte multilayer films have been shown to significantly reduce platelet adhesion on the decellularized heart valves [125]. Although there is no study using synthetic elastomers as drug carriers to reduce thrombogenicity so far, the chemical structure of synthetic elastomers can be tailored for the controlled release of bioactive molecules [126].

c. Towards the development of bio-responsive and bio-instructive HVTE scaffolds

The required function of tissue-engineered scaffolds has evolved towards being cell-instructive materials to promote tissue regeneration [127]. As the most abundant cell type in valves, the VIC population is diverse and plastic, which can switch from quiescent (fibroblast-like) phenotype to activated (myofibroblast-like) or diseased (osteoblastic) phenotype [128]. It is important to regulate the VIC phenotypes because the transition between different VIC phenotypes is known to be involved in both, valvular disease progression towards calcification as well as the valve regeneration [129-131]. Therefore, tissue-engineered scaffolds, which can instruct VIC activities and phenotypic changes to promote healthy valve regeneration, are of great interest. VIC phenotypes and activities such as cellular adhesion, alignment, morphology, *de novo* protein synthesis and activation state have been shown to be influenced by soluble factors [132], matrix composition [133], matrix architecture [76], bioactive peptides [76], matrix stiffness [134] and material surface chemistry [135]. Although it has not been explored yet, synthetic biodegradable elastomeric scaffolds have the potential to encapsulate and release VIC-responsive biomolecules in a predictable manner [126]. Moreover, scaffold mechanical properties and surface chemistry

can be tuned by modifying the chemical structural of elastomers, which is a notable advantage of synthetic biodegradable elastomer over natural polymers. Therefore, we envision that biodegradable synthetic elastomer-based scaffolds will be useful to investigate and regulate VIC cellular activities.

1.4 CLINICAL TRANSLATION OF SCAFFOLDS FOR HVTE

The success of *in vitro* research on biodegradable synthetic elastomeric scaffolds for HVTE led to multiple *in vivo* animal studies (in calf [34], sheep [46, 47, 64, 136] and non-human primate models [64]). These studies have revealed the feasibility of scaffold implantation by different methods including minimally invasive and trans-catheter implantation. Moreover, the implanted scaffolds exhibited adequate functionality with suitable valve integrity, mobility and also supported valve ECM remodeling processes. However, such encouraging results in animal models are still far from clinical translation. Here, we identify several major reasons/challenges that may be responsible for this limited success. The first hurdle is the lack of long term safety and efficacy study of implanted tissue-engineered scaffolds. As for the studies reviewed here, the vast majority of them are done in the *in vitro* setting (**Table 1–4**). Among the few *in vivo* studies, most of them reported the follow-up of the implanted valve functionality for less than 20 weeks. Extended follow-up study will elucidate the fate of tissue-engineered heart valves as well as the underlying tissue remodeling mechanisms *in vivo* [64]. The long-term *in vivo* study can also determine the toxicity and/or adverse effect of degradation products *in vivo* [27], which is critical for the administrative approval to move forward into clinical setting. The second major challenge is the *in vivo* calcification of the scaffolds [137]. Calcification has been one critical drawback

and leading cause of failure of heart valves, especially bio-prosthetic valve. Although synthetic elastomers seem to have less calcification problems than bioprosthesis *in vivo* [34, 52], the concern of potential calcification still exists because most of the studies were performed in sheep model, which is a less thrombogenic model than human. The concern of calcification can be alleviated by surface modification of the elastomeric scaffold or by the encapsulation of anti-thrombotic therapeutics. The third challenge for most of the current tissue-engineered heart valves is the leaflet contraction. Tissue-engineered constructs made from either synthetic polymers (such as PGA/PLLA [73]) or natural polymers (such as fibrin [138]) have been shown to suffer from the shortening of the tissue over the period of time after implantation in sheep model. The transplanted cells (often in activated state which exhibit contractile phenotype) have been identified to induce the valve contraction [139]. Therefore, elastomeric scaffolds that can control cellular activation and contractility will have tremendous impact on the successful translation of HVTE. Lastly, although research in HVTE has come a long way since its conception (pioneered by R. Langer, JP. Vacanti and JE. Meyer in 1995 [140]), the development of a functional TEHV construct ready for clinical translation is time-consuming like any other tissue engineering endeavors. For example, Hoerstrup group has been focused on non-woven PGA mesh coated with P4HB scaffold for more than fifteen years. Only after the completion of a series of *in vitro* biomechanical and biocompatibility characterizations [35,56,57,62,63], the preliminary *in vivo* animal studies were performed [71–74]. It also highlighted the importance of focusing on certain promising scaffolds to keep optimizing their properties (scaffold architecture, biomechanics, biodegradability) and processing techniques (fast production rate, uniformity between batches, accuracy in micro- to nano-meter level structure) before the successful clinical translation of the tissue-engineered constructs.

1.5 SUMMARY AND FUTURE PROSPECTS

Recent literature suggests that the scaffold architecture including multi-scale (nano-, micro- to macro-scale) hierarchy and anisotropy, mechanical properties, degradation profile and biocompatibility are the key factors that will determine the success of functional tissue engineering strategies to repair, restore or replace the damaged heart valves. For mechanical properties, biodegradable elastomers are specifically suitable for HVTE, where the mechanically dynamic *in vivo* microenvironment demands recreation of compliant and elastic tissue-engineered constructs. Researchers now appreciate the importance of multiple mechanical testing at different scales and aspects in determining the fate of tissue-engineered scaffolds. Another challenge in the field is limited data and lack of consensus on the most appropriate degradation profile of tissue-engineered scaffold. Therefore, tissue-engineered constructs should be tested empirically in specific *in vivo* settings. Elastomers with wide range of tunable degradation profiles are usually favored to provide flexibility in controlling the degradation rates. Current research has broadened the definition of biocompatibility beyond cytotoxicity and inertness. Any immune response or thrombogenicity events might cause systematic adverse effects and can even be life-threatening. Furthermore, the state-of-the-art tissue engineering has already shifted from developing bio-inert and safe materials towards bioactive materials, which can instruct cellular behavior and tissue regeneration while mitigating the biocompatibility concerns simultaneously. Overall, the future research directions in HVTE scaffolds are to rationally design biodegradable, biomimetic and bioactive heart valves by taking these aspects into consideration. Long-term safety and efficacy study of promising tissue-engineered constructs made of promising elastomers is needed to ultimately move the potential scaffolds forward to the clinical setting. More importantly, multidisciplinary approaches with scientists in materials science, tissue

engineering, valve biology, and valve mechanics working side by side will be instrumental to realize the true clinical translation and huge potential of tissue-engineered heart valves.

2.0 HYPOTHESIS AND SPECIFIC AIMS

2.1 BACKGROUND

The huge challenges and unmet needs in managing valvular heart diseases motivate us to innovate heart valve tissue engineering strategy. In this dissertation, I aim to apply micro- and nanotechnology-based strategies to directly address several prominent yet unsolved issues in the design of tissue engineered heart valve such as architectural and mechanical mismatch, thrombogenicity, and calcification.

Micro- and nanotechnology refer to an array of techniques used for the fabrication of materials with micron and nanoscale features, respectively [141]. The past decades have witnessed the exponential growth in micro- and nanotechnologies as promising tools to address the challenges in tissue engineering and drug delivery [142]. Fine control over the micro- and nanoscale structural features of biomaterials can be used to resemble the microenvironment of native tissues and modulate their bioactivity [143]. In this dissertation, I aim to engineer biocompatible nanocomposite scaffolds made from synthetic biodegradable elastomers and bioactive cerium oxide nanoparticles (CNPs) to mimic the anisotropic architecture and mechanical properties of the native valves as well as mitigate the thrombogenicity and calcification tendency of the current valve substitutes.

2.1.1 ECM-mimetic micro-/nanofibrous scaffolds

Every tissue in the body is composed of fibrous extracellular matrix (ECM) made of proteins and glycoproteins that act as substrate to host the cells and signaling molecules [144]. Therefore, micro-/nanofibrous scaffolds have gained increasing attention because of their unique properties to interface with cells at the same scale as native ECM [145]. The smaller size of the fibers results in the high surface area and porosity, which support and facilitate cell attachment and spreading, and transport of nutrients and waste [142].

Micro-/nanofibrous scaffolds can be engineered to mimic one or multiple structural and functional roles of the ECM by different fabrication methods including self-assembly, phase separation, and fiber spinning [144]. Among all, electrospinning has gained immense interests due to its facile setup and operation, versatility, and controllability. So far, electrospinning is one of the most common micro-/nanofiber fabrication methods and has been used with a wide variety of synthetic polymers and biopolymers [146].

Generally, a basic electrospinning setup consists of a polymer source (or sources), a high voltage supply, and a grounded collector. The solution is loaded in a reservoir where high voltage is applied. If the electric potential is high enough to overcome the surface tension, a jet of solution will be pulled out towards the collector. During this process, the solvent is being evaporated and whipping instability produces the accumulation of fiber meshes [147]. Overall, the fiber diameter can be engineered ranging from 50-2000 nm, with pore size from 2-465 μm, and porosity up to 90% [148]. These structural features can be fine-tuned by the optimization of an array of electrospinning parameters such as solvent composition, the concentration of polymer solution, the collector, applied voltage, spinneret-to-collector distance, and polymer flow rate [146].

Although standard electrospinning often yields random-oriented fibers, electrospinning process also allows control over fiber alignment/orientation resulting in properties that are direction-dependent (anisotropy). These scaffolds are of greater interest in soft tissue engineering because many native tissues such as valve leaflets have anisotropic ECM structure. One method to induce fiber alignment in electrospun scaffolds is by a rotating drum collector. The fiber anisotropy can be controlled by rotating speed of the collector [102, 149, 150]. Alternatively, fiber alignment could be controlled using a system with differentially grounded pairs of electrodes [151-153]. In this way, different rosette patterns of fibers were generated in a layer-by-layer manner by varying the state of the electrodes (grounded or not).

In this dissertation, I will design and test a valve leaflet-inspired electrospinning collector to obtain anisotropic fibrous scaffolds. In addition, I propose to electrospin a novel series of polyethylene glycol (PEG) functionalized (PEGylated) biodegradable elastomers to serve two goals: 1) to tune the elastomeric mechanical properties to mimic those of the native valves, and 2) to incorporate PEG moiety in polymer backbone to mitigate thrombogenicity.

2.1.2 CNPs as a potential therapy to mitigate valve calcification

Valve calcification remains a major healthcare burden in developed countries, resulting in ~17,000 deaths per year in the United States and currently affecting a quarter of the senior population older than 65 [1]. Calcification of the aortic valve, if not treated properly, can impair the normal valve movement and eventually lead to valve stenosis and heart failure. Of the different mechanisms of valve calcification, oxidative stress has been recognized as a key upstream driving force in the early stages of the disease [154] . Increased reactive oxygen species (ROS) such as superoxide and hydrogen peroxide (H_2O_2) levels were found in the calcified

regions of human stenotic valve tissues [155]. Moreover, instead of being merely a consequence of valve calcification progression, ROS production was found to precede the valve calcification in a mice model [156]. However, the benefits of antioxidant therapies, which directly target oxidative stress to treat valve calcification, are yet to be studied.

Nanomedicine is a promising strategy to improve physiochemical properties, enhance therapeutic efficacy and reduce systemic toxicity of carriers and payloads. Because of their small size, nanoparticles can enter the cells and are considered as valuable biomedical tools for different therapeutic applications [157]. However, to the best of our knowledge, there is no nanoparticle-based therapy reported for treating valvular heart diseases. Here, I focus on CNPs, which have shown multiple therapeutic applications such as treating neurodegenerative diseases [158], diabetes [159], ocular diseases [160], and other oxidative stress-related diseases [161]. CNPs also possess good safety profiles as demonstrated in multiple animal models [162, 163].

CNPs have been historically utilized in corrosion protection coatings for metal alloys [164] and fuel cell oxidation catalysis [165]. In the bulk state, cerium oxide can exist as pure CeO_2 (Ce^{4+}) or Ce_2O_3 (Ce^{3+}), whereas at the nanoscale, cerium oxide crystal structure comprises both Ce^{3+} and Ce^{4+} oxidation states [162]. Oxygen vacancies are developed as a result of the presence of Ce^{3+} ions in the crystal lattice as the particle size of cerium oxide is reduced. These oxygen vacancies are responsible for the important catalytic activity of CNPs, allowing them to switch between Ce^{3+} and Ce^{4+} oxidation states. This activity enables the self-regenerative properties of CNPs. Recently, the biomedical field has focused on utilizing the unique catalytic activities of CNPs for mimicking the antioxidant properties of enzymes such as superoxide dismutase (SOD) and catalase (CAT) [166, 167]. CNPs are also effective scavengers for hydroxyl radical, nitric oxide radical, and peroxynitrite, making them broad spectrum

antioxidants. Since oxidative stress is one of the main inducers and driving factors of valve calcification, I propose that CNP encapsulation in the nanocomposite scaffolds as a strategy to mitigate valve calcification.

It is well known that nanoparticle shapes and sizes can have significant effects on their biological activities, such as cellular uptake, intracellular localization, and therapeutic activity [168, 169]. However, most of the studies that use CNPs as antioxidants have been carried out without specifying nanoparticle shape. I will investigate the effect of CNPs shape on mitigating oxidative stress in this dissertation since this has not been well elucidated before.

2.2 CENTRAL HYPOTHESIS & SPECIFIC AIMS

The central hypothesis of this dissertation is: a nanocomposite fibrous scaffold combining PEGylated elastomers and CNPs will recreate a suitable microenvironment to recapitulate the anisotropic mechanical properties of the heart valve with reduced thrombogenicity and calcification tendency.

To test this hypothesis, three specific aims are proposed:

Aim 1 will develop fibrous scaffolds of PEGylated elastomers, which mimic the anisotropic mechanical properties of the heart valve and possess less thrombogenicity. This aim is further divided into three sub-aims:

Sub-aim 1.1: Synthesis and characterization of a novel series of biodegradable PEGylated elastomers (reported in chapter 3 of this dissertation).

Sub-aim 1.2: Fabrication and characterization of the fibrous scaffolds of PEGylated elastomers (reported in chapter 4).

Sub-aim 1.3: Fabrication and biaxial mechanical characterization of anisotropic fibrous scaffolds (as reported in chapter 5).

Aim 2 will develop shape-specific CNPs to inhibit calcification of human valvular interstitial cells (hVICs), as reported in chapter 6. Two sub-aims are further proposed:

Sub-aim 2.1: Development and characterization of oxidative stress-mediated VIC calcification model.

Sub-aim 2.2: Evaluation of efficacy of antioxidant CNPs in inhibiting oxidative stress-induced VIC calcification *in vitro*.

Aim 3 will develop PEGylated elastomer-CNPs nanocomposite fibrous scaffolds with reduced calcification tendency, as reported in chapter 7.

The successful completion of these studies will not only create technologies that can be interfaced to mitigate the current challenges of mechanical mismatch, thrombogenicity and calcification in the valve replacement therapies, but also offer an opportunity to fine tune the physico-chemical, mechanical, and biological properties of a variety of tissue engineered scaffolds.

3.0 SYNTHESIS AND CHARACTERIZATION OF A NOVEL SERIES OF BIODEGRADABLE PEGYLATED ELASTOMERS

[Xue Y, Patel A, Sant V, and Sant S. (2015) European Polymer Journal 72. 163–179.]

3.1 BACKGROUND

There is a growing interest in developing novel biocompatible and biodegradable materials for multiple biomedical applications such as tissue engineering and drug delivery [22, 28, 145]. For successful regeneration of soft and mechanically demanding tissues like heart valves and myocardium, it is important that tissue engineered scaffolds 1) are biodegradable and promote cell growth and tissue regeneration; 2) have tunable mechanical and degradation properties to match the regeneration/healing rate of the target tissue; and 3) endure the dynamic *in vivo* microenvironment and mechanically mimic the native extracellular matrix (ECM) to maintain tissue integrity. Biodegradable synthetic elastomers stand out as one of the most promising materials for soft tissue engineering because of their tunable mechanical compliance, biodegradation rates and excellent biocompatibility [23, 170]. Previous research has focused on thermoplastic polymer/elastomers such as polyurethanes (PU), poly (lactic acid) (PLA), poly (glycolic acid) (PGA), poly (ε-caprolactone) (PCL) and their block copolymers [171, 172]. Although crystalline segments in the structures of these thermoplastic elastomers provide

mechanical strength, they resist degradation [28, 173]. Therefore, these materials suffer from heterogeneous degradation profiles and demonstrate non-linear loss of mechanical strength during degradation [174]. Such degradation profile is usually not preferred in tissue engineering applications because it may lead to sudden mechanical failure of the scaffold before substantial degradation and tissue regeneration [174].

Recent years witnessed significant advances in the development of biodegradable thermoset elastomers. Poly (glycerol sebacate) (PGS) is a benchmark polymer in this class and has been extensively studied for its synthesis and fabrication [82, 175, 176], biocompatibility [83, 177], degradation [178], and tissue engineering applications [87, 88, 179-181]. Rapid *in vivo* degradation rates of PGS limits its potential use for applications in regeneration of tissues that regenerate slowly. To circumvent this limitation, poly (1,3-diamino-2-hydroxypropane-co-polyol sebacate) (APS) elastomers were synthesized by incorporating amide bonds in the PGS backbone to reduce the *in vivo* degradation rate [182, 183]. APS elastomers possess tunable degradability and mechanical properties, as well as excellent *in vitro* and *in vivo* biocompatibility [182, 183]. Airway stents made from APS via microfabrication method have shown good biocompatibility [184]. However, due to their poor solubility in common organic/aqueous solvents, APS elastomers are amenable only to few fabrication methods, such as thermally cured films or microfabrication. Moreover, the poor solubility of APS pre-polymer restricts further chemical modification to fine-tune the physicochemical properties. Importantly, altering the selection of polyols, monomer ratio, and curing conditions of APS elastomers has provided a relatively narrow range of elastic modulus (0.56-4.34 MPa) and tensile strength (0.24-1.69 MPa) [183]. Thus, it is worthwhile to broaden the spectrum of physicochemical, mechanical, and degradation properties of APS by chemical modification.

Polyethylene glycol (PEG) is a biocompatible, hydrophilic polyether that has been widely applied in drug delivery [185]. A wide range of thermoplastics including PLA, PCL, and poly(lactic-co-glycolic acid) (PLGA) have been copolymerized with PEG to tune their physical properties [186], drug loading capacity [187], drug release kinetics [188, 189], and improve their biocompatibility [190, 191]. Of note, thermoset PGS elastomers have recently been copolymerized with PEG to obtain PGS-co-PEG polymers to improve hydration and enhance the utility for biomedical applications [192].

We hypothesize that incorporation of PEG into the APS structure will yield poly (1,3-diamino-2-hydroxypropane-co-glycerol sebacate)-co-poly (ethylene glycol) (APS-co-PEG) copolymers with tunable physicochemical, mechanical, and degradation properties. This will expand the repertoire and property spectrum of currently available elastomers for biomedical applications. Here, we report the synthesis and characterization of a series of APS-co-PEG polymers with varying PEG mole % ranging from 10-40% of sebacic acid (SA) and PEG molecular weight ranging from 400Da to 4kDa.

3.2 METHODS

3.2.1 Polymer synthesis

Sebacic acid (SA), glycerol (G) and 1,3-diamino-2-hydroxy-propane (DAHP) were purchased from Sigma-Aldrich. The APS pre-polymer was synthesized according to the previously published method of the polycondensation reaction of DAHP, G and SA [175]. Briefly, a round bottom flask was charged with a molar ratio of 2:1:3 of DAHP: G: SA monomer mixture. The

reactants were heated under argon atmosphere at 120 °C for 3 h. Approximately 300 mTorr vacuum was applied to the reaction system and the reaction continued for another 9 h at 120°C to obtain APS pre-polymer. The pre-polymer samples were characterized for their chemical composition.

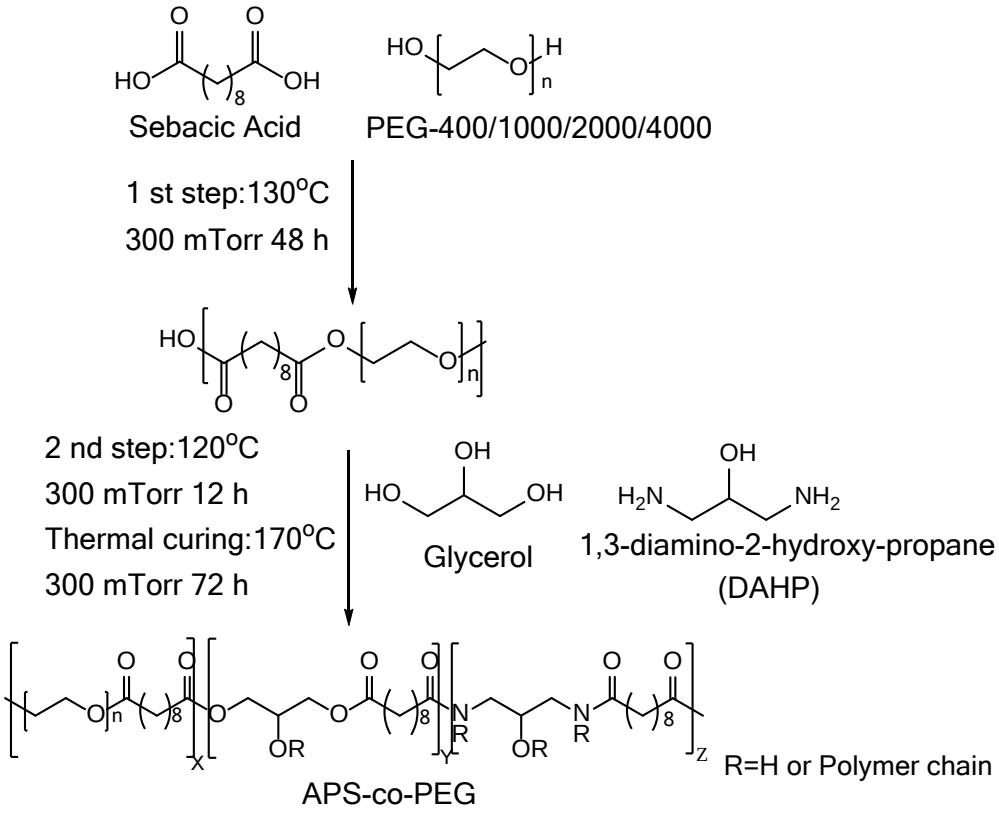

Figure 1. The synthesis scheme of APS-co-PEG elastomers.

Nomenclature of APS-co-PEG: APS-xPEGy, where "x" represents the PEG/Sebacic acid molar ratios (15%, 25%, 40%) and y represents the PEG molecular weight (400, 1000, 2000, 4000). The molar ratio between glycerol and DAHP is constantly 0.5.

The synthesis of APS-co-PEG is shown in **Fig. 1**. Briefly, APS-co-PEG pre-polymers were synthesized via a one-pot two-step condensation polymerization. The first step is the polycondensation between SA and PEG. The mixture was heated in a round bottom flask at

130°C under Argon atmosphere for 2 h and the reaction was continued at 120°C under reduced pressure of 300 mTorr for 24, 48 or 72 h to optimize the time of the first reaction. In the second step, specific amounts of G and DAHP (**Table 5** and **6**) were added into the round bottom flask and mixed thoroughly with the reactants. The reaction was stirred at 120°C under Argon atmosphere for 30 min and continued at 120°C under the reduced pressure of 300 mTorr for 12 or 48 h to obtain APS-co-PEG pre-polymers. The pre-polymers obtained were subjected to chemical and thermal characterization.

Table 5. Effect of PEG molar ratio on the molecular weight of APS-co-PEG pre-polymers

Polymer	Molar Ratio (SA: GLY: DAHP:PEG)	M_w/PDI	Theoretical/Actual PEG molar percentage (%)
APS-15PEG1K	3:0.85:1.7:0.45	2850/1.19	15/17.7
APS-25PEG1K	3:0.75:1.5:0.75	4024/1.35	25/25.5
APS-40PEG1K	3:0.6:1.2:1.2	4997/1.26	40/44.1

Table 6. Effect of PEG molecular weight on the molecular weight of APS-co-PEG pre-polymers.

Polymer	Molar Ratio (SA: GLY: DAHP:PEG)	M_w/PDI	Theoretical/Actual PEG molar percentage (%)
APS-25PEG400	3:0.75:1.5:0.75	1836/1.03	25/31.1
APS-25PEG1K	3:0.75:1.5:0.75	4024/1.35	25/25.5
APS-25PEG2K	3:0.75:1.5:0.75	5064/1.17	25/31.3
APS-25PEG4K	3:0.75:1.5:0.75	5618/1.34	25/24.3

The effect of first and second step reaction time and monomer feeding ratio on the molecular weight and polydispersity of APS-40PEG1K pre-polymer were explored to optimize the reaction conditions. The optimized reaction time and monomer feeding ratio were then used to synthesize a library of APS-co-PEG pre-polymers by varying mole percentage of PEG to SA (15%, 25% or 40%) and molecular weights of PEG (400Da, 1kDa, 2kDa, 4kDa). The pre-polymers were denoted as APS-xPEGy, where x represents the PEG to SA mole percentage and y represents the PEG molecular weight. The detailed molar ratios of the reactants in various pre-polymers can be found in **Table 5** and **6**. Product yield: 61.4-72.6%.

3.2.2 Polymer film fabrication by thermal crosslinking

APS pre-polymer was uniformly spread on a Teflon dish and thermally cured at 170°C for 72 h in a vacuum oven to fabricate the APS polymer film. The thickness of the film was around 1.5mm. Similarly, the APS-co-PEG pre-polymer was spread on a Teflon dish and thermally cured at 170°C for 24, 48 or 72 h in a vacuum oven. The thickness of films was kept constant around 1.5mm.

3.2.3 Proton nuclear magnetic resonance (^{1}H-NMR)

The synthesized APS-co-PEG pre-polymers were analyzed using nuclear magnetic resonance (^{1}H-NMR) spectroscopy (Bruker 400). SA and PEG were dissolved in DMSO-d6 and the pre-polymer samples were dissolved in $CDCl_3$ and the spectra were recorded at 400 MHz. ^{1}H-NMR (400 MHz, $CDCl_3$, δ/ppm): 1.30 (m,-CH2-), 1.62 (m,-CH2CH2O(CO)-), 2.35 (m,-CH2O(CO)-), 3.64 (m,-OCH2CH2O-), 3.72 (m,-NCH2CHOHCH2N-), 4.22 (m,-OCH2CHOHCH2O-). The

peak assignments in the ^{1}H-NMR spectra for APS-co-PEG pre-polymers are also denoted in **Fig. 2a.** To calculate the PEG:SA ratio, peaks of methylene hydrogen within PEG (3.65 ppm) and SA (the combination of 1.30, 1.62, and 2.35 ppm) in ^{1}H-NMR spectra were integrated using TopSpin software.

3.2.4 Fourier-transform infrared spectroscopy (FTIR)

Chemical composition of the pre-polymers was studied using Fourier Transform Infrared (FTIR) spectroscopy with attenuated total reflection (ATR-FTIR). The FTIR spectra were recorded in absorption mode with a resolution of 4 cm^{-1} using Bruker Vertex 70 FTIR spectrometer. The results are presented as an average of 256 scans. Ester, amide I and amide II peaks intensity were integrated for semi-quantitative analysis using Origin8 software.

3.2.5 Differential scanning calorimetry (DSC) analysis

Differential Scanning Calorimeter (DSC, Mettler Toledo) was utilized to study the thermal properties of APS-co-PEG pre-polymers. Sample (approx. 5 mg) was sealed in an aluminum pan and first heated from room temperature to 150°C (1st cycle), then cooled to −70°C (2nd cycle), and finally reheated to 150°C (3rd cycle) at a heating/cooling rate of 10°C/min. All the processes were carried out under nitrogen atmosphere. Crystallization temperature (T_c) and enthalpy (ΔH_c) were obtained from the cooling cycle (150°C to -70°C, 2nd cycle) whereas glass transition temperature (T_g), melting temperature (T_m) and enthalpy (ΔH_m) were obtained from the heating cycle (-70°C to 150°C, 3rd cycle). DSC data was analyzed using STARe software.

3.2.6 Uniaxial tensile testing

The mechanical properties of APS and APS-co-PEG polymer films were evaluated using uniaxial tensile testing with ADMET MTEST Quattro mechanical testing system (n=4). Thermally crosslinked polymer films were cut into rectangular shape (10 mm* 7 mm). Samples were stretched until failure at a constant jogging speed of 10 mm/min. The stress (MPa) was obtained by dividing the applied force (N) with cross-section area (mm^2) and % elongation (strain) was obtained from the displacement using $((L-L_0)/L_0*100)$, where L_0 was initial gauge length and L was instantaneous gauge length. Ultimate tensile strength (UTS) was recorded as the maximum stress at sample failure. Elastic modulus was calculated from the linear stress-strain curve between 5 and 15% strain.

3.2.7 Hydration and degradation study

The hydrophilicity of thermally crosslinked polymer films was determined by contact angle measurements and hydration study. The contact angles of polymer films were measured using VCA 2000 video contact angle goniometer (AST products, n=4). A droplet of de-ionized water was deposited on the sample film using a 21-gauge needle and high-resolution image of the droplet was captured. The contact angles were determined using the VCA software.

For hydration and degradation study, samples were cut into rectangular shape (around 15mm*7mm) and immersed in Dulbecco's phosphate buffer saline (DPBS, Corning) at 37 °C in a dry bath shaker (50 RPM) after recording their initial weight (W_0) and thickness (t_0) (n=3). Samples were taken out from the DPBS solution at regular time intervals, wiped with kimwipes to remove excess surface water, and vacuum dried for 10 mins. The weights (W_t) and thickness

(tt) of samples at time t as well as at equilibrium (W_{eq} and t_{eq}) were recorded. The hydration of the polymer films was determined by Eq. (1). The degradation study was carried out for 14 days in DPBS at 37°C after the equilibrium hydration was achieved. The mass loss of polymer films during degradation was determined by Eq. (2). The decrease in thickness of the films was determined by Eq. (3). Degraded samples were dried in desiccator and examined by FTIR to study the changes in their chemical structure. Morphology of degraded films was studied by scanning electron microscope (SEM) imaging (JEOL 6335F Field Emission SEM). Dried films before and after degradation were sputter-coated with 5nm of gold-palladium using Cressington 108 auto sputter-coater and images were obtained using accelerated voltage of 3kV and a working distance of 8 mm.

$$\text{Equilibrium hydration (\%)} = (W_{eq} - W_0)/ W0 \times 100 \quad \text{Eq. (1)}$$

$$\text{Mass loss (\%)} = (W_{eq} - W_t)/ Weq \times 100 \quad \text{Eq. (2)}$$

$$\text{Decrease in thickness (\%)} = (t_{eq} - t_t)/ t_{eq} \times 100 \quad \text{Eq. (3)}$$

3.2.8 *In vitro* biocompatibility by alamarBlue® assay

The mouse myoblast cells (C2C12) ATCC (CRL-1772™) were obtained from Dr. Adam Feinberg's lab (Carnegie Mellon University, Pittsburgh, PA). The cells were cultured in Dulbecco's Modified Eagle Medium (DMEM, Corning Cellgro) supplemented with 10% Fetal Bovine Serum (FBS, Hyclone, Thermofisher Scientific) and 1% Penicillin/Streptomycin (Corning Cellgro). Cells in passage 2-7 were used. The films (0.5 cm x 0.5 cm) were sterilized by exposing to 70% isopropanol under UV light for 30 min, washed with DPBS thrice and seeded with C2C12 cells using a seeding density of 50,000 cells/scaffold. Cells were allowed to adhere for 40 min and then 500µL of medium was added. After 24 hours, all films were

transferred to new wells and the proliferation rate of adhered cells on day 1 and 3 was assessed using an alamarBlue® assay (Invitrogen) following the standard protocol. Briefly, cell-seeded scaffolds (n=3) were treated with 10% alamarBlue® in growth media for 3.5 h at 37°C. The fluorescence intensity was then measured using microplate reader (Gen5 Biotek) at excitation/emission wavelengths of 530/590 nm. AlamarBlue® solution (10%) incubated without any cells were used for blank correction.

The films seeded with C2C12 cells were fixed in 4% paraformaldehyde solution (20 min) after 3 days in culture to study cell adhesion and spreading. The films were then washed with DPBS three times, followed by permeablization and blocking using 0.1% Triton X-100 and 3% bovine serum albumin (BSA) in DPBS, respectively. Cell nuclei and actin were stained using NucBlue® Fixed Cell Stain (Life Technologies) and ActinGreen™ 488 ReadyProbes® Reagent (Life Technologies), respectively. To eliminate the strong autofluorescence of APS and APS-co-PEG polymers, samples were treated with Sudan Black [193]. Briefly, 0.3% (w/v) Sudan Black solution was prepared in 70% ethanol and filtered through 0.45 μm syringe filter. Polymer films were immersed in this solution for 24 h and washed three times before imaging. Confocal images were obtained using inverted confocal laser scanning microscope (Olympus Fluoview 1000) under 20X and 40X objectives.

3.2.9 Statistical analysis

Experimental data were presented as mean ± standard deviation. Student's paired t-test was used for comparisons between two groups. Statistical differences between multiple groups were analyzed using one-way ANOVA followed by Tukey's post-hoc analysis. p values less than 0.05 were considered significant.

3.3 RESULTS AND DISCUSSION

3.3.1 Pre-polymer synthesis and chemical characterization

APS-co-PEG pre-polymers were synthesized by two-step polycondensation reaction (**Fig. 1**). The synthesis conditions of APS-co-PEG pre-polymers, such as reaction time for the first and second step as well as monomer feeding ratio were first optimized based on the molecular weight characterization of APS-40PEG1K by GPC (**Table 7**). Among all the conditions in our trials, optimum durations for the 1st and 2nd step reaction to obtain low polydispersity index (PDI) were determined to be 48 h and 12 h, respectively. It is well known that the monomer feeding ratio plays an important role in determining the MW of final product during step polymerization [194]. As DAHP and G both have three functional groups, we also synthesized a batch with SA:G:DAHP:PEG molar ratio of 3:0.4:0.8:1.2, in which case, all free hydroxyl groups are expected to react with carboxylic groups of SA (stoichiometry balance, denoted as APS-40PEG1K STOIC). As expected, an increase in molecular weight was observed for APS-40PEG1K STOIC due to the strict stoichiometry (**Table 7**). However, the mechanical properties of the polymeric film were adversely affected (data discussed in the mechanical properties section). The decrease in the mechanical properties of APS-40PEG1K STOIC films was attributed to the unavailability of free hydroxyl groups required for crosslinking of polymeric chains during the thermal crosslinking step. Therefore, this monomer feeding ratio was not adopted for further experiments.

Table 7. Molecular weight of APS-40PEG1K pre-polymers under different reaction condition.

Polymer	1ST STEP TIME	2ND STEP TIME	MOLAR RATIO (SA: G: DAHP:PEG)	M_w/PDI
APS-40PEG1K	24h	48h	3:0.6:1.2:1.2	3536/1.43
	24h	12h	3:0.6:1.2:1.2	4399/1.56
	48h	12h	3:0.6:1.2:1.2	4997/1.26
	72h	12h	3:0.6:1.2:1.2	5387/1.39
	48h	12h	3:0.4:0.8:1.2 (Stoichiometry balance)	6060/1.81

APS-40PEG1K (SA:G:DAHP:PEG molar ratio of 3:0.6:1.2:1.2) synthesized under optimal conditions was subjected to chemical characterization by 1H-NMR and FTIR. 1H-NMR characterization of the first step reaction product exhibited a new peak at 4.2 ppm (**Fig. 2a**) corresponding to the αH adjacent to the ester bond, indicating the formation of new ester bonds and a successful reaction between SA and PEG. In addition, the methylene hydrogen peaks of SA were present at 1.30, 1.62, and 2.35 ppm, and that of PEG at ppm and 3.65 ppm, respectively. In the second step, G and DAHP were added to obtain APS-co-PEG pre-polymer. The ^{1}H-NMR spectrum of the copolymer APS-40PEG1K after completion of 2nd step did not show any peaks from the monomers G or DAHP (**Fig. 2a**). Instead, due to the ester and amide bond formation, the αH in glycerol shifted from 3.5-3.7 ppm to 4.2 ppm and that in DAHP shifted from 2.5-2.7 ppm to 3.72 ppm. Taken together, these results indicated successful completion of the reaction. The actual mole % of PEG calculated from ^{1}H-NMR by comparing methylene hydrogen within PEG and SA correlated well with the theoretical mole %, indicating good control over the polymer synthesis process (**Table 5**).

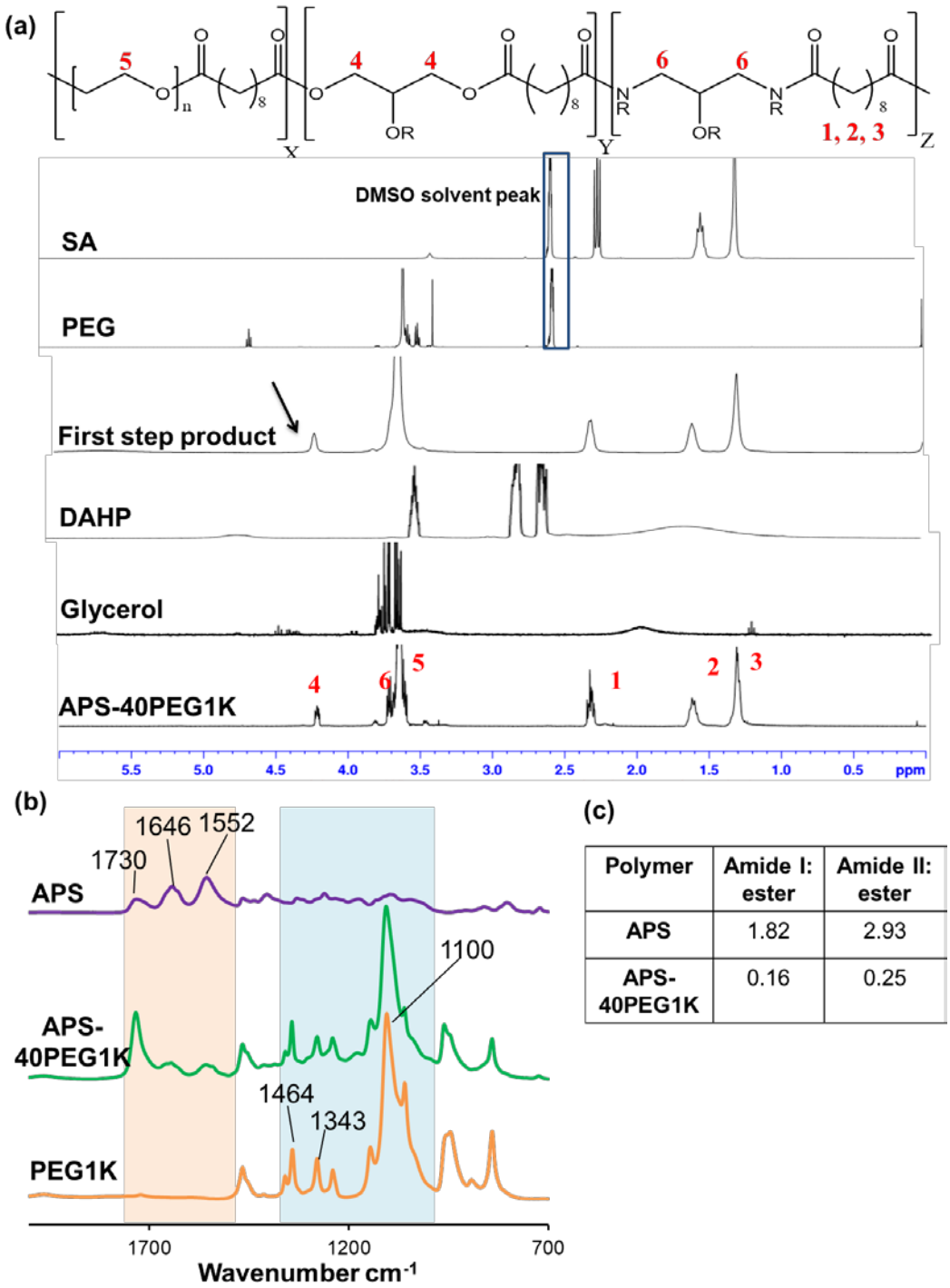

Polymer	Amide I: ester	Amide II: ester
APS	1.82	2.93
APS-40PEG1K	0.16	0.25

Figure 2. The chemical characterization of APS-co-PEG elastomers by H-NMR and FTIR.

(a). H-NMR spectra of DAHP, glycerol and APS-40PEG1K pre-polymer. Peaks assignment for APS-15PEG1K are shown as a representative for APS-co-PEG pre-polymers. First step product had the peak at 4.2ppm (pointed by the arrow), which was the peak of αH beside the newly formed ester bond. The αH in G and DAHP has shifted from 3.5-3.7 ppm and 2.5-2.7 ppm to 4.20 ppm and 3.72 ppm, respectively.

The FTIR spectra of APS-40PEG1K pre-polymer, APS pre-polymer and PEG further demonstrated successful completion of the reaction (**Fig. 2b**). Of note, the carbonyl peak (1730 cm^{-1}) observed in the spectra of APS and APS-40PEG1K indicated the formation of ester bonds between SA and G/PEG while amide (1646 and 1552 cm^{-1}) peaks indicated bonds between SA and DAHP in the pre-polymer chains. In addition, the intensity ratios of the amide I (1646 cm^{-1}) to carbonyl peak of ester bond (1730 cm^{-1}) and amide II (1552 cm^{-1}) to carbonyl peak of ester bond (1730 cm^{-1}) were lower in the FTIR spectrum of APS-40PEG1K than the corresponding ratios observed in the spectrum of APS (**Fig. 2c**). This is due to the reduced amide bond formation in APS-co-PEG pre-polymer than that in APS and may be attributed to the reduced SA: DAHP ratio with addition of PEG (**Table 5**). The increase in ester bond formation with addition of PEG also suggested that PEG was covalently bonded to SA and not physically blended in the copolymer structure. In addition, peaks at 1100, 1464 and 1343 cm^{-1} characteristic of C-O-C stretching and C-H bending peaks of PEG [187, 195] were observed in the spectrum of APS-40PEG1K pre-polymer, but not in the APS pre-polymer spectrum (**Fig. 2b**). Taken together, these data indicated successful covalent linkage of PEG to APS backbone.

Based on the optimized reaction conditions, we synthesized a series of APS-co-PEG pre-polymers by changing PEG mole % (15, 25 and 40% of PEG1K) and PEG molecular weight

(400Da, 1kDa, 2kDa and 4kDa at 25% PEG) to tune the physicochemical, mechanical and degradation properties of the copolymer. These polymers were labeled as APS-15PEG1K, APS-25PEG1K, APS-40PEG1K (**Table 5**), and APS-25PEG400, APS-25PEG2K, and APS-25PEG4K (**Table 6**). Indeed, compared to the poor solubility of APS in major solvents (only soluble in 1,1,1,3,3,3-hexafluoroisopropanol, HFIP), APS-co-PEG pre-polymers exhibited increased hydrophilic nature and could be dissolved in commonly used solvents such as chloroform and ethanol (**Table 8**). For instance, APS solubility was less than 5mg/ml in ethanol and chloroform, while APS-co-PEG solubility was more than 200mg/ml in both solvents. The increased copolymer solubility allowed for their chemical characterization by NMR spectroscopy and GPC and potentially increased the processability of the pre-polymer.

Table 8. Solubility of APS-co-PEG pre-polymers in different solvents (mg/ml).

Polymer	chloroform	ethanol	HFIP
APS	<5	<5	>150
APS-15PEG1K	>100	>200	>150
APS-25PEG1K	>100	>250	>150
APS-40PEG1K	>250	>300	>150
APS-25PEG400	>100	>250	>150
APS-25PEG2K	>250	>300	>150
APS-25PEG4K	>250	>300	>150

The effect of PEG mole % on the chemical properties of APS-co-PEG pre-polymers is shown in **Fig. 3**. M_w /PDI and actual PEG molar percentage for each pre-polymer are listed in

Table 5. Molecular weight of APS-co-PEG pre-polymers increased with the increase in PEG mole %. This trend is in accordance with that observed for PGS-co-PEG pre-polymers, where pre-polymer molecular weight also increased with PEG mole % [192]. In all batches, the actual mole % of PEG from NMR correlated well with the theoretical estimation (**Table 5**), indicating good control over the polymer synthesis process. As expected, the intensity ratio of the amide I to carbonyl peak (1646/1730 cm^{-1}) and Amide II to carbonyl peak of ester bond (1552/1730 cm^{-1}) decreased with increasing PEG mole % in the pre-polymer (**Fig. 3 b and c**). With the increase in PEG mole %, intensity of C-O-C stretching peak (1110 cm^{-1}) and C-H bending peaks (1464 & 1343 cm^{-1}) of PEG also increased, indicating increased amount of PEG segments in the copolymer chains (**Fig. 3 b**).

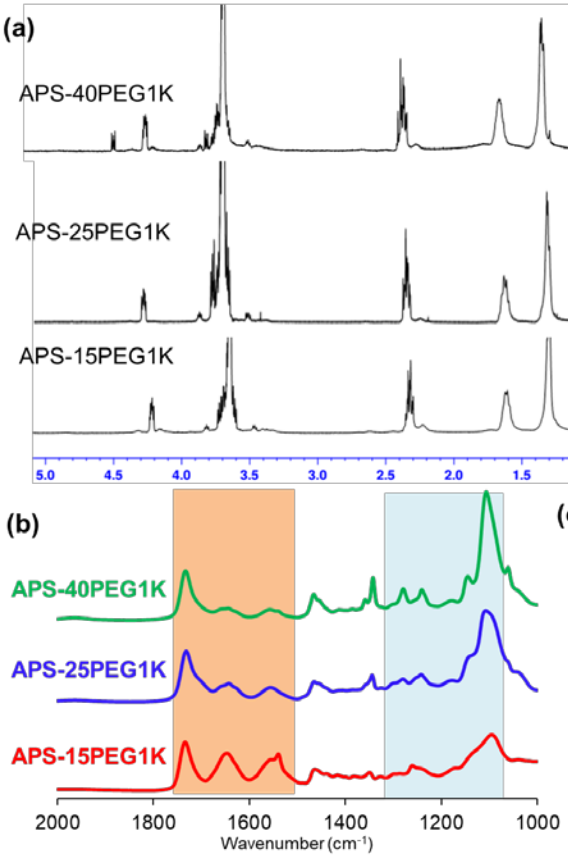

(c)

Polymer	Amide I: ester	Amide II: ester
APS-15PEG1K	0.93	0.96
APS-25PEG1K	0.25	0.29
APS-40PEG1K	0.16	0.25

Figure 3. The chemical characterization of APS-15PEG1K, APS-25PEG1K, APS-40PEG1K pre-polymers.

(a) H-NMR spectra APS-15PEG1K, APS-25PEG1K, APS-40PEG1K pre-polymers. (b) FTIR spectra APS-15PEG1K, APS-25PEG1K, APS-40PEG1K pre-polymers. (c) Decrease in bond intensity ratio of amide peaks I/II (1646/1552 cm-1) to ester peak (1730 cm-1) suggests decreased amide formation due to reduced DAHP molar ratio to SA and increased ester formation due to PEG incorporation into APS backbone.

The effect of PEG molecular weight on the chemical properties of APS-co-PEG pre-polymers is summarized in **Table 6** and **Fig. 4**. Their analyses are similar to those obtained from **Table 5** and **Fig. 3**. Briefly, the effect of increasing PEG molecular weight was similar to that of increasing PEG mole % and led to a predominant increase in intensity of C-O-C stretching peak (1110 cm^{-1}) and C-H bending peaks (1464 & 1343 cm^{-1}) of PEG, indicating increased amount of PEG segments in the co-polymer chains.

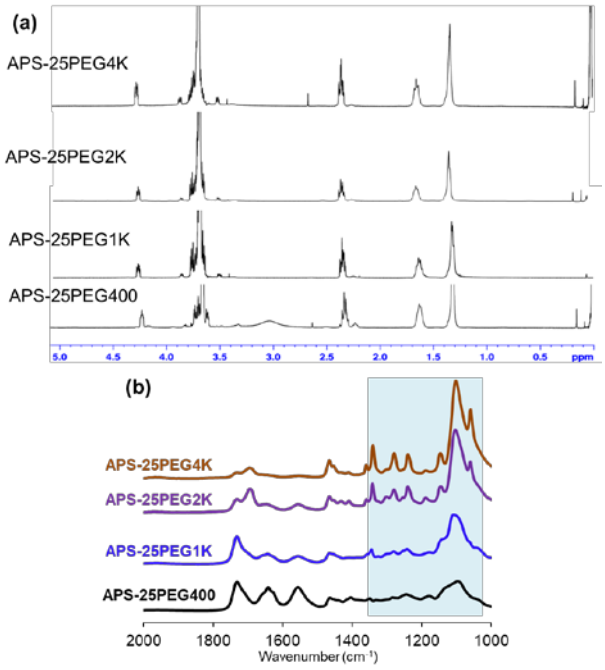

Figure 4. The chemical characterization of APS-25PEG400, APS-25PEG1K, APS-25PEG2k, APS-25PEG4k pre-polymers.

(a) H-NMR spectra of APS-25PEG400, APS-25PEG1K, APS-25PEG2k, APS-25PEG4k pre-polymers. (b) FT-IR spectra of APS-25PEG400, APS-25PEG1K, APS-25PEG2k, APS-25PEG4k pre-polymers

DSC was used to examine the thermal properties of APS-co-PEG pre-polymers. Ideal elastomers for biomedical applications should have a T_g lower than body temperature to ensure that the elastomeric properties could be exhibited *in vivo* [28]. PEG is a known a semi-crystalline polymer with different degree of crystallinity determined by molecular weight [196, 197] while APS is determined to be amorphous [182]. Therefore, it is worthwhile to interrogate the effect of PEG incorporation on the thermal properties of newly synthesized polymers. In this study, the samples were first heated to 150°C to eliminate thermal history. The cooling cycle (from 150°C to -70°C) was used to obtain T_c and ΔH_c while the second heating cycle (-70°C to 150°C) was used to obtain T_g, T_m and ΔH_m.

The effect of PEG mole % on the thermal properties of APS-co-PEG pre-polymers is summarized in **Fig. 5**. Similar to APS pre-polymer, APS-15PEG1K did not show any crystallization peak. Increase in the PEG concentration to 25% resulted in the appearance of crystallization peak at -28.37°C. With further increase in PEG concentration to 40%, T_c shifted to higher temperatures and higher ΔH_c indicated improved crystallization capacity. Previously, Li et al. reported that decreasing the content of rigid segments in poly (ester urethane) elastomers increased the chain flexibility and improved the crystallization capacity of the elastomer [198]. Similarly, improved crystallization was observed in APS-co-PEG copolymers containing higher

than 15 mole % PEG and could be attributed to the increased crystalline PEG segments and increased chain flexibility resulting from incorporation of PEG segments. The T_g of APS was determined to be 5.98°C (**Fig. 5b and c**). APS-15PEG1K and APS-25PEG1K were observed to have much lower T_g of -33.29°C and -39.09°C, respectively. The T_g of APS-40PEG1K cannot be clearly identified in the temperature range studied here. Decrease in T_g with increase in PEG mole% may be due to enhanced polymer chain flexibility by a higher number of PEG segments in the copolymer chain [194]. This also suggests that PEG exhibits its plasticizer effect on the copolymer chains. Low T_g (below body temperature) promises the application of these elastomers in tissue engineering. Also, higher T_m and ΔH_m were observed with the increase in the PEG mole%. This observation was in agreement with the previous thermal study on PCL-PEG, where increasing content of PEG resulted in higher T_m and stronger melting peaks [187]. It also indicated that the crystallization tendency as well as the degree of crystallization was higher in APS-co-PEG pre-polymers with higher PEG content [197].

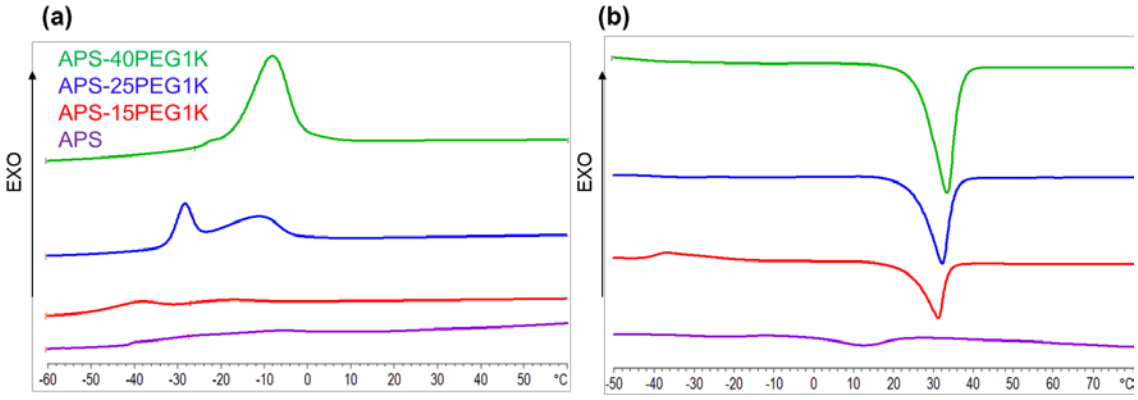

(c)

SUMMARY	T_g(°C)	T_c(°C)	ΔH_c (Jg^{-1})	T_m(°C)	ΔH_m (Jg^{-1})
APS	5.98	NA	NA	NA	NA
APS-15PEG1K	-33.29	NA	NA	31.16	34.09
APS-25PEG1K	-39.09	-28.37	51.58	32.18	54.46
APS-40PEG1K	NA	-8.22	76.91	33.28	83.39

Figure 5. Effect of PEG molar ratio on the thermal properties of APS-co-PEG pre-polymers.

(a) DSC curves of the cooling cycle (2nd) of APS-co-PEG pre-polymers, (b) DSC curves of the heating cycle (3rd) of APS-co-PEG pre-polymers, (c) Summary of the thermal properties of APS-co-PEG pre-polymers.

The effect of PEG molecular weight on the thermal properties of APS-co-PEG pre-polymers with 25 mole % PEG is summarized in **Fig. 6**. APS-25PEG400, which has the lowest PEG MW (400Da), did not show melting/crystallization peaks. Increasing PEG MW to 1000, 2000, and 4000Da resulted in a dramatic shift in crystallization peaks to higher temperatures of -28.37, 20.57 and 23.89°C, respectively with simultaneous increase in ΔH_c. A similar effect was observed for T_m and ΔH_m (**Fig. 6b** and **6c**). These results correlated well with the published results that PEG of higher molecular weight (either alone or in a copolymer network) resulted in higher T_m and ΔH_m [187, 197]. In summary, addition of PEG (at high mole % or higher MW) resulted in increased crystallinity of the copolymer thereby increasing crystallization enthalpies (**Fig. 5c** and **6c**). A similar trend was observed ΔH_m also suggesting an increased mobility of copolymer chains in the presence of PEG.

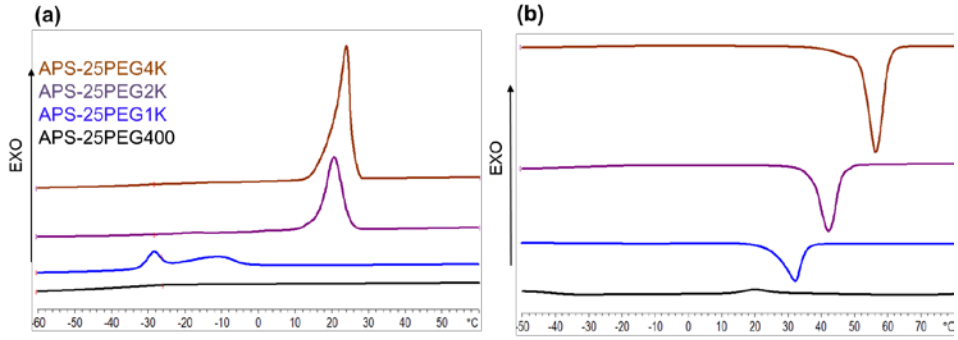

(c)

SUMMARY	T_g(°C)	T_c(°C)	ΔH_c (Jg^{-1})	T_m(°C)	ΔH_m (Jg^{-1})
APS-25PEG400	-38.57	NA	NA	NA	NA
APS-25PEG1K	-39.09	-28.37	51.58	32.18	54.46
APS-25PEG2K	NA	20.57	90.96	42.11	91.64
APS-25PEG4K	NA	23.89	127.62	56.28	140.33

Figure 6. Effect of PEG molecular weight on the thermal properties of APS-co-PEG pre-polymers.

(a) DSC curves of the cooling cycle (2nd) of APS-co-PEG pre-polymers, (b) DSC curves of the heating cycle (3rd) of APS-co-PEG pre-polymers, (c) Summary of the thermal properties of APS-co-PEG pre-polymers.

3.3.2 Chemical properties of APS-co-PEG films

The synthesized APS-co-PEG pre-polymers were subsequently fabricated into elastomer films by thermal crosslinking. In this study, pre-polymers were thermally cured under vacuum for 24 h to 72 h. Unfortunately, APS-co-PEG pre-polymers containing longer PEG chains (APS-25PEG2K and APS-25PEG4K) cannot be fabricated into polymer films even after 96 h of curing at a temperature of 170°C. It suggests that longer PEG chains may have impeded crosslinking between hydroxyl and carboxylic groups due to steric hindrance created by the long polyether chains. This problem could potentially be overcome by increasing the mole fraction of G or DAHP. All other APS-co-PEG pre-polymer series, once cured, could not be dissolved in any solvents and did not flow upon heating, indicating successful thermal crosslinking. The crosslinking process was also confirmed by comparing the FTIR spectra of the pre-polymer and cured film samples. Of note, the intensity ratios of the amide I to carbonyl peak of ester bond (1646/1730 cm^{-1}) and amide II to carbonyl peak (1552/1730 cm^{-1}) were lower in spectrum of cured elastomer than those of the pre-polymers (**Fig. 7**), indicating formation of new ester bonds in cured elastomer during the process of crosslinking as reported for cured APS films [182].

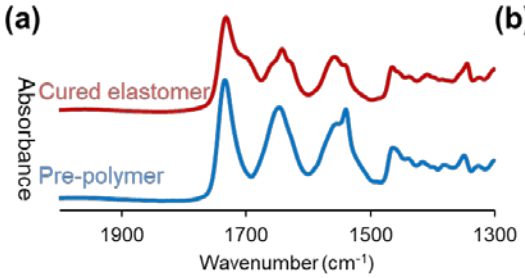

(b)

Polymer	Amide I: ester	Amide II: ester
Pre-polymer	0.93	0.96
Cured Polymer	0.45	0.60

Figure 7. FT-IR spectra of APS-15PEG1K pre-polymer and cured elastomer.

3.3.3 Mechanical properties of APS-co-PEG films

It is important that the APS-co-PEG polymer films maintain their elastomeric properties after PEG incorporation for their application in soft tissue engineering. It is also envisioned that different PEG ratios could widely tune the mechanical properties to broaden the narrow property spectrum of APS. Earlier reports have shown that the monomer feeding ratio, curing time, and curing temperature all play a role in determining the mechanical properties of polymeric materials [82, 83, 199]. APS-co-PEG pre-polymers could not be crosslinked at temperatures lower than 170 °C, hence the curing temperature was fixed at 170°C. Hence, we explored 1) curing time; 2) PEG mole % and molecular weight; and 3) monomer feeding ratio to tune the mechanical properties of APS-co-PEG pre-polymers. It was found that APS-25PEG400 and APS-15PEG1K could be crosslinked within 24 h, while APS-25PEG1K and APS-40PEG1K required 48 h and 72 h for thermal curing, respectively. Thus, pre-polymers with higher PEG mole % required a longer time for thermal crosslinking. This may suggest that longer PEG segments in the pre-polymer interfere with the crosslinking mechanism due to increased steric hindrance. These data are also in accordance with our observation that pre-polymers with higher molecular weight (PEG 2K and 4K) could not be crosslinked even after 96 h of thermal curing.

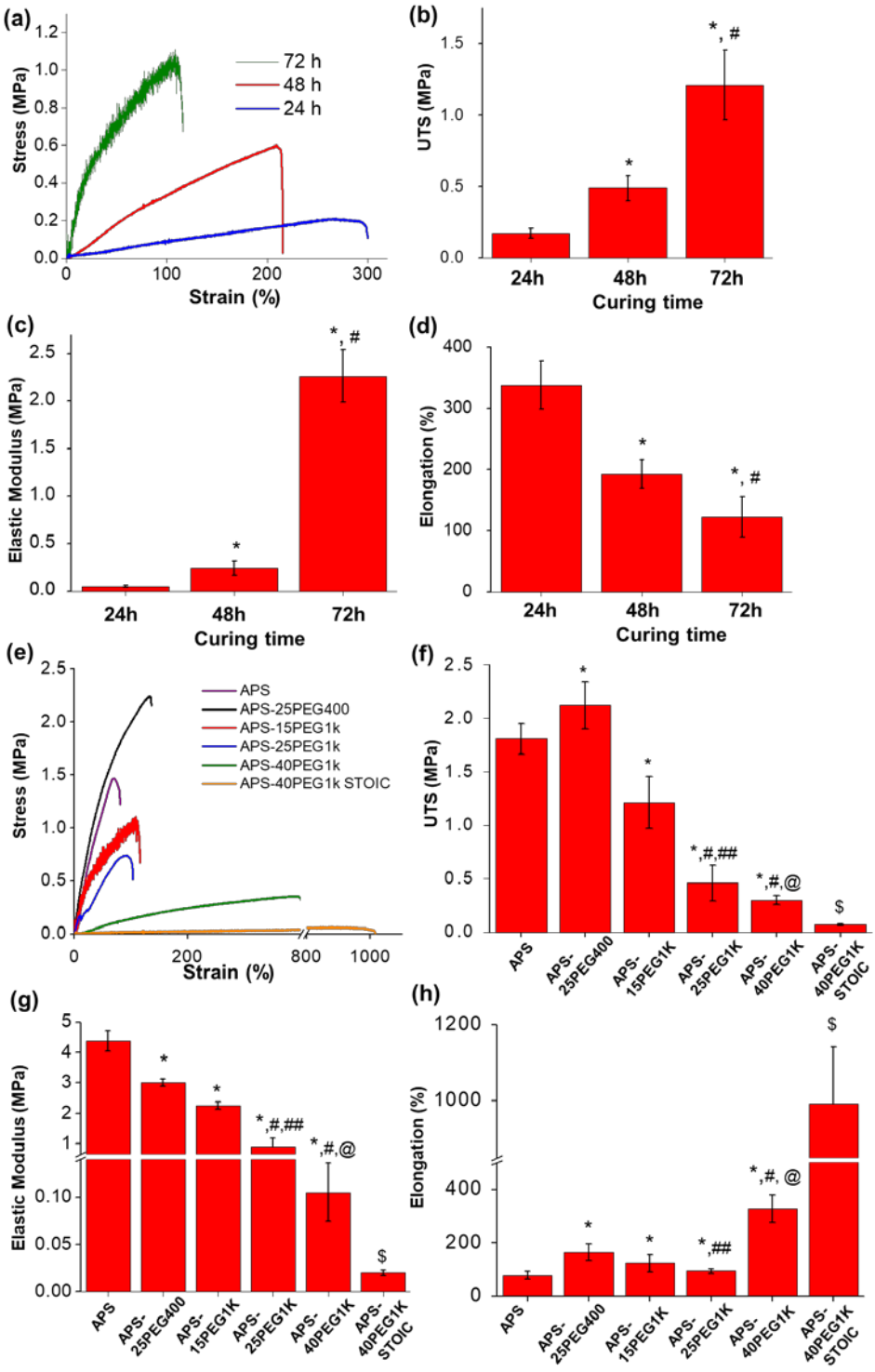

Figure 8. Mechanical properties of APS-co-PEG polymer film.

(a)-(d) Effect of curing time on the mechanical properties of APS-co-PEG polymer film (N=4) Significant differences at $p < 0.05$ (*) compared to 24 h curing and (#) compared to 48 h curing.

(e)-(h) Effect of PEG ratio and stoichiometry ratio on the mechanical properties of APS-co-PEG polymer film (N=4). All films were thermally cured for 72h. Significant differences at $p < 0.05$ (*) compared to APS, (#) compared to APS-15PEG1K, (##) compared to APS-25PEG400, (@) compared to APS-25PEG1K, ($) compared to APS-40PEG1K.

The effect of curing time on the mechanical properties of the polymer films is summarized in **Fig. 8 a-d**. APS-15PEG1K exhibited different mechanical properties after curing at 12, 48, or 72 h. The crosslinking density increased with curing time, which resulted in a significant increase in UTS (0.17 MPa to 1.21 MPa) and elastic modulus (0.05 MPa to 2.26 MPa), while elongation was reduced significantly from 338% to 123% ($p<0.05$, One-way ANOVA). Importantly, by only changing the curing time of the same pre-polymer, we were able to tune more than a 6-fold difference in UTS and 40 fold differences in elastic modulus. Similar trends of mechanical properties were also observed in APS-25PEG1K that was cured for 48 h and 72 h (**Table 9**).

Table 9. Summary of the mechanical properties of APS-co-PEG polymer film (N=4).

	APS-15PEG1K 24h	APS-15PEG1K 48h	APS-15PEG1K 72h	APS-25PEG1K 48h	APS-25PEG1K 72h	APS-25PEG400 72h	APS-40PEG1K 72h	APS-40PEG1K 72h Stoic
UTS(MPa)	0.17±0.03	0.49±0.09	1.21±0.24	0.13±0.02	0.46±0.17	2.12±0.22	0.30±0.04	0.07±0.008
Elastic Modulus (MPa)	0.05±0.01	0.24±0.07	2.26±0.28	0.10±0.01	0.9±0.24	3.01±0.12	0.11±0.03	0.02±0.002
Elongation at break (%)	338±39	193±24	123±33	317±74	93±9	165±32	326±52	993±149

The effect of PEG content and monomer feeding ratio on the mechanical properties of the polymer films are summarized in **Fig. 8 e-h**. Here, curing time for each copolymer film was fixed at 72 h to ensure direct comparison of different APS-co-PEG elastomers. The increase in PEG mole % from 15% to 40% resulted in the significant reduction in UTS (from 1.21 MPa to 0.30 MPa) and elastic modulus (from 2.26 MPa to 0.11 MPa) ($p<0.05$, One-way ANOVA). This also led to significant increase in elongation (123 to 326%) ($p<0.05$, One-way ANOVA) suggesting the formation of more elastic and ductile films. The effect of PEG molecular weight on the mechanical properties of the films was assessed by comparing APS-25PEG400 with APS-25PEG1K. APS-25PEG400 exhibited significantly higher UTS, elastic modulus, and elongation ($p<0.05$, Student's paired t-test). As the presence of higher molecular weight PEG segments in APS-25PEG1K increased its degree of crystallization (**Fig. 6**), it was expected that the corresponding films should be stronger and stiffer than low molecular weight PEG containing pre-polymer (APS-25PEG400) [194]. However, opposite trends were observed. These results could be explained based on the reduced crosslinking density. It is noteworthy to mention that presence of higher mole % or molecular weight of PEG segments interfered with the crosslinking of thermally cured films, leading to reduced crosslinking density at the same thermal curing condition. This result was in accordance with our observation that APS-25PEG2K and APS-25PEG4K cannot be cured due to the steric hindrance of increased PEG segments posed on the crosslinking process. Another possible explanation for reduced UTS and increased elongation with higher PEG concentration and molecular weight can be based on the plasticizer effect of PEG (reduced T_g observed by DSC, **Figs. 5 and 6**) as reported previously for chitosan films [200]. The addition of PEG into chitosan films resulted in reduced T_g as well as tensile stress along with higher elongation, which was attributed to its plasticizer effect [200].

The effect of monomer feeding ratio on the mechanical properties of the films was assessed by comparing APS-40PEG1K and APS-40PEG1K STOIC polymer. APS-40PEG1K STOIC exhibited significantly weaker mechanical properties as shown in **Table 9** (4 fold reduction in UTS). This may be attributed to the reduced availability of free hydroxyl groups (of G and DAHP) for crosslinking, leading to a reduced crosslinking density and consequently, decreased UTS and elastic modulus, however remarkably higher extensibility (more than 1000%) ($p<0.05$, Student's paired t-test). When compared to the mechanical properties of existing elastomers, APS-40PEG1K STOIC is among the most elastic ones, with a similar elastic modulus (0.02 ± 0.002 MPa) to that of human smooth muscle [201]. However, its weak mechanical strength may limit its biomedical application.

In summary, these results demonstrate that the mechanical properties of APS-co-PEG elastomers could be carefully tuned by varying curing time, PEG ratio as well as monomer feeding ratio. APS-co-PEG expanded the mechanical properties of APS by increasing UTS, reducing elastic modulus and increasing elongation. APS-co-PEG polymers possessed much wider range of mechanical properties compared to the existing thermoset elastomers such as PGS [82], APS [182] and PGS-co-PEG [192] (**Fig. 9**) as evident from the comparative fold change (highest/lowest values). For example, APS-co-PEG series of elastomers offer 150-fold change in elastic modulus compared to only 40-fold change for PGS-co-PEG series. Similarly, UTS values for APS-co-PEG series showed 34-fold change vs only 14.9-fold change for PGS-co-PEG series. Such wide range of mechanical properties of APS-co-PEG elastomers and ability to further fine-tune them by changing crosslinking time, PEG amount or MW will be useful in many applications in tissue engineering.

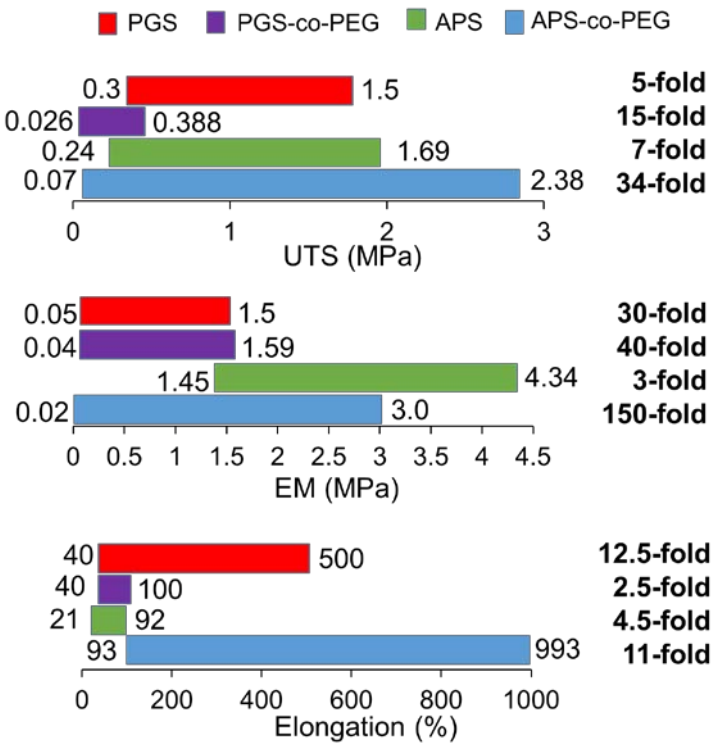

Figure 9. Summary of mechanical properties of PGS, APS, and APS-co-PEG polymer films.

3.3.4 Hydration properties and physiological degradability

Hydration and degradation studies were carried out on copolymer films cured for 72 h. Hydration is an important factor for tissue engineering applications because it influences the mechanical properties, diffusion properties, and degradation rate of the scaffolds *in vivo* [111, 192, 202]. It has been shown that the addition of PEG to the hydrophobic polymer backbone imparts hydrophilic characteristic to block copolymers [203]. To assess the hydrophilicity of crosslinked polymer films, the water-in-air contact angle of the copolymer films fabricated from different pre-polymers was measured. Increase in amount or molecular weight of PEG in the copolymer chain exhibited significant decrease in contact angles ($p<0.05$, One-way ANOVA) due to the increase in hydrophilicity of the APS-co-PEG polymers (**Fig. 10a**). Hydration of the

APS-co-PEG films was then investigated by monitoring the water uptake capacity. The swelling study under physiological conditions (DPBS, pH 7.4) revealed that APS-25PEG400 and APS-15PEG1K reached the equilibrium hydration on day 1, while copolymers containing higher PEG content (APS-25PEG1K and APS-40PEG1K) reached the equilibrium hydration on day 2. These data imply that increased amount of PEG chains in the copolymer films leads to delayed equilibrium hydration. It is possible that different crosslinking densities of APS-co-PEG may influence the kinetics of hydration [204]. Importantly, there was almost a 10-fold difference in equilibrium hydration between APS (14.0 ± 2.3%) and APS-40PEG1K (133.5 ± 3.7%) elastomer films ($p<0.05$, One-way ANOVA) (**Fig. 10b**). A high water uptake within a tissue-engineered scaffold is important to promote the mechanical deformation with minimum hysteresis under dynamic *in vivo* conditions [111, 202]. Therefore, PEG incorporation enables the tuning of hydration properties.

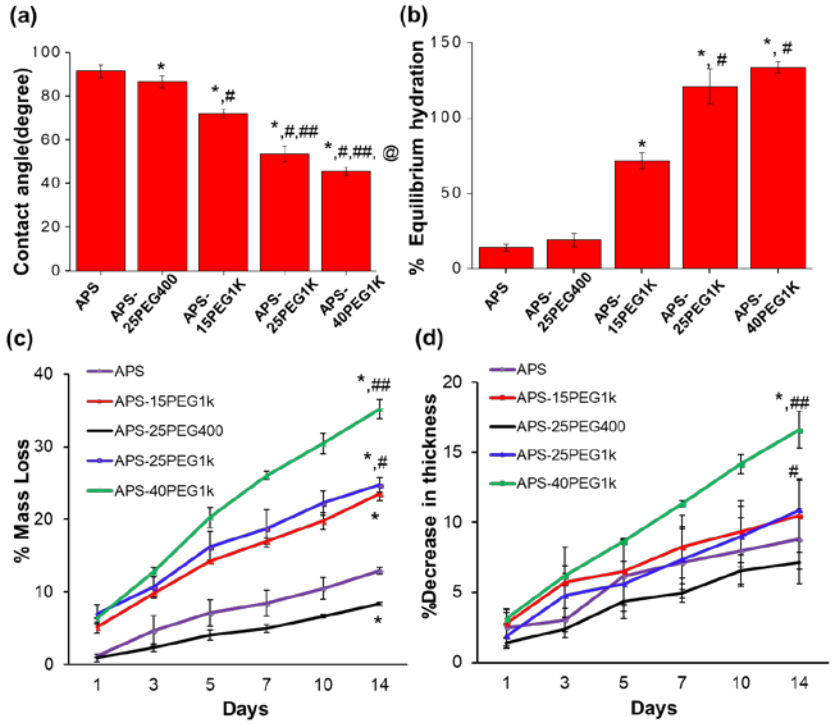

Figure 10. Hydration and degradation properties of APS and APS-co-PEG polymer films.

(a) Water in air contact angle measurement of APS and APS-co-PEG polymer films (n=4). Significant differences at $p < 0.05$ (*) compared to APS, (#) compared to APS-25PEG400, (##) compared to APS-15PEG1K, (@) compared to APS-25PEG1K. (b) Equilibrium hydration of APS and APS-co-PEG polymer films in DPBS (n=3). Significant differences at $p < 0.05$ (*) compared to APS and (#) compared to APS-15PEG1K. (c) The percent weight loss of APS and APS-co-PEG polymer films in DPBS after equilibrium hydration was reached (n=3). (d) The percent change in thickness of APS and APS-co-PEG polymer films in DPBS after equilibrium hydration was reached (n=3). Significant differences at $p < 0.05$ (*) compared to APS, (#) compared to APS-25PEG400, (##) compared to APS-15PEG1K.

The degradation study was conducted after each polymer film reached equilibrium hydration. On day 14 after equilibrium hydration, APS, APS-25PEG400, APS-15PEG1K, APS-25PEG1K, and APS-40PEG1K polymer films exhibited 12.93 ± 0.5%, 8.33 ± 0.2%, 23.5 ± 1.0%, 24.7 ± 1.0% and 35.2 ± 1.3% of mass loss, respectively (**Fig. 10c**). The increase in degradation rate with the PEG molar ratio was due to the increased hydrophilicity of polymer network, resulting in higher water uptake (**Fig. 10a, b**) and thus, accelerating the rate of hydrolysis. Diffusion of water into polymer chains is also determined by T_g of the polymer. In general, lower T_g leads to higher rate of water diffusion in the bulk [92]. As shown in **Fig. 5 and 6**, incorporation of PEG in the copolymers decreased their glass transition temperature from 5.98°C (APS) to below -30°C for APS-co-PEG polymers, thus enhancing their water uptake capacity and degradation except in APS-25PEG400. The results are consistent with previous results reported for the degradation of PEGylated elastomer [192]. However, APS-25PEG400 showed slower degradation than APS and other APS-co-PEG elastomers (**Fig. 10c**) despite of

similar water uptake to that of APS, suggesting minor role of water uptake in its degradation. Further, addition of PEG may increase the crystallinity of the polymer structure and therefore, slow down the degradation rates. However, we did not observe any cold crystallization peak in the DSC of APS-25PEG400, ruling out that possibility. Thus, slower degradation observed for APS-25PEG400 cannot be explained in our studies and needs further investigation. During degradation, there was a gradual decrease in thickness along with the mass loss in each polymer film, which was also observed in the degradation study of PGS film [205]. The percentage decrease in thickness on day 14 for APS, APS-25PEG400, APS-15PEG1k, APS-25PEG1k, and APS-40PEG1k polymer films were 8.8 ± 2.2%, 7.13 ± 1.5%, 10.5 ± 2.6%, 10.9 ± 2.1%, and 16.6 ± 2.3%, respectively (**Fig. 10d**). Almost constant rates of mass loss and linear decreases in the film thickness were observed in all series of APS-co-PEG elastomers. This suggested that the degradation of APS-co-PEG films was probably via the surface erosion mechanism. Ideally, the degradation mechanism should be further confirmed by examining the change in molecular weight of the sample during degradation. However, since APS and APS-co-PEG elastomers are thermoset elastomers, it is difficult to measure their molecular weight once they are crosslinked.

Instead, we compared the morphology of as-prepared and degraded samples by SEM (**Fig. 11**). APS-40PEG1K, which exhibited the highest rate of degradation after 14 days, was further characterized for change in film morphology after degradation. Both APS and APS-40PEG1K samples before degradation showed almost smooth surface, while the roughness of film surface increased in degraded films. Of note, no pores or cracks were observed on the surfaces of degraded samples. Importantly, cross-section of both degraded APS and APS-40PEG1K films showed morphology similar to that of films before degradation, indicating that the central portion of the films had little or no degradation. High magnification SEM images

suggested that APS-40PEG1K films might have degraded via surface erosion. Previous degradation study of PLGA, a representative thermoplastic polymer, exhibited bulk degradation, accompanying surface fracture and pore formation, a hallmark of heterogeneous degradation [183]. Such degradation mechanism is usually not favored as it results in sudden and drastic change in mechanical properties during degradation, leading to mechanical failure of the scaffold [92]. On the contrary, elastomers degraded by surface erosion are expected to exhibit gradual change in the mechanical properties due to their homogeneous surface degradation and a constant rate of mass loss, as observed in case of APS-co-PEG elastomers (**Fig. 10c, d and Fig. 11**).

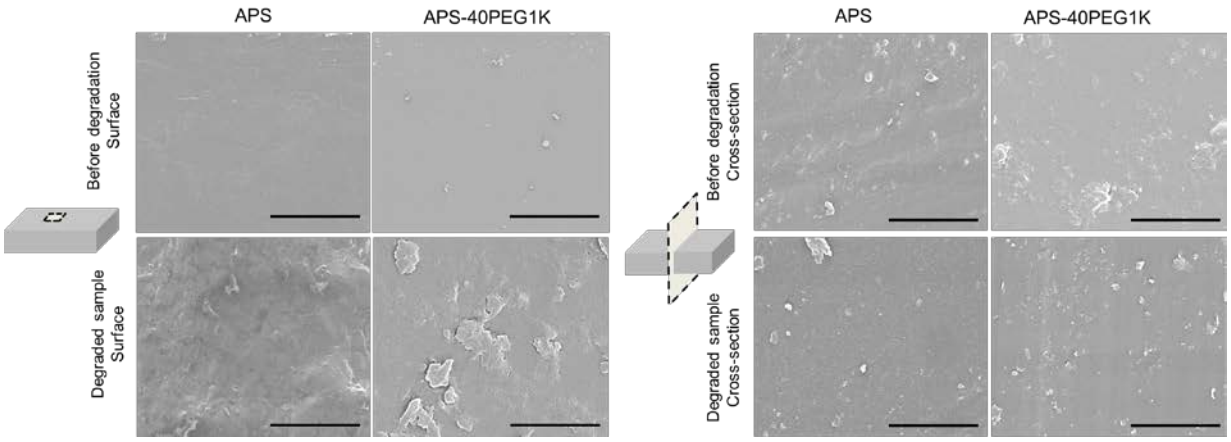

Figure 11. SEM images of as prepared APS and APS-40PEG1K film and APS and APS-40PEG1K film after 14days in PBS degradation.

Images were taken on both the surface and the cross section of the sample. Scale bars represent 1 μm in all images.

Thus, mechanical properties of degraded APS and APS-40PEG1K were measured to determine the effect of degradation. APS showed almost 30% decrease in UTS after about 13% mass loss. On the other hand, APS-40PEG1K showed similar decrease in UTS even after three-

fold higher (35.2 ± 1.3%) mass loss (**Fig. 12a**). Interestingly, APS-40PEG1K exhibited increased elastic modulus after degradation (**Fig. 12b**), which was probably due to the preferential loss of the amorphous region compared to crystalline domains. Both APS and APS-40PEG1K elastomers exhibited reduced elongation after degradation (**Fig. 12c**). These results are in accordance with previous reports where elastomer films showed reduced elongation after degradation/hydration [192, 206]. APS-co-PEG elastomers demonstrated gradual change in mechanical strength and elastic modulus after degradation, which shows their important advantage over classical polyesters such as PCL, PLGA and their copolymers since these polyesters exhibit large discrepancy in their mechanical properties in dry and wet conditions. It is suggested that this may be one of the reasons for the mechanical failure of these classical polyesters *in vivo* [207].

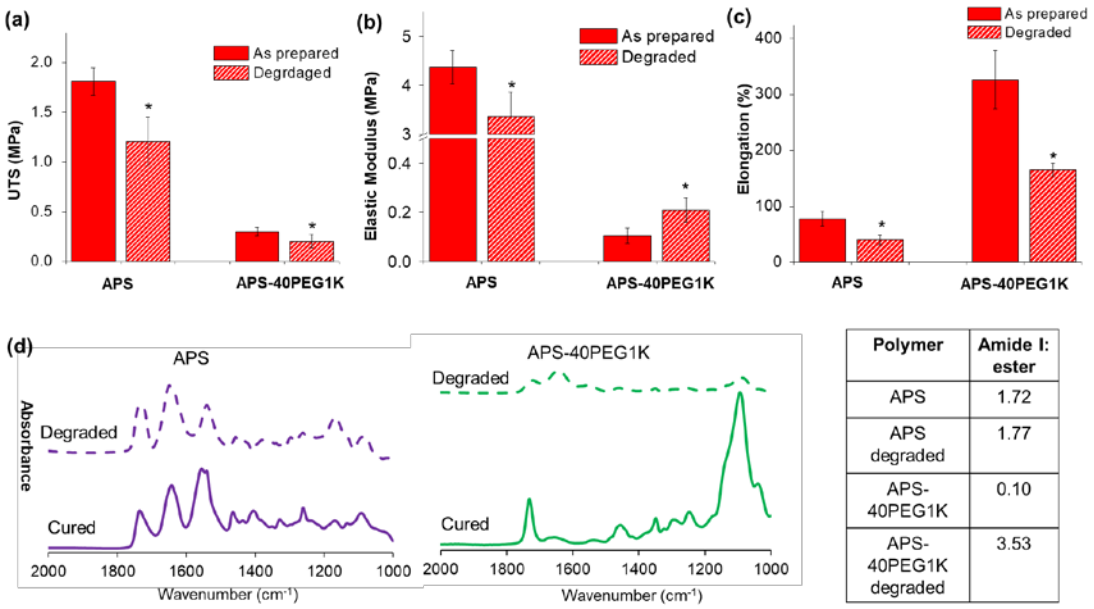

Polymer	Amide I: ester
APS	1.72
APS degraded	1.77
APS-40PEG1K	0.10
APS-40PEG1K degraded	3.53

Figure 12. Comparison between as prepared and degraded APS and APS-40PEG1K films. (a)-(c) Mechanical properties of APS and APS-40PEG1K polymers after 14 days of degradation in PBS. (N=3) $p < 0.05$ (*) compared to as prepared samples. (d) FT-IR spectra of APS and APS-40PEG1K cured polymers and cured polymer after degradation of 14 days in PBS.

Further, FTIR studies were performed on the degraded samples (**Fig. 12d**) in order to determine the functional groups of copolymer films susceptible to hydrolysis during degradation. In the FTIR spectra of APS-40PEG1K after degradation, marked increase in the intensity ratios of the amide I to carbonyl peaks of ester bond (1646/1730 cm^{-1}) was observed. Additionally, by comparing the spectra of APS-40PEG1K before and after degradation, a marked reduction in intensity of C-O-C stretching peak (1110 cm^{-1}) and C-H bending peaks (1464 & 1343 cm^{-1}) of PEG was noted (**Fig. 12d**). Taken together, these data indicated that APS-co-PEG copolymers degrade by preferential hydrolysis of ester bonds over amide bonds, resulting in faster loss of PEG segments, confirming the increased elastic modulus after degradation.

Overall, the preliminary degradation study demonstrated the ability to tune the degradation rates of APS-co-PEG elastomers over a wider range. Of note, the degradation of APS-40PEG1K is via surface erosion and preferential hydrolysis at the ester bonds in the APS-co-PEG backbone. The degradation of other APS-co-PEG elastomers needs to be studied individually and complete degradation study such as enzymatic degradation over longer periods of time *in vitro* and *in vivo* is required for the determination of suitable applications for this novel class of elastomers.

3.3.5 Cell attachment and viability

The biocompatibility of APS-co-PEG elastomers was studied by examining the cellular activities of C2C12 cells seeded on APS and APS-co-PEG elastomer films (**Fig. 13**). One of the most prominent properties of biodegradable elastomers is that they can withstand the dynamic stretch and relax without the mechanical failure [28]. This property is critical for tissue engineering

applications, particularly for soft tissues like skeletal muscle. Previously, we have shown that elastomeric APS/PCL electrospun scaffold is a promising candidate for skeletal muscle tissue engineering [208]. C2C12 cell line is one of the widely used cell lines for the regeneration of skeletal muscle [209]. Therefore, C2C12 cell line is chosen as the model cell line to examine the biocompatibility of APS-co-PEG. Since films were transferred to the new wells 24 h after initial seeding, cell metabolic activities measured by alamarBlue® assay on day 1 reflect the initial cell attachment to the films. AlamarBlue® fluorescence reading on day 1 suggested that the attachment of C2C12 cells on APS-co-PEG films was lower than APS film (**Fig. 13a**), which may be due to reduced cell adhesion on the film surface in the presence of hydrophilic PEG segments. However, cells cultured on all films exhibited significant increase ($p < 0.05$) in metabolic activities on day 3 as compared to day 1 (**Fig. 13a**). This suggests that once cells are attached to the films, the presence of PEG did not affect cell proliferation. The increase of PEG molecular weight or molar ratio did not significantly affect cell proliferation. Of note, cells seeded on APS-co-PEG films exhibited higher proliferation rates than that of APS films as indicated by the larger fold increase of alamarBlue® fluorescence reading between day 1 and day 3 (**Fig. 13b**). In order to minimize the strong autofluoresence of APS and APS-co-PEG polymers while imaging, the films were stained with Sudan Black as reported previously [193]. On day 3, C2C12 cells cultured on APS and APS-co-PEG films exhibited similar cell spreading (**Fig. 13c**). Cell morphology appears different for different polymers. This may be attributed to the differences in initial cell attachment and cell number. As shown in **Fig. 13a**, APS showed the highest metabolic activity and thus, cell number compared to PEGylated polymers on day 1 and 3 which is also evident in **Fig. 13c**, showing completely confluent cells on APS. On the other hand, APS-25PEG1K and APS-40PEG1K had less number of cells and hence, more available

area for spreading, which may have resulted in the observed differences in their morphology. These results suggest that APS-co-PEG elastomers support cell proliferation and can potentially be used for tissue engineering applications.

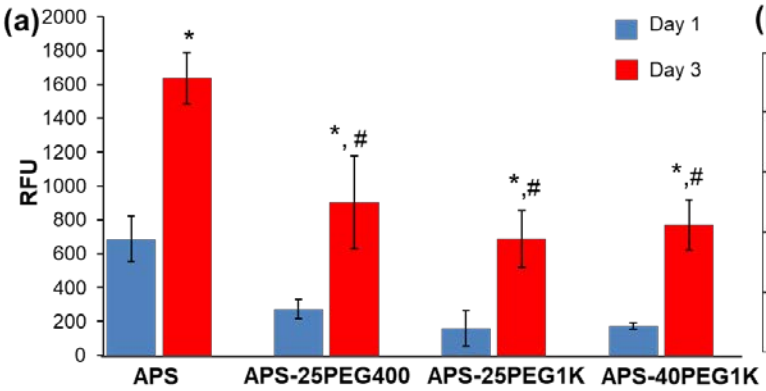

(b)

Fold Change	Day3: Day1
APS	2.38
APS-25PEG400	3.30
APS-25PEG1K	2.45
APS-40PEG1K	4.47

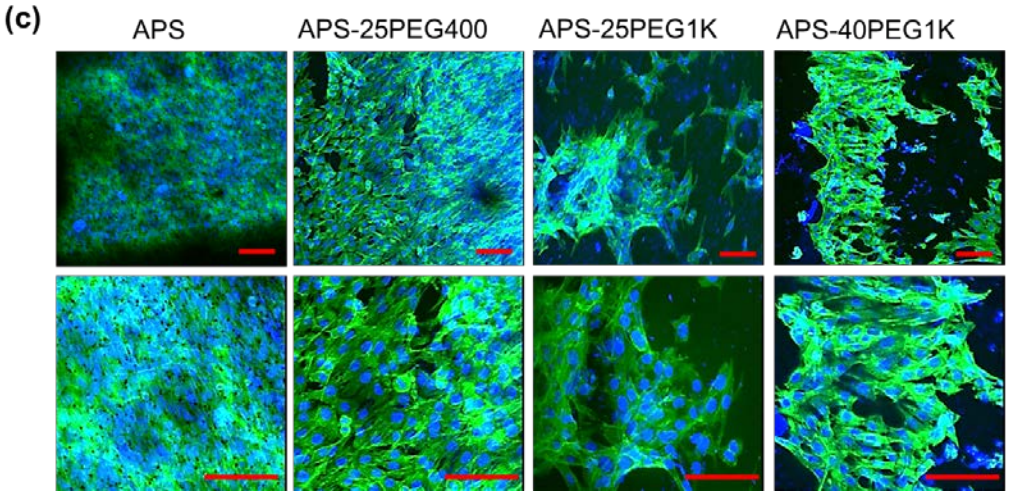

Figure 13. Cytocompatibility of APS-co-PEG films.

(a) Metabolic activity (Alamar blue) of C2C12 cells on APS and APS-co-PEG films showing increased cell proliferation over 3 days on all films. (N=3) $p < 0.05$ (*) compared to day 1 readings in each group, (#) compared to APS day 3 reading. (b) Fold change of the RFU reading from day 3 to day 1 calculated from data in (a). (c) C2C12 cells on APS and APS-co-PEG films showing similar cell morphology at day 3. Cells were fixed and actin cytoskeleton was stained with ActinGreen (green) and nuclei stained with NucBlue (blue). Scale bars represent 100 µm in all images.

3.3.6 Summary

We successfully synthesized a series of novel APS-co-PEG elastomers by varying the molar percentage and molecular weight of PEG. The physicochemical, mechanical, and degradation properties could be tailored by altering the amount and molecular weight of PEG within the APS backbone. APS-co-PEG films showed increased hydrophilicity and wide range of mechanical and degradation properties. Importantly, APS-40PEG1K degraded by surface erosion with gradual change in mechanical properties during degradation. The incorporation of PEG reduced the initial attachment of C2C12 cells but supported cell growth and spreading. This study demonstrated that APS-co-PEG elastomers have broadened the property spectrum of currently available elastomers and will allow fine-tuning of physicochemical, mechanical and degradation properties of tissue engineered scaffolds to match that of a wide range of tissues to facilitate their regeneration.

4.0 FABRICATION AND CHARACTERIZATION OF ELECTROSPUN NANOFIBERS OF PEGYLATED ELASTOMERS

[Xue Y, Yatsenko T, Patel A, Stolz DB, Phillippi JA, Sant V, and Sant S. (2017) Polymers for Advanced Technologies, 28: 1097–1106.]

4.1 BACKGROUND

One important goal of tissue engineering (TE) is to fabricate extracellular matrix (ECM)-mimetic biomaterial scaffolds [145] that can provide initial structural support and guidance to the seeded or recruited cells and allow for diffusion of nutrients and waste through the porous matrix [142]. Through appropriate biochemical and/or biomechanical guidance cues, cells can migrate, proliferate and differentiate in the scaffold and eventually, degrade the scaffold matrix and replace it with *de novo* synthesized ECM [142]. In addition to the scaffold architecture, another important design principle for TE scaffolds is to create mechanically analogous tissue substitutes [102]. Specifically, for soft tissues such as skeletal muscle and heart valves, biodegradable synthetic elastomers are considered to be one of the most promising materials because of their outstanding mechanical compliance and the ability to withstand cyclic mechanical loading without early structural failure [28, 180, 210]. Moreover, synthetic elastomers offer many

advantages over natural polymers such as facile production with less batch-to-batch variation and less immunogenicity [28, 210].

Currently, biodegradable thermoplastic polymers such as poly lactic-co-glycolic acid (PLGA) are widely used for various TE applications [22, 211]. However, these polymers often suffer from bulk degradation mechanisms *in vivo*, causing unfavorable sudden mechanical failure [183]. Therefore, there is a growing interest in biodegradable thermoset elastomers such as poly (1,3-diamino-2-hydroxypropane-co-polyol sebacate) (APS) [182, 184, 208]. Biodegradable thermoset elastomers usually degrade by surface degradation, leading to more predictable loss of mechanical properties while cells infiltrate the matrix and secrete their own ECM [92].

Our group has recently synthesized a series of PEGylated biodegradable thermoset elastomers, poly(1,3-diamino-2-hydroxypropane-co-glycerol sebacate)-co-poly(ethylene glycol) (APS-co-PEG) by varying PEG molecular weights and molar percentages [212, 213]. PEG is a well-recognized nontoxic polymer, which has been shown to reduce protein adsorption [190] and thrombogenicity of the implanted medical devices including TE scaffolds in general and currently available heart valve substitutes, in particular [120, 214]. Importantly, we have demonstrated that the mechanical properties of APS-co-PEG elastomers can be tuned by the choice of PEG molar percentage, PEG molecular weight, monomer feed ratio and cross-linking time [213]. Specifically, cross-linked APS-co-PEG elastomeric films exhibited a wide range of ultimate uniaxial tensile strength (0.07–2.38 MPa), elastic modulus (0.02–3.0 MPa) and elongation (93–993%). Additionally, the solubility of APS-co-PEG pre-polymers in common organic solvents was significantly improved compared to non-PEGylated APS elastomers [213].

Electrospinning has been comprehensively investigated for applications in TE due to its versatility and ease in processing porous scaffolds with high surface area-to-volume ratio that

can mimic native fibrous ECM [87, 88, 215-217]. We and others have shown that the electrospinning of thermoset elastomer pre-polymer along with a carrier polymer can result in elastomeric electrospun scaffolds [89, 180, 181, 208, 218]. As an example, poly(glycerol sebacate) (PGS), a benchmark biodegradable thermoset elastomer, has been studied extensively as electrospun scaffolds [87, 179, 180, 216], demonstrating the feasibility and effectiveness of electrospinning of thermoset elastomer pre-polymer along with a carrier polymer. The electrospun PGS/PCL scaffolds have tunable mechanical properties and improved biological properties than that of PCL alone. Moreover, PGS/PCL scaffolds have been shown to promote cell attachment/spreading, promote *de novo* ECM synthesis and support stem cell differentiation [87, 179, 180, 216].

This study reports the fabrication and characterization of electrospun scaffolds composed of newly synthesized APS-co-PEG elastomers with varying PEG molar ratio (APS-15PEG, APS-25PEG and APS-40PEG). PCL is used as a carrier polymer. We also demonstrate that these scaffolds support adhesion/spreading of skeletal muscle cells (C2C12) and human aortic valve cells. Importantly, we demonstrate that PEGylation of elastomers markedly reduces platelet adhesion on these scaffolds while maintaining their excellent mechanical properties, suggesting potential applications in soft tissue engineering such as skeletal muscle and heart valve tissue engineering.

4.2 METHODS

4.2.1 Materials

All organic solvents used in the study and 1, 3-diamino-2-hydroxy-propane (DAHP), glycerol (G), sebacic acid (SA), poly (ε-caprolactone) (PCL, Mw=70-90 kDa) were purchased from Sigma-Aldrich (St. Louis, MO). PEG (Mw=1kDa) was obtained from Dow Chemical (Midland, MI). Cell culture supplies including media, trypsin-EDTA and antibiotics were obtained from Corning (Corning, NY), unless otherwise mentioned.

4.2.2 Polymer synthesis

APS and APS-co-PEG pre-polymers were synthesized as described in section 3.2.1.

4.2.3 Scaffold fabrication by electrospinning

Following APS and APS-co-PEG polymer synthesis, porous scaffolds were fabricated using the electrospinning technique. Electrospinning parameters such as polymer concentration, voltage and distance were varied (**Table 10**) to obtain the optimal electrospinning conditions that result in bead-free fibers. Briefly, APS or APS-co-PEG (APS-15PEG, APS-25PEG and APS-40PEG) and ε-PCL were dissolved in hexafluoroisopropanol (HFIP) in a 4:1 w/w ratio with total polymer concentration kept constant at 17.5% w/v in HFIP. Electrospinning was conducted on a conventional electrospinning setup, using aluminum foil as collector. Solutions were electrospun at 17 kV for 1 h at a rate of 1 mL/h. The distance between the needle and collector was kept

constant at 10 cm. The obtained electrospun scaffolds were dried in a vacuum desiccator for 1 week. Scaffolds were then soaked in deionized water to allow for the removal of any sprayed polymer and remaining solvent. APS-PCL scaffold were used as control scaffold in all experiments.

Table 10. The optimization process of electrospinning parameters.

Polymer Concentration	Polymer Ratio	Distance (cm)	Voltage (kV)
15%	4:1	10	10
17.5%			
20 %			
17.5%	5:1	10	10
	4:1		
	2:1		
17.5%	4:1	8	10
		10	
		12	
17.5%	4:1	10	8
			10
			12
			14
			15
			17

4.2.4 Fourier-transform infrared spectroscopy (FTIR)

Chemical composition of the scaffolds was studied using Fourier Transform Infrared (FTIR) spectroscopy with attenuated total reflection (ATR-FTIR). The spectra were recorded in absorption mode with a resolution of 4 cm^{-1} using Bruker Vertex 70 FTIR spectrometer (Bruker, Billerica, MA). The results are presented as an average of 256 scans. The intensities of ester,

amide I, and amide II peaks were integrated for semi-quantitative analysis using Origin8 software as reported earlier [212].

4.2.5 Scanning electron microscopy (SEM)

Scaffold morphology and porosity was characterized using scanning electron microscopy (SEM) (JEOL 6335F Field Emission SEM, Japan). Fibrous scaffolds were sputter-coated with 5 nm of gold-palladium using Cressington 108 auto sputter-coater (Cressington Scientific Instruments, UK) and images were obtained using accelerated voltage of 3kV. Fiber diameter measurements were performed using NIH ImageJ software. 100 fibers were considered for calculating fiber diameters.

4.2.6 Differential scanning calorimetry (DSC) analysis

The thermal properties of electrospun scaffolds were studied by differential scanning calorimeter (DSC) (Mettler Toledo, Allison Park, PA). The scaffold (approx. 5 mg) was sealed in an aluminum pan and first heated from room temperature to 150 °C, then cooled to −70 °C, and finally reheated to 150 °C at a heating/cooling rate of 10 °C/min. All the processes were carried out under nitrogen atmosphere. Crystallization temperature (T_c) and enthalpy (ΔH_c) were obtained from the cooling cycle (150 °C to -70 °C) whereas glass transition temperature (T_g), melting temperature (T_m) and enthalpy (ΔH_m) were obtained from the second heating cycle (-70 °C to 150 °C). DSC data was analyzed using STARe software.

4.2.7 Uniaxial mechanical testing

Scaffold mechanical properties were studied using uniaxial tensile tests with ADMET MTEST Quattro mechanical testing system (ADMET, Norwood, MA). Scaffolds were cut into rectangular shapes (15×7 mm^2, n=8 per group) and stretched until failure at a constant jogging speed of 10 mm/min. The stress (MPa) was obtained by dividing the applied force (N) with cross-section area (mm^2); percent elongation (strain, ε) was obtained from equation 1, where L_o was initial gauge length and L was instantaneous gauge length. Ultimate tensile strength (UTS), maximum strain to total failure (% elongation), toughness (area under the curve of stress-strain curve), and elastic modulus in the linear region at 5-15% strain was recorded for each scaffold tested. Cyclic mechanical testing was performed at a jogging rate of 10 mm/min, by sample extension until 20% elongation during 10 consecutive cycles.

$$\text{Elongation } (\varepsilon, \%) = (L-L_o)\times 100/L_o \quad \textit{Eq. (1)}$$

4.2.8 Degradation study

In vitro degradation properties were studied by submerging 10×10 mm^2 scaffold samples (n=3) in 10 mL PBS solution in 50 mL falcon tubes. Solutions were maintained in a shaking incubator at 37 °C and 50 rpm. At predetermined intervals, the scaffolds were weighed after gentle washing in deionized water and fresh PBS solution was replaced in the falcon tubes. Mass loss, compared to the original hydrated scaffold mass, and solution pH were measured. The percentage of mass loss was calculated using Equation 2, where W_o is the initial weight of as-prepared scaffold and W_t is the weight of scaffold at each time point.

$$\text{Mass loss } (\%) = (W_o - W_t)\times 100/W_o \quad \text{Eq. (2)}$$

4.2.9 Cytocompatibility of electrospun scaffolds using mouse myoblast (C2C12) cells

The preliminary cytocompatibility of the electrospun scaffolds was studied by evaluating attachment, spreading and proliferation of mouse myoblast cells (C2C12) from ATCC (CRL-1772™) (kind gift from Dr. Adam Feinberg (Carnegie Mellon University, Pittsburgh PA)) seeded onto the scaffolds. The cells were cultured in Dulbecco's Modified Eagle Medium (DMEM) supplemented with 10% Fetal Bovine Serum (FBS) (Hyclone, Marlborough, MA) and 1% Penicillin/Streptomycin solution. Cells in passages 3-7 were used. The scaffolds (9 mm x 9 mm, n=3) were sterilized by exposing to 70% isopropanol under UV light for 30 min, washed with DPBS thrice, and seeded with C2C12 cells at a density of 45,000 cells/scaffold in a 24-well plate. The media was replenished every day.

The cell attachment and spreading of C2C12 cells were studied by staining actin (ActinGreen™ 488 ReadyProbes® Reagent, Life Technology, Waltham, MA) and nuclei of seeded cells (NucBlue® Fixed Cell Stain, Life Technology, Waltham, MA) after 6h of culture. The cell-seeded scaffolds were fixed in 4% paraformaldehyde solution (30 min), washed with DPBS thrice, followed by permeabilization and blocking using 0.1% Triton X-100 and 3% bovine serum albumin (BSA) in DPBS. Confocal images were obtained using an inverted confocal laser scanning microscope (Olympus Fluoview 1000, Japan) under 20X and 40X objectives.

The metabolic activity was measured over a period of 7 days using the alamarBlue® assay (Invitrogen, Carlsbad, CA) according to the manufacturer's protocol. Briefly, cell-seeded scaffolds (n=4) were treated with 10% v/v alamarBlue® solution in growth medium for 4 h at 37 °C. The fluorescence intensity was then measured using a microplate reader (Gen5 Biotek,

Winooski, VT) at excitation/emission wavelengths of 530/590 nm. alamarBlue® solution (10% w/v) incubated without any cells was used for blank correction.

4.2.10 Platelet adhesion assay

Human platelet-rich plasma (PRP) with a platelet density of 1 million/mL was obtained as a kind gift from Dr. Rocky Tuan lab (University of Pittsburgh, Pittsburgh, PA). Platelet adhesion assay protocol was adopted from literature [36]. The scaffolds (9 mm x 9 mm) were placed in 0.5 ml of PRP in a 24-well plate. All scaffolds were then incubated at 37 °C for 1h with gentle mixing. Scaffolds were rinsed twice with PBS and fixed with glutaraldehyde solution in PBS (2.5% v/v) for 2 h at room temperature; then the samples were dehydrated in vacuum and images using SEM as described above.

4.2.11 Adhesion and spreading of human aortic valve cells

Freshly isolated human aortic valve cells were a kind gift from Dr. Thomas Gleason (University of Pittsburgh, Pittsburgh, PA), obtained from human aortic valves with the University of Pittsburgh's Institutional Review Board approval and with informed patient consent. Valve tissues were digested in 2.5 mg/mL Collagenase IV with DMEM (+1% Penicillin/Streptomycin +1% Fungizone) for 30 min at 37 °C with gentle rocking. Digested tissue was passed through 70 µm filter and saved at 37 °C. Undigested tissue was further digested with 0.8 mg/mL Collagenase IV for 1h at 37 °C with gentle rocking. Digested tissue was passed through 70 µm filter and pool with previous digested tissue. The pooled digested tissue was centrifuged at 2000 rpm for 5 min at 4 °C and then the supernatant was discarded. Cells were resuspended in T75

flask with 12 mL Endothelial medium supplemented by Gentamicin (60µL) and Fungizone (120 µL). The cells were propagated using Endothelial Cell Growth Media Kit (Cell Applications, San Diego, CA) according to established protocols. The scaffolds (9 mm x 9 mm) were sterilized by exposing to 70% isopropanol under UV light for 30 min, washed with DPBS thrice, and seeded with valve cells using a seeding density of 300,000 cells/scaffold in a 24-well plate. After 4 days in culture, the cell-seeded scaffolds were fixed and permeabilized as described above. Human valve cell adhesion and spreading were studied by staining actin (ActinGreen™ 488 ReadyProbes® Reagent), α-smooth muscle actin (α-SMA, Mouse Anti-Human Actin, Dako, Carpinteria, CA) and nuclei of the seeded cells (NucBlue® Fixed Cell Stain). Confocal images were obtained as described above.

4.2.12 Statistical analysis

Experimental data are presented as mean ± standard deviation. Data between multiple groups were analyzed using one-way ANOVA or two-way ANOVA followed by Tukey's post-hoc analysis. P-values less than 0.05 were considered as significant.

4.3 RESULTS AND DISCUSSION

4.3.1 Fabrication of electrospun scaffold and scaffold morphology

The electrospinning conditions for preparing fibrous APS/PCL and APS-co-PEG/PCL were first optimized according to **Table 10**. It was found that hybrid APS/PCL and all APS-co-PEG/PCL

electrospun scaffolds with proper fiber formation could be successfully fabricated using optimized electrospinning parameters, namely total polymer concentration (17.5% w/v), solvents (HFIP), voltage (17kV), flow rate (1 mL/h) and collector-to-needle distance (10 cm). PCL was used as a carrier polymer. The weight ratio between APS-co-PEG and PCL was kept constant at 4:1 throughout the study to highlight the effect of APS-co-PEG.

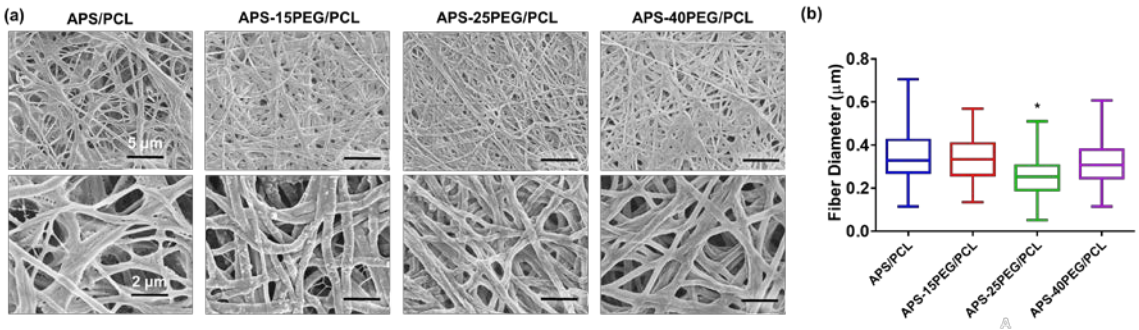

Figure 14. Fiber morphology of electrospun APS-co-PEG/PCL scaffolds studied by scanning electron microscopy.

(a) Fiber morphology of electrospun APS-co-PEG/PCL scaffolds studied by scanning electron microscopy at ×5000 (top) and ×15000 (bottom) magnification. Scale bars in top rows represent 5 µm; scale bars in bottom rows represent 2 µm (b) Average fiber diameters (n=100 fibers per group), * $p<0.05$ with respect to APS/PCL scaffolds.

Scanning electron microscopy revealed fibrous and porous structure of all scaffolds (**Fig. 14a**). The nanofibrous porous structure of electrospun scaffolds mimics the fibrous structure of native ECM and has been shown to improve the exchange of nutrients and waste products and promote cell attachment/spreading, thereby leading to higher cell proliferation [219]. SEM image analysis revealed that the average fiber diameters of all electrospun scaffolds were approximately 300 nm (**Fig. 14b**). These scaffolds exhibit a desirable fiber diameter range since cells seeded on

polymer scaffold secrete ECM proteins, like collagen, which often form fibrils of similar size [220]. It should be noted that different PEGylated elastomers did not significantly alter fiber morphology and the average fiber diameter of all scaffolds remained in the same range (around 300 nm). This is attributed to the processing of all polymer blends using constant electrospinning parameters such as polymer concentration, voltage and needle-to-collector distance, which have been shown to be the main determinants for scaffold morphology and average diameter [146].

4.3.2 Chemical properties of electrospun scaffolds

FTIR was used to characterize the chemical composition of electrospun scaffolds. The detailed FTIR analysis on APS-co-PEG polymers was presented in our previous studies [212, 213]. Briefly, APS-co-PEG polymers showed characteristic carbonyl (1730 cm^{-1}), amide I (1646 cm^{-1}), amide II (1552 cm^{-1}) peak from APS moiety and C-O-C stretching (1110 cm^{-1}) and C-H bending (1464 &1343 cm^{-1}) peaks of PEG moiety in their FTIR spectra. FTIR curves of APS-co-PEG/PCL scaffolds showed peaks from both APS-co-PEG and PCL (**Fig. 15a**). Amide to carbonyl peak intensity ratios can be used to determine the ratio of amide and ester bonds in the polymer blends [212]. Since there is ester bond but no amide bond in the PCL structure, the FTIR spectra of APS-co-PEG/PCL scaffolds showed decreased amide I: carbonyl and amide II: carbonyl ratios when compared to those of APS-co-PEG polymer alone, respectively (**Fig. 15b**). In addition, with the increase in PEG molar ratio, there is further decrease in amide: carbonyl ratio in the FTIR spectra of APS-co-PEG/PCL scaffolds, which is similar to the trend observed in APS-co-PEG elastomers [212]. Overall, FTIR results suggest that PCL was physically blended in the scaffolds with no chemical interaction with APS or APS-co-PEG elastomers, as the

characteristic carbonyl peaks of PCL (~1730 cm^{-1}) were not shifted after incorporation of PCL into the scaffolds.

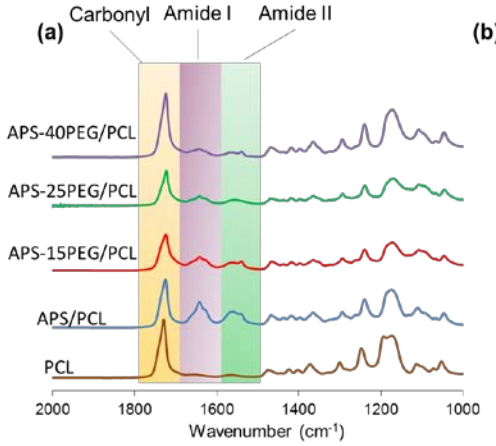

(b)

Polymer	Peak Integration Ratio Amide I: carbonyl		Peak Integration Ratio Amide II: carbonyl	
	Polymer alone	Polymer /PCL Scaffold	Polymer alone	Polymer /PCL Scaffold
APS	1.82	0.72	2.93	0.52
APS-15PEG	0.93	0.34	0.96	0.31
APS-25PEG	0.25	0.22	0.29	0.20
APS-40PEG	0.16	0.11	0.25	0.11

Figure 15. FTIR characterization of electrospun scaffolds.

(a) FTIR spectra of electrospun PCL, APS/PCL and APS-co-PEG/PCL scaffold. Ester, amide I and amide II peaks are highlighted for semi-quantitative analysis. (b) Polymer/PCL showed decreased amide peaks I (1646 cm-1) to carbonyl peak (1730 cm-1) and amide II (1552 cm-1) to carbonyl peak (1730 cm-1) intensity ratio than those of corresponding polymer alone group.

4.3.3 Thermal properties of electrospun scaffolds

The thermal properties of the scaffolds were investigated by DSC (**Fig. 16a and b**). In this study, the scaffolds were first heated to 150 °C to eliminate the thermal history. The cooling cycle (from 150 °C to -70 °C) was used to obtain crystallization temperature (T_c) and enthalpy (ΔH_c) while the second heating cycle (-70 °C to 150 °C) was used to obtain glass transition temperature (T_g), melting temperature (T_m) and enthalpy (ΔH_m). PCL, being semicrystaline polymer, did not exhibit T_g in the temperature range studied here. APS/PCL scaffolds exhibited T_g of -1.4 °C, which decreased with increasing PEG molar percentage in the APS-co-PEG elastomers from 15

to 40 mole% (**Fig. 16c**). This may be attributed to the plasticizer effect of PEG, consistent with our previous report on characterization of PEGylated elastomers [213]. It should be noted that all the scaffolds had a T_g in the range of -23 to -1 °C, which is significantly lower than the body temperature. Low T_g is usually favorable for the elastomeric scaffold since such material will be elastic *in vivo* [211]. We also examined the crystallization and melting behaviors of the scaffolds. There were no significant differences in T_c and T_m of all scaffolds, further supporting our conclusion that PCL is physically blended with APS or APS-co-PEG elastomers (**Fig. 16a-c**). As revealed by high values of ΔH_c and ΔH_m, electrospun PCL scaffolds maintained crystalline nature of PCL polymers while the presence of amorphous APS polymers in APS/PCL hybrid scaffolds reduced the crystallinity of these scaffolds. Interestingly, there was an increase in ΔH_c and ΔH_m of APS-co-PEG/PCL hybrid scaffolds with the increase in the PEG ratio in APS-co-PEG elastomers. This observation is in accordance with previous reports that the addition of PEG resulted in the increased crystallization tendency as well as the degree of crystallization [187, 197].

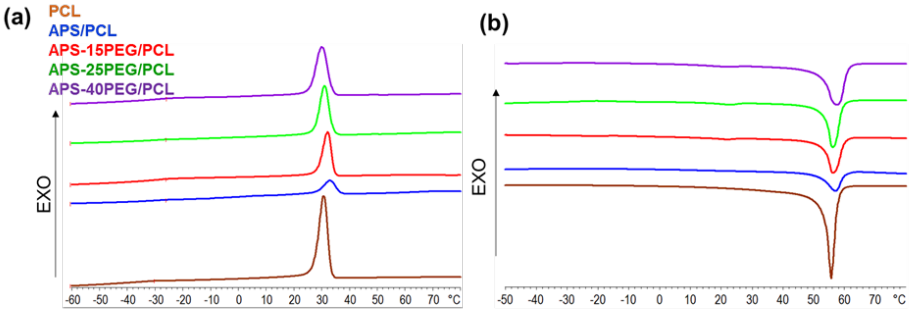

(c)

Polymer Scaffold	T_g(°C)	T_c(°C)	ΔH_c (Jg^{-1})	T_m(°C)	ΔH_m (Jg^{-1})
PCL	NA	30.6	50.0	55.6	58.4
APS/PCL	-1.4	32.7	11.6	56.9	15.3
APS-15PEG/PCL	-14.5	32.1	26.5	56.1	23.7
APS-25PEG/PCL	-15.4	30.8	31.7	56.2	29.4
APS-40PEG/PCL	-23.9	29.9	38.3	57.7	34.6

Figure 16. Thermal properties of electrospun APS-co-PEG/PCL scaffolds.

(a) DSC curves of the cooling cycle and (b) the heating cycle of APS-co-PEG pre-polymers; (c) Summary of the thermal properties of electrospun scaffolds. T_g: glass transition temperature; T_c: crystallization temperature; ΔH_c: crystallization enthalpy; T_m: melting temperature; ΔH_m: melting enthalpy.

4.3.4 Uniaxial mechanical properties of electrospun scaffolds

To test the mechanical properties of the scaffolds, uniaxial tensile test was performed (**Fig. 17a**). The ultimate tensile stress (**Fig. 17b**), stiffness (**Fig. 17c**) and toughness (**Fig. 17d**) of scaffolds increased with PEG concentration in APS-co-PEG ($p<0.05$, One-way ANOVA). This direct relationship was expected since the increase in degree of crystallization (**Fig. 16c**) usually leads to stronger and stiffer materials [221]. Overall, APS-co-PEG/PCL scaffolds showed tunable mechanical properties. It is noteworthy that the mechanical properties of these scaffolds may be further tuned by changing the ratio of APS-co-PEG/PCL ratio and other electrospinning parameters. It has been widely acknowledged that tailoring the mechanical properties of TE scaffold with that of native tissue is crucial to guide the tissue regeneration [92]. Therefore, APS-co-PEG/PCL scaffolds with wide range of mechanical properties might be promising constructs for TE biomaterials used in an array of tissues.

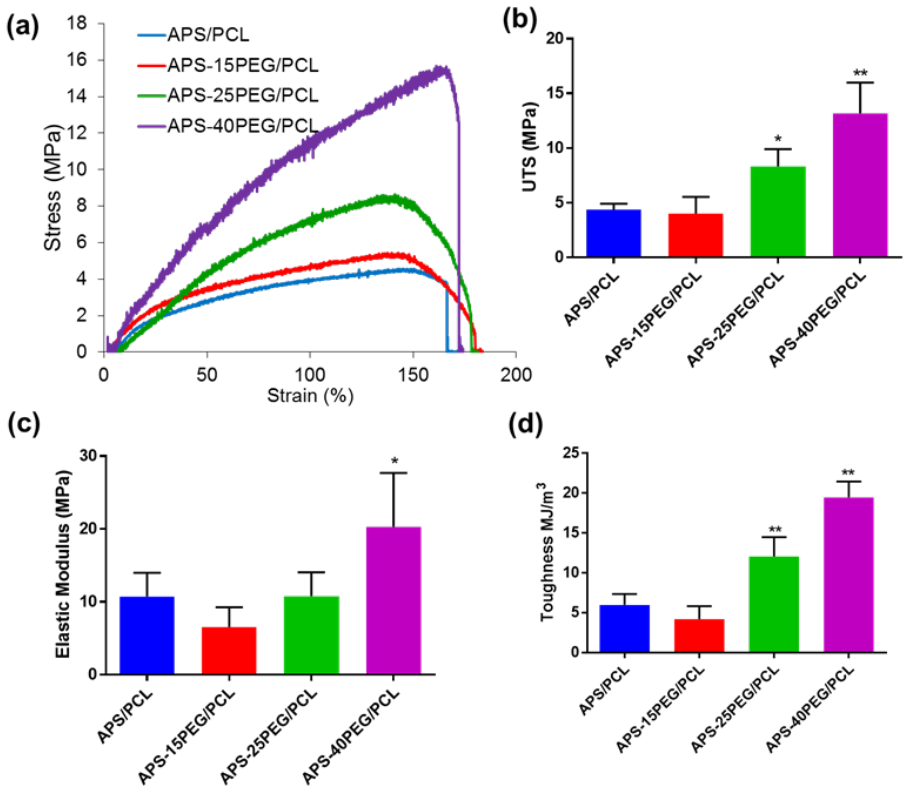

Figure 17. Mechanical properties of electrospun APS/PCL and APS-co-PEG/PCL scaffolds. (a) Representative stress strain curves of APS-PEG/PCL electrospun scaffold; (b) ultimate tensile strength (UTS); (c) elastic modulus; and (d) toughness of APS-co-PEG/PCL scaffolds (n=8). Significant differences at $p < 0.01$ (*) or $p<0.001$ (**) when compared to APS/PCL.

4.3.5 Physiological degradability

From the *in vitro* degradation study, it was found that all scaffolds degraded at a similar rate, with no statistical differences between APS-co-PEG/PCL and APS/PCL (**Fig. 18a**). All scaffolds exhibited around 50% mass loss after 2 weeks in PBS. Degradation of all scaffolds followed a linear trend suggesting that the primary mechanism was probably through surface degradation

[222]. Scaffold degradation by surface erosion is generally considered advantageous since it maintains the scaffold geometry with gradual decrease in mechanical properties unlike the sudden mechanical failure observed during bulk degradation. Interestingly, the varying amounts of PEG did not influence the degradation rate of scaffolds unlike in the case of thermally cross-linked APS-co-PEG films [213]. This may be attributed to multiple reasons. First, in our previous study, the varying degradation rates of thermally cross-linked APS-co-PEG films containing different PEG amounts were partially attributed to the different crosslinking density of the polymer structure [213]. However, in this study, APS-co-PEG pre-polymers were used, which rules out the possible influence of polymer crosslinking density thereby minimizing the difference in degradation rates. Also, nanofibrous APS-co-PEG/PCL scaffolds have significantly higher surface area than those of the cross-linked films, resulting in higher degradation rates than film scaffolds.

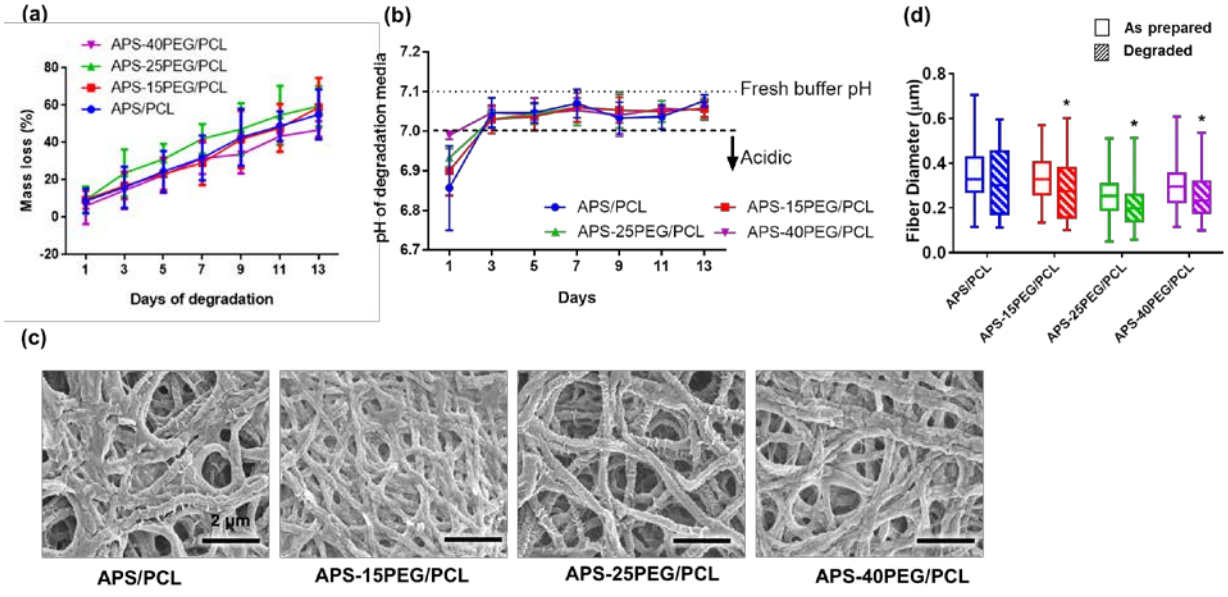

Figure 18. Degradation properties of electrospun APS/PCL and APS-co-PEG/PCL scaffolds. (a) Percentage mass loss of APS-co-PEG/PCL scaffold after degradation in PBS at 37oC (n=3); (b) Change in pH of PBS during degradation (n=3); (c) Scaffold morphology after 14 days of

degradation. All scale bars represent 2 μm. (d) Average fiber diameters of as prepared and degraded scaffolds. (n=100 fibers per group) * $p<0.05$

The pH change during degradation is an important parameter since acidic degradation products might cause *in vivo* inflammatory responses [223]. A slightly lower pH compared to the initial buffer pH of 7.1 was observed throughout the study for all experimental groups (**Fig. 18b**), indicating that acidic degradation products were released from all scaffolds particularly at the beginning of the study. However, the pH of degradation solution in all APS-co-PEG/PCL groups was found to be near or higher than 7 at all times during degradation (**Fig. 18b**). Of note, on day 1, all APS-co-PEG/PCL scaffolds had less pH reduction in degradation media than APS/PCL scaffold. Also, the drop of pH in degradation solution was less after day 1, despite a constant rate of mass loss rate (**Fig. 18a**). These results suggested that APS-co-PEG/PCL scaffolds might lead to less *in vivo* inflammatory responses due to acidic degradation products, but confirmation will require further study.

Scaffold morphology was investigated after 2-week degradation by SEM (**Fig. 18c**). SEM images showed that all scaffolds maintained nanofibrous structure even after about 50% mass loss, although the scaffold surface showed increased roughness. Furthermore, mean fiber diameter of each group was significantly reduced after the degradation study, affirming that the degradation was probably by surface degradation (open vs. lined squares in **Fig. 18d**) ($p<0.05$, Two-way ANOVA).

4.3.6 Cytocompatibility of electrospun scaffolds

Biocompatibility is a crucial factor in determining the application of TE scaffolds. A mouse myoblast cell line (C2C12) was chosen as a model system to evaluate biocompatibility of different scaffolds. Initial attachment and spreading of C2C12 cells on scaffolds were examined by immunostaining of cell nuclei and cytoskeleton after 6h of culture following cell seeding (**Fig. 19a**). APS/PCL (control) scaffolds exhibited high initial cell attachment and spreading morphology, which is consistent with previous study on APS/PCL scaffold [208]. As expected, APS-co-PEG/PCL groups showed reduction in initial cell attachment, which may be attributed to the increased scaffold hydrophilicity resulted from the presence of PEG in the elastomer [224]. Previously, APS-co-PEG elastomer films also showed reduced initial cell attachment compared to APS film [213]. However, APS-co-PEG/PCL scaffolds did support cell spreading, indicated by the stretched cell morphology similar to APS/PCL groups 6h post cell seeding. Cell proliferation on scaffolds were investigated from day 1 to day 7 using alamarBlue® assay, which measures the metabolic activity of cells (**Fig. 19b**). We observed that all the scaffolds supported cell proliferation, indicated by an increase in alamarBlue® fluorescence reading from day 1 through day 7. Of note, there was no difference in cell proliferation between APS-co-PEG/PCL scaffolds and APS/PCL scaffolds on day 1 and day 3. However, on day 7, there was a higher metabolic activity for cells seeded on APS-25PEG/PCL scaffolds than all other scaffolds ($p<0.05$, Two-way ANOVA). All other APS-co-PEG/PCL scaffolds had similar cell viabilities to that of APS/PCL scaffold, consistent with the notion that they all support cell proliferation. These results indicate that APS-co-PEG/PCL scaffolds are biocompatible and can be explored further for soft tissue engineering.

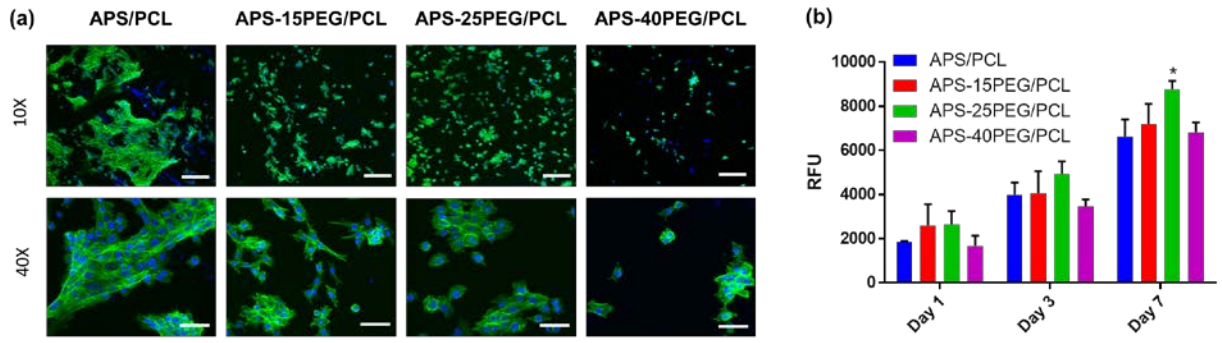

Figure 19. Cytocompatibility of electrospun APS/PCL and APS-co-PEG/PCL scaffolds with mouse myoblast (C2C12).

4.3.7 Potential of APS-co-PCL scaffolds for heart valve tissue engineering

Current heart valve substitutes such as mechanical valves have thrombogenicity issue or suffer from poor mechanical compliance, which results in the biomechanical mismatch between the device and the tissue, ultimately leading to the device failure [225]. Tissue engineered heart valve substitutes with tailored mechanical properties offer important alternative therapeutic strategy for patients with valvular heart disease [12, 76, 78, 226]. More importantly, tissue engineered heart valves can be designed from biodegradable polymers functionalized to reduce the thrombogenicity observed with mechanical valve substitutes. It has been shown that the presence of a PEG moiety can markedly decrease the thrombogenicity of polymeric materials [214, 227]. Therefore, PEGylated elastomers offer excellent opportunities for heart valve TE where high mechanical compliance of the elastomers can sustain dynamic mechanical environment present in the native valve tissue. Furthermore, presence of PEG in the elastomer backbone can mitigate the thrombogenicity observed for currently available heart valve substitutes.

To test our hypothesis that PEGylation results in less thromobogenicity, we exposed control PCL, APS/PCL and PEGylated APS/PCL (APS-15PEG/PCL, APS-25PEG/PCL and APS-40PEG/PCL) scaffolds to PRP and investigated their ability to resist platelet adhesion. All APS-co-PEG/PCL scaffolds displayed lower platelet adhesion than PCL and APS/PCL scaffolds as qualitatively assessed from SEM images (**Fig. 20**). Furthermore, the morphology of adhered platelets was evaluated by Cooper's classification of platelet adsorption [227, 228]. In PCL and APS/PCL groups, adhered platelets exhibited spreading and dendritic morphology, which represent late stage of platelet activation. On the other hand, platelets in APS-PEG/PCL groups exhibited round morphology with no pseudopodia. Overall, these results indicate the better hemocompatibility of PEGylated APS-co-PEG/PCL scaffolds.

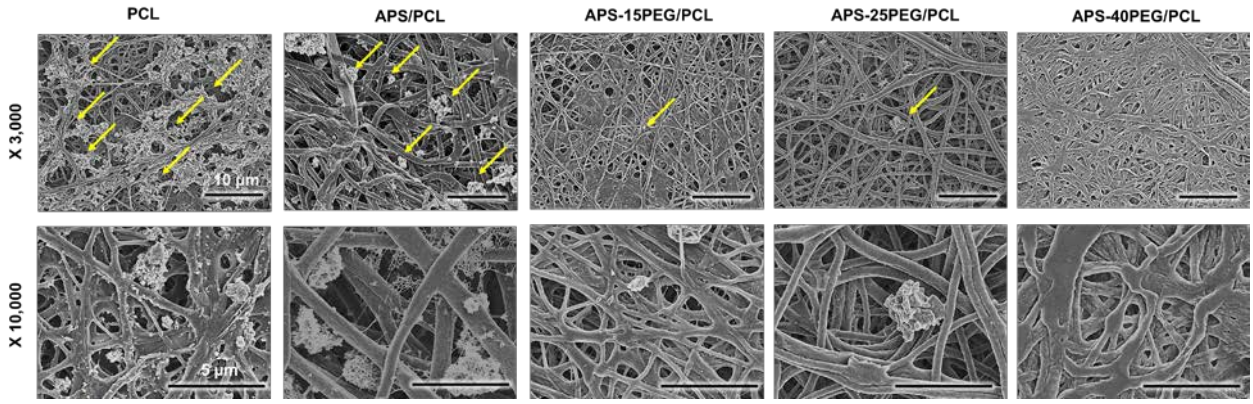

Figure 20. SEM images of platelet adhesion assay at ×3,000 and ×10,000 magnification. Arrows indicate platelet adhesion. Scale bars in top row represent 10 μm. Scale bars in bottom row represent 5 μm.

Another advantage of PEGylated elastomers as material for heart valve TE is their elastomeric properties, which can maintain the scaffold integrity in dynamic mechanical environment in cardiovascular system. Mechanically analogous scaffolds have shown beneficial effect in maintaining the structural integrity of the scaffold in dynamic *in vivo* setting and

guiding cell proliferation and tissue regeneration [229]. Hence, we compared the uniaxial mechanical properties of APS-co-PEG scaffolds with that of the native valve tissue (available from the literature, [110]). We also investigated cyclic mechanical properties and cell attachment/spreading as initial assessment of suitability of APS-co-PEG scaffolds for potential heart valve TE application. Comparing the APS-co-PEG/PCL scaffold properties to those of human heart valves, it is observed that the stress-strain curves of APS-25PEG/PCL overlap closely with that of human aortic valve tissues reported in the published literature [110] (**Fig. 21a**). In fact, both, the scaffolds and the heart valves exhibit initial flat region in the curve, where the material undergoes strain but experiences very little stress (0-5% strain). The resilience of APS-25PEG/PCL scaffold was further investigated by cyclic tensile tests. It was observed that APS-25PEG/PCL scaffolds could withstand 10 cycles of loading and unloading with minimal energy loss during the process (**Fig. 21b**). This is especially important for heart valve TE application since the implanted scaffold should withstand the dynamic mechanical environment *in vivo*, ideally over the lifespan of the patient. As a proof of concept, human aortic valve cells were cultured on APS-25PEG/PCL scaffolds for 4 days. It was found that human valve cells could attach and spread on APS-25PEG/PCL scaffolds and express the valve interstitial cell marker α-SMA (**Fig. 21c**). Taken together, APS-25PEG/PCL scaffolds may have potential in heart valve TE and further detailed studies are underway to investigate cellular behaviors of human valve interstitial cells seeded on these scaffolds.

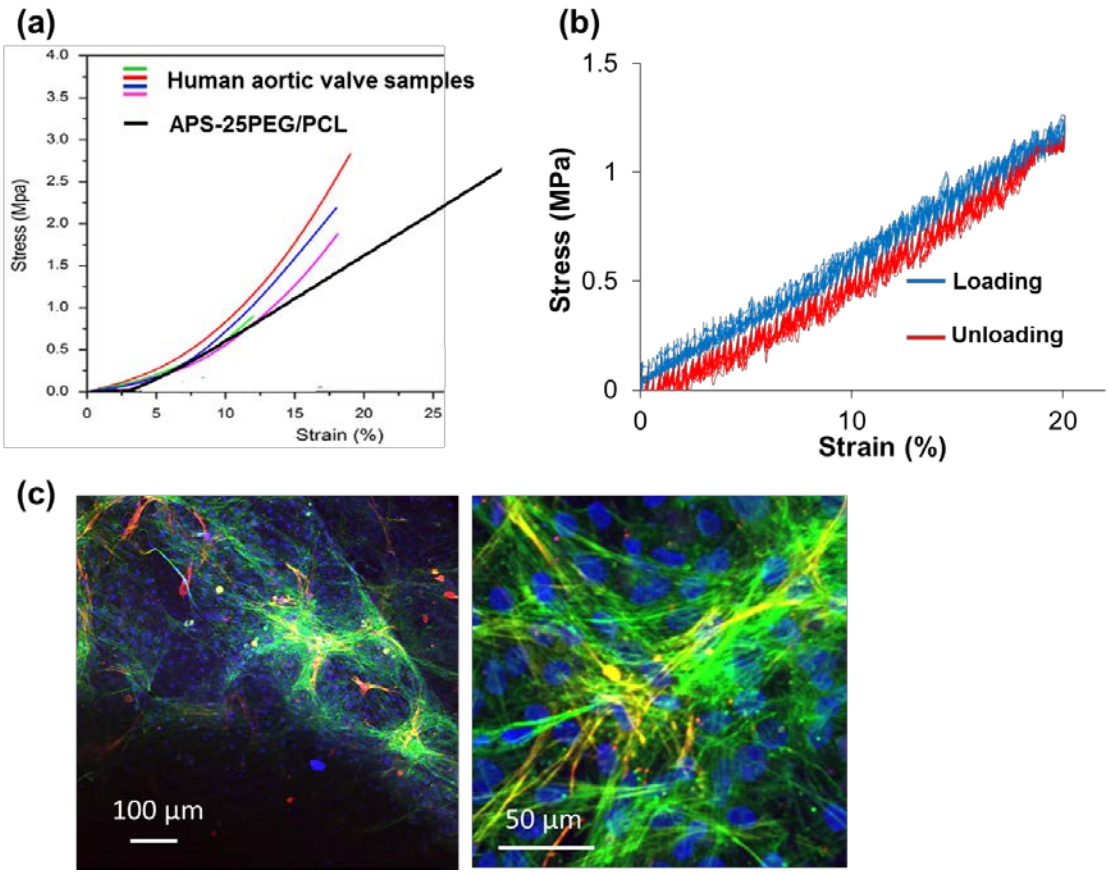

Figure 21. Mechanical and biological properties of electrospun APS-co-PEG/PCL scaffolds applicable to heart valve TE.

(a) Overlay of the stress-strain curve of APS-25PEG/PCL with those from different human aortic valves. (data on human aortic valve samples adopted from Hasan et al. 2014); (b) Stress-strain curve of APS-25PEG/PCL scaffold during 10 cycles of tensile loading; (c) Spreading and morphology of human aortic valve cells seeded on APS-25PEG/PCL scaffold at 4 days after seeding. Actin cytoskeleton was stained with actinGreen (green); α-SMA was stained with anti-smooth muscle actin (red) and nuclei stained with NucBlue (blue).

4.3.8 Summary

A series of APS-co-PEG/PCL nanofibrous electrospun scaffolds have been successfully fabricated using PEGylated elastomers. The APS-co-PEG/PCL scaffolds exhibited low T_g below body temperature and wide range of mechanical properties, which may be exploited for various tissue engineering applications. The scaffolds degraded via surface erosion without creating acidic degradation environment. Importantly, APS-co-PEG/PCL scaffolds exhibited similar or better cell proliferation than APS-PCL scaffold. Our results show that APS-25PEG/PCL scaffold is mechanically analogous to human aortic valve, can withstand cyclic mechanical stretch, exhibits reduced platelet adhesion and supports valvular cell attachment/spreading. Overall, APS-co-PEG/PCL scaffolds may be promising scaffold for soft tissue engineering such as heart valve tissue engineering.

5.0 ANISOTROPIC FIBROUS SCAFFOLD FABRICATION AND THEIR BIAXIAL MECHANICAL CHARACTERZATION

[Xue Y, Ravishankar P., Zeballos MA, Sant V, Balachandran K, and Sant S. *Manuscript in submission*]

5.1 BACKGROUND

Scaffold-based tissue engineering approach has emerged as one of the central themes in regenerative medicine and disease modeling. The fabrication of extracellular matrix (ECM)-mimetic biomaterial scaffolds is an important strategy to improve tissue engineering outcomes [145]. Such ECM-mimetic scaffolds provide the initial structural support to the seeded or recruited cells and allow for diffusion of nutrients and waste, and more importantly, present suitable biophysical and biomechanical cues to guide the normal cell and tissue functions [142].

Soft tissues, such as heart valve leaflets, possess unique biophysical and biomechanical features that confer on them complex non-linear, exponential stress-strain properties [230, 231]. Their anisotropic nature enables them to withstand a larger stiffness in the circumferential (or fiber [232]) direction compared to its radial (or cross-fiber [232]) direction. These microenvironmental cues also determine the behavior of valvular cells. The phenotype of valvular interstitial cells (VICs), the most abundant and plastic cell population in the valve, could be modulated by the

cell culture substrates/matrix [233, 234]. It has been revealed that matrix stiffness affects the activation and osteo-differentiation of VICs [235-237]. Moreover, the morphology and architecture of the matrix have been shown to instruct the attachment and spreading of VICs [76, 78]. Several studies have performed uniaxial testing on tissue-engineered scaffolds, but this testing modality is insufficient to fully characterize the scaffold mechanical properties as it fails to capture the complex cross-coupling (stress along one axis are affected by the strain level along the perpendicular axis) experienced by anisotropic tissues [232, 238]. Planar biaxial testing helps to overcome this problem and provides a better understanding of the anisotropic mechanical properties. The stress applied to an anisotropic sample like heart valve leaflet in a planar biaxial tester represents the actual stress states/conditions experienced *in vivo*. Thus, biaxial mechanical testing helps in optimization of the critical features of scaffolds to withstand *in vivo* mechanical environment and support cellular behaviors for normal tissue regeneration. Although the anisotropic mechanical properties of native valves have been extensively studied using biaxial tensile testing [108, 109, 232, 238, 239], the biaxial tensile properties of tissue engineered scaffolds have rarely been studied.

Currently, hydrogel-based substrates have been the popular VIC culture platforms for studying the effect of matrix properties on the VIC behavior [131, 237]. Although hydrogels are viscoelastic in nature with easily tunable matrix stiffness [130, 240], most hydrogel-based systems mostly employed in their bulk hydrogel form fail to closely mimic the fibrous structure of the native valve ECM. Overall, scaffolds with fibrous structures as well as anisotropic and tunable mechanical properties are still limited.

To fabricate fibrous scaffolds mimicking native ECM, electrospinning of different natural and synthetic polymers have been widely used [215, 241]. We have previously developed

isotropic (random) fibrous scaffolds by electrospinning polymer blends of poly(1,3-diamino-2-hydroxypropane-co-glycerol sebacate)-co-poly(ethylene glycol) (APS-co-PEG) and polycaprolactone (PCL) [242]. By changing the PEG amount (15-40 mole%) in APS-co-PEG polymer, the uniaxial mechanical properties of these scaffolds could be readily modulated [242]. Interestingly, one of the polymers (APS-25PEG) yielded scaffolds with uniaxial mechanical properties similar to those of native valve leaflet [242]. Electrospinning also enables the modulation of scaffold mechanical properties by simply changing the polymer formulation parameters (such as polymer concentration and co-polymer ratios) [243-245]. Specifically, the polymer blend system developed by our group enabled modulation of three key parameters in the polymer formulation: 1) PEG amount in APS-co-PEG, 2) APS-co-PEG concentration in polymer blend with PCL, and 3) total polymer concentration. However, these scaffolds possessed isotropic fiber alignment and failed to recapitulate the anisotropic nature of heart valve.

The electrospinning collector can be designed to control the fiber morphology [80, 153]. As an example, aligned fibers were obtained when two parallel gold electrodes were used to collect electrospun polymer fibers [153]. Further, these aligned fibers were assembled into multilayered structures with more sophisticated patterns [153]. Others have designed the electrospinning collectors to modulate the fiber morphology to match that of a native valve [41]. In this study, we designed a valve leaflet-inspired ring-shaped collector to fabricate anisotropic fibrous scaffolds made of synthetic polymer blends of APS-co-PEG and PCL.

In this study, we aim to fabricate fibrous scaffolds with anisotropic fiber alignment (structure) and study its effect on the biaxial tensile behaviors of scaffold (function). We hypothesized that electrospinning polymer solution on a valve leaflet-inspired ring-shaped collector will yield anisotropic scaffolds compared to the isotropic scaffolds obtained on a

conventional flat aluminum foil surface. We further hypothesized that by changing the three parameters in the APS-co-PEG/PCL polymer blend formulation, namely 1) PEG amount in APS-co-PEG, 2) APS-co-PEG concentration, and 3) total polymer concentration will enable widely tunable structural and mechanical properties of fibrous scaffolds.

5.2 METHODS

5.2.1 Materials

All organic solvents used in the study and the chemicals, 1, 3-diamino-2-hydroxy-propane, glycerol, sebacic acid, poly (ε-caprolactone) (PCL, M_w = 70–90 kDa) were purchased from Sigma-Aldrich (St. Louis, MO). Polyethylene Glycol (PEG, M_w = 1 kDa) was obtained from Dow Chemical (Midland, MI). Cell culture supplies including media, trypsin–EDTA, and antibiotics were obtained from Corning (Corning, NY), unless otherwise mentioned. APS-co-PEG pre-polymers were prepared via the one-pot two-step condensation polymerization as described earlier [213]. Here, three APS-co-PEG pre-polymers were synthesized by varying PEG mole percentage (15%, 25%, and 40% of PEG to sebacic acid) and labeled as APS-15PEG, APS-25PEG, and APS-40PEG.

5.2.2 Electrospinning process

Fibrous scaffolds were fabricated by electrospinning. Briefly, blends of APS-co-PEG (APS-15PEG, APS-25PEG, and APS-40PEG) and ε-PCL of different polymer concentrations were

dissolved in a mixture of ethanol and chloroform at a volume ratio of 1:9 (detailed formulation and nomenclature summarized in **Table 11-13**). For fabricating isotropic scaffolds, electrospinning was conducted using a conventional electrospinning set-up with a flat aluminum foil as a collector. For fabricating anisotropic scaffolds, a custom-made ring-shaped copper wire (**Fig. 22a**) was used as a collector. For both electrospinning set-ups, solutions were electrospun at 17 kV at a rate of 1 mL/h. The distance between the 21G needle and collector was kept at 12 cm. The obtained electrospun scaffolds were dried in a vacuum desiccator overnight before further experiments.

Table 11. Polymer formulations to study the effect of PEG amount in APS-co-PEG.

APS-co-PEG type	APS-co-PEG concentration (w/v)	PCL concentration (w/v)
APS-15 PEG	6%	12%
APS-25 PEG		
APS-40 PEG		

Table 12. Polymer formulations to study the effect of APS-25PEG concentration.

APS-co-PEG type	APS-co-PEG concentration (w/v)	PCL concentration (w/v)
APS-25 PEG	3%	12%
	4%	
	6%	
	12%	

Table 13. Polymer formulations to study the effect of total polymer concentration.

APS-co-PEG type	APS-co-PEG concentration (w/v)	PCL concentration (w/v)
APS-25 PEG	5%	10%
	6%	12%
	8%	16%

5.2.3 Morphology of electrospun scaffolds

Scaffold morphology and fiber alignment was characterized using scanning electron microscopy (SEM) (Zeiss Sigma500 VP, UK). Fibrous scaffolds were sputter-coated with 5 nm of gold–palladium using Denton auto sputter coater (Denton Vacuum, Moorestown, NJ), and images were obtained using accelerated voltage of 3 kV. Images were analyzed for fiber diameters and alignment using NIH ImageJ Software with DiameterJ [246] and OrientationJ [247] plugins. At least four images (at 2000X magnification) were used from each group for analysis.

5.2.4 Uniaxial mechanical testing

Scaffold mechanical properties were studied using uniaxial tensile tests with MTEST Quattro mechanical testing system (ADMET, Norwood, MA). Scaffolds were cut into rectangular shapes (~15 × 7 mm^2, n = 4 per group) and stretched at a constant displacement rate of 10 mm/min until sample failure. All anisotropic fibrous scaffolds were tested with the fibers oriented in the direction of the stress. The stress (MPa) was obtained by dividing the applied force (N) with cross-section area (mm^2) while percentage elongation (strain, ε) was obtained from $\varepsilon\ (\%)=100\times(L-L_0)/\ L_0$, where, L_0 was initial gauge length and L was instantaneous gauge length. Elastic modulus in the linear region at 5–15% strain was calculated for each scaffold tested.

5.2.5 Biaxial mechanical testing

The electrospun scaffolds were cut into 12 × 12 mm^2 (n = 6 per group) and mounted on a frame with the specimen edges aligned to the circumferential and longitudinal axis of the planar biaxial

system (TestResources Inc., USA). After mounting, four dots were made using a permanent marker on the sample for deformation tracking. All tests were performed in 0.9% saline maintained at 37 °C. The specimens were brought to a tare load of 0.05N along each axis and preconditioned equibiaxially with a maximum membrane tension of 90 N/m for 20 cycles on each axis to mimic the physiological condition experienced by native aortic valves [102, 108]. After preconditioning, three more equibiaxial cycles (90:90 tension ratio on each axis) were conducted and used for analysis. A high-speed camera (Basler AG, Germany) and software (Pylon, Basler AG, Germany) was used to capture the deformation of the scaffolds under the equibiaxial protocol. A custom-developed MATLAB code was used to track the movement of the dots and calculate the deformation gradient tensor (F) [232]. The Green's strain (E) was calculated using: E=0.5(F^T×F-I), where I is the identity matrix. The equibiaxial stress-strain curves were plotted and analyzed to calculate the samples' linear modulus, and degree of anisotropy (**Fig. 22b**). The linear modulus (LM) calculated as the slope of the stress-strain curve at the linear region experienced at high loads. The degree of anisotropy (DA) was calculated by the ratio of maximum strains experienced on both axes at maximum loading. The DA closer to 1 denotes that the samples are isotropic in behavior while DA less than 1 denotes anisotropic behavior.

5.2.6 Isolation and culture of human valve interstitial cells (hVICs)

Human aortic valve interstitial cells (hVICs) were isolated from a healthy donor with normal valve function. De-identified human valvular tissues were collected from the University of Pittsburgh Medical Center (UPMC) as per the protocols approved by the University of Pittsburgh Institutional Review Board, PRO16050264 (St. Hilaire) and PRO0702120 with informed consent

(Dr. Gleason). The hVICs were isolated from donor tissue as per our previously reported protocol [248]. The hVICs were then propagated and cultured using DMEM supplemented with 10% fetal bovine serum according to the established protocol. All experiments were carried out by using cells between passages 4 and 8.

5.2.7 Seeding of hVICs on scaffold

Prior to cell seeding, the scaffolds (10×10 mm^2) were sterilized by exposing to 70% isopropanol under UV light for 30 min and rinsed with 1X DPBS thrice to remove any residual ethanol. The hVICs were seeded on to these scaffolds at a density of 100,000 cells/scaffold in a 24-well plate. After 24 h, scaffolds were transferred to a new well to remove the non-adherent cells. The culture was continued with media being replenished every other day.

5.2.8 Cell proliferation by alamarBlue® assay

The proliferation of hVICs seeded on the scaffolds was measured via monitoring cell metabolic activity over a period of 14 days using the alamarBlue® assay (Invitrogen, Carlsbad, CA) following the manufacturer's protocol. Briefly, cell-seeded scaffolds were treated with 10% v/v alamarBlue® solution in hVIC culture medium for 4 h at 37°C. The fluorescence intensity of solution in each well was then measured using a microplate reader (Gen5 Biotek, Winooski, VT) at excitation/emission wavelengths of 530/590 nm. alamarBlue® solution (10% w/v) incubated without any cells was used for blank correction.

5.2.9 Immunofluorescence staining

The morphology and spreading of hVICs were studied by staining actin (ActinGreen™ 488 ReadyProbes® Reagent, Life Technology, Waltham, MA) and nuclei of cells (NucBlue® Fixed Cell Stain, Life Technology, Waltham, MA) seeded on isotropic and anisotropic scaffolds (APS-25PEG/PCL, 6+12%) after 7 days of culture. The cell-seeded scaffolds were fixed in 4% paraformaldehyde solution (30 min), followed by permeabilization and blocking using 0.1% Triton X-100 and 3% bovine serum albumin in DPBS. Confocal images were obtained using an inverted confocal laser scanning microscope (Olympus Fluoview 1000, Japan) under 10X objectives. The images were quantified for its actin orientation using NIH ImageJ Software using OrientationJ [247] plugin as previously described.

5.2.10 Statistics

Experimental data are presented as mean ± standard deviation unless otherwise mentioned. Data between multiple groups were analyzed using one-way or two-way ANOVA followed by Tukey's post-hoc analysis. p values less than 0.05 were considered as significant.

5.3 RESULTS AND DISCUSSION

5.3.1 Fabrication of anisotropic fibrous scaffold

Based on our established polymer blend formulation of APS-co-PEG and PCL, we tuned the PEG amount in APS-co-PEG copolymer, concentration of APS-co-PEG, and the total polymer concentration to test the versatility of the proposed electrospinning collector and obtain scaffolds with a wide range of mechanical properties. All polymer formulations to be tested in this study (**Table 11-13**) were successfully electrospun onto both collectors using the same sets of electrospinning parameters. This enabled decoupling the effects of the collector and polymer formulation on the structural and mechanical properties of fibrous scaffolds.

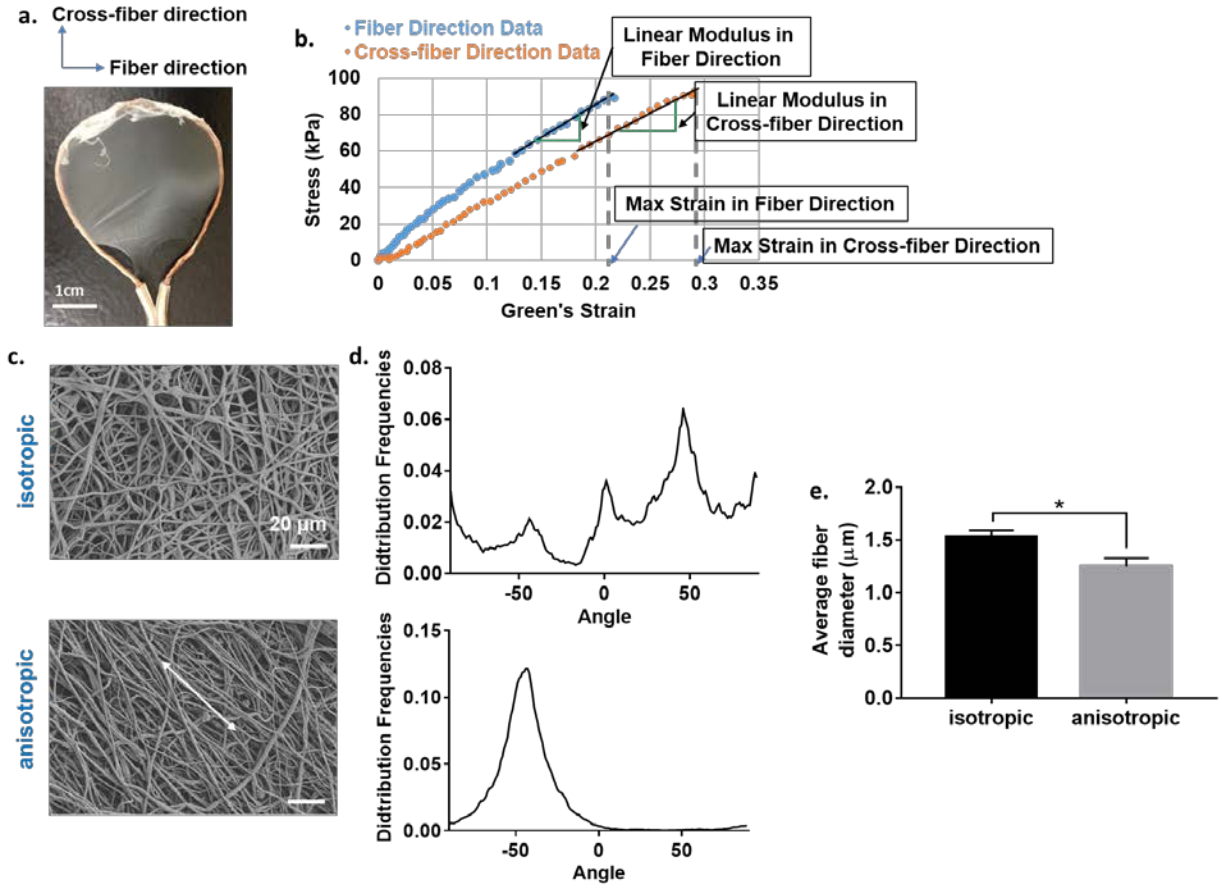

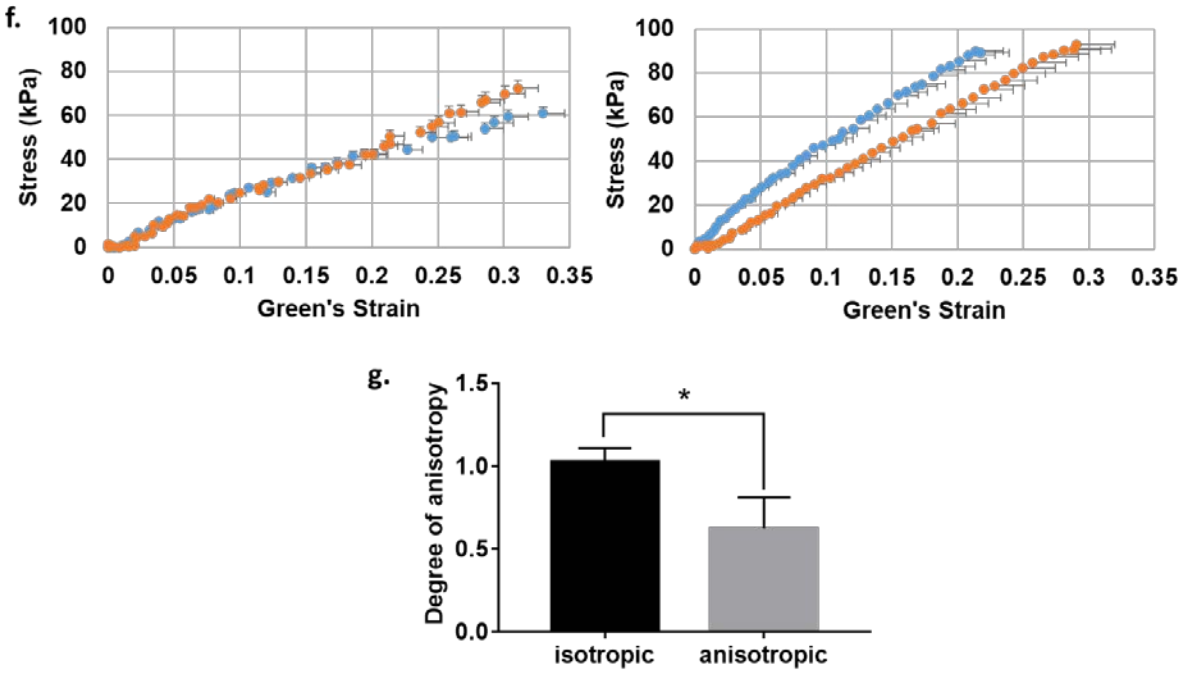

Figure 22. Electrospun fiber collected on ring collector showed anisotropy.

(a) Image of the ring collector; (b) Example of how linear modulus and max strain (used to calculate degree of anisotropy) were analyzed from the equibiaxial stress-strain curves; (c) SEM images of isotropic and anisotropic APS-25 PEG:PCL (6+12%, w/v) scaffolds, arrow indicates the fiber alignment; (d) Fiber alignment quantification by OrientationJ plugin in NIH ImageJ (n=at least 4 images); (e) Average fiber diameter quantified by NIH ImageJ (n=at least 4 images); (f) Biaxial stress-strain plots of fibrous scaffold; (g) Degree of anisotropy calculated from biaxial stress-strain plots. *indicates $p<0.05$ (Unpaired t-test).

Taking APS-25PEG:PCL (6+12%) formulation as an example, we first aimed to compare the differences between scaffolds collected on the flat aluminum foil and ring-shaped collectors. SEM image quantification revealed that fibrous scaffolds obtained from the flat aluminum foil had randomly aligned fibers showing an isotropic characteristic while those collected on the

ring-shaped collector were more aligned and anisotropic as shown by the sharp peak in the fiber alignment quantification (**Fig. 22c and d**). It was also revealed that the fibers collected on two collectors possessed different average diameters (1.527 μm ± 0.065 μm for isotropic scaffold and 1.246 μm ± 0.081 μm for isotropic scaffold) although other electrospinning parameters were kept constant (**Fig. 22e**). This is in accordance with previous reports that the geometry of the electrospinning collector could influence the fiber architecture including fiber diameter [249].

Compared to the uniaxial tensile testing, biaxial tensile testing is considered to be a more accurate characterization method to quantify the mechanical behavior of anisotropic tissues such as heart valves. Hence, we compared the differences in mechanical properties between the scaffolds obtained on flat aluminum foil and ring-shaped collector by the equibiaxial mechanical testing. These tests demonstrated that the scaffolds collected on the flat aluminum foil exhibited similar mechanical properties in two perpendicular directions, showing an isotropic behavior. On the other hand, scaffolds obtained on the ring-shaped collector behaved differently in their fiber and cross-fiber directions, showing mechanical anisotropy (**Fig. 22f**). Further quantification revealed that the scaffolds collected on aluminum foil had a DA closer to 1, indicating an isotropic mechanical behavior while the DA of scaffolds collected on the ring-shaped collector was significantly lower (and less than 1), suggesting an anisotropic behavior (**Fig. 22g**). As hypothesized, we showed that electrospinning on to a ring-shaped collector could be utilized to produce anisotropic scaffolds. In the following sections, we refer to the scaffolds collected on aluminum foil as isotropic scaffolds and those from the ring-shaped collector as anisotropic scaffolds.

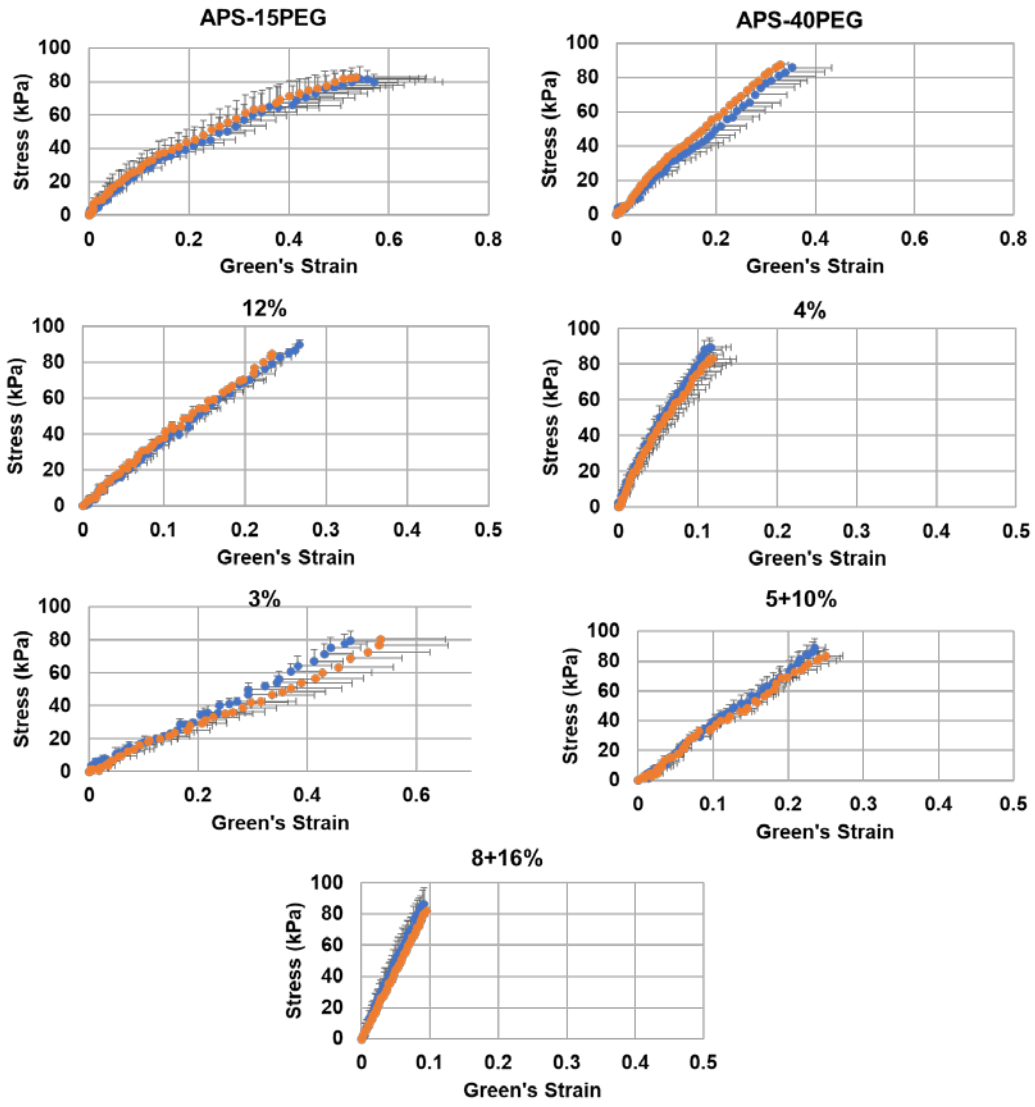

Figure 23. Biaxial stress-strain plots of isotropic fibrous scaffolds.

5.3.2 Effect of PEG amount in APS-co-PEG polymer on the mechanical properties of anisotropic electrospun scaffolds

We then aimed to elucidate the effect of polymer formulation on the scaffold mechanical properties and screen for the polymer formulation that can mimic the native valve mechanical properties. Our previous studies had indicated that the PEG amount in APS-co-PEG (PEG molar

ratio in the polymer backbone from 15%-40%) influenced the scaffold mechanical properties [213]. Here, the concentration of APS-co-PEG and PCL were kept constant at 6% and 12%, respectively, to decouple the effect of PEG amount in APS-co-PEG (**Table 11**). The corresponding results regarding the isotropic scaffolds from same formulations are reported in **Fig. 23**. Since isotropic scaffolds displayed similar mechanical properties in the two directions, we focused on the anisotropic scaffolds in the following studies due to their unique structural and mechanical properties.

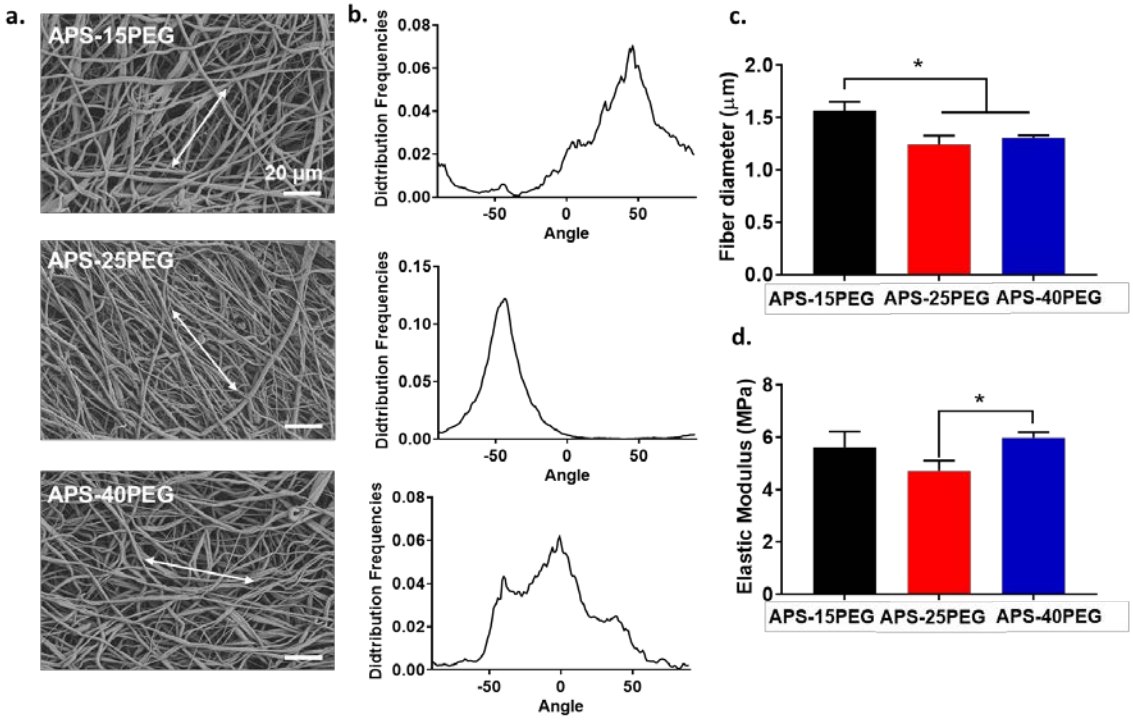

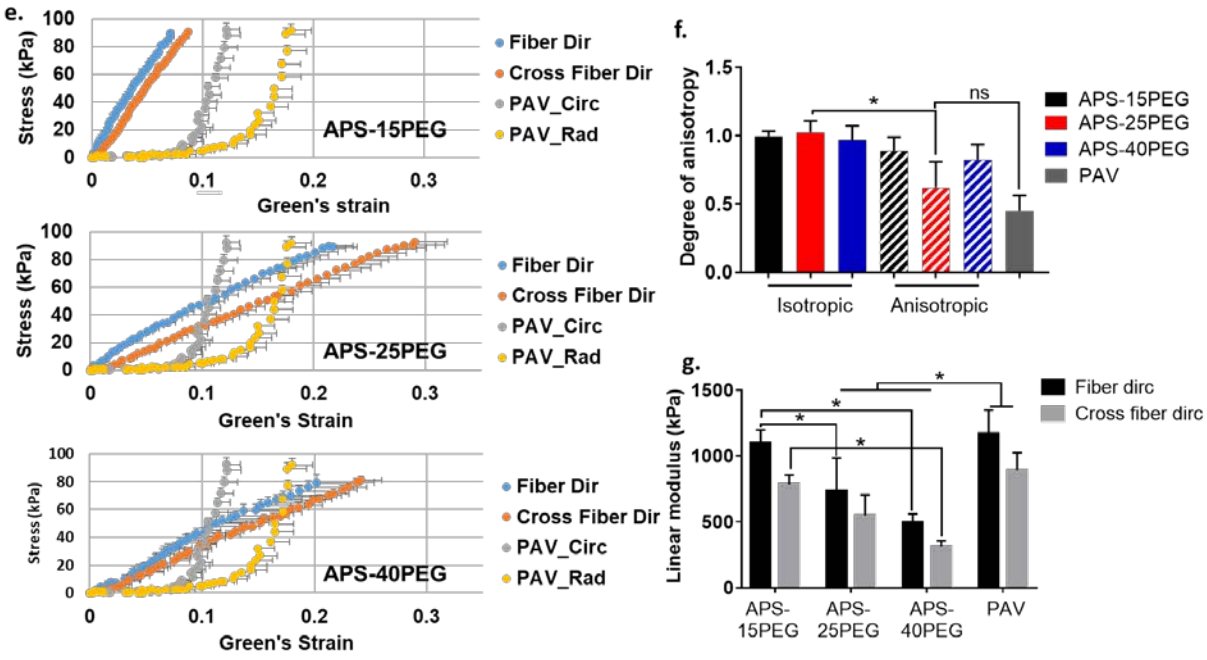

Figure 24. PEG amount in APS-co-PEG affected the scaffold structural and mechanical properties.

(a) SEM images at magnification of 2000X; (b) Fiber alignment quantification by OrientationJ plugin in NIH ImageJ (n=at least 4 images); (c) Average fiber diameter quantified by NIH ImageJ (n=at least 4 images); (d) Elastic modulus of scaffolds obtained from uniaxial tensile test; (e) Biaxial stress-strain plots of fibrous scaffolds; (f) Degree of anisotropy (DA) and (g) Linear modulus calculated from biaxial stress-strain plots. *indicates $p<0.05$ (One-way ANOVA, Tukey's post-hoc test). PAV: porcine aortic valve.

SEM images and quantification revealed the anisotropic fiber alignment of electrospun scaffolds shown by the sharp peak of fiber orientation distribution from all three groups (**Fig. 24a** and **b**). It was also observed from **Fig. 24b** that APS-25PEG scaffold seemed to have a higher degree of fiber alignment as compared to the other two types of scaffolds. All scaffolds had average fiber diameter ranging from 1-1.5 μm. Of note, APS-15PEG scaffolds had

significantly higher average fiber diameter than the other two copolymer formulations (**Fig. 24c**). It suggested that changing the amount of PEG in APS-co-PEG impacted the fiber morphology. Such effects may probably be due to the change in the hydrophilicity of polymer solutions with the changes in the PEG amount [146]. Uniaxial mechanical test showed that the scaffolds had an elastic modulus within the range of 4-6 MPa while native valve has been shown to have modulus from 2-15 MPa [110]. We also observed that APS-40PEG scaffolds had significantly higher modulus than APS-25PEG scaffolds (**Fig. 24d**). This is in agreement with our previous study on isotropic APS-co-PEG scaffolds where a higher modulus of APS-40PEG was attributed to its higher degree of crystallization [213].

Biaxial mechanical behavior of the scaffolds was also influenced by the amount of PEG in APS-co-PEG (**Fig. 24e**). In accordance with the fiber alignment quantification (**Fig. 24b**), APS-25PEG scaffold demonstrated the lowest DA among the three formulations and was significantly lower than its isotropic counterpart (**Fig. 24f**). Interestingly, the anisotropic APS-25PEG scaffold possessed a DA close to that of a porcine aortic valve (PAV). It was also noted that for APS-15PEG and APS-40PEG scaffolds, the DA of isotropic and anisotropic scaffolds were not significantly different. This observation was in agreement with the quantification of fiber alignment (**Fig. 24b**), indicating that the fiber architecture affected the anisotropy in biaxial tensile properties. The linear modulus of scaffolds in the fiber direction and cross-fiber direction was quantified from the equibiaxial stress-strain curves (**Fig. 24g**). APS-15PEG and APS-25PEG scaffolds had a linear modulus close to that of PAV at around 1000 kPa. Also, APS-15PEG scaffolds had significantly higher linear modulus compared to APS-25PEG and APS-40PEG scaffolds. This trend was not in complete agreement with the elastic modulus results from the uniaxial tensile test (**Fig. 24d**). We speculate that both, fiber architecture (alignment, **Fig. 24b**

and fiber diameter, **Fig. 24c**) and the intrinsic properties of the polymer blends (such as the crystallinity of the formulation) contributed to the scaffolds' biaxial mechanical behaviors. It is also possible that when scaffolds were stressed on both axes simultaneously, the mechanical behaviors may differ from those when stressed uniaxially.

It is also noted that the polymeric scaffolds and native valve tissue were not identical in their biaxial mechanical behaviors. As shown in the equibiaxial stress-strain plots obtained using physiological level of stress (**Fig. 24e**), PAV displayed non-linear mechanical behavior with two distinct linear regions. The initial toe region is attributed to the stretching of coiled collagen fibers, which is followed by a second stage where further elongation of the straightened collagen fibers results in a steep rise in tensile stress until the tissue attains maximum extensibility [250]. On the other hand, polymeric scaffolds, in general, as shown by us and others [250-253], have a relatively linear mechanical behavior. We speculate that the observed differences may also be due to the missing gel-like and glycoprotein-enriched spongiosa layer of native valve in the fabricated fibrous scaffolds. It is well known that spongiosa layer provide shock-absorbing and viscoelastic mechanical behaviors to the valve.

Overall, we demonstrated that the amount of PEG in the APS-co-PEG polymer backbone modulated fiber alignment and biaxial mechanical properties. Due to the lowest DA (and similar to that of PAV) achieved by anisotropic APS-25PEG scaffold, we selected APS-25PEG as a polymer of choice in the following studies.

5.3.3 Effect of APS-co-PEG concentration on the mechanical properties of anisotropic electrospun scaffolds

We continued to study the effect of APS-co-PEG concentration on the structural and mechanical properties of fibrous scaffolds. The concentration of APS-co-PEG in the polymer blend can potentially impact the scaffold properties via changes in hydrophilicity, polarity, and crystallinity [254, 255]. However, this effect has not been carefully investigated in our previous study. Here, the concentration of PCL (carrier polymer, which dominates the solution viscosity) was kept constant at 12% w/w while changing the concentration of APS-25PEG from 3% to 12% (**Table 12**). This study design allowed the investigation on the effect of APS-25PEG concentration. However, it should be noted that the total polymer concentration was also changed in the process. To better study the effect of total polymer concentration (solution viscosity), we fixed the ratio between APS-25PEG and PCL at 1:2 and proportionately increased both polymer concentrations in section 5.3.4.

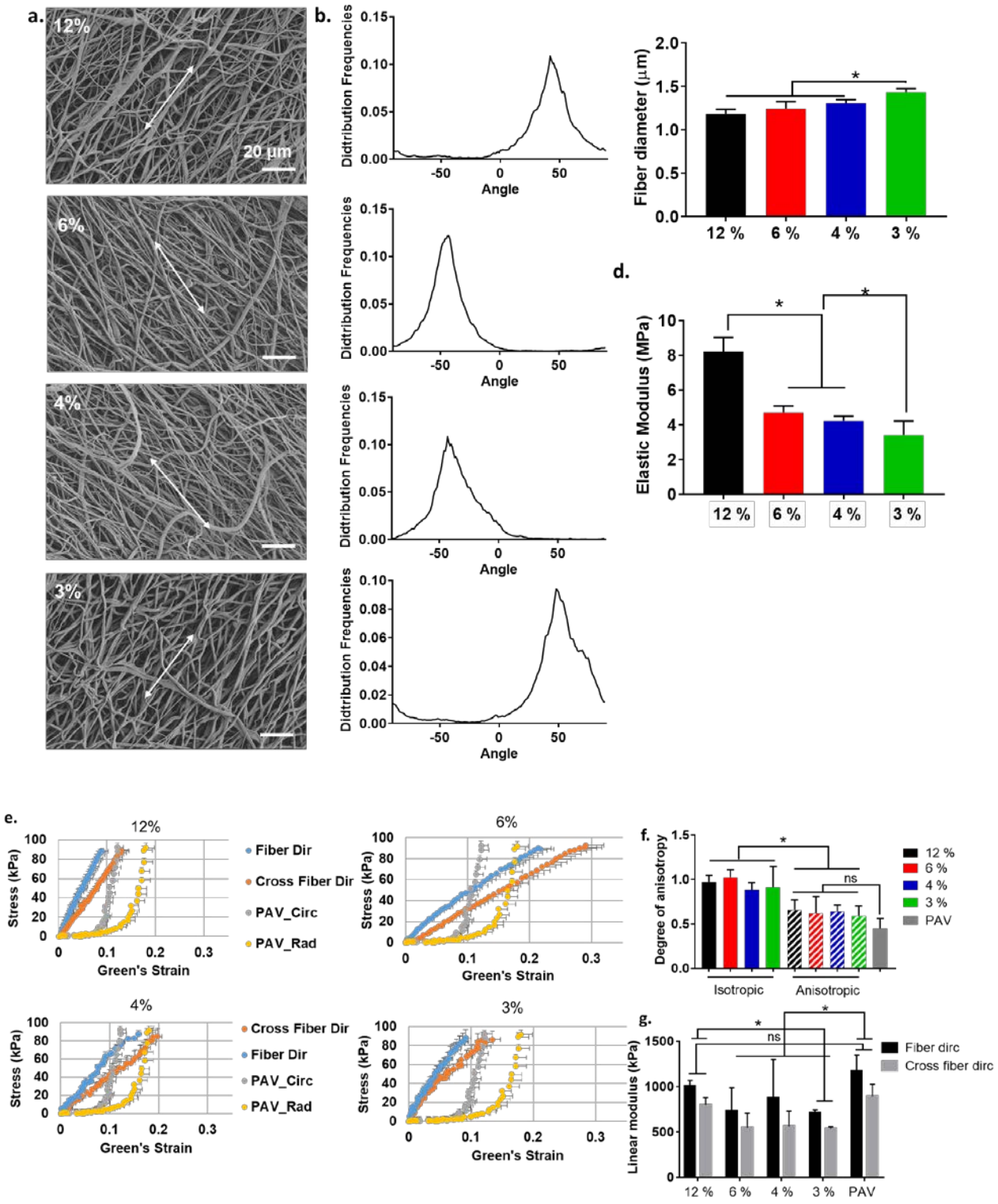

Figure 25. APS-25PEG concentration (3-12%) in the polymer blend affected the structural and mechanical properties of fibrous scaffolds.

(a) SEM images at magnification of 2000X; (b) Fiber alignment quantification by OrientationJ plugin in NIH ImageJ (n=at least 4 images); (c) Average fiber diameter quantified by NIH ImageJ (n=at least 4 images); (d) Elastic modulus of scaffolds obtained from uniaxial tensile test; (e) Biaxial stress-strain plots of fibrous scaffolds; (f) Degree of anisotropy and (g) Linear modulus calculated from biaxial stress-strain plots. *indicates $p<0.05$ (One-way ANOVA, Tukey's post-hoc test).

SEM images and quantification revealed the anisotropic fiber alignment of all electrospun scaffolds with different APS-25PEG concentrations (**Fig. 25a and b**). All APS-25PEG scaffolds had high degrees of fiber alignment as observed by the single sharp peak in their fiber alignment distribution. Decrease in the APS-25PEG concentration (from 12% to 3%) resulted in an increase in average fiber diameter (**Fig. 25c**) and reduction in elastic modulus as measured by uniaxial mechanical testing (**Fig. 25d**). It is well-known that electrospun fiber diameter inversely correlates with the elastic modulus [256], which is in line with our observations. These results suggested that APS-25PEG concentration played an important role in determining the fiber morphology and elastic modulus.

Regardless of the APS-25PEG concentration, biaxial tensile testing revealed that all scaffolds exhibited anisotropy shown by the different mechanical behaviors in the fiber and cross-fiber directions (**Fig. 25e**). It was noted that the APS-25PEG concentration had no/minimal effect on the DA as DA of all scaffolds was similar to that of PAV (**Fig. 25f**). These results are in accordance with the fiber alignment quantification as shown in **Fig. 25b**. Similar to that noted in **Fig. 25d**, a decrease in APS-25PEG concentration (from 12% to 3%) showed a trend of reduction in the linear modulus obtained from the biaxial tests (**Fig. 25g**). We speculate that the

reduction in the modulus may be due to the increased fiber diameter with decreasing APS-25PEG concentration, as explained earlier. Interestingly, the scaffold prepared with 12% APS-25PEG had linear modulus similar to the PAV in both fiber and cross-fiber directions. Overall, APS-25PEG concentration in the polymer blend served as a tunable parameter to modulate biaxial mechanical properties of the electrospun scaffolds without affecting their anisotropy.

5.3.4 Effect of total polymer concentration on the mechanical properties of anisotropic electrospun scaffolds

Finally, we investigated the effect of total polymer concentration on the structural and mechanical properties of fibrous scaffolds. Polymer concentration in the electrospinning solution has been considered as a key parameter in determining the fiber architecture and uniaxial mechanical properties [244, 245, 257]. However, the effect of polymer concentration on the scaffold's anisotropic fiber alignment and biaxial mechanical properties remains largely unexplored. Therefore, we formulated polymer blends of APS-25PEG and PCL by keeping a constant weight ratio of 1:2 and the total polymer concentration was changed from 5+10% to 6+12% and 8+16% (**Table 13**).

SEM image quantification revealed that the scaffolds were aligned with one single narrow peak in distribution of fiber alignment (**Fig. 26a and b**). The increase in the total polymer concentration (from 5+10% to 8+16%) resulted in the increase in the average fiber diameter (**Fig. 26c**) and elastic modulus (**Fig. 26d**). This observation is in agreement with the existing literature that increase in the total polymer concentration without changing other electrospinning parameters often leads to an increase in fiber diameter and tensile properties such as elastic modulus [244, 258]. Such effect of increased polymer concentration and hence, increased

solution viscosity has been attributed to the higher frequency of polymer chain entanglements and opposing jet stretching under the applied electric field [243, 259], thus increasing the average fiber diameter.

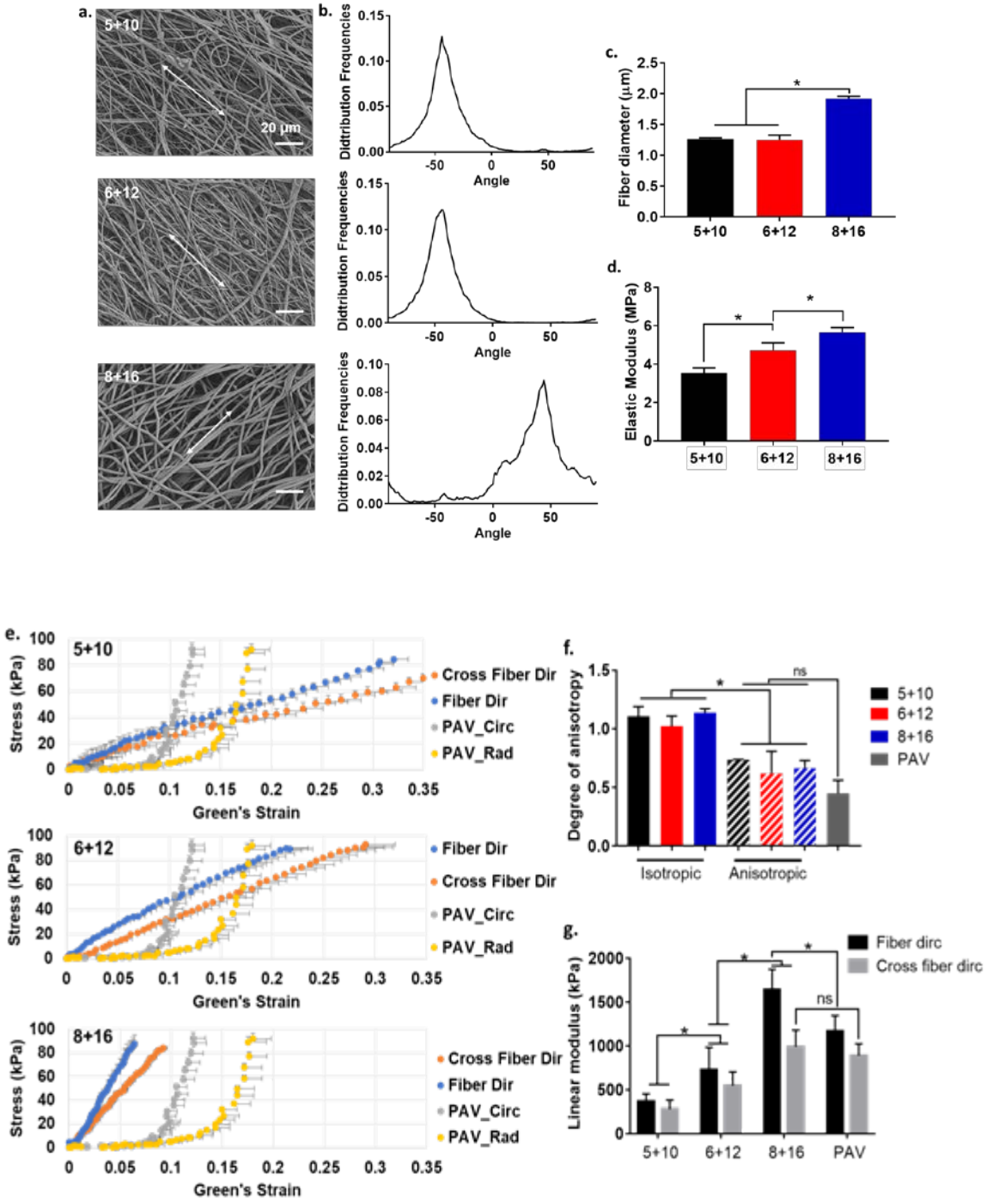

Figure 26. Total polymer concentration affected the structural and mechanical properties of scaffolds.

(a) SEM images at magnification of 2000X; (b) Fiber alignment quantification by OrientationJ plugin in NIH ImageJ (n=at least 4 images); (c) Average fiber diameter quantified by NIH ImageJ (n=at least 4 images); (d) Elastic modulus of scaffolds obtained from uniaxial tensile test; (e) Biaxial stress-strain plots of fibrous scaffolds; (f) Degree of anisotropy and (g) Linear modulus calculated from biaxial stress-strain plots. *indicates $p<0.05$ (One-way ANOVA, Tukey's post-hoc test)

Biaxial tensile testing revealed that all three scaffolds displayed a mechanical anisotropy in the fiber and cross-fiber direction as compared to their isotropic counterparts (**Fig. 26e and f**). Regardless of the total polymer concentration (from 5+10% to 8+16%), the DA of all the scaffolds was similar to that of PAV (**Fig. 26f**) and this observation correlated with the fiber alignment distribution (**Fig. 26b**). Based on **Fig. 25 and 26**, anisotropy of fiber alignment is mainly determined by the electrospinning collector rather than the polymer formulation of APS-25PEG and PCL. Similar to the uniaxial tensile properties, linear modulus from biaxial testing revealed the same trend where the increase in polymer concentration led to stiffer scaffolds (**Fig. 26g**). Of note, 8+16% had similar linear modulus to PAV in the radial direction but higher in the circumferential direction. Therefore, changing total polymer concentration provides an alternative method to tune the structural and biaxial mechanical properties of fibrous scaffolds.

Interpreting from all the above results, we concluded that fiber alignment closely affected the biaxial mechanical properties of fibrous scaffolds. Specifically, anisotropic fiber alignment led to anisotropic biaxial tensile properties while isotropic fiber alignment resulted in similar

tensile properties in two perpendicular directions. Moreover, we demonstrated the feasibility of tuning the structural and mechanical properties of the fibrous scaffold by changing multiple polymer formulation parameters.

5.3.5 The cellular behavior of hVIC on isotropic and anisotropic scaffolds

We further examined the effect of fiber anisotropy in directing the cellular behaviors of cultured cells. We selected hVICs as our cell model. In human valves, VICs are the most abundant cell type and actively involved in a number of activities related to the valve development, ECM remodeling, and direct disease progression [260, 261].

After 14 days of culture, the metabolic activity of cells seeded on the scaffolds was assessed via alamarBlue® assay (**Fig. 27**). All scaffolds showed an increase in the metabolic activity of hVICs over time, indicating the active cell proliferation on the scaffolds. Importantly, there was no difference observed between the isotropic and anisotropic scaffolds of the same polymer formulation. Previously, we have shown the comparable cytocompatibility of isotropic APS-co-PEG and PCL composite scaffolds to PCL only scaffolds [242]. Taken together, these results indicated that the cytocompatibility of scaffolds was not affected by their architecture or formulation. This is advantageous as it allows the changes in polymer formulation to modulate other cellular behaviors without influencing cell proliferation.

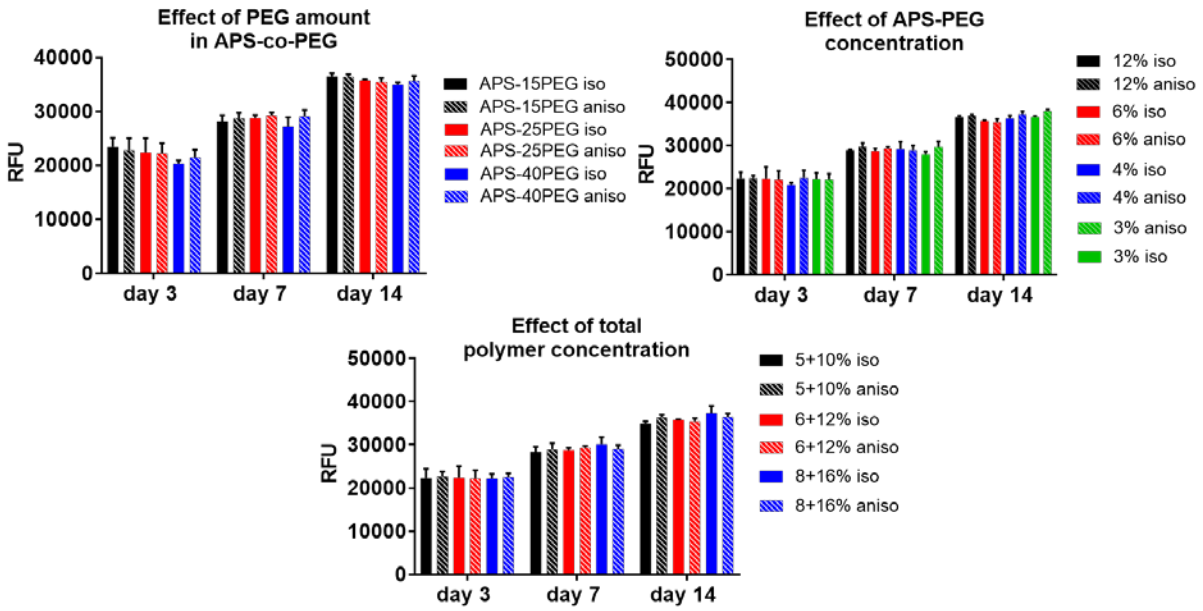

Figure 27. Isotropic and anisotropic scaffolds supported the proliferation of hVICs as demonstrated by alamarBlue® assay at day 3, 7, and 14.

It has been shown that the architecture of the cell culture substrate can direct the cell attachment and alignment, including VICs [78, 89]. Therefore, we investigated the cell-instructive ability of our anisotropic scaffolds by seeding them with hVICs. We chose scaffolds prepared using APS-25 PEG:PCL (6+12%) to demonstrate the difference between isotropic and anisotropic scaffolds since these scaffolds showed the lowest DA and comparable mechanical properties to PAV. After 7 days of culture, hVICs seeded on the isotropic scaffold demonstrated a random cell alignment. On the contrary, the cells on anisotropic scaffolds adopted a more aligned morphology as demonstrated by a single narrow peak in the quantification of actin orientation (**Fig. 28**). Thus, we showed that the anisotropic scaffold may serve as a promising lead for developing heart valve tissue engineered scaffolds which can instruct cellular alignment via the anisotropic fiber alignment and mechanical properties.

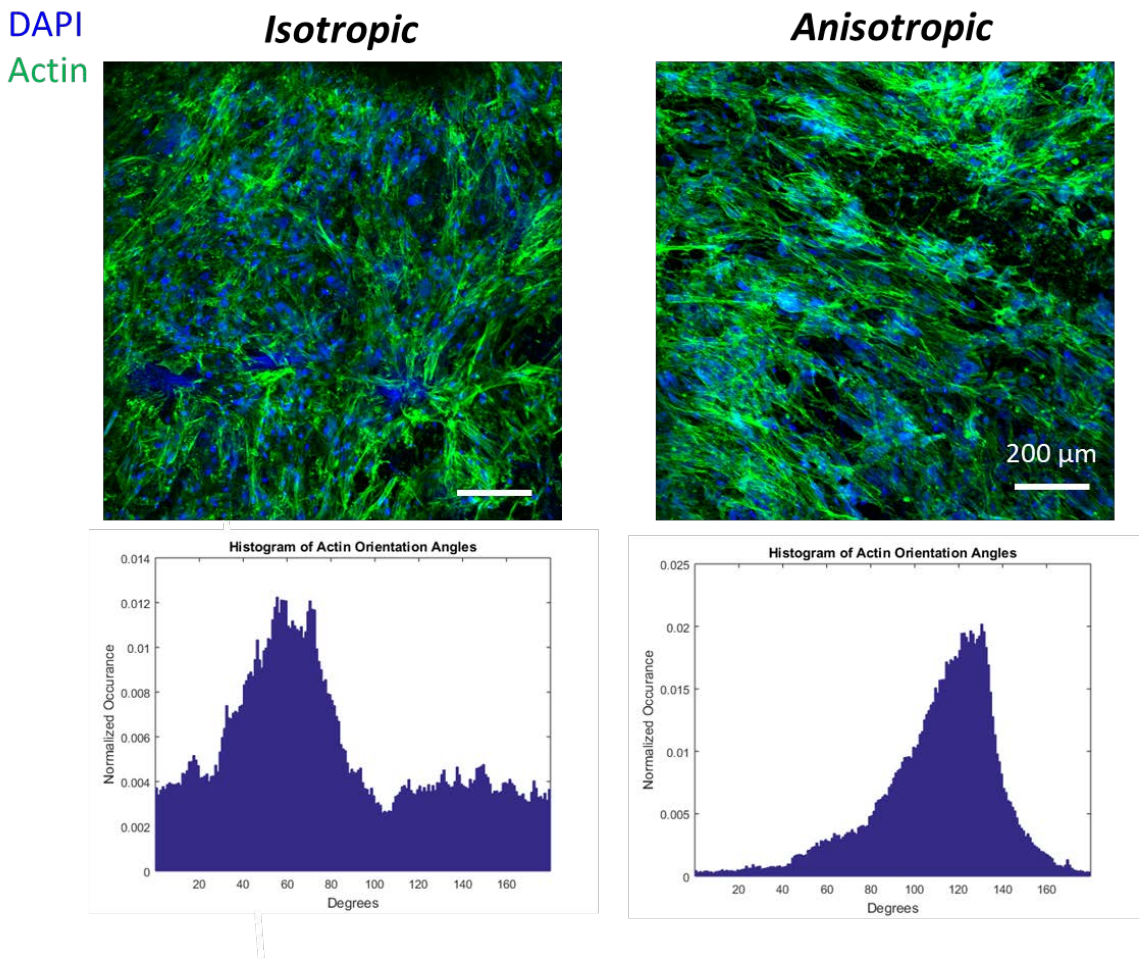

Figure 28. hVICs displayed different morphology when cultured on isotropic and anisotropic scaffolds.

5.3.6 Conclusion

Overall, we demonstrated the feasibility to fabricate anisotropic fibrous scaffolds with tunable and controllable structural and mechanical properties. Fine-tuning of polymer formulations and electrospinning collector yielded scaffolds with valve-mimetic mechanical properties. This study provides a facile alternative strategy to the current pool of fabrication methods for biologically relevant tissue-engineered scaffolds. Although the fibrous scaffolds developed in this study were

not identical to the native valve tissue in their biaxial mechanical behaviors, we envision this study will inspire fibrous tissue-engineered scaffold design from its architectural and mechanical perspectives.

6.0 SHAPE-SPECIFIC NANOCERIA MITIGATE OXIDATIVE STRESS-INDUCED CALCIFICATION IN PRIMARY HUMAN VALVULAR INTERSTITIAL CELL CULTURES

[Xue Y, St. Hilaire C, Hortells L, Phillippi JA, Sant V, and Sant S. *Cellular and Molecular Bioengineering* (2017) 10: 483.]

6.1 BACKGROUND

Valve calcification remains a major healthcare burden in developed countries, resulting in ~17,000 deaths per year in the United States and currently affecting a quarter of the senior population older than 65 [1]. Calcification of the aortic valve, if not treated properly, can impair the normal valve movement and eventually lead to valve stenosis and heart failure [262]. Currently, the mainstream treatment option for valve calcification is valve replacement using either mechanical valves or bioprostheses, the former requires life-long anticoagulant therapy and the latter is still unfortunately susceptible to calcification and also need re-operation [263, 264].

There is a lack of pharmacological treatments for valve calcification [265]. Therefore, it is of great significance to elucidate the underlying mechanisms responsible for valve calcification, which can further be targeted for development of new therapies to prevent, halt, or

reverse calcification [266]. Potential mechanisms contributing to valve calcification include inflammatory cell infiltration [267], lipid accumulation [7], oxidative stress [154, 268], and local mechanical stress [269], all of which initiate an active cell-driven process that drives valve interstitial cells (VICs) to acquire myofibroblast phenotype and/or to differentiate into osteoblast phenotype [128]. As a result, excessive amounts of extracellular matrix proteins and calcium phosphate are secreted, which stiffen the valve and compromise its opening and closing [270]. Of the different mechanisms of valve calcification, oxidative stress has been recognized as a key upstream driving force in the early stages of the disease [154]. Increased reactive oxygen species (ROS) such as superoxide and hydrogen peroxide (H_2O_2) levels were found in the calcified regions of human stenotic valve tissues [155]. Moreover, instead of being merely a consequence of valve calcification progression, ROS production was found to precede the valve calcification in a mice model [156]. ROS have also been shown to induce fibrosis and mineralization by promoting pro-fibrotic and pro-osteogenic signaling pathways such as AKT pathway and TGF-β pathway [271, 272]. Furthermore, adenoviral transduction of catalase (CAT), a key antioxidant enzyme, decreased oxidative stress-induced differentiation of quiescent or myofibroblastic VIC into osteogenic phenotype and reduced calcific nodule deposition in human valve sclerosis-derived cells [273]. However, the benefits of antioxidant therapies, which directly target oxidative stress to treat valve calcification, are yet to be studied.

It should be noted that much of the current understanding of valve calcification is based on *in vitro* studies using either porcine or ovine models [274]. However, these animal models may not fully share the pathobiology of human valve calcification. It was reported that porcine VICs did not form mineral deposits when treated with osteogenic media with TGF-β1 [275] and became contact-inhibited monolayers, which behave unstably during long-term cell culture

[276]. Other studies have utilized non-valvular cells, such as vascular smooth muscle cells, as a cell model to study the calcification progression and explore potential therapeutics [277]. Although oxidative stress is a central component in directing both valvular and vascular calcification [278], there are striking differences in the mechanisms of inducing oxidative stress in these two types of calcifications [268]. Specifically, increased expression and activity of NAD(P)H oxidase is a major source of ROS production in vascular, but not valvular, calcification [279]. Additionally, when blood vessels are under oxidative stress, there is usually a compensatory increase in the activity of antioxidant enzymes (e.g. catalase, CAT and superoxide dismutase, SOD) [280]. However, in calcified valves, the activities of these antioxidant enzymes were found to be greatly reduced, which further exacerbate the oxidative stress-induced damage [155]. Therefore, use of human (normal or patient-derived) VICs (hVICs) (where calcific deposits initiate [281]) is of significant importance to delineate the underlying ROS-mediated mechanisms of initiation and progression of human valve calcification. Furthermore, hVICs-based cell model will be more physiologically relevant for screening potential therapeutics *in vitro*. In this study, the first goal was to determine if the hydrogen peroxide (H_2O_2)-mediated oxidative stress could induce calcification in hVICs. We isolated hVICs from normal valve donor and patients with aortic valve stenosis. We further characterized normal and diseased hVICs for baseline SOD and CAT activity, mRNA expression levels of myofibroblast and calcification markers, as well as their response to H_2O_2-mediated oxidative stress. We also developed an *in vitro* oxidative stress-induced valve calcification model whereby treatment of inorganic phosphate (Pi) in presence of H_2O_2 induced calcification in diseased hVICs.

The second goal of the study was to investigate the potential of cerium oxide nanoparticles (CNPs) to mitigate oxidative stress-mediated valve calcification as a novel

therapeutic intervention. CNPs act as self-regenerative ROS scavengers due to their catalytic activities by switching between Ce^{3+} and Ce^{4+} oxidation states [282]. CNPs can scavenge ROS such as H_2O_2 and superoxide by acting as CAT and SOD-mimetics, respectively [283-285]. CNPs are also effective scavengers for hydroxyl radical, nitric oxide radical, and peroxynitrite, making them broad spectrum antioxidants [282, 283]. CNPs have already been explored for several different cardiovascular applications as demonstrated in several studies *in vitro* [286, 287] and *in vivo* [163, 288]. Thus, we hypothesized that ROS scavenging ability of CNPs can be exploited for preventing or treating oxidative stress-induced valve calcification.

Metal oxide nanoparticles like CNPs can be synthesized in various shapes and sizes using controlled synthesis conditions [289]. However, most of the studies that use CNPs as antioxidants have been carried out without specifying nanoparticle shape. It is well known that nanoparticle shapes and sizes can have significant effect on their biological activities, such as intracellular uptake and localization [168] and therapeutic activity [169]. However, the effect of CNP shape on their ROS-scavenging activity has not been elucidated. Hence, we synthesized CNPs with controlled shapes such as spheres, short rods (SR), long rods (LR) and cubes. We compared the ROS modulating effect of shape-specific CNPs in diseased hVICs and investigated their potential therapeutic benefits in oxidative stress-induced valve calcification model *in vitro*.

6.2 METHODS

6.2.1 Collection of human tissue samples and isolation and culture of human valvular interstitial cells (hVICs)

We used de-identified human valvular tissues recovered at University of Pittsburgh Medical Center (UPMC) as per protocols approved by the University of Pittsburgh Institutional Review Board, PRO16050264 (St. Hilaire) and PRO0702120 with informed consent (Dr. Gleason). The subjects or their designates have given permission for the use of this tissue for medical research. Tissue and cell specimens do not have identifiers associated with them in order to protect human subjects' identifiable information, privacy and confidentiality. Tissues and cells were collected regardless of gender, race or ethnic composition. To collect control tissue samples from autopsy, we have a Committee for Oversight of Research and Clinical Training Involving Decedents (CORID) protocol # 729.

Human aortic valve cells were isolated from a healthy donor with normal valve (referred to as 'normal') and two patients with pre-operative diagnosis of valve stenosis (referred to as 'Diseased-1' and 'Diseased-2'). These hVICs were a kind gift from Dr. Thomas Gleason lab. Valve tissues were digested in Collagenase IV (2.5 mg/mL) with DMEM (+1% Penicillin/Streptomycin +1% Fungizone) for 30 min at 37 °C with gentle rocking. Digested tissue was passed through 70 µm filter and saved at 37 °C. Undigested tissue was further digested with Collagenase IV (0.8 mg/mL) for 1 h at 37 °C with gentle rocking. Digested tissue was again passed through 70 µm filter and pooled with the previously digested tissue. The pooled digested tissue was centrifuged at 2000 rpm for 5 min at 4 °C and then the supernatant were discarded. CD31-negative cells (VICs) were separated from the total cell population by

bead separation (Miltenyi, USA). Specifically, the entire population of VICs were mixed with Fc Blocking Reagent (Miltenyi 130-091-935) followed by addition of anti-CD31 beads (Miltenyi 130-091-935). After 15 min incubation at 4˚C, the mixture was passed through a 30 μm pre-separation filter (Miltenyi 130-041-407) into a 25 MS MACS Separation Column (Miltenyi 130-042-201) and washed three times with culture medium. The resulting flow-through was retained as the CD31-negative portion of the cell population. The normal hVICs were propagated and cultured using DMEM supplemented with 10% fetal bovine serum according to established protocol [38]. Both diseased hVICs were propagated and cultured using Endothelial Cell Growth Media Kit (referred to as 'hVIC culture media') (Cell Applications, San Diego, CA) unless mentioned otherwise. All the experiments were carried out by using cells between passage 4 and 8.

6.2.2 Von Kossa Histological Stain

Valves were excised from a healthy control (normal) and a patient with calcified valves (diseased). Tissue sections were fixed in freshly prepared paraformaldehyde (PFA, 4% w/v) in PBS for 2-4 h then washed with PBS for 1-2 h. Tissues were then serially washed in 30%, 50%, and 70% ethanol for 1-2 h each wash, then submitted to the University of Pittsburgh pathology core for embedding and sectioning onto glass slides. For Von Kossa staining, slides were heated to 65°C for 1 h, then deparaffinized by two 30 min washes in 100% xylene, followed by 3 min washes in 100% (twice), then one each of 90%, 80%, 70%, and 50% ethanol, followed by deionized water. Slides were then immersed in silver nitrate (3%, w/v) and exposed to UV light for 30 min, rinsed 3x in distilled water, then immersed in sodium thiosulfate (5%, w/v), rinsed in

3x in distilled water, and finally, counter stained with nuclear fast red for 5 min. Images were acquired using the EVOS® XL Imaging system.

6.2.3 Immunostaining of CD31 and α-Smooth Muscle Actin (α-SMA)

hVICs (50,000 cells/well) were cultured in 24-well plates for 2 days and fixed with PFA (4% w/v) for 20 min at room temperature. Subsequently, cell monolayers were permeabilized with Triton X-100 (0.1%, v/v) followed by blocking with bovine serum albumin (BSA, 3%, w/v) to avoid non-specific binding. Cell monolayers were incubated with primary antibodies against CD31 (Dako, pre-diluted) and α-smooth muscle actin (α-SMA; Dako, 1:200) diluted in blocking buffer for 2 h at room temperature along with a negative control (without primary antibody). After washing thrice with PBS, hVICs were incubated with Alexa Fluor 488-conjugated secondary antibodies (1:100) for 1 h at room temperature. Nuclei were counterstained with Hoechst (1:200). Images were acquired on a confocal microscope (Olympus Fluoview, Olympus) as a z-stack containing a series of 5 µm slices using 20X or 40X objectives.

6.2.4 Superoxide dismutase (SOD) and catalase (CAT) assays

SOD and CAT activity of normal and diseased hVICs were determined by SOD activity assay kit (Epigentek) and CAT activity assay kit (Cayman Chemical), respectively. Briefly, cell lysates were prepared by addition of radioimmunoprecipitation (RIPA) assay buffer containing Tris (50 mM, pH 7.4), NaCl (150 mM), sodium deoxycholate (0.5% w/v), NP-40 (1% w/w), phenylmethane sulfonyl fluoride (PMSF, 0.05 mM) and protease inhibitor cocktail to the harvested cells on ice. The enzyme activity was measured in the extracted cell lysates according

to the manufacturers' protocols. The enzyme activity was normalized to the total protein content, which was quantified by microbicinchoninic acid (BCA) protein assay (Pierce BCA, Thermo Scientific) according to the manufacturer's protocol.

6.2.5 Quantitative polymerase chain reaction (qPCR)

mRNA expression of *Vimentin (VIM), α-SMA* and *Runt-related transcription factor 2 (RUNX-2)* and *Osteopontin (OPN)* were measured using real time quantitative polymerase chain reaction (qPCR). RNA was isolated using GeneJET RNA purification kit (Thermo Scientific, Lithuania, EU) according to the manufacturer's protocol. RNA quality was measured by absorbance ratio at 260/280 nm. Expression of *VIM, α-SMA, OPN* and *RUNX-2* were analyzed by qRT-PCR using iTaq Universal SYBR one-step RT-PCR kit (BioRad Laboratories Inc., USA). Briefly, reaction mixtures containing 20 ng mRNA, 5 µL of 2X SYBR green master mix and respective primers (0.2 µM) were amplified in triplicate samples using an amplification protocol of 40 cycles of denaturation for 15 sec at 95 °C, annealing for 30 sec at 55 °C and extension for 30 sec at 72 °C (7500 Fast Real-Time PCR System, Applied Biosystems, USA). Gene expression was quantified using the ΔΔCT algorithm. Gene expressions in normal hVICs or respective untreated control of each patient cells served as a control for calculating fold change in mRNA expression as specified in each figure. Primer sequences are provided in **Table 14**.

Table 14. Summary of primers used.

	Name	Sequence
1.	β-actin F	5'-ACC TTCTAC AAT GAG CTG CG-3'
	β-actin R	5'-CCT GGA TAG CAA CGT ACA TGG-3'
2.	Vimentin F	5'-CAA CCT GGC CGA GGA CAT-3'
	Vimentin R	5'-ACG CAT TGT CAA CAT CCT GTC T-3'
3.	α-SMA F	5'-GGA ATC CTG ACC TTG AAG-3'
	α-SMA F	5'-CAC GAA GCT CAT TGT AGA-3'
4.	RUNX-2 F	5'-CAGTTCCCAAGCATTTCATCC-3'
	RUNX-2 R	5'-TCAATATGGTCGCCAAACAG-3'
5.	Osteopontin F	5'-TTGCAGCCTTCTCAGCCAA-3'
	Osteopontin R	5'-GATGCCTAGGAGGCAAAAGC-3'

6.2.6 Intracellular ROS detection by DCFH-DA assay

The intracellular ROS levels in hVICs were measured by 2,7-Dichlorodihydrofluorescein diacetate (DCFH-DA) assay (Cayman chemical, USA). For DCFH-DA detection, media was removed and DCFH-DA (20 μM, 100 μL) in Hank's Balanced Salt Solution (HBSS) were added to each well and incubated for 30 min at 37 °C. DCFH-DA was then removed and cells were washed with HBSS. Subsequently, different treatments were given as described below and fluorescence intensity was measured at excitation/emission wavelength of 485/528 nm using a microplate reader (Synergy HT, BioTek instruments, USA). To ensure that the change in the fluorescence intensity was not due to the differences in the cell density or cell death, we adopted uniform cell seeding density and have selected the dose of H_2O_2 and CNPs that didn't induce significant cell death.

6.2.7 Acute and long-term H_2O_2 treatment

To determine the acute effect of H_2O_2 on hVIC behaviors, hVICs were seeded in a 96-well plate (9,000 cells/well) or a 24-well plate (100,000 cells/well) and allowed to attach for 24 h. Subsequently, hVICs were exposed to media containing H_2O_2 (100 μM, 100 μL) for 24 h. Cells were then subjected to ROS detection by DCFH-DA assay as described above. % ROS level was calculated using the equation below. Cell lysates and mRNA were analyzed for SOD/CAT activity and expression of *VIM, α-SMA, OPN* and *RUNX-2*, respectively. Cells without H_2O_2 treatment were used as negative control.

$$\% \text{ ROS level} = RFU_{H2O2} / RFU_{negative} \times 100\%$$

To determine the long-term effect of H_2O_2 on hVIC behavior, hVICs were seeded in a 24-well plate (100,000 cells/well) and allowed to attach for 24 h. Subsequently, hVICs were exposed to media containing H_2O_2 (100 μM, 100 μL) for up to 14 days with change of media (containing H_2O_2) every day. Calcium content of cell monolayers were analyzed at day 3, 7 and 14. Cell lysates were analyzed for SOD/CAT activity on day 14. Cells without H_2O_2 treatment were used as negative control.

6.2.8 Synthesis of shape-specific CNPs

CNPs prepared in this study are denoted based on their shapes as observed in Transmission Electron Microscopy (TEM), namely cube, short rod (SR) and long rod (LR) and sphere. Spherical CNPs were prepared by ultra-sonication method [290]. Briefly, cerium nitrate hexahydrate (5 g, Sigma Aldrich, USA) and methoxy polyethylene glycol (mPEG, 5000 Da, 1 g, Acros Organics, USA) were dissolved in deionized water (100 mL). Subsequently, sodium

hydroxide solution (5 mg/mL in deionized water, Sigma Aldrich, USA) was added at a rate of 5 mL/min under constant sonication and stirring until the pH of the solution became 10. CNPs were washed with deionized water and ethanol several times until the pH of supernatant became neutral. CNPs were obtained by centrifugation followed by overnight drying at 100 °C. Cube, SR, and LR CNPs were synthesized by hydrothermal method [289]. Briefly, cerium nitrate hexahydrate (0.868 g) was dissolved in deionized water (5 mL) and added in a drop-wise manner to sodium hydroxide solution (35 mL, 6 M for cube and SR while 9 M for LR) with stirring for 30 min at room temperature. The solution was then sealed in a hydrothermal reactor and allowed to react at 100°C (SR and LR) or 180 °C (cube) for 24 h. Subsequently, CNPs were washed with deionized water and ethanol for several times until the pH of the supernatant became neutral. CNPs were obtained by centrifugation followed by drying overnight at 60 °C.

6.2.9 Physicochemical characterization of CNPs

The shapes of different CNPs were examined by TEM. Low concentration dispersions of CNPs were imaged on copper grids using electron microscope (JEOL 1011, Joel, Tokyo, Japan) operated at an accelerating voltage of 80 kV. Images were acquired without any staining. For characterization of particle size (hydrodynamic diameter), stock CNP dispersions (1 mg/mL) in HEPES buffer (pH=4, GE Healthcare, USA) were diluted to 25 µg/mL in hVIC culture media prior to measurements. Particle sizes were measured by dynamic light scattering (DLS) using a Malvern Zetasizer (Zetasizer 3000, Malvern, USA). To determine the effect of CNP shape on oxidation state of cerium (Ce^{3+} or Ce^{4+}), the UV-Vis spectra (wavelengths 200-400 nm) were recorded using CNP dispersion (25 µg/mL) in deionized water using a SpectraMax M5e plate reader (Molecular Devices LLC, USA).

6.2.10 AmplexRed® assays

The H_2O_2 scavenging ability of CNPs was measured using Amplex® Red Hydrogen Peroxide Assay according to the manufacturer's protocol (ThermoFisher Scientific, USA). CNPs (5, 25 and 100 µg/mL) dispersed in HEPES buffer (0.01 M, 60 µL) were allowed to react with H_2O_2 solution (10 µM, 60 µL) at room temperature for 30 min. Subsequently, equal volume (50 µL) of the reactants and working solution of Amplex® Red reagent (100 µM) and Horseradish Peroxidase (HRP, 0.2 U/mL) were allowed to react at room temperature for 30 min (n=4). The fluorescence intensity was then measured using microplate reader (Synergy HT, BioTek instruments, USA) at excitation/emission wavelengths of 540/590 nm. HEPES buffer (0.01 M) and butylated hydroxytoluene (BHT; 25 µM in 0.01M HEPES buffer) served as negative and positive control, respectively. Scavenged H_2O_2 was calculated using equation below.

$$\text{Scavenged } H_2O_2\ (\%) = (RFU_{negative} - RFU_{CNP}) / RFU_{negative} \times 100\%$$

6.2.11 Cytotoxicity of CNPs by alamarBlue® assay

The dose-dependent cytotoxicity of CNPs were determined by alamarBlue® assay (Thermo Scientific, USA) according to the manufacturer's protocol. Briefly, hVICs (9,000 cells/well) were seeded in a 96-well plate and allowed to attach for 24 h. Subsequently, hVICs were incubated with shape-specific CNPs (0.01 - 100 µg/mL) in hVIC culture media (200 µL) for 24 h. The cells were then incubated with alamarBlue® solution (10% v/v) prepared in hVIC culture media for 3 h at 37 °C. Fifty-microliter solution from each well was transferred to a 96-well plate and the fluorescence intensity was measured at excitation/emission wavelength of 530/590 nm using a microplate reader (Synergy HT, BioTek instruments, USA). The wells containing

alamarBlue® in media without cells were used as a negative control. Viability of CNP-treated cells was calculated using those without CNP treatment as 100% viability as per equation below.

$$\% \text{ Viability} = RFU_{CNP} / RFU_{negative} \times 100\%$$

6.2.12 Treatment of CNPs to scavenge or prevent acute oxidative stress

To determine shape-dependent effect of CNPs on scavenging H_2O_2-mediated pre-existing oxidative stress, the diseased hVICs were seeded in a 96-well plate (9,000 cells/well) or a 24-well plate (100,000 cells/well) and allowed to attach for 24 h. Subsequently, hVICs were exposed to media containing H_2O_2 (100 μM, 100 μL). After 4 h incubation, CNPs were added at different doses (from 0.1-100 μg/mL, 100 μL) without removal of H_2O_2. The incubation was continued for another 24 h. Cells were then subjected to ROS detection by DCFH-DA assay. Cells treated with 100 μM H_2O_2 and 0 μg/mL CNPs served as positive control as 100% ROS generation and cells without H_2O_2 and CNPs served as negative control as 0% ROS generation.

$$\% \text{ ROS generation} = (RFU_{CNP} - RFU_{negative})/(RFU_{positive} - RFU_{negative}) \times 100\%$$

Alternatively, to investigate shape-dependent effect of CNPs on preventing acute ROS generation, hVICs were first exposed to media containing CNPs (25 μg/mL, 100 μL). After 24 h incubation, H_2O_2 (100 μM, 100 μL) were added without removal of CNPs. The incubation was continued for another 4 h. Cells were then subjected to ROS detection by DCFH-DA assay. Cells without any treatment with H_2O_2 and CNPs were used as negative control for ROS generation. Cells received hVIC culture media without CNPs and H_2O_2 containing were used as negative control as 100% ROS level.

$$\% \text{ ROS level} = RFU_{test} / RFU_{negative} \times 100\%$$

To further determine the effect of CNP treatment on antioxidant enzyme activity as well as calcification potential, cell lysates and mRNA of LR CNP-treated groups (25 μg/mL) were analyzed for SOD/CAT activity and expression of *VIM, α-SMA, OPN* and *RUNX-2*, respectively. Cells without any treatment (neither H_2O_2 nor LR CNPs) were used as negative control while those exposed to only H_2O_2 without CNP treatment were used as positive control.

6.2.13 Alizarin Red S staining

The calcified nodule formation in hVIC cultures were determined by Alizarin Red S (ARS) staining [291]. At specific time points, media was removed, and cells were fixed using PFA (4%, w/v) for 15 min and incubated with ARS solution (40 mM, pH 4.3) for 30 min. Samples were washed with deionized water four times before imaging.

6.2.14 Calcium content quantification

Intracellular calcium was quantified as reported previously [292]. Calcium was extracted from cell monolayers by incubation with nitric acid (1 M) for 1 h. The supernatant (35 μL) was mixed with O-cresolphthalein (0.25 mg/mL, 35 μL) and 2-amino-2-methyl-1-propanol (150 mg/mL, 87.5 μL) at room temperature for 20 min and the absorbance was measured at 575 nm. The amounts of proteins were then quantified by micro BCA protein assay (Pierce BCA, Thermo Scientific) as mentioned earlier and data is presented as amount of calcium normalized to the amount of protein.

6.2.15 ROS-mediated VIC calcification model

To establish the Pi-induced calcification model in the presence of H_2O_2, diseased hVICs were cultured in 24-well plate (100,000 cells/well) in hVIC culture media for 48 h followed by calcification media (MEM-alpha supplemented with 10% fetal bovine serum) containing an additional 1 mM sodium phosphate monobasic (Pi) alone or in presence of 100 μM H_2O_2. Media was replenished every other day. ROS levels were measured after 2 h of each treatment by DCFH-DA assay. Calcification in hVICs cultures was determined using ARS staining and calcium content quantification at day 1, 4, and 7. To confirm that observed calcification was indeed mediated by oxidative stress, cells were also co-treated in parallel with an antioxidant (Vitamin E, 25 μM).

To test the potential of CNPs in preventing calcification, hVICs were treated with LR CNPs (25 μg/mL) in the presence of Pi and H_2O_2 containing media. ROS were measured 2 h post-treatment while ARS staining and calcium content quantification were carried out 7 days after treatments.

6.2.16 Statistical analysis

Experimental data are presented either as mean ± standard error of the mean (SEM) or as mean ± standard deviation (SD) as specified in each figure legend. Multiple comparisons were analyzed for significance using one-way ANOVA or two-way ANOVA followed by Tukey's post-hoc analysis. P-values less than 0.05 were considered as significant.

6.3 RESULTS AND DISCUSSION

6.3.1 Characterization of patient derived hVICs

Human heart valve consists of two major cell types, namely VICs and valvular endothelial cells (VECs) [128]. In this study, we isolated hVIC population from three different subjects, a normal healthy control (referred to as 'normal') and two patients with diseased (stenotic) aortic valves. The presence or absence of calcification in the valves from which hVICs were isolated was confirmed via histological analysis of neighboring tissue using Von Kossa stain (**Fig. 29**). Phenotype of hVICs was evaluated by immunofluorescence staining for α-SMA (VIC marker) and CD31 (VEC marker). All three cell populations stained positively for α-SMA but did not express CD31 (**Fig. 30A**), confirming that the cells used are predominantly interstitial cell population with no presence of an endothelial cell contaminant. Also, normal hVICs showed higher expression of α-SMA as compared to the diseased hVICs, which suggests that these diseased cells had less myofibroblastic VIC population. VICs are widely recognized as a heterogeneous and plastic cell population with diverse phenotypes including quiescent fibroblast, activated myofibroblast, diseased osteoblast and endothelial/mesenchymal progenitor cells [128]. The expression of α-SMA in hVICs is in accordance with earlier reports that VICs are spontaneously activated into myofibroblast phenotype, expressing α-SMA, in two-dimensional (2D) culture [261].

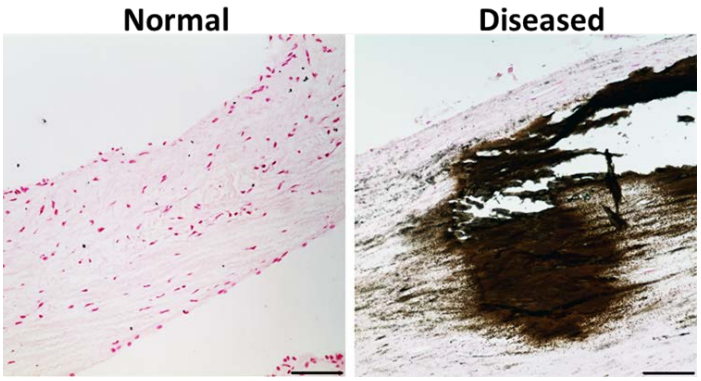

Figure 29. Valves isolated from a normal healthy control and a diseased patient were stained with Von Kossa.

Scale bar = 100 µm.

We further characterized the differences between normal and diseased hVICs by quantifying mRNA expression of key VIC markers including VIM (quiescent VIC marker [293]), α-SMA (activated VIC marker [293]), RUNX-2 and OPN (osteoblastic VIC marker [294]). Compared to the normal hVICs, both diseased hVICs demonstrated higher RUNX-2 and OPN levels, while showing similar mRNA levels of VIM (**Fig. 30B**). These results suggest that osteoblastic markers were upregulated in diseased hVICs isolated from patients with valve stenosis (a late stage of valve calcification). These results are in agreement with other reports that proposed involvement of osteoblastic differentiation of VICs during valve calcification process [154]. Diseased hVICs also exhibited reduced α-SMA levels compared to normal hVICs consistent with reduced α-SMA protein expression observed by immunostaining (**Fig. 30A**). Taken together, reduced expression levels of myofibroblast marker (*α-SMA*) coupled with increased levels of osteoblast (calcification) markers (*RUNX-2* and *OPN*) in diseased hVICs suggest that diseased valves may have less myofibroblastic VIC population and more osteoblastic VIC population. This is highly plausible given that diseased VICs used in this study

were isolated from patients with valve calcification. Similar results were also observed in an *in vitro* VIC calcification model where α-SMA expression peaked and preceded the calcification and was then reduced in the later stage of calcification process [295].

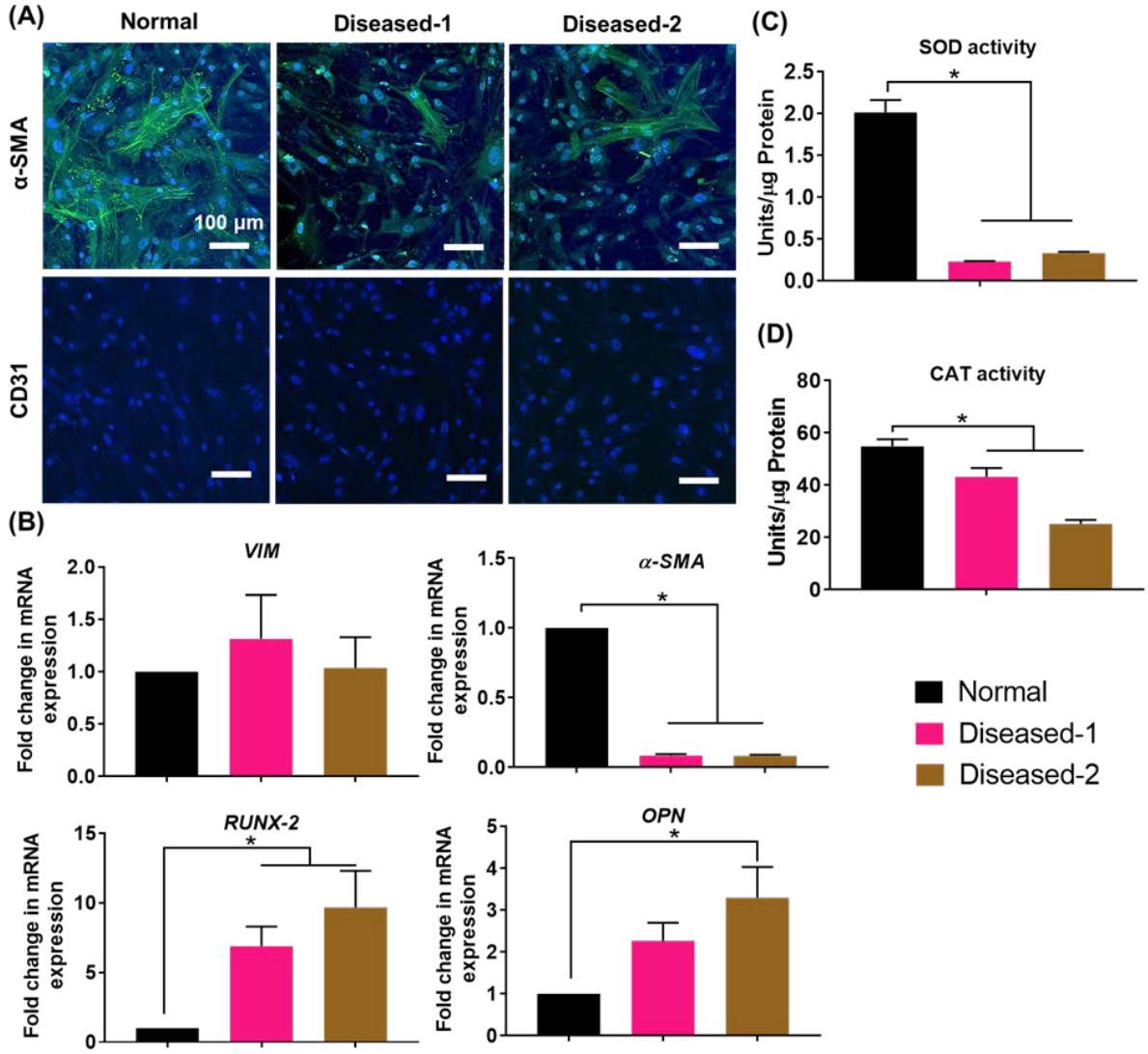

Figure 30. Patient-derived diseased hVICs exhibited higher expression of calcification markers and impaired antioxidant mechanisms.

(A) Immunofluorescence staining of patient-derived hVICs revealed α–SMA positive but CD31 negative cell population and similar morphology among the three populations in 2D culture. Scale bar = 100 μM; (B) Patient-derived diseased hVICs exhibited no change in expression of

VIM, downregulated α-SMA expression (VIC activation marker) and upregulated RUNX-2 and OPN (calcification markers) when compared with normal hVICs (n=4); Patient-derived diseased hVICs exhibited decreased (C) SOD and (D) CAT activity when compared with normal hVICs (n=4); *indicates $p<0.05$ (One-way ANOVA). Data are presented as mean ± SEM.

Impaired oxidative stress defense mechanisms due to reduced antioxidant enzyme expression and activity have been found in valve calcification [154, 268]. SOD and CAT are two key functional antioxidant enzymes in resolving oxidative stress [296]. Therefore, we measured the enzyme activities of SOD and CAT in normal and diseased hVICs (**Fig. 30C and D**). Diseased hVICs showed significantly lower SOD and CAT activities compared to normal hVICs similar to what was reported in human valve tissues [155]. Impairment of antioxidant enzyme activity may contribute to increased accumulation of H_2O_2. Indeed, Miller et al. demonstrated that calcified human aortic valves generate excessive amounts of superoxide and peroxide due to the impaired antioxidant defense mechanisms, namely, valvular CAT deficiency and reduced nitric oxide production [155].

6.3.2 H_2O_2-mediated oxidative stress in patient derived hVICs

We compared the behaviors of normal and diseased hVICs in response to exogenous oxidative stress. H_2O_2 is a major type of peroxide found in a wide range of tissues and a major driving factor for ROS-mediated diseases [297]. Recent studies have highlighted the involvement of H_2O_2 in driving oxidative stress and exacerbating valve calcification [273, 277]. Therefore, H_2O_2 was selected to induce oxidative stress in the current study. It was found that acute H_2O_2 treatment (24 h) induced higher levels of ROS measured by DCFH-DA assay in the diseased

hVICs than in normal hVICs (**Fig. 31A**). Compromised or deficient defense mechanisms that are responsible for removal of ROS may have resulted in higher amount of (un-scavenged) ROS in the diseased hVICs. Indeed, we observed reduced antioxidant enzyme activities in both the diseased hVICs compared to normal hVICs (**Fig. 30C and D**). Furthermore, normal hVICs showed significantly decreased SOD and CAT activities after acute H_2O_2 treatment (**Fig. 31B and C**). We offer two explanations for this outcome. First, it is possible that these enzymes were utilized to scavenge H_2O_2-mediated oxidative stress. This explanation aligns with a recent report showing that the increased levels of ROS in the valve tissues were associated with the decreased local antioxidant enzyme activities rather than the induction of compensatory antioxidant enzymes activity, as seen in other tissues such as blood vessels [155]. Second, since both diseased hVICs showed lower antioxidant enzyme activities compared to those of normal hVICs (**Fig. 30C and D**), it is possible that their inherent antioxidant capacities were already deficient and could not adequately neutralize the oxidative stress assault.

To further elucidate the effect of acute H_2O_2 treatment on the phenotypic changes in hVICs, mRNA expression of VIM, α-SMA, RUNX-2 and OPN were compared before and after acute H_2O_2 treatment in normal and diseased hVICs (**Fig. 31D**). In all three hVICs, mRNA expression of VIM and α-SMA were unaffected, indicating H_2O_2 may not have a direct impact on the VIC activation in 2D cell culture. Importantly, H_2O_2-induced RUNX-2 and OPN mRNA expression levels were upregulated in both the diseased hVICs but not in normal hVICs. The differential behaviors of diseased and normal hVICs could be due to the ability of normal hVICs to better resolve H_2O_2-induced acute oxidative stress than that of diseased VICs (**Fig. 31A**). These data indicate that acute unresolved H_2O_2-induced oxidative stress promoted the differentiation of quiescent or myofibroblastic hVICs towards the osteoblast-like phenotype,

which may contribute to the valve calcification process. Previously, acute H_2O_2 treatment has been shown to upregulate gene expression of RUNX-2 in vascular smooth muscle cells [298], and the osteogenic transcription factors MSX2 in mouse aorta adventitial myofibroblasts [299]. The current study supports prior studies demonstrating that oxidative stress is one of the critical factors contributing to ectopic calcification. Taken together, the diseased hVICs showed impaired abilities to scavenge ROS and respond to oxidative stress-induced changes by promoting gene expression of upstream markers of calcification. Hence, diseased VICs were chosen as the cell model for studying the oxidative stress-induced calcification and exploring potential calcification prevention agents.

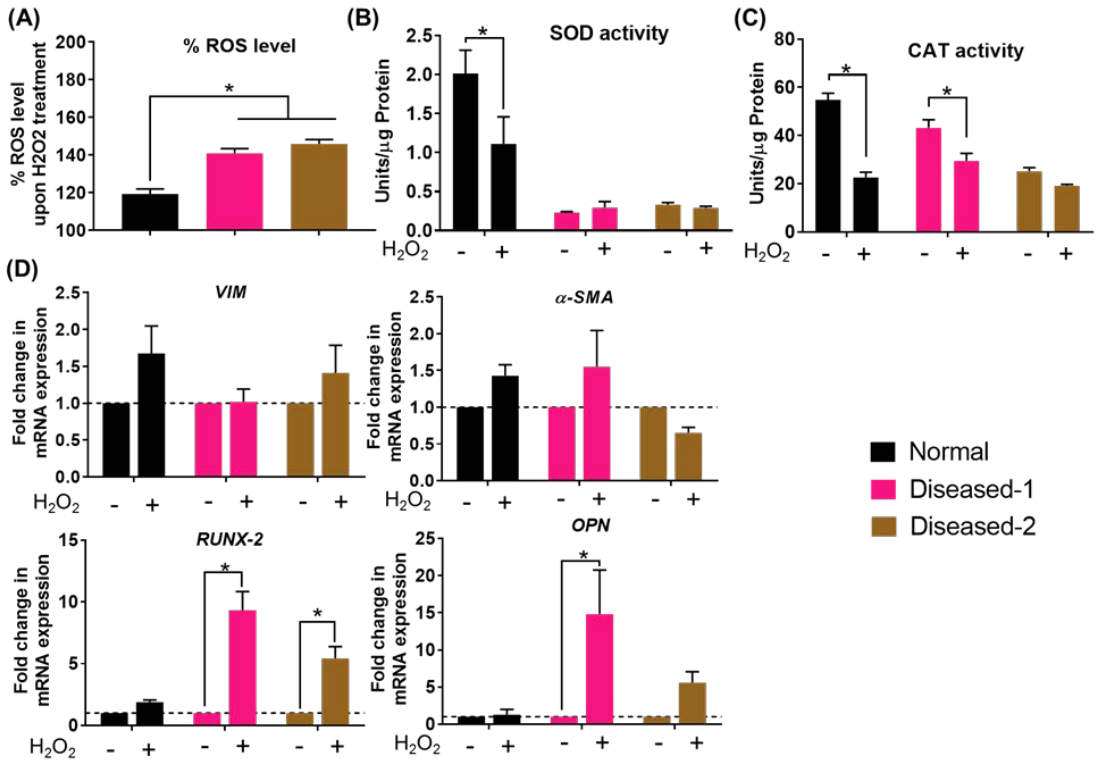

Figure 31. Patient-derived diseased hVICs were more susceptible to H_2O_2-mediated oxidative stress and stress-induced upregulation of calcification markers.

(A) Acute treatment with exogenous H_2O_2 (100 μM, 24 h) resulted in higher intracellular ROS levels in the diseased hVICs than the normal hVICs (n=4). *indicates $p<0.05$ (One-way ANOVA); (B, C) Normal hVICs, but not diseased hVICs demonstrated reduction in the SOD/CAT activities after H_2O_2 treatment. (n=4); (D) H_2O_2-mediated oxidative stress did not affect VIM and α-SMA expression in normal and diseased hVICs. Diseased hVICs exhibited elevated expression of calcification markers compared to the untreated controls while normal hVICs maintained basal expression levels of calcification makers after treatment with H_2O_2. *indicates $p<0.05$ (Two-way ANOVA). Data are presented as mean ± SEM.

6.3.3 CNPs characterization and abiotic ROS scavenging properties

In the light of lack of pharmacological treatments for valve calcification, we explored shape-specific CNPs as a novel antioxidant therapy for the treatment of oxidative stress-induced valve calcification. Furthermore, we investigated the effect of CNP shape on their antioxidant properties. Four shape-specific CNPs were synthesized via hydrothermal reactions (cube, short rod (SR) and long rod (LR) CNPs) or ultra-sonication (sphere CNPs) between cerium nitrate and sodium hydroxide and characterized for their physico-chemical properties. TEM revealed uniform shapes in each batch of the nanoparticles (**Fig. 32A**), thus enabling investigation on the effect of nanoparticle shapes on their antioxidant properties. Synthesized shape-specific CNPs showed aspect ratio ranging from 1:1 to 21:1 (measured by TEM image analysis) and hydrodynamic sizes ranging from 120 nm to 220 nm (**Table 15**). The oxidation state of cerium is a key characteristic of CNPs as their antioxidant activity is highly dependent on their ability to switch reversibly between Ce^{3+} and Ce^{4+} oxidation state [282, 283]. UV-Vis absorbance is a facile method to determine the oxidation state of CNPs in aqueous solution [300]. None of the

CNPs demonstrated significant peak at 250 nm (**Fig. 32B**), suggesting low or negligible percentage of Ce^{3+} population [300]. SR, LR and sphere CNPs showed strong absorbance peaks at 300 nm (**Fig. 32B**), suggesting predominant presence of Ce^{4+} population [300]. Cube CNPs showed less intense absorbance peaks at 300 nm, indicating lower percentage of Ce^{4+} population in cube CNPs compared to SR, LR and sphere CNPs.

Table 15. Aspect ratio and hydrodynamic size of four shape-specific CNPs.

	Cube	Short Rod (SR)	Long Rod (LR)	Sphere
Aspect ratio#	1:1	8:1	21:1	1:1
Hydrodynamic size (nm)##	220.1±3.6	121.8±0.8	119.7±1.5	121.1±1.2

Aspect ratio is defined as the ratio of length to width of a nanoparticle as measured by TEM image analysis.

Hydrodynamic size is determined by using CNP suspension (25 µg/mL) in hVIC culture media by dynamic light scattering.

The intrinsic ability of CNPs to scavenge H_2O_2 (non-cellular) was measured by Amplex® Red assay. SR, LR and sphere CNPs exhibited significantly higher dose-dependent H_2O_2 scavenging ability (5-100 µg/mL) than cube CNPs (**Fig. 32C**). This observation is in accordance with a previous report that cube CNPs synthesized by hydrothermal method had lower ROS scavenging ability than that of other shapes such as rod and sphere [301]. As suggested earlier, this may be attributed to differences in the morphology, agglomeration, and Ce^{3+}/Ce^{4+} ratio of different shape-specific CNPs [301]. Additionally, the lower ROS scavenging ability of cube CNPs may also be associated with its lower Ce^{4+} population as shown in **Fig. 32B** since catalase

(CAT)-mimetic activity of CNPs requires predominantly Ce^{4+} oxidation state to scavenge H_2O_2 [302].

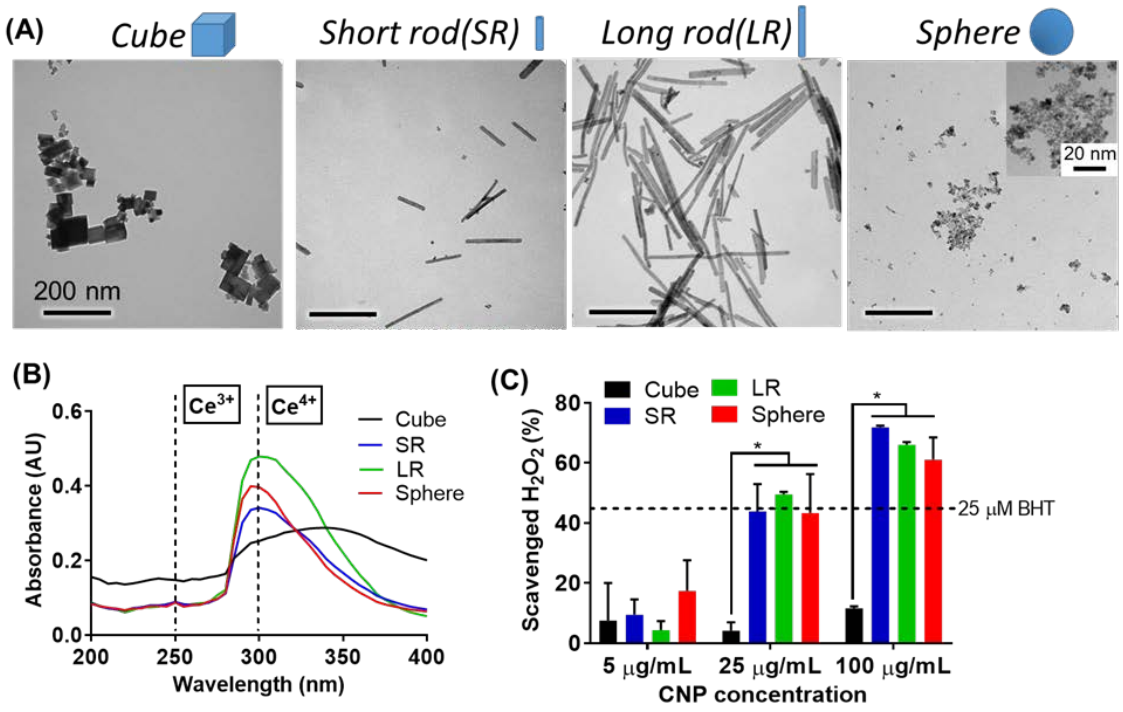

Figure 32. Physico-chemical characterization of shape-specific CNPs.

(A) Transmission electron microscopy (TEM) images revealed shape-specific CNPs with defined shapes. Scale bar = 200 nm; (B) UV-Vis spectra of shape-specific CNPs showing presence of predominantly Ce^{4+} oxidation state; (C) Hydrogen peroxide (H_2O_2) scavenging ability of shape-specific CNPs measured by AmplexRed assay (n=4). * indicates $p<0.05$ (Two-way ANOVA). Data are presented as mean ± SD.

To measure the acute cytotoxicity of CNPs, the diseased hVICs were exposed to different doses of CNPs (0.01 μg/mL-100 μg/mL in hVIC culture media) for 24 h. None of the CNPs posed significant acute cytotoxicity (**Fig. 33**), demonstrating their good cytocompatibility. Of note, low dose of CNP treatment (0.01 μg/mL) showed increased cell viability when compared

with untreated control. CNPs have been shown to enhance primary mouse embryonic fibroblast proliferation at similar low dose range, which was attributed to its ability to maintain redox balance for enhanced intracellular homeostasis and metabolism [303]. Our results indicate that shape-specific CNPs do not exhibit acute cytotoxicity in the dose range of 0.01-100 μg/mL.

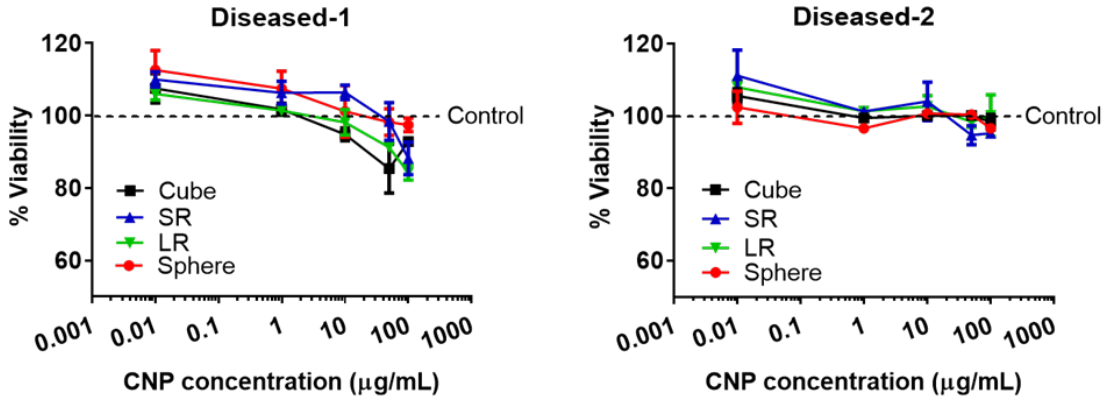

Figure 33. Shape-specific CNPs demonstrate no significant acute (24 h) cytotoxicity in the diseased hVICs as measured by alamarBlue® assay.

(n=3, Data are presented as mean ± SEM)

6.3.4 *In vitro* ROS scavenging properties of CNPs in hVICs

The ROS scavenging ability of CNPs in the diseased hVICs were first determined by measuring the intracellular ROS levels in response to 4 h pre-treatment of H_2O_2 (100 μM) to induce acute oxidative stress followed by 24 h CNP treatment (0.1-100 μg/mL). This experimental design allows us to explore the dose- and shape-dependent activity of CNPs to scavenge pre-existing ROS induced by pre-treatment of H_2O_2. Consistent with the results from the non-cellular H_2O_2 scavenging assay (**Fig. 32C**), SR, LR and sphere CNPs exhibited dose-dependent ROS scavenging ability in both populations of diseased hVICs (**Fig. 34A**). It is noted that at 100

μg/mL, SR, LR and sphere CNPs were able to scavenge all the ROS generated by H_2O_2. On the other hand, cube CNPs were unable to scavenge pre-existing ROS even at a high dose of 100 μg/mL. Although antioxidant activity of CNPs has already been reported in a variety of *in vitro* and *in vivo* studies [163, 286], shape-dependent effect on the ROS scavenging activity has only been studied in a non-cellular system [301] and remains unexplored in cellular systems. Here, for the first time, we demonstrated that CNPs exhibited shape-dependent ROS scavenging activity in the diseased hVICs under acute oxidative stress. Since the IC_{50} values of SR, LR and sphere CNPs in scavenging ROS in the diseased hVICs were less than 25 μg/mL (**Table 16**), we chose 25 μg/mL as an effective dose for exploring the shape-dependent effects of CNPs in the following studies. We compared therapeutic activity of different shapes at a single dose of 25 μg/mL (**Fig. 34B**). SR, LR and sphere CNPs but not cube CNPs exhibited ROS scavenging ability in both diseased hVICs.

Table 16. Summary of IC_{50} values of shape-specific CNPs in scavenging ROS in the diseased hVICs

IC_{50} (μM)	Cube	SR	LR	Sphere
Diseased-1	N/A	21.7±1.34	22.8±1.36	16.45±1.22
Diseased-2	N/A	12.55±0.88	13.46±1.13	17.18±1.15

The ability of CNPs to prevent ROS generation in the diseased hVICs was evaluated by measuring the intracellular ROS levels after 24 h CNP pre-treatment (25 μg/mL) followed by 4 h treatment of H_2O_2 (100 μM) to induce oxidative stress. Diseased-1 hVICs pre-treated with SR, LR and sphere CNPs but not cube CNPs showed significant reduction in ROS levels compared to 0 μg/mL CNP pre-treated group (**Fig. 34C**). Diseased-2 hVICs pre-treated with all CNPs showed significant reduction in ROS levels compared to cells without CNP treatment (**Fig. 34C**). These results indicated the ability of CNPs in protecting hVICs from exogenous oxidative stress.

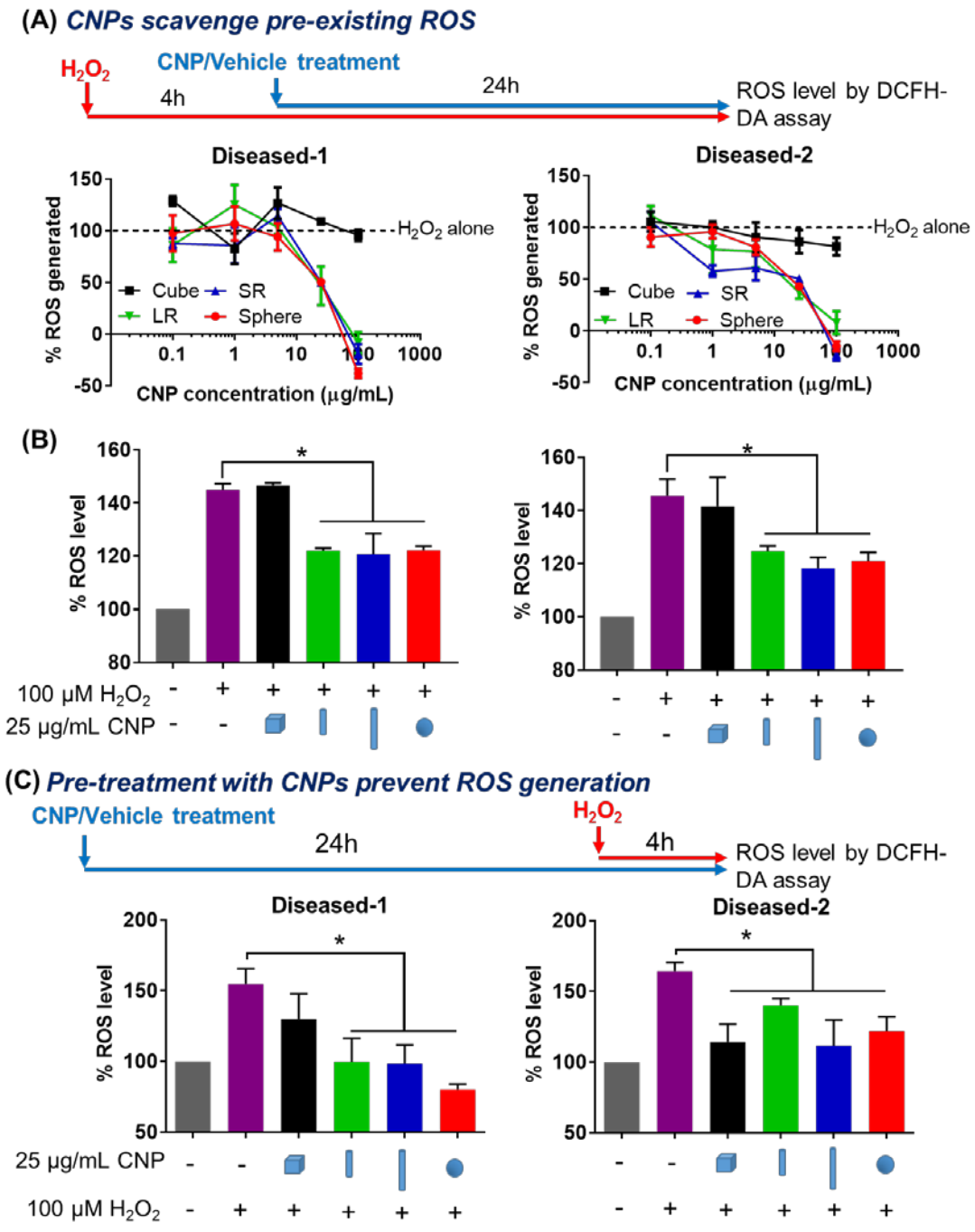

Figure 34. Shape-specific CNPs scavenged acute H_2O_2-mediated oxidative stress in the diseased hVICs.

(A) As illustrated in the experimental workflow, SR, LR and sphere but not cube CNPs scavenged in a dose-dependent manner, pre-existing intracellular ROS generated by H_2O_2 (100

μM, 4 h) in both diseased hVICs as measured by DCFH-DA assay (n=4). *indicates $p<0.05$ (Two-way ANOVA); **(B)** At the dose of 25 μg/mL, SR, LR and sphere but not cube CNPs scavenged pre-existing intracellular ROS generated by H_2O_2 (100 μM, 4 h) in diseased hVICs as measured by DCFH-DA assay (n=4). *indicates $p<0.05$ (One-way ANOVA); **(C)** As illustrated in the experimental workflow, pre-treatment with CNPs (25 μg/mL, 24 h) prevented intracellular ROS accumulation following treatment with H_2O_2 (100 μM, 4 h) in diseased hVICs in a shape-dependent manner (n=4). * indicates $p<0.05$ compared to H_2O_2 only treatment (One-way ANOVA). Data are presented as mean ± SEM.

Together, these data show that LR CNPs are effective in scavenging pre-existing ROS and in preventing ROS generation in both diseased hVICs. Therefore, we chose to focus on LR CNPs and study their therapeutic effects in combating oxidative stress-induced VIC calcification in the following studies.

To elucidate the mechanisms by which LR CNPs are able to reduce the intracellular ROS, we further measured the SOD/CAT activities of the diseased hVICs after H_2O_2 pre-treatment followed by LR CNP treatment. LR CNP treatment significantly increased SOD and CAT activities in both diseased hVIC populations (**Fig. 35A and B**). In addition to its intrinsic ability to scavenge ROS (**Fig. 32C**), LR CNPs may have exerted their ROS scavenging effect by enhancing the cellular antioxidant enzyme activities as means of maintaining redox balance. CNPs are known for their broad spectrum antioxidant mechanisms [283, 284]; however, to the best our knowledge, the ability of CNPs to enhance cellular antioxidant enzyme activity *in vitro* has not been demonstrated. Due to limited studies in the field, the exact antioxidant mechanisms (scavenging of radicals, superoxides or peroxides) required for inhibiting valve calcification

remain elusive. Previously, antioxidants such as tempol and lipoic acid [277], as well as adenovirus-mediated over-expression of SOD or CAT [273], have been explored for treating valve calcification. In these previous studies, supplement of antioxidant (either in the form of small molecule drug or antioxidant enzyme) did not demonstrate consistent therapeutic effects on mitigating the progression of valve calcification. Therefore, CNPs with broad intrinsic ROS scavenging mechanisms as well as the ability to enhance cellular antioxidant enzyme activities (SOD/CAT-mimetic) may be advantageous in mitigating oxidative stress-induced valve calcification.

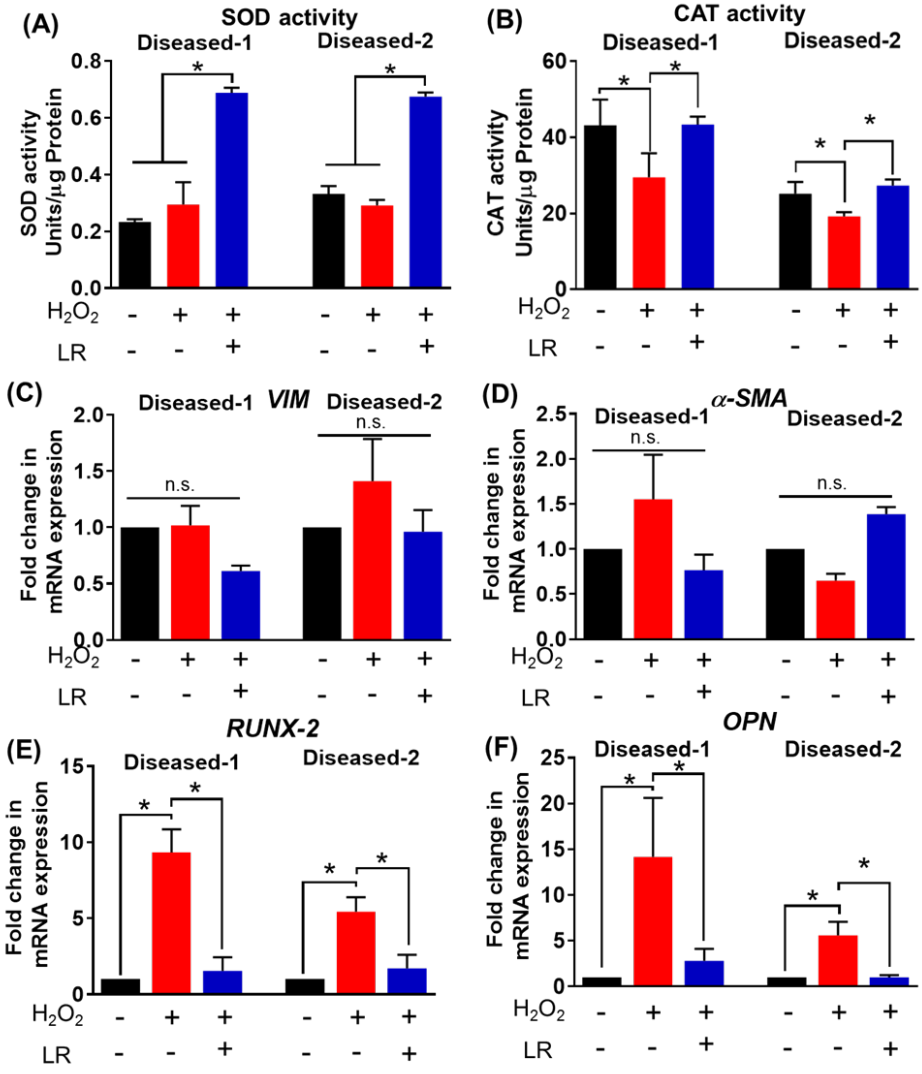

Figure 35. Shape-specific CNPs scavenged acute H_2O_2-mediated oxidative stress in the diseased hVICs.

LR CNP treatment upregulated SOD (A) and CAT (B) activity after H_2O_2-mediated oxidative stress (100 μM, 24 h) in the diseased hVICs (n=3); LR CNPs didn't change expression of fibroblast and myofibroblast markers in the diseased hVICs (C) and (D); LR CNPs decreased H_2O_2-induced expression of calcification markers in the diseased hVICs (E) and (F) (n=3). *indicates $p<0.05$ (One-way ANOVA). Data are presented as mean ± SEM.

Given the excellent ROS scavenging ability of CNPs in hVICs (**Fig. 34**), we further evaluated if CNP treatment can inhibit oxidative stress-induced upregulation of markers that precede calcification. As shown in **Fig. 35C**, LR CNP treatment after oxidative stress induction by H_2O_2 had no significant effect on the mRNA expression levels of VIM and α-SMA but reduced the expression of upstream calcification markers (RUNX-2 and OPN) in the diseased hVICs. Since we also observed that oxidative stress was able to upregulate calcification marker expression (**Fig. 31D**), this noted reduction in the presence of LR CNPs suggests that LR CNP is able to scavenge ROS (**Fig. 34**) and upregulate SOD/CAT activities (**Fig. 35A and B**). These results suggest that LR CNPs may be able to mitigate oxidative stress-induced calcification in hVIC cultures.

6.3.5 *In vitro* calcification model of hVICs

Although we observed increased calcium content in the Diseased-1 hVICs cultured with long term (14-day) H_2O_2 treatment, H_2O_2 treatment alone did not induce ARS-positive calcific nodule formation in the Diseased-1 hVICs (data not shown). Therefore, we further explored to enhance

oxidative stress (H_2O_2)-induced calcification by combining with the inorganic phosphate (Pi)-induced *in vitro* calcification model. Although Pi-induced *in vitro* calcification model has been widely used in studying ectopic vascular and breast calcification [292, 304], we did not find any report on Pi-induced valve calcification *in vitro*. Nonetheless, hyperphosphatemia is suggested to be one of the major driving factors for *in vivo* calcification [270], further highlighting the significance of studying Pi-induced valve calcification *in vitro*. To optimize the experimental conditions for Pi-induced hVIC calcification, Diseased-1 hVICs were treated with different concentrations of Pi (1-10 mM) for 14 days and calcification was evaluated by ARS staining and calcium content quantification. Treatment with exogenous Pi alone induced ARS-positive calcific nodule formation in Diseased-1 hVICs in a dose-dependent manner (**Fig. 36**) and 1 mM Pi was sufficient to induce a substantial amount of calcification and therefore, chosen as the dose for further study.

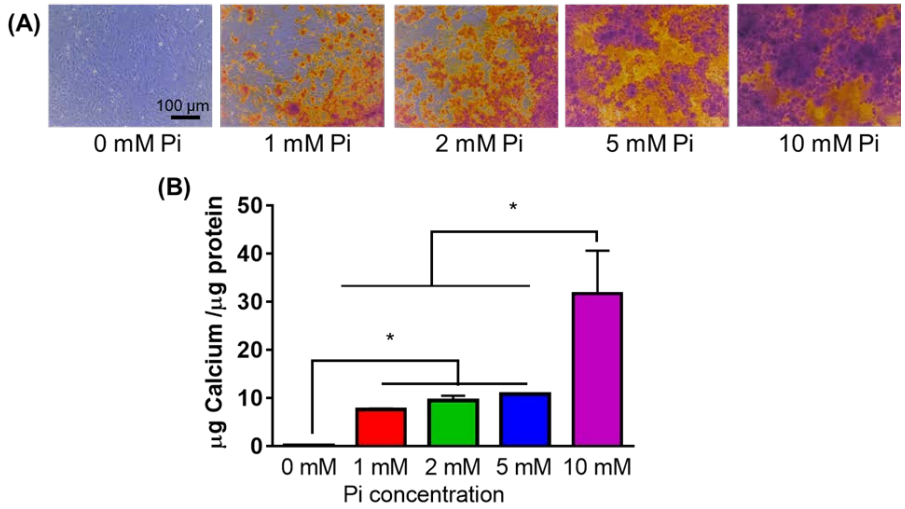

Figure 36. Inorganic phosphate (Pi) induced calcification in a dose-dependent manner in diseased-1 hVICs in 14 days.

(A) positive Alizarin Red S staining and (B) calcium content quantification by o-cresolphthalein assay (n=3). * indicates $p<0.05$ (One-way ANOVA). Data are presented as mean ± SEM.

To investigate the role of oxidative stress in promoting hVIC calcification, H_2O_2 (100 μM) was supplemented with the Pi-containing (1 mM) calcification media. The presence of Pi and oxidative stress (H_2O_2) recapitulated two major microenvironmental cues that co-exist in the calcified valves [266, 268] to serve as a physiologically relevant *in vitro* diseased model. The acute ROS generation was measured by DCFH-DA assay 2 h post-treatment with the calcification media. In accordance with a previous study that showed Pi-induced acute ROS generation *in vitro* (within 1-2 h) [305], we also observed Pi-induced ROS generation in the Diseased-1 hVICs, which was enhanced by the addition of H_2O_2 and reduced by concurrent administration of antioxidant Vitamin E (**Fig. 37A**). Similar results of ROS generation were also observed in the Diseased-2 hVICs when treated with Pi alone, Pi+H_2O_2, and Pi+H_2O_2+Vitamin E (**Fig. 38**). Diseased-1 hVICs were chosen as the cell model for further study. The addition of H_2O_2 increased Pi-induced positive ARS staining and calcium content in a time-dependent manner compared to Pi alone treatment in a 7-day study. Such increased calcification was diminished by the concurrent administration of vitamin E (**Fig. 37B and C**), thus validating the role of exogenous oxidative stress in promoting VIC calcification. This observation is in agreement with the previous finding that ROS generation precede and mediate valve calcification [156]. Overall, these data demonstrate that oxidative stress could further exacerbate calcification progression in hVICs in a Pi-induced calcification model.

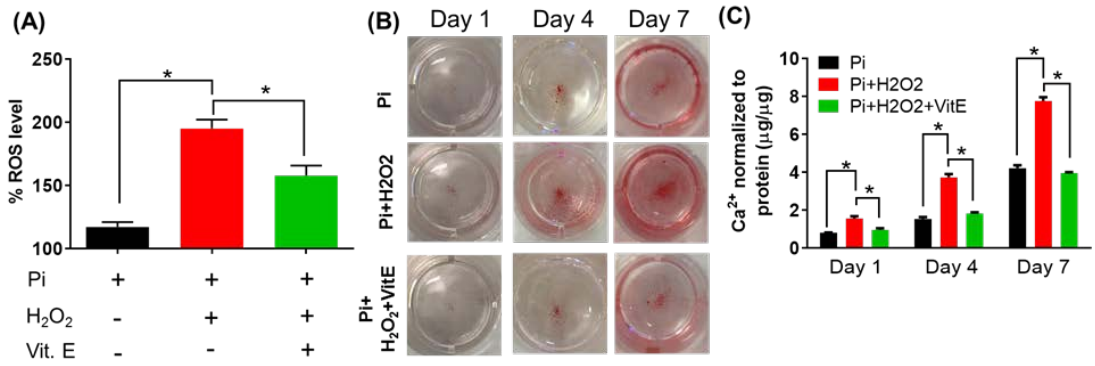

Figure 37. H_2O_2-mediated oxidative stress further enhanced calcification in the inorganic phosphate (Pi)-induced *in vitro* calcification model.

Diseased-1 hVICs were cultured in the presence of additional Pi (1mM) alone, Pi + H_2O_2 (100 µM) or Pi + H_2O_2 + Vitamin E (50 µM) for 2 h, 1, 4 and 7 days. (A) Addition of $H_2O_2$for 2 h increased intracellular ROS levels compared to Pi alone treatment and addition of Vitamin E prevented such H_2O_2-induced ROS (n=4). *indicates $p<0.05$ (One-way ANOVA); (B) Positive alizarin red S (ARS) in Pi-treated cultures exhibited a time-dependent increase that was enhanced by addition of H_2O_2. Co-treatment with antioxidant Vitamin E inhibited H_2O_2-induced ARS positive staining; (C) Diseased-1 hVICs showed increased calcium content when treated with Pi + H_2O_2 when compared with Pi treatment alone as measured by o-cresolphthalein assay. Co-treatment of hVICs with Vitamin E inhibited the calcium secretion in the presence of Pi and H_2O_2 (n=3). *indicates $p<0.05$ (Two-way ANOVA). Data are presented as mean ± SEM.

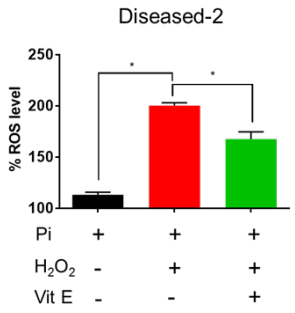

Figure 38. Addition of H_2O_2 increased intracellular ROS levels within 2 h in Diseased-2 hVICs. Addition of Vitamin E prevented such increase (n=4). * indicates $p<0.05$ (One-way ANOVA). Data are presented as mean ± SEM.

6.3.6 Anti-calcification properties of CNPs in hVICs calcification model

We further tested the hypothesis that CNPs will be able to mitigate the oxidative stress-induced hVIC calcification *in vitro*. As expected, the concurrent administration of LR CNPs decreased the H_2O_2-induced ROS generation (2 h) (**Fig. 39A**). We further revealed that long term (7-day) co-treatment of LR CNPs with Pi and H_2O_2 significantly increased the SOD and CAT activities in the Diseased-1 hVICs (**Fig. 39B and C**), suggesting the beneficial role of CNPs in modulating cellular antioxidant enzymes to combat oxidative stress. These results agree with the observation of increased SOD and CAT activities in diseased hVICs after short-term (24 h) co-treatment of LR CNPs with H_2O_2 (**Fig. 35A and B**).

Finally, the therapeutic benefit of LR CNPs in mitigating the Pi and H_2O_2-induced calcification was demonstrated by ARS staining and calcium quantification. Compared to the control group treated only with Pi and H_2O_2 without CNP treatment, the addition of LR CNPs reduced calcified nodule formation as revealed by less ARS staining and decreased total calcium content (**Fig. 39D**), which may be attributed to the ROS scavenging ability of LR CNPs. Previously, CNPs have been shown to inhibit osteogenic differentiation of primary mouse bone marrow stromal cells revealed by inhibition of mineralized nodules formation and alkaline phosphatase activity [306]. However, the underlying mechanisms were not explored. Our results strongly suggest that SOD/CAT-mimetic activity coupled with their ROS scavenging ability

allow CNPs to efficiently mitigate H_2O_2-induced oxidative stress and hence, inhibit the *in vitro* calcification in hVIC cultures.

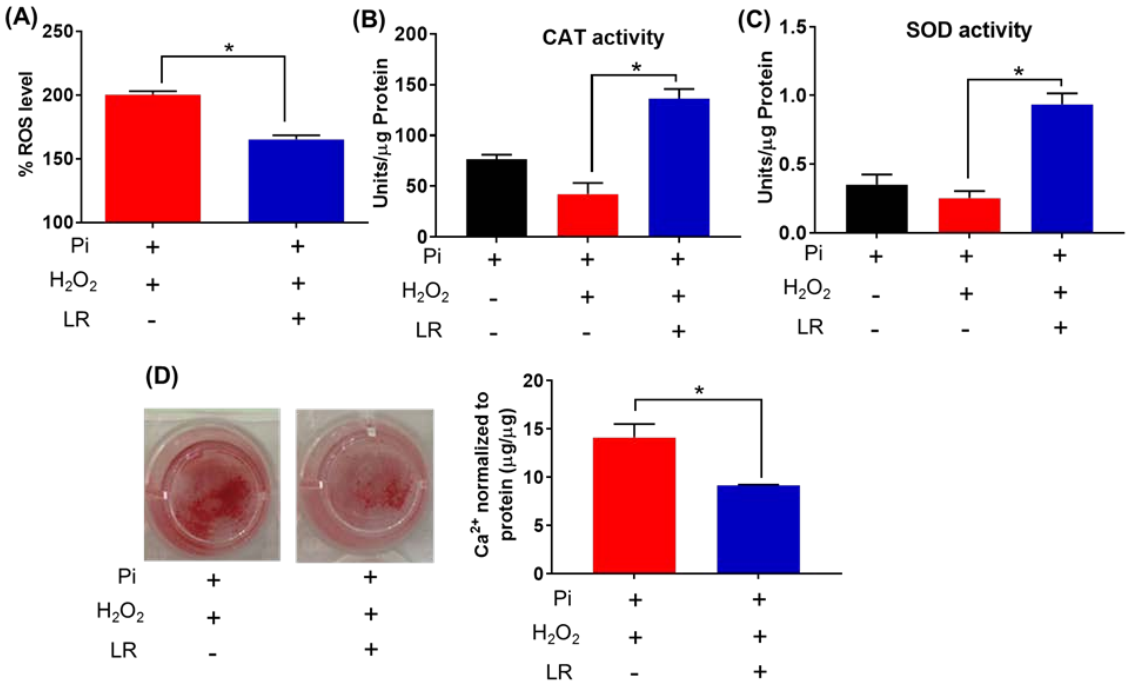

Figure 39. LR CNPs decreased calcium content in Pi and H_2O_2-induced calcification model. (A) LR CNPs reduced Pi+H_2O_2-induced acute intracellular ROS levels after 2 h treatment measured by DCFH-DA assay (n=4); LR CNPs enhanced SOD (B) and CAT (C) activities of diseased hVICs after 7-day treatment (n=3). (D) After 7-day treatment, LR CNPs reduced Pi + H_2O_2-induced calcification as revealed by decreased Alizarin Red S staining and calcium content by O-cresolphthalein assay (n=3); *indicates $p<0.05$ (One-way ANOVA). Data are presented as mean ± SEM.

6.3.7 Study limitations and outlook

The current study investigated the role of oxidative stress in mediating valve calcification by developing novel ROS-induced hVIC calcification model *in vitro* and proposed CNPs as a novel

potential treatment option. Although the presence of both Pi and oxidative stress were taken into consideration in our study, there are some limitations that we would like to acknowledge. First, the current studies were conducted in 2D cell culture, which may not directly reflect the VIC activities *in vivo* since VICs are known to undergo phenotypic changes in 2D cultures [295]. Future study investigating the role of oxidative stress and potential therapeutics in a 3D VIC culture system using suitable matrix will be informative. Second, in the current study, LR CNPs were co-administrated with Pi and H_2O_2. However, to further facilitate the translation of the therapy, it is worthwhile to explore the effect of time of treatment with LR CNPs on preventing and possibly, reversing the progression of pre-existing calcification caused by Pi and H_2O_2. Last but not least, we studied only two different calcified VIC populations and one normal VIC population. Therefore, it might not be appropriate to generalize our observations for all stenotic and normal VICs based on such small sample size. In order to make general conclusions on each group (normal vs. diseased) on the whole, future studies are required to include calcified and normal VIC populations from larger number of patients to fully understand gene regulation across normal physiology and various pathological states.

In order to facilitate the potential translation of CNP for valve calcification therapy, we envision that the local delivery of CNPs via a tissue-engineered construct [264] or polymeric drug carrier [307] will minimize the systemic exposure and prevent the calcification of valve replacement.

6.3.8 Summary

In conclusion, we demonstrated that hVICs derived from calcified valves exhibited impaired antioxidant defense mechanisms and were more susceptible to oxidative stress than normal

hVICs. CNPs scavenged H_2O_2-induced oxidative stress in hVICs in a shape- and dose-dependent manner. The intrinsic ROS scavenging ability of CNPs and their ability to induce cellular antioxidant enzyme activities may confer protection to hVICs from oxidative stress-exacerbated calcification. In a nutshell, our results suggest CNPs to be a promising antioxidant therapy for treating valvular calcification and deserve further investigations.

7.0 PEGYLATED ELASTOMER-CNP NANOCOMPOSITE FIBROUS SCAFFOLDS WITH REDUCED CALCIFICATION TENDENCY

7.1 BACKGROUND

As the mainstay of treatment for valvular heart diseases, the currently available valve replacements are far from ideal [31, 264]. To name a few, valve replacement by a bioprosthetic valve often lead to ectopic calcification *in vivo* and its tendency towards mechanical failure further shortens its durability [8]. On the other hand, mechanical valve replacements demand long-term anticoagulant therapy and may be subjected to life-threatening hemodynamic failure [9, 10]. More importantly, both valve replacements are not viable and cannot grow with patients [11]. As a result, these valve replacements are likely to require re-operation, often multiple re-operations, especially for pediatric patients [12].

Tissue engineering based regenerative heart valve therapy, which employs a viable valve replacement with the potential to grow and remodel upon implantation is of huge interest. Prior research in the field have not only illustrated several key parameters in the design of tissue engineered valve as mentioned in Chapter 1 [78, 95, 101, 264, 308] but also led to several important achievements such as the encouraging proof-of-concept results from preliminary large animal studies and clinical trials [136, 309]. It has been widely acknowledged that a biodegradable tissue-engineered valve replacement, which can withstand the dynamic *in vivo*

environment, mimic the native valve ECM structure and properties, and guide the valve regeneration, is highly advantageous [310-312]. Many studies have demonstrated the feasibility and functionality of scaffolds, which possess these properties individually [37, 38, 57, 58, 74, 181]. However, fewer studies have incorporated multiple design criteria in a single tissue engineered valve. Moreover, since calcification of native valves and valve replacements have been shown to be an active rather than a passive degenerative process [313], the implanted tissue engineered scaffold are also susceptible to calcification and thereby device failure [128]. Unfortunately, most of the current studies on heart valve tissue engineering have overlooked the potential issue of scaffold calcification and specific strategy to overcome this problem is in critical need.

Applying the tissue engineering principles, we have previously developed biodegradable, anti-thrombogenic, anisotropic, and elastomeric fibrous scaffolds, which could mimic the mechanical aspects of the native valve and support human valvular interstitial cell (hVIC) proliferation ([242] and Chapter 5). Specifically, we have demonstrated that the scaffolds made from biodegradable elastomer blends of PCL and APS-25PEG were able to mimic the uniaxial and biaxial mechanical properties of native valve leaflet hVICs ([242] and Chapter 5). We have also revealed the unique properties of cerium oxide nanoparticles (CNPs) in mitigating the oxidative stress-induced calcification of hVICs due to their reactive oxygen species (ROS) scavenging properties [248]. Biocompatible rod and sphere shaped CNPs could scavenge both abiotic and intracellular ROS in a dose-dependent manner. Therefore, these two CNPs were effective in mitigating the oxidative stress-induced calcification in hVICs.

Engineering nanocomposite biomaterial represents an emerging approach to confer functionality to the original biomaterial [314]. In the current study, we hypothesized that CNP

encapsulated elastomeric scaffolds will have diminished potential of calcification without interfering with the other desired properties of the scaffold. Towards this goal, we investigated the rod and sphere CNPs encapsulated APS-25PEG-PCL scaffold. We first demonstrated the feasibility of co-electrospinning nanoparticles with polymer solution followed by examining the effect of CNP encapsulation on the morphology, mechanical properties, ROS scavenging properties, cytocompatibility, and anti-calcification properties of these nanocomposite scaffolds.

7.2 METHODS

7.2.1 Materials

All chemical and biological agents used in the study were same as reported in the previous chapters, unless otherwise noted. APS-co-PEG polymers were synthesized according to section 3.2.1. CNPs were prepared according to section 6.2.8.

7.2.2 Scaffold fabrication by electrospinning

Briefly, CNPs (0.5% or 1% w/w to total polymer weight) were first added to a mixture of ethanol and chloroform at a volume ratio of 1:9 (detailed material formulation in **Table 17**). This suspension was dispersed using a probe sonicator (Sonic Dismembrator Model 500, Fisher Scientific, USA) for 15s at 10% amplitude every 10s over a 20 min time period. APS-25PEG and ε-PCL (6% and 12% w/v, respectively) were then dissolved in this suspension. To fabricate anisotropic scaffolds, a custom-made ring-shaped copper wire was used as electrospinning

collector. Solutions were electrospun at 17 kV at a rate of 1 mL/h. The distance between the 21G needle and collector was kept at 12 cm. The obtained electrospun scaffolds were dried in a vacuum desiccator overnight before further experiments.

Table 17. Polymer and CNP formulations for fabricating nanocomposite scaffolds

APS-25PEG/PCL (6%/12%, w/v)		
CNP shape	Long rod (LR)	Sphere
CNP dose (w_{cnp}:$w_{total\ polymer}$)	0%	
	0.5%	0.5%
	1%	1%

7.2.3 Scanning electron microscopy (SEM)

Scaffold morphology was characterized using scanning electron microscopy (SEM) (Zeiss Sigma500 VP, UK). Fibrous scaffolds were sputter-coated with 5 nm of gold–palladium using Denton auto sputter coater (Denton Vacuum, Moorestown, NJ), and images were obtained using accelerated voltage of 3 kV. Images were analyzed for fiber diameters and alignment using NIH ImageJ Software with DiameterJ [246] and OrientationJ [247] plugins. At least four images (at 2000X magnification) from each group were used for analysis.

7.2.4 Uniaxial mechanical testing

Scaffold mechanical properties were studied using uniaxial tensile tests with MTEST Quattro mechanical testing system (ADMET, Norwood, MA). Scaffolds were cut into rectangular shapes (~15 × 7 mm^2, n = 4 per group) and stretched at a constant displacement rate of 10 mm/min until

the sample failure. The stress (MPa) was obtained by dividing the applied force (N) with cross-section area (mm^2); percent elongation (strain, ε) was obtained from $\varepsilon\ (\%)=100\times(L-L_0)/L_0$, where L_0 was initial gauge length and L was instantaneous gauge length. Elastic modulus was calculated in the linear region at 5–15% strain.

7.2.5 Abiotic reactive oxygen species (ROS) scavenging assay

The ROS scavenging capabilities of scaffolds were measured using the 2,2-Diphenyl-1-picrylhydrazyl (DPPH) assay. Stocks of DPPH (Aldrich, USA, 1 mM) were prepared in ethanol prior to the assay. Scaffolds (10 mg) were first immersed in ethanol (800 μL) and vortexed vigorously. The DPPH stock solution (200 μL) was then added to the scaffold containing solution (800 μL) and mix well. The mixture was allowed to reaction in dark for 30 min at room temperature. Subsequently, the absorbance was read at 520 nm (n = 4) using a microplate reader (Synergy HT, BioTek Instruments, USA). The scaffolds with 0% CNPs served as a negative control. Percentage of DPPH scavenged was calculated from the formula below:

$$\text{Scavenged DPPH (\%)} = (A_{\text{negative control}}-A_{\text{test}})/A_{\text{negative control}} * 100\%$$

7.2.6 Culture of hVICs on nanocomposite scaffolds

The hVICs were obtained and cultured according to our prior publication [248]. For both biocompatibility and calcification study, the scaffolds (10 × 10 mm^2) were first sterilized by exposing to 70% isopropanol under UV light for 30 min and rinsed with 1X DPBS thrice to remove any residual ethanol. The hVICs were seeded on to these scaffolds at a density of

100,000 cells/scaffold in a 24-well plate. After 24 h, cell seeded scaffolds were transferred to new wells to avoid the interference of from the unattached cells.

7.2.7 *In vitro* biocompatibility by alamarBlue® assay

The hVIC proliferation on scaffold was measured via monitoring cell metabolic activity at day 7 and 21 using the alamarBlue® assay (Invitrogen, Carlsbad, CA) following the protocol described in section 4.2.9. At day 21, hVICs were decellularized by trypsin and the scaffolds were collected for mechanical testing.

7.2.8 *In vitro* calcification model on electrospun scaffolds

After cell seeding, hVICs were allowed to attach to scaffold for 48 h followed by changing to calcification media. First, to establish the role of oxidative stress in promoting calcification, hVICs were cultured on 0% CNP scaffold using MEM-alpha supplemented with 10% fetal bovine serum (FBS) containing an additional 1 mM sodium phosphate monobasic (Pi) and 100 μM H_2O_2. The cells cultured using the same media except without 100 μM H_2O_2 were served as negative control. Next, hVICs were cultured on 0% CNP or 1% rod scaffolds using MEM-alpha supplemented with 10% FBS containing an additional 1 mM Pi and 100 μM H_2O_2. The cells cultured on the 0% CNP scaffolds were served as positive control. Media was replenished every day. Calcification in hVICs cultures was determined using calcium content quantification (as described in section 7.2.9) and mRNA expression of calcification and fibrosis genes (*α-SMA, OPN, RUNX-2, COLLAGEN-1,* as described in section 7.2.10) at day 7.

7.2.9 Cellular calcium content quantification

At day 7, hVICs were trypsinized from the scaffolds to obtain the cell pellets. Calcium was then extracted from the cell pellets by incubation with nitric acid (1M) for 1h followed by centrifugation. The supernatant (35 µL) was mixed with O-cresolphthalein (0.25 mg/mL, 35 µL) and 2-amino-2-methyl-1-propanol (150 mg/mL, 87.5 µL) at room temperature for 20 min and the absorbance was measured at 575 nm.

7.2.10 Analysis of mRNA expression by qPCR

Similar to section 6.2.9, hVIC cell pellets were obtained at day 7. This was followed by RNA extraction and qRT-PCR as described in section 6.2.5.

7.2.11 Statistical analysis

Experimental data are presented either as mean ± standard error of the mean (SEM) or as mean ± standard deviation (SD) as specified in each figure legend. Multiple comparisons were analyzed for significance using one-way ANOVA or two-way ANOVA followed by Tukey's post-hoc analysis. P-values less than 0.05 were considered as significant.

7.3 RESULTS AND DISCUSSION

7.3.1 Fabrication of nanocomposite scaffolds and scaffold morphology

We first studied the feasibility of co-electrospinning CNPs with polymer blends to obtain nanocomposite scaffolds. Sphere and rod CNPs showed excellent antioxidant properties in our earlier studies ([248] and Chapter 6), and thus, were selected in the current study. Meanwhile, APS-25PEG/PCL (6+12%) formulation studied in our previous report yielded anisotropic fiber alignment and biaxial mechanical properties similar to the porcine aortic valve leaflet (Chapter 5). Therefore, we interfaced sphere and rod CNPs into the APS-25PEG/PCL (6+12%) formulation at two different concentrations (0.5% and 1% w/w to the total polymer concentration, **Table 17**). All CNP-encapsulated scaffolds were successfully fabricated using ring-shaped electrospinning collector (as reported in Chapter 5). We first investigated the effect of CNP encapsulation on the scaffold morphology. SEM imaging revealed that 1% sphere and rod CNP-encapsulated scaffolds maintained their micro/nano-fibrous structure as seen in low magnification (2000 X) images (**Fig. 40a and b**) without obvious nanoparticle aggregation as seen in high magnification images (5000 X) (**Fig. 40c and d**). Furthermore, CNP-encapsulated scaffolds maintained the anisotropic fiber alignment as revealed by the single sharp peak in the quantification of fiber orientation (**Fig. 40e and f**). These results suggested that CNPs were amenable to be encapsulated into the polymer formulation without interfering with the electrospinning process.

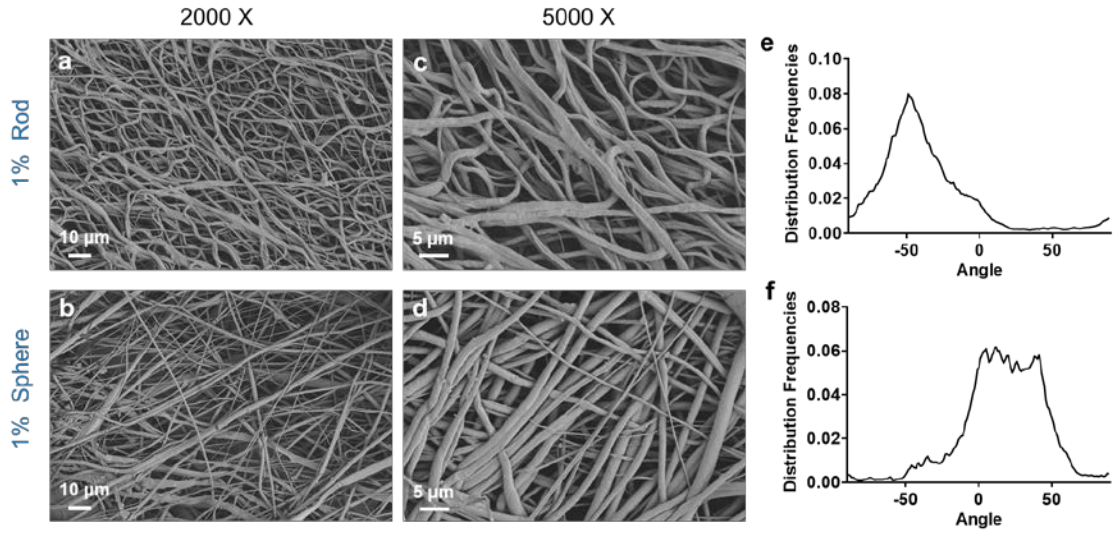

Figure 40. SEM images and fiber alignment of 1% sphere and rod CNP-encapsulated scaffolds. (a, b): SEM images at 2000X magnification; and (c, d): 5000X magnification; (e, f): Fiber alignment quantification by OrientationJ plugin in NIH ImageJ (n=at least 4 images)

7.3.2 ROS scavenging ability of electrospun scaffolds

One of the major rationales of encapsulating CNPs into the fibrous scaffolds is to utilize their ROS scavenging ability to create scaffolds with enhanced ROS scavenging properties. Therefore, we first examined whether the CNPs encapsulation could improve the ROS scavenging ability of fibrous scaffolds. The DPPH scavenging assay is a direct measurement of the radical scavenging properties of a therapeutic agent [315]. Compared to the 0% CNP scaffold of the same weight, sphere and rod CNP encapsulated scaffolds resulted in significant reduction in DPPH level (**Fig. 41**), indicating their enhanced radical scavenging abilities. This observation was in agreement with our previous results that rod and sphere CNPs displayed similar antioxidant properties in aqueous dispersion [248, 285]. It was also noted that there is no significant difference between scaffolds containing different CNP concentrations (0.5% and 1%). These results indicated that

CNP encapsulation in fibrous scaffold led to enhanced ROS scavenging ability of nanocomposite scaffolds.

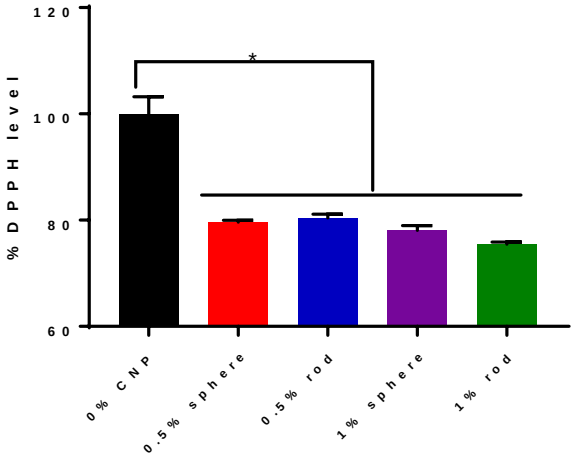

Figure 41. The radical scavenging capability of CNP-encapsulated nanocomposite scaffolds by DPPH assay.

*indicates $p<0.05$ as compared to 0% CNP scaffold (n = 3, One-way ANOVA, Tukey's Post-hoc test).

7.3.3 Viability of hVICs cultured on scaffolds

We have previously shown that APS-25PEG/PCL scaffold supported hVIC proliferation ([242] and Chapter 5) and both rod and sphere CNPs possessed minimal cytotoxicity to hVICs at concentration less than 100 μg/mL ([248] and Chapter 6). However, it is challenging to extrapolate these results when CNPs are encapsulated into fibrous scaffolds where multiple factors such as nanoparticle dissolution and release could potentially cause the fluctuation of CNP concentration in the culture media. Therefore, we monitored the hVIC viability 1 and 3 weeks after seeding onto the CNP-encapsulated scaffolds. The hVICs cultured on CNP-

encapsulated scaffolds demonstrated cell viability similar to those cultured on 0% CNP scaffolds at both time points (**Fig. 42**), indicating that up to 1% w/w encapsulation, CNP-encapsulated scaffolds supported the hVIC proliferation similar to the prototype APS-25PEG/PCL scaffold.

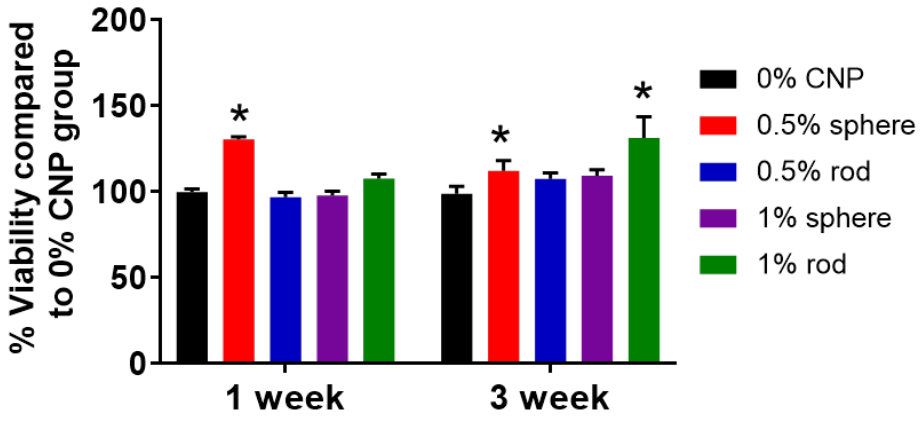

Figure 42. The hVIC cytocompatibility of CNP encapsulated electrospun scaffolds after 1 week and 3 week of culture by alamarBlue® assay.

*indicates $p<0.05$ as compared to 0% CNP scaffold (n = 4, One-way ANOVA, Tukey's Post-hoc test).

7.3.4 Mechanical properties of nanocomposite scaffolds

Next, we continued to study the effect of CNP encapsulation on the mechanical properties of the electrospun scaffolds. Acting as filler, nanoparticles are known to reinforce the mechanical properties of polymeric scaffolds when encapsulated in polymeric scaffold [316]. In the current study, encapsulation of neither 0.5% nor 1% sphere CNPs changed the stiffness of the scaffold significantly (**Fig. 43**). On the contrary, encapsulation of both 0.5% and 1% rod CNP resulted in a significant increase in the scaffold stiffness (**Fig. 43**). It was speculated that such differences could be due to the size of the two types of CNPs. Sphere CNPs had lower actual particle size

than that of rod CNPs (**Fig. 32**) and may not be able to effectively reinforce the scaffold. Overall, such effects of CNPs on the mechanical properties of the scaffold provide us with alternative strategy to fine tune the scaffold mechanical properties if necessary.

Additionally, at the end of the three-week culture, we measured the mechanical properties of the decellularized scaffolds. The stiffness of all scaffolds increased as compared to corresponding as-prepared scaffolds (**Fig. 43**), indicating the possible *de novo* ECM protein deposition during the culture. These promising results obtained in this preliminary cytocompatibility study on the CNP-encapsulated scaffolds warrant further long-term studies on the biocompatibility of CNP-encapsulated scaffolds and their degradation products.

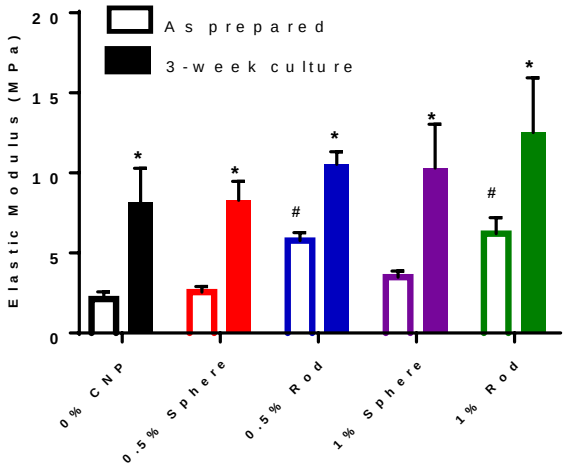

Figure 43. The elastic modulus of CNP encapsulated nanocomposite scaffolds (as prepared and after 3-week hVIC culture) by uniaxial tensile tests.

# indicates $p<0.05$ as compared to as prepared 0% CNP group.

* indicates $p<0.05$ as compared between “as prepared” and “3 week culture” of each group of samples (n=4, Two-way ANOVA, Tukey’s Post-hoc test).

7.3.5 *In vitro* calcification of electrospun scaffolds

We further hypothesized that CNP-encapsulated scaffolds with ROS scavenging properties could diminish oxidative stress-induced hVIC calcification. To test this hypothesis, we first demonstrated calcification promoting ability of oxidative stress in hVICs cultured on the fibrous scaffolds. We used H_2O_2 (100 μM) to induce oxidative stress. The hVICs were cultured on APS-25PEG/PCL scaffold with or without additional H_2O_2 (100 μM) for 7 days. Compared to the hVICs cultured without H_2O_2, hVICs cultured with H_2O_2 showed increased degree of calcification as demonstrated by the increase in intracellular calcium content (**Fig. 44a**) and mRNA expression of *RUNX-2* and *OPN* (VIC osteogenic differentiation markers) and *α-SMA* and *COL-1* (VIC myofibroblast activation and fibrosis markers) (**Fig. 44b**). These results are in accordance to the previous hVIC calcification study conducted on 2D cell culture [248]. Therefore, we continued to examine whether hVICs cultured on CNP-encapsulated scaffolds would mitigate calcification when challenged by oxidative stress (in the form of H_2O_2). Herein, we selected 1% rod CNP-encapsulated scaffolds based on their cytocompatibility and ROS scavenging properties (**Fig. 41 and 42**). At the end of the 7-day calcification study, hVICs cultured on 1% rod CNP-encapsulated scaffolds demonstrated reduced intracellular calcium content compared to 0% CNP scaffold (**Fig. 44c**). Furthermore, to elucidate the phenotypic changes in hVICs seeded on scaffolds with and without CNPs, mRNA expression of various markers including were quantified out by qRT-PCR. The hVICs cultured on 1% rod CNP encapsulated scaffold exhibited reduced mRNA expression of osteogenic related (*RUNX-2* and *OPN*) and fibrosis related (*α-SMA* and *COL-1*) gene (**Fig. 44d**). These results provided preliminary evidence that CNP-encapsulated scaffolds could mitigate hVIC calcification. It also suggested the beneficial roles of CNP under oxidative stress in reducing both, the osteogenic and

myofibroblastic differentiation of hVICs, which are two major mechanisms in directing valvular calcification [274].

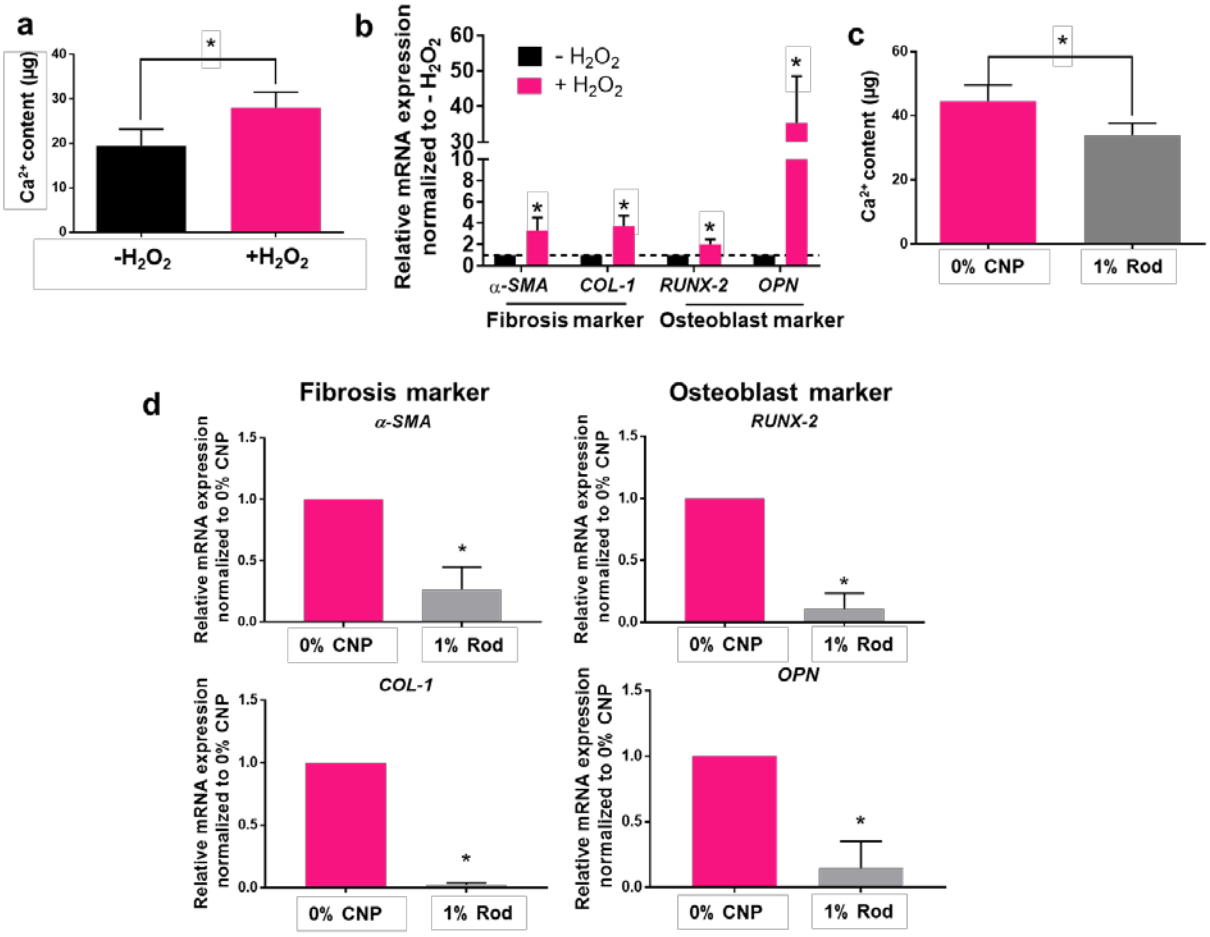

Figure 44. Oxidative stress-induced *in vitro* hVIC calcification on fibrous scaffolds.

The effect of oxidative stress (H_2O_2) on (a) intracellular calcium content; and (b) the fibrosis and osteogenic related gene expression of hVIC; (c) Encapsulation of CNP mitigated intracellular calcium deposition; and (d) the effect of CNP encapsulation on the fibrosis and osteogenic related gene expression of hVICs. *indicates $p<0.05$ (Unpaired t-Test).

7.3.6 Summary

In conclusion, we have demonstrated the feasibility of fabricating CNP-encapsulated nanocomposite scaffolds using different CNP shapes and concentrations. CNP encapsulation enhanced the ROS scavenging properties of the scaffolds compared to those without CNPs. In addition, CNP encapsulation could be used to maintain (via sphere CNP encapsulation) or increase (via sphere CNP encapsulation) the scaffold stiffness. At the concentrations tested (0.5 and 1% w/w), no significant cytotoxicity was observed for CNP-encapsulated scaffolds. Most importantly, in an oxidative stress-induced hVIC calcification model, CNP-encapsulated scaffolds demonstrated diminished calcification tendency as compared to those without CNPs. We envision that encapsulation of CNPs into the fibrous scaffolds represent a promising strategy to tackle the calcification issue of the most tissue-engineered heart valve constructs.

8.0 CONCLUSIONS AND FUTURE PERSPECTIVES

8.1 MAJOR CONCLUSIONS

Tissue engineering-based technology stands as a promising enabling strategy to serve the clinical unmet needs in treating valvular heart diseases. Pioneered by leaders such as Langer and Vacanti back in the early 1990s, the past decades have witnessed the exponential growth of studies to understand and apply the principles of tissue engineering for recreating various tissues and organs, either alone or in combination. To this end, one of the central dogmas that have been repeatedly practiced and proven is to create ECM-mimetic biocompatible tissue-engineered construct.

Engineering heart valves are of immense interests due to 1) the increasing patient number; 2) the limited choices of treatment; and 3) the significant drawbacks of these treatments. However, the unique function and architecture of the heart valve pose huge challenges in recreating valve replacement faithfully. Prior studies have identified several key aspects when engineering heart valves. Specifically, a tissue-engineered valve needs to withstand the dynamic *in vivo* environment while being mechanically compliable for valve opening and closing. It also needs to be anisotropic in its geometry and mechanical properties to guide the regeneration and carry out the essential opening and closing movement. Due to its vital position (inside the heart) and blood-contacting nature, the biocompatibility of the tissue-engineered valve needs to be

carefully scrutinized. Unfortunately, these critical features have been rarely studied in combination.

I approached this scientific problem by designing and applying novel materials and scaffolds using micro-/nanotechnology. In Chapter 3 and 4, I reported the synthesis, fabrication, and characterization of a novel series of biodegradable and biocompatible elastomers named APS-co-PEG. It was demonstrated that the scaffolds made from these elastomers had widely tunable elasticity and less thrombogenicity compared to the un-PEGylated prototype polymer. In Chapter 5, I described a novel optimization of electrospinning process to fabricate anisotropic scaffolds, which emulate the anisotropic architecture and mechanical properties of native valves. It was further demonstrated that the mechanical properties of scaffolds could be tuned by polymer formulation. In chapter 6, I tested antioxidant CNPs as novel therapeutic agents to prevent valvular calcification. It was demonstrated that CNPs scavenged intracellular oxidative stress and consequently mitigated calcification. Lastly, in chapter 7, I combined the two micro-/nanotechnologies to fabricate CNP encapsulated anisotropic fibrous scaffolds as a proof-of-concept prototype of tissue-engineered heart valve. Overall, the work presented in this dissertation demonstrated the feasibility and effectiveness to incorporate multiple design criteria when constructing tissue-engineered valves. Additionally, the technologies developed herein allow the fabrication of scaffolds with widely tunable properties and can be re-purposed for other soft tissue engineering applications.

8.2 STUDY LIMITATIONS

The current studies are not without limitations. This section will present the main limitations in my studies from three aspects and provide insights to overcome these limitations.

First of all, although we have recreated anisotropic fibrous scaffolds (chapter 5), which mimic the anisotropic mechanical properties of the native valve, the tri-layered structure of native valve ECM (as described in section 1.3.1) has not been recapitulated in this study. It has been reported that the three layers of the valve ECM work in an orchestrated manner to maintain the normal valve opening and closing cycles. In this dissertation, the middle proteoglycan-rich spongiosa layer was not taken into the design of tissue-engineered heart valve scaffold. Although being a relatively thin layer as compared to the fibrosa, the spongiosa layer provides excellent shock-absorbing properties to reduce the friction, dampen vibrations, and resist delamination. Potential strategy to overcome this limitation and further improve the overall scaffold design could be the fabrication of elastomeric fiber-hydrogel composite scaffolds to recapitulate this important structural feature.

Secondly, although we were able to achieve anisotropic fiber alignment, and degree of anisotropy and linear modulus similar to the native valves (chapter 5), I would like to acknowledge that the polymeric scaffolds and native valve tissue were not identical in their biaxial mechanical behaviors. As shown in the equibiaxial stress-strain plots (**Fig. 24**), native valves displayed non-linear mechanical behavior with two distinct linear regions. The initial toe region is attributed to the stretching of coiled collagen fibers which is followed by a second stage where further elongation of the straightened collagen fibers results in a steep rise in tensile stress until the tissue attains maximum extensibility. On the other hand, the polymeric scaffolds, in general, have relatively linear mechanical behaviors. It was suspected that such difference in the

biaxial mechanical properties could be attributed to the structural differences such as the lack of the gel-like spongiosa layer in our fibrous scaffolds to provide shock-absorbing properties.

Last but not the least, in a proof-of-concept study (chapter 7), the feasibility of CNP encapsulation in elastomeric fibrous scaffold as one approach to mitigate valve calcification was demonstrated. However, the encouraging preliminary results also raise more important yet unanswered questions with regard to the functionality of this nanocomposite scaffold. For example, how will CNPs exert their effects after encapsulation? Will CNPs be released? If yes, how will the polymer formulation affect the release profile? Additionally, in terms of its long-term effect, whether and how will CNPs be eliminated *in vivo*? How will CNP encapsulation modulate the local redox balance, which is crucial for the immune infiltration and subsequent tissue regeneration?

Overall, the study limitations identified here will guide the future studies to improve the scaffold design and understand the mechanisms of action of nanocomposite scaffolds.

8.3 FUTURE DIRECTIONS

It is believed that the work presented in this dissertation opens up to more sophisticated investigations to facilitate the development of tissue-engineered heart valve therapy. This section will first discuss the immediate research directions on the continuation of the current work and then discuss some long-term research goals for the successful clinical translation of this therapy.

First, the scaffold design can be further improved to achieve a better mimicry of the mechanical properties of native valve. As mentioned in section 8.2, strategy such as a fiber-hydrogel composite scaffold may enable the non-linear biaxial tensile behaviors. Next, the

functionality (continuous opening and closing) of the scaffold needs to be assessed in a physiologically relevant bioreactor, which can provide the proper flow conditions. The structural integrity and degradation of the scaffold, *de novo* ECM synthesis, and cellular phenotypic changes during this dynamic culture system need to be further investigated. Moreover, prior to the implantation in the valve position *in vivo*, the suitability of the scaffolds to be sutured or for minimally invasive transcatheter technology needs to be studied and validated.

Looking forward, the field of tissue-engineered heart valve is still in its infancy. There remain huge challenges and opportunities to facilitate its clinical translation in terms of the mechanistic understanding of tissue regeneration process and product development of tissue-engineered valve.

In terms of the mechanistic understanding, there is little knowledge available regarding the immune response to tissue-engineered valves and more profound investigations are required. Upon implantation, almost all biomaterials initiate host responses with immune cell infiltration and cytokine secretion. Such host responses to biomaterials are often necessary and beneficial in removing cellular debris due to injury and deterring the progression of infection. However, sustained and uncontrolled immune responses will eventually result in chronic inflammation and tissue fibrosis. Although little is known on valve regeneration, prior studies on skeletal muscle and vascular tissue engineering have suggested that the differentiation of monocytes towards the alternative macrophage phenotype (M2) in the early regeneration process would be beneficial in creating suitable conditions for tissue formation. Therefore, scaffolds that can harness the innate immune response by skewing the macrophage differentiation and/or selective recruitment of immune cells to facilitate tissue regeneration will be advantageous. This goal can be achieved by

the encapsulation or grafting of biological molecules such as cytokines and growth factors or via the biophysical cues such as roughness, matrix stiffness, and micro-/nano-architecture.

A successful medical product/device needs to be amenable to large scale manufacturing and should have a long shelf life as well as a straightforward regulatory process to be appealing to the biomedical industry and patients. Conventional tissue engineering strategy involves the *in vitro* culture of cell-seeded scaffold until its maturation followed by implantation. Such strategy is often lengthy and costly in its process and may hit multiple regulatory hurdles due to the complex components. Therefore, scaffolds designed for *in situ* tissue engineering which offer the off-the-shelf availability may be more promising in terms of the clinical translation of tissue engineering technology. Recently, encouraging results from Baaijens and Bouten groups have demonstrated the feasibility and functionality of an *in situ* tissue engineered heart valve made from electrospun polycarbonate scaffold [136]. In a 12-month study in the sheep model, tissue engineered valves maintained hemodynamic performance where a native-like, layered ECM structure slowly formed and replaced the graft. Also, moving forward, more preclinical studies, which can elucidate the underlying principles and mechanisms of scaffold design, neo-tissue formation, and host responses of *in situ* tissue engineering are warranted. Moreover, the issue of scale-up manufacturing of such scaffolds needs to be addressed. Electrospinning technology has been investigated for the large-scale industrial manufacturing. Flat electrospun mat can be fabricated at around 200 g of fibers/h using free surface electrospinning technology where numerous electrospinning jets emerge simultaneously to produce a large sheet of fibers collected on a negatively charged parallel electrode. However, fabricating electrospun scaffolds with a unique shape and geometry remains largely unexplored and presents new challenges that need to

be addressed such as 1) manufacturing in large quantity; 2) reproducibility during fabrication; and 3) safety and environmental control of electrospinning.

In conclusion, the results of the present work contributed to the current knowledge of design, synthesis, fabrication, and characterization of functional and biocompatible tissue-engineered heart valve. To facilitate its clinical translation, a strong collaboration among material scientists, biomedical engineers, pharmacists, clinicians, and industrial engineers is essential to provide new insights and progress towards mending a diseased heart valve.

BIBLIOGRAPHY

1. Mozaffarian, D., et al., *Heart Disease and Stroke Statistics—2016 Update.* Circulation, 2016. **133**(4): p. e38-e360.
2. Loffredo, C.A., *Epidemiology of cardiovascular malformations: prevalence and risk factors.* Am J Med Genet, 2000. **97**(4): p. 319-25.
3. Kalter, H., *Mortality and Maldevelopment*. 2007.
4. Sanz-Garcia, A., et al., *Heart valve tissue engineering: how far is the bedside from the bench?* Expert Reviews in Molecular Medicine, 2015. **17**.
5. d'Arcy, J.L., et al., *Valvular heart disease: the next cardiac epidemic.* Heart, 2011. **97**(2): p. 91-93.
6. Yacoub, M.H. and L.H. Cohn, *Novel approaches to cardiac valve repair: from structure to function: Part I.* Circulation, 2004. **109**(8): p. 942-50.
7. Butcher, J.T., G.J. Mahler, and L.A. Hockaday, *Aortic valve disease and treatment: The need for naturally engineered solutions.* Advanced Drug Delivery Reviews, 2011. **63**(4-5): p. 242-268.
8. Kvidal, P., et al., *Observed and relative survival after aortic valve replacement.* Journal of the American College of Cardiology, 2000. **35**(3): p. 747-756.
9. Basude, S., et al., *Low-molecular-weight heparin or warfarin for anticoagulation in pregnant women with mechanical heart valves: what are the risks? A retrospective observational study.* BJOG: An International Journal of Obstetrics & Gynaecology, 2012. **119**(8): p. 1008-1013.
10. Hammermeister, K., et al., *Outcomes 15 years after valve replacement with a mechanical versus a bioprosthetic valve: Final report of the Veterans Affairs randomized trial.* Journal of the American College of Cardiology, 2000. **36**(4): p. 1152-1158.
11. Tillquist, M.N. and T.M. Maddox, *Cardiac crossroads: deciding between mechanical or bioprosthetic heart valve replacement.* Patient Preference and Adherence, 2011. **5**: p. 91-99.
12. Cheung, D.Y., B. Duan, and J.T. Butcher, *Current progress in tissue engineering of heart valves: multiscale problems, multiscale solutions.* Expert Opinion on Biological Therapy, 2015. **15**(8): p. 1155-1172.
13. Langer, R. and J.P. Vacanti, *Tissue engineering.* Science, 1993. **260**(5110): p. 920-6.
14. Langer, R., et al., *Tissue engineering: biomedical applications.* Tissue Eng, 1995. **1**(2): p. 151-61.
15. Vacanti, J.P., et al., *Transplantation of cells in matrices for tissue regeneration.* Adv Drug Deliv Rev, 1998. **33**(1-2): p. 165-182.

16. Vacanti, J.P. and R. Langer, *Tissue engineering: the design and fabrication of living replacement devices for surgical reconstruction and transplantation.* Lancet, 1999. **354 Suppl 1**: p. SI32-4.
17. Lutolf, M.P. and J.A. Hubbell, *Synthetic biomaterials as instructive extracellular microenvironments for morphogenesis in tissue engineering.* Nature Biotechnology, 2005. **23**(1): p. 47-55.
18. Boon, N.A. and P. Bloomfield, *The medical management of valvar heart disease.* Heart, 2002. **87**(4): p. 395-400.
19. Laflamme, M.A. and C.E. Murry, *Heart regeneration.* Nature, 2011. **473**(7347): p. 326-335.
20. Iyer, R.K., et al., *Engineered cardiac tissues.* Curr Opin Biotechnol, 2011. **22**(5): p. 706-14.
21. Hirt, M.N., A. Hansen, and T. Eschenhagen, *Cardiac tissue engineering: state of the art.* Circ Res, 2014. **114**(2): p. 354-67.
22. Li, Y., G.A. Thouas, and Q.Z. Chen, *Biodegradable soft elastomers: synthesis/properties of materials and fabrication of scaffolds.* Rsc Advances, 2012. **2**(22): p. 8229-8242.
23. Lee, L.Y., et al., *Biodegradable elastomer for soft tissue engineering.* European Polymer Journal, 2009. **45**(11): p. 3249-3256.
24. Barrett, D.G. and M.N. Yousaf, *Design and Applications of Biodegradable Polyester Tissue Scaffolds Based on Endogenous Monomers Found in Human Metabolism.* Molecules, 2009. **14**(10): p. 4022-4050.
25. Niklason, L.E., et al., *Functional arteries grown in vitro.* Science, 1999. **284**(5413): p. 489-93.
26. Yang, J., et al., *Synthesis and evaluation of poly(diol citrate) biodegradable elastomers.* Biomaterials, 2006. **27**(9): p. 1889-98.
27. Hinderer, S., E. Brauchle, and K. Schenke-Layland, *Generation and Assessment of Functional Biomaterial Scaffolds for Applications in Cardiovascular Tissue Engineering and Regenerative Medicine.* Advanced Healthcare Materials, 2015: p. n/a-n/a.
28. Chen, Q.Z., S.L. Liang, and G.A. Thouas, *Elastomeric biomaterials for tissue engineering.* Progress in Polymer Science, 2013. **38**(3-4): p. 584-671.
29. Jana, S., et al., *Scaffolds for tissue engineering of cardiac valves.* Acta Biomaterialia, 2014. **10**(7): p. 2877-2893.
30. Morsi, Y.S., *Bioengineering strategies for polymeric scaffold for tissue engineering an aortic heart valve: an update.* The International Journal of Artificial Organs, 2014. **37**(9): p. 651-667.
31. Kheradvar, A., et al., *Emerging Trends in Heart Valve Engineering: Part I. Solutions for Future.* Annals of Biomedical Engineering, 2014. **43**(4): p. 833-843.
32. Santerre, J.P., et al., *Understanding the biodegradation of polyurethanes: from classical implants to tissue engineering materials.* Biomaterials, 2005. **26**(35): p. 7457-70.
33. Zdrahala, R.J., *Small caliber vascular grafts. Part II: Polyurethanes revisited.* J Biomater Appl, 1996. **11**(1): p. 37-61.
34. Daebritz, S.H., et al., *Introduction of a flexible polymeric heart valve prosthesis with special design for mitral position.* Circulation, 2003. **108 Suppl 1**: p. II134-9.
35. Courtney, T., et al., *Design and analysis of tissue engineering scaffolds that mimic soft tissue mechanical anisotropy.* Biomaterials, 2006. **27**(19): p. 3631–3638.

36. Kidane, A.G., et al., *A novel nanocomposite polymer for development of synthetic heart valve leaflets.* Acta Biomaterialia, 2009. **5**(7): p. 2409-2417.
37. Aleksieva, G., et al., *Use of a special bioreactor for the cultivation of a new flexible polyurethane scaffold for aortic valve tissue engineering.* Biomed Eng Online, 2012. **11**: p. 92.
38. Amoroso, N.J., et al., *Microstructural manipulation of electrospun scaffolds for specific bending stiffness for heart valve tissue engineering.* Acta Biomaterialia, 2012. **8**(12): p. 4268-4277.
39. Fan, R., et al., *Optimal elastomeric scaffold leaflet shape for pulmonary heart valve leaflet replacement.* Journal of Biomechanics, 2013. **46**(4): p. 662-669.
40. Thierfelder, N., et al., *In Vitro Comparison of Novel Polyurethane Aortic Valves and Homografts After Seeding and Conditioning.* ASAIO Journal, 2013. **59**(3): p. 309-316.
41. Hobson, C.M., et al., *Fabrication of elastomeric scaffolds with curvilinear fibrous structures for heart valve leaflet engineering.* Journal of Biomedical Materials Research Part A, 2015. **103**(9): p. 3101-3106.
42. Freier, T., *Biopolyesters in tissue engineering applications.* Polymers for Regenerative Medicine, 2006: p. 1-61.
43. Steinbuchel, A., *Perspectives for biotechnological production and utilization of biopolymers: Metabolic engineering of polyhydroxyalkanoate biosynthesis pathways as a successful example.* Macromolecular Bioscience, 2001. **1**(1): p. 1-24.
44. Sodian, R., et al., *Evaluation of biodegradable, three-dimensional matrices for tissue engineering of heart valves.* ASAIO J, 2000. **46**(1): p. 107-10.
45. Sodian, R., et al., *Fabrication of a trileaflet heart valve scaffold from a polyhydroxyalkanoate biopolyester for use in tissue engineering.* Tissue Engineering, 2000. **6**(2): p. 183-188.
46. Sodian, R., et al., *Early in vivo experience with tissue-engineered trileaflet heart valves.* Circulation, 2000. **102**(19 Suppl 3): p. III22-9.
47. Hoerstrup, S.P., et al., *Functional living trileaflet heart valves grown in vitro.* Circulation, 2000. **102**(19 Suppl 3): p. III44-9.
48. Hoerstrup, S.P., et al., *Tissue engineering of functional trileaflet heart valves from human marrow stromal cells.* Circulation, 2002. **106**(12 Suppl 1): p. I143-50.
49. Sodian, R., et al., *Application of stereolithography for scaffold fabrication for tissue engineered heart valves.* ASAIO J, 2002. **48**(1): p. 12-6.
50. Engelmayr, G.C., Jr., et al., *A novel bioreactor for the dynamic flexural stimulation of tissue engineered heart valve biomaterials.* Biomaterials, 2003. **24**(14): p. 2523-32.
51. Grabow, N., et al., *Mechanical and structural properties of a novel hybrid heart valve scaffold for tissue engineering.* Artif Organs, 2004. **28**(11): p. 971-9.
52. Stamm, C., et al., *Biomatrix/Polymer Composite Material for Heart Valve Tissue Engineering.* The Annals of Thoracic Surgery, 2004. **78**(6): p. 2084-2093.
53. Sodian, R., et al., *Tissue Engineering of Autologous Human Heart Valves Using Cryopreserved Vascular Umbilical Cord Cells.* The Annals of Thoracic Surgery, 2006. **81**(6): p. 2207-2216.
54. Schmidt, D., et al., *Living autologous heart valves engineered from human prenatally harvested progenitors.* Circulation, 2006. **114**(1 Suppl): p. I125-31.
55. Schmidt, D., et al., *Engineering of biologically active living heart valve leaflets using human umbilical cord-derived progenitor cells.* Tissue Eng, 2006. **12**(11): p. 3223-32.

56. Wu, S., et al., *Study on Decellularized Porcine Aortic Valve/Poly (3-hydroxybutyrate-co-3-hydroxyhexanoate) Hybrid Heart Valve in Sheep Model.* Artificial Organs, 2007. **31**(9): p. 689-697.
57. Hong, H., et al., *Fabrication of Biomatrix/Polymer Hybrid Scaffold for Heart Valve Tissue Engineering in Vitro.* ASAIO Journal, 2008. **54**(6): p. 627-632.
58. Hong, H., et al., *Fabrication of a novel hybrid heart valve leaflet for tissue engineering: an in vitro study.* Artif Organs, 2009. **33**(7): p. 554-8.
59. Schaefermeier, P.K., et al., *Design and Fabrication of Three-Dimensional Scaffolds for Tissue Engineering of Human Heart Valves.* European Surgical Research, 2009. **42**(1): p. 49-53.
60. Kortsmit, J., et al., *Nondestructive and Noninvasive Assessment of Mechanical Properties in Heart Valve Tissue Engineering.* Tissue Engineering Part A, 2009. **15**(4): p. 797-806.
61. Sodian, R., et al., *Use of Human Umbilical Cord Blood-Derived Progenitor Cells for Tissue-Engineered Heart Valves.* The Annals of Thoracic Surgery, 2010. **89**(3): p. 819-828.
62. Cox, M.A.J., et al., *Tissue-Engineered Heart Valves Develop Native-like Collagen Fiber Architecture.* Tissue Engineering Part A, 2010. **16**(5): p. 1527-1537.
63. Schmidt, D., et al., *Minimally-Invasive Implantation of Living Tissue Engineered Heart Valves.* Journal of the American College of Cardiology, 2010. **56**(6): p. 510-520.
64. Weber, B., et al., *Injectable living marrow stromal cell-based autologous tissue engineered heart valves: first experiences with a one-step intervention in primates.* European Heart Journal, 2011. **32**(22): p. 2830-2840.
65. Emmert, M.Y., et al., *Stem Cell–Based Transcatheter Aortic Valve Implantation.* JACC: Cardiovascular Interventions, 2012. **5**(8): p. 874-883.
66. Weber, B., et al., *Prenatally engineered autologous amniotic fluid stem cell-based heart valves in the fetal circulation.* Biomaterials, 2012. **33**(16): p. 4031-4043.
67. Ye, Q., et al., *Scaffold precoating with human autologous extracellular matrix for improved cell attachment in cardiovascular tissue engineering.* ASAIO J, 2000. **46**(6): p. 730-3.
68. van Lieshout, M.I., et al., *Electrospinning versus knitting: two scaffolds for tissue engineering of the aortic valve.* J Biomater Sci Polym Ed, 2006. **17**(1-2): p. 77-89.
69. Van Lieshout, M., et al., *A knitted, fibrin-covered polycaprolactone scaffold for tissue engineering of the aortic valve.* Tissue Eng, 2006. **12**(3): p. 481-7.
70. Engelmayr, G.C., et al., *Cyclic flexure and laminar flow synergistically accelerate mesenchymal stem cell-mediated engineered tissue formation: Implications for engineered heart valve tissues.* Biomaterials, 2006. **27**(36): p. 6083-6095.
71. Del Gaudio, C., A. Bianco, and M. Grigioni, *Electrospun bioresorbable trileaflet heart valve prosthesis for tissue engineering: in vitro functional assessment of a pulmonary cardiac valve design.* Ann Ist Super Sanita, 2008. **44**(2): p. 178-86.
72. Del Gaudio, C., et al., *Electrospun bioresorbable heart valve scaffold for tissue engineering.* Int J Artif Organs, 2008. **31**(1): p. 68-75.
73. Gottlieb, D., et al., *In vivo monitoring of function of autologous engineered pulmonary valve.* The Journal of Thoracic and Cardiovascular Surgery, 2010. **139**(3): p. 723-731.
74. Ramaswamy, S., et al., *The role of organ level conditioning on the promotion of engineered heart valve tissue development in-vitro using mesenchymal stem cells.* Biomaterials, 2010. **31**(6): p. 1114-1125.

75. Brugmans, M.M.C.P., et al., *Poly-ε-caprolactone scaffold and reducedin vitrocell culture: beneficial effect on compaction and improved valvular tissue formation.* Journal of Tissue Engineering and Regenerative Medicine, 2013: p. n/a-n/a.
76. Tseng, H., et al., *Anisotropic Poly(Ethylene Glycol)/Polycaprolactone Hydrogel–Fiber Composites for Heart Valve Tissue Engineering.* Tissue Engineering Part A, 2014. **20**(19-20): p. 2634-2645.
77. Hinderer, S., et al., *Engineering of a bio-functionalized hybrid off-the-shelf heart valve.* Biomaterials, 2014. **35**(7): p. 2130-2139.
78. Sohier, J., et al., *The potential of anisotropic matrices as substrate for heart valve engineering.* Biomaterials, 2014. **35**(6): p. 1833-1844.
79. Jahnavi, S., et al., *Engineering of a polymer layered bio-hybrid heart valve scaffold.* Materials Science and Engineering: C, 2015. **51**: p. 263-273.
80. Jana, S., A. Lerman, and R.D. Simari, *In Vitro Model of a Fibrosa Layer of a Heart Valve.* ACS Applied Materials & Interfaces, 2015. **7**(36): p. 20012-20020.
81. Brugmans, M.M.C.P., et al., *Superior Tissue Evolution in Slow-Degrading Scaffolds for Valvular Tissue Engineering.* Tissue Engineering Part A, 2015.
82. Wang, Y., et al., *A tough biodegradable elastomer.* Nat Biotechnol, 2002. **20**(6): p. 602-6.
83. Rai, R., et al., *Synthesis, properties and biomedical applications of poly(glycerol sebacate) (PGS): A review.* Progress in Polymer Science, 2012. **37**(8): p. 1051-1078.
84. Sales, V.L., et al., *Protein precoating of elastomeric tissue-engineering scaffolds increased cellularity, enhanced extracellular matrix protein production, and differentially regulated the phenotypes of circulating endothelial progenitor cells.* Circulation, 2007. **116**(11 Suppl): p. I55-63.
85. Masoumi, N., et al., *Laser microfabricated poly(glycerol sebacate) scaffolds for heart valve tissue engineering.* Journal of Biomedical Materials Research Part A, 2013. **101A**(1): p. 104-114.
86. Masoumi, N., et al., *Valvular interstitial cell seeded poly(glycerol sebacate) scaffolds: Toward a biomimetic in vitro model for heart valve tissue engineering.* Acta Biomaterialia, 2013. **9**(4): p. 5974-5988.
87. Sant, S., et al., *Effect of biodegradation and de novo matrix synthesis on the mechanical properties of valvular interstitial cell-seeded polyglycerol sebacate-polycaprolactone scaffolds.* Acta Biomater, 2013. **9**(4): p. 5963-73.
88. Eslami, M., et al., *Fiber-reinforced hydrogel scaffolds for heart valve tissue engineering.* J Biomater Appl, 2014. **29**(3): p. 399-410.
89. Masoumi, N., et al., *Electrospun PGS:PCL Microfibers Align Human Valvular Interstitial Cells and Provide Tunable Scaffold Anisotropy.* Advanced Healthcare Materials, 2014. **3**(6): p. 929-939.
90. Masoumi, N., et al., *Tri-layered elastomeric scaffolds for engineering heart valve leaflets.* Biomaterials, 2014.
91. Eslami, M., et al., *Expression of COLLAGEN 1 and ELASTIN Genes in Mitral Valvular Interstitial Cells within Microfiber Reinforced Hydrogel.* Cell J, 2015. **17**(3): p. 478-88.
92. Amsden, B., *Curable, biodegradable elastomers: emerging biomaterials for drug delivery and tissue engineering.* Soft Matter, 2007. **3**(11): p. 1335-1348.
93. Dvir, T., et al., *Nanotechnological strategies for engineering complex tissues.* Nature Nanotechnology, 2010. **6**(1): p. 13-22.

94. Iatridis, J.C., *Function follows form.* Nature Materials, 2009. **8**(12): p. 923-924.
95. Simionescu, D.T., et al., *Form Follows Function: Advances in Trilayered Structure Replication for Aortic Heart Valve Tissue Engineering.* J Healthc Eng, 2012. **3**(2): p. 179-202.
96. Rodriguez, K.J., et al., *Manipulation of valve composition to elucidate the role of collagen in aortic valve calcification.* BMC Cardiovascular Disorders, 2014. **14**(1).
97. Gould, R.A., et al., *Cyclic strain anisotropy regulates valvular interstitial cell phenotype and tissue remodeling in three-dimensional culture.* Acta Biomaterialia, 2012. **8**(5): p. 1710-1719.
98. Bouten, C.V.C., et al., *Substrates for cardiovascular tissue engineering.* Advanced Drug Delivery Reviews, 2011. **63**(4-5): p. 221-241.
99. Vesely, I. and R. Noseworthy, *Micromechanics of the fibrosa and the ventricularis in aortic valve leaflets.* J Biomech, 1992. **25**(1): p. 101-13.
100. Sacks, M.S. and A.P. Yoganathan, *Heart valve function: a biomechanical perspective.* Philos Trans R Soc Lond B Biol Sci, 2007. **362**(1484): p. 1369-91.
101. Jana, S., et al., *Drug delivery in aortic valve tissue engineering.* J Control Release, 2014. **196**: p. 307-23.
102. Courtney, T., et al., *Design and analysis of tissue engineering scaffolds that mimic soft tissue mechanical anisotropy.* Biomaterials, 2006.
103. Mason, B.N., J.P. Califano, and C.A. Reinhart-King, *Matrix Stiffness: A Regulator of Cellular Behavior and Tissue Formation.* 2012: p. 19-37.
104. Suresh, S., *Biomechanics and biophysics of cancer cells☆.* Acta Biomaterialia, 2007. **3**(4): p. 413-438.
105. Badylak, S.F., *The extracellular matrix as a scaffold for tissue reconstruction.* Seminars in Cell & Developmental Biology, 2002. **13**(5): p. 377-383.
106. Schoen, F.J., *Heart valve tissue engineering: quo vadis?* Curr Opin Biotechnol, 2011. **22**(5): p. 698-705.
107. Mavrilas, D. and Y. Missirlis, *An approach to the optimization of preparation of bioprosthetic heart valves.* J Biomech, 1991. **24**(5): p. 331-9.
108. Stella, J.A. and M.S. Sacks, *On the Biaxial Mechanical Properties of the Layers of the Aortic Valve Leaflet.* Journal of Biomechanical Engineering, 2007. **129**(5): p. 757.
109. Stella, J.A., J. Liao, and M.S. Sacks, *Time-dependent biaxial mechanical behavior of the aortic heart valve leaflet.* J Biomech, 2007. **40**(14): p. 3169-77.
110. Hasan, A., et al., *Biomechanical properties of native and tissue engineered heart valve constructs.* Journal of Biomechanics, 2014. **47**(9): p. 1949-1963.
111. Place, E.S., N.D. Evans, and M.M. Stevens, *Complexity in biomaterials for tissue engineering.* Nat Mater, 2009. **8**(6): p. 457-70.
112. Bongio, M., et al., *Development of bone substitute materials: from 'biocompatible' to 'instructive'.* Journal of Materials Chemistry, 2010. **20**(40): p. 8747.
113. Lau, T.T. and D.-A. Wang, *Bioresponsive hydrogel scaffolding systems for 3D constructions in tissue engineering and regenerative medicine.* Nanomedicine, 2013. **8**(4): p. 655-668.
114. Reimer, J., et al., *Implantation of a Tissue-Engineered Tubular Heart Valve in Growing Lambs.* Annals of Biomedical Engineering, 2016.
115. Syedain, Z., et al., *6-month aortic valve implantation of an off-the-shelf tissue-engineered valve in sheep.* Biomaterials, 2015. **73**: p. 175-84.

116. Mazzitelli, D., et al., *Complete Aortic Valve Cusp Replacement in the Pediatric Population Using Tissue-Engineered Bovine Pericardium.* Ann Thorac Surg, 2015. **100**(5): p. 1923-5.
117. Lapidot, S., et al., *Clues for biomimetics from natural composite materials.* Nanomedicine, 2012. **7**(9): p. 1409-1423.
118. Balcells, M. and E.R. Edelman, *Effect of pre-adsorbed proteins on attachment, proliferation, and function of endothelial cells.* Journal of Cellular Physiology, 2002. **191**(2): p. 155-161.
119. Ratner, B.D., et al., *Biomaterials Science: An Introduction to Materials in Medicine*. 2012: Elsevier Science.
120. Nagura, M., et al., *Anti-thrombogenicity of styrene-butadiene-styrene triblock copolymer grafted with poly(ethylene glycol)s.* Journal of Applied Polymer Science, 2009. **113**(4): p. 2462-2476.
121. Kutikov, A.B. and J. Song, *Biodegradable PEG-Based Amphiphilic Block Copolymers for Tissue Engineering Applications.* ACS Biomaterials Science & Engineering, 2015. **1**(7): p. 463-480.
122. Kannan, R.Y., et al., *The Antithrombogenic Potential of a Polyhedral Oligomeric Silsesquioxane (POSS) Nanocomposite.* Biomacromolecules, 2006. **7**(1): p. 215-223.
123. Endo, M., et al., *Thrombogenicity and Blood Coagulation of a Microcatheter Prepared from Carbon Nanotube−Nylon-Based Composite.* Nano Letters, 2005. **5**(1): p. 101-105.
124. Meng, J., et al., *Improving the blood compatibility of polyurethane using carbon nanotubes as fillers and its implications to cardiovascular surgery.* Journal of Biomedical Materials Research Part A, 2005. **74A**(2): p. 208-214.
125. Ye, X., et al., *The Effect of Heparin-VEGF Multilayer on the Biocompatibility of Decellularized Aortic Valve with Platelet and Endothelial Progenitor Cells.* PLoS ONE, 2013. **8**(1): p. e54622.
126. Guan, J., J.J. Stankus, and W.R. Wagner, *Biodegradable elastomeric scaffolds with basic fibroblast growth factor release.* Journal of Controlled Release, 2007. **120**(1-2): p. 70-78.
127. Hench, L.L., *Third-Generation Biomedical Materials.* Science, 2002. **295**(5557): p. 1014-1017.
128. Schoen, F.J., *Mechanisms of Function and Disease of Natural and Replacement Heart Valves.* Annual Review of Pathology: Mechanisms of Disease, 2012. **7**(1): p. 161-183.
129. Chen, J.H. and C.A. Simmons, *Cell-Matrix Interactions in the Pathobiology of Calcific Aortic Valve Disease: Critical Roles for Matricellular, Matricrine, and Matrix Mechanics Cues.* Circulation Research, 2011. **108**(12): p. 1510-1524.
130. Mabry, K.M., R.L. Lawrence, and K.S. Anseth, *Dynamic stiffening of poly(ethylene glycol)-based hydrogels to direct valvular interstitial cell phenotype in a three-dimensional environment.* Biomaterials, 2015. **49**: p. 47-56.
131. Mabry, K.M., S.Z. Payne, and K.S. Anseth, *Microarray analyses to quantify advantages of 2D and 3D hydrogel culture systems in maintaining the native valvular interstitial cell phenotype.* Biomaterials, 2016. **74**: p. 31-41.
132. Jian, B., et al., *Progression of aortic valve stenosis: TGF-β1 is present in calcified aortic valve cusps and promotes aortic valve interstitial cell calcification via apoptosis.* The Annals of Thoracic Surgery, 2003. **75**(2): p. 457-465.

133. Brody, S., et al., *The effect of cholecyst-derived extracellular matrix on the phenotypic behaviour of valvular endothelial and valvular interstitial cells.* Biomaterials, 2007. **28**(8): p. 1461-1469.
134. Duan, B., et al., *Stiffness and adhesivity control aortic valve interstitial cell behavior within hyaluronic acid based hydrogels.* Acta Biomaterialia, 2013. **9**(8): p. 7640-7650.
135. Rush, M.N., K.E. Coombs, and E.L. Hedberg-Dirk, *Surface chemistry regulates valvular interstitial cell differentiation in vitro.* Acta Biomaterialia, 2015. **28**: p. 76-85.
136. Kluin, J., et al., *In situ heart valve tissue engineering using a bioresorbable elastomeric implant – From material design to 12 months follow-up in sheep.* Biomaterials, 2017. **125**: p. 101-117.
137. Brody, S. and A. Pandit, *Approaches to heart valve tissue engineering scaffold design.* Journal of Biomedical Materials Research Part B: Applied Biomaterials, 2007. **83B**(1): p. 16-43.
138. Flanagan, T.C., et al., *In VivoRemodeling and Structural Characterization of Fibrin-Based Tissue-Engineered Heart Valves in the Adult Sheep Model.* Tissue Engineering Part A, 2009. **15**(10): p. 2965-2976.
139. Syedain, Z.H., et al., *Decellularized Tissue-Engineered Heart Valve Leaflets with Recellularization Potential.* Tissue Engineering Part A, 2013. **19**(5-6): p. 759-769.
140. Shinoka, T., et al., *Tissue engineering heart valves: valve leaflet replacement study in a lamb model.* Ann Thorac Surg, 1995. **60**(6 Suppl): p. S513-6.
141. Ramalingam, M. and Institute of Electrical and Electronics Engineers., *Micro and nanotechnologies in engineering stem cells and tissues*. IEEE Press series in biomedical engineering. 2013, Hoboken, N.J.: John Wiley & Sons. xvii, 306 pages.
142. Bae, H., et al., *Development of functional biomaterials with micro- and nanoscale technologies for tissue engineering and drug delivery applications.* Journal of Tissue Engineering and Regenerative Medicine, 2014. **8**(1): p. 1-14.
143. Ma, P.X., *Biomimetic materials for tissue engineering.* Advanced Drug Delivery Reviews, 2008. **60**(2): p. 184-198.
144. Vajtai, R., *Springer Handbook of Nanomaterials*. 2013.
145. Langer, R. and D.A. Tirrell, *Designing materials for biology and medicine.* Nature, 2004. **428**(6982): p. 487-92.
146. Pelipenko, J., P. Kocbek, and J. Kristl, *Critical attributes of nanofibers: Preparation, drug loading, and tissue regeneration.* International Journal of Pharmaceutics, 2015. **484**(1-2): p. 57-74.
147. Mauck, R.L., et al., *Engineering on the Straight and Narrow: The Mechanics of Nanofibrous Assemblies for Fiber-Reinforced Tissue Regeneration.* Tissue Engineering Part B: Reviews, 2009. **15**(2): p. 171-193.
148. Deng, M., et al., *Biomimetic Structures: Biological Implications of Dipeptide-Substituted Polyphosphazene-Polyester Blend Nanofiber Matrices for Load-Bearing Bone Regeneration.* Advanced Functional Materials, 2011. **21**(14): p. 2641-2651.
149. Sundaray, B., et al., *Electrospinning of continuous aligned polymer fibers.* Applied Physics Letters, 2004. **84**(7): p. 1222-1224.
150. Ayres, C., et al., *Modulation of anisotropy in electrospun tissue-engineering scaffolds: Analysis of fiber alignment by the fast Fourier transform.* Biomaterials, 2006. **27**(32): p. 5524-5534.

151. Li, D. and Y. Xia, *Electrospinning of Nanofibers: Reinventing the Wheel?* Advanced Materials, 2004. **16**(14): p. 1151-1170.
152. Li, D., et al., *Collecting Electrospun Nanofibers with Patterned Electrodes.* Nano Letters, 2005. **5**(5): p. 913-916.
153. Li, D., Y. Wang, and Y. Xia, *Electrospinning Nanofibers as Uniaxially Aligned Arrays and Layer-by-Layer Stacked Films.* Advanced Materials, 2004. **16**(4): p. 361-366.
154. Miller, J.D., R.M. Weiss, and D.D. Heistad, *Calcific Aortic Valve Stenosis: Methods, Models, and Mechanisms.* Circulation Research, 2011. **108**(11): p. 1392-1412.
155. Miller, J.D., et al., *Dysregulation of Antioxidant Mechanisms Contributes to Increased Oxidative Stress in Calcific Aortic Valvular Stenosis in Humans.* Journal of the American College of Cardiology, 2008. **52**(10): p. 843-850.
156. Miller, J.D., et al., *Lowering Plasma Cholesterol Levels Halts Progression of Aortic Valve Disease in Mice.* Circulation, 2009. **119**(20): p. 2693-2701.
157. Fang, R.H. and L. Zhang, *Nanoparticle-Based Modulation of the Immune System.* Annual Review of Chemical and Biomolecular Engineering, 2016. **7**(1): p. 305-326.
158. Das, M., et al., *Auto-catalytic ceria nanoparticles offer neuroprotection to adult rat spinal cord neurons.* Biomaterials, 2007. **28**(10): p. 1918-1925.
159. Pourkhalili, N., et al., *Biochemical and cellular evidence of the benefit of a combination of cerium oxide nanoparticles and selenium to diabetic rats.* World J Diabetes, 2011. **2**(11): p. 204-10.
160. Chen, J., et al., *Rare earth nanoparticles prevent retinal degeneration induced by intracellular peroxides.* Nature Nanotechnology, 2006. **1**(2): p. 142-150.
161. Zhou, D., et al., *Neuroprotective potential of cerium oxide nanoparticles for focal cerebral ischemic stroke.* Journal of Huazhong University of Science and Technology [Medical Sciences], 2016. **36**(4): p. 480-486.
162. Das, S., et al., *Cerium oxide nanoparticles: applications and prospects in nanomedicine.* Nanomedicine, 2013. **8**(9): p. 1483-1508.
163. Niu, J., et al., *Cardioprotective effects of cerium oxide nanoparticles in a transgenic murine model of cardiomyopathy.* Cardiovascular Research, 2007. **73**(3): p. 549-559.
164. Ivanov, V.K., A.B. Shcherbakov, and A.V. Usatenko, *Structure-sensitive properties and biomedical applications of nanodispersed cerium dioxide.* Russian Chemical Reviews, 2009. **78**(9): p. 855-871.
165. Jung, H., D.B. Kittelson, and M.R. Zachariah, *The influence of a cerium additive on ultrafine diesel particle emissions and kinetics of oxidation.* Combustion and Flame, 2005. **142**(3): p. 276-288.
166. Korsvik, C., et al., *Superoxide dismutase mimetic properties exhibited by vacancy engineered ceria nanoparticles.* Chemical Communications, 2007(10): p. 1056.
167. Heckert, E.G., et al., *The role of cerium redox state in the SOD mimetic activity of nanoceria.* Biomaterials, 2008. **29**(18): p. 2705-2709.
168. Li, Y., M. Kröger, and W.K. Liu, *Shape effect in cellular uptake of PEGylated nanoparticles: comparison between sphere, rod, cube and disk.* Nanoscale, 2015. **7**(40): p. 16631-16646.
169. Jo, D.H., et al., *Size, surface charge, and shape determine therapeutic effects of nanoparticles on brain and retinal diseases.* Nanomedicine: Nanotechnology, Biology and Medicine, 2015. **11**(7): p. 1603-1611.

170. Bettinger, C.J., *Synthesis and microfabrication of biomaterials for soft-tissue engineering.* Pure and Applied Chemistry, 2009. **81**(12): p. 2183-2201.
171. Khan, M., et al., *Advanced materials for co-delivery of drugs and genes in cancer therapy.* Adv Healthc Mater, 2012. **1**(4): p. 373-92.
172. Liu, X., J.M. Holzwarth, and P.X. Ma, *Functionalized synthetic biodegradable polymer scaffolds for tissue engineering.* Macromol Biosci, 2012. **12**(7): p. 911-9.
173. Storey, R.F. and T.P. Hickey, *Degradable polyurethane networks based on d,l-lactide, glycolide, ε-caprolactone, and trimethylene carbonate homopolyester and copolyester triols.* Polymer, 1994. **35**(4): p. 830-838.
174. Stuckey, D.J., et al., *Magnetic Resonance Imaging Evaluation of Remodeling by Cardiac Elastomeric Tissue Scaffold Biomaterials in a Rat Model of Myocardial Infarction.* Tissue Engineering Part A, 2010. **16**(11): p. 3395-3402.
175. Bruggeman, J.P., et al., *Biodegradable poly(polyol sebacate) polymers.* Biomaterials, 2008. **29**(36): p. 4726-4735.
176. Engelmayr, G.C., et al., *Accordion-like honeycombs for tissue engineering of cardiac anisotropy.* Nature Materials, 2008. **7**(12): p. 1003-1010.
177. Gao, J., et al., *Poly(glycerol sebacate) supports the proliferation and phenotypic protein expression of primary baboon vascular cells.* Journal of Biomedical Materials Research Part A, 2007. **83A**(4): p. 1070-1075.
178. Wang, Y.D., Y.M. Kim, and R. Langer, *In vivo degradation characteristics of poly(glycerol sebacate).* Journal of Biomedical Materials Research Part A, 2003. **66A**(1): p. 192-197.
179. Tong, Z., et al., *Controlling the fibroblastic differentiation of mesenchymal stem cells via the combination of fibrous scaffolds and connective tissue growth factor.* Tissue Eng Part A, 2011. **17**(21-22): p. 2773-85.
180. Sant, S., et al., *Hybrid PGS-PCL microfibrous scaffolds with improved mechanical and biological properties.* Journal of Tissue Engineering and Regenerative Medicine, 2011. **5**(4): p. 283-291.
181. Gaharwar, A.K., et al., *Anisotropic poly (glycerol sebacate)-poly (ϵ-caprolactone) electrospun fibers promote endothelial cell guidance.* Biofabrication, 2014. **7**(1): p. 015001.
182. Bettinger, C.J., et al., *Amino alcohol-based degradable poly(ester amide) elastomers.* Biomaterials, 2008. **29**(15): p. 2315-2325.
183. Bettinger, C.J., et al., *In vitro and in vivo degradation of poly(1,3-diamino-2-hydroxypropane-co-polyol sebacate) elastomers.* Journal of Biomedical Materials Research Part A, 2009. **91A**(4): p. 1077-1088.
184. Wang, J., et al., *Fully Biodegradable Airway Stents Using Amino Alcohol-Based Poly(ester amide) Elastomers.* Advanced Healthcare Materials, 2013. **2**(10): p. 1329-1336.
185. Knop, K., et al., *Poly(ethylene glycol) in Drug Delivery: Pros and Cons as Well as Potential Alternatives.* Angewandte Chemie International Edition, 2010. **49**(36): p. 6288-6308.
186. Zhu, K.J., L. Xiangzhou, and Y. Shilin, *Preparation, characterization, and properties of polylactide (PLA)–poly(ethylene glycol) (PEG) copolymers: A potential drug carrier.* Journal of Applied Polymer Science, 1990. **39**(1): p. 1-9.

187. Zhou, S., X. Deng, and H. Yang, *Biodegradable poly(ε-caprolactone)-poly(ethylene glycol) block copolymers: characterization and their use as drug carriers for a controlled delivery system.* Biomaterials, 2003. **24**(20): p. 3563-3570.
188. Sant, S., M. Thommes, and P. Hildgen, *Microporous structure and drug release kinetics of polymeric nanoparticles.* Langmuir, 2008. **24**(1): p. 280-287.
189. Sant, S., V. Nadeau, and P. Hildgen, *Effect of porosity on the release kinetics of propafenone-loaded PEG-g-PLA nanoparticles.* J Control Release, 2005. **107**(2): p. 203-14.
190. Sant, S., S. Poulin, and P. Hildgen, *Effect of polymer architecture on surface properties, plasma protein adsorption, and cellular interactions of pegylated nanoparticles.* Journal of Biomedical Materials Research Part A, 2008. **87A**(4): p. 885-895.
191. Deng, X., et al., *In vitro degradation and release profiles for poly-dl-lactide-poly(ethylene glycol) microspheres containing human serum albumin.* J Control Release, 2001. **71**(2): p. 165-73.
192. Patel, A., et al., *Highly elastomeric poly(glycerol sebacate)-co-poly(ethylene glycol) amphiphilic block copolymers.* Biomaterials, 2013. **34**(16): p. 3970-83.
193. Jaafar, I.H., et al., *Improving fluorescence imaging of biological cells on biomedical polymers.* Acta Biomaterialia, 2011. **7**(4): p. 1588-1598.
194. Allcock, H.R., J.E. Mark, and F.W. Lampe, *Contemporary polymer chemistry*. 3rd ed. 2003, Upper Saddle River, N.J.: Prentice Hall. xviii, 814 p.
195. Shameli, K., et al., *Synthesis and Characterization of Polyethylene Glycol Mediated Silver Nanoparticles by the Green Method.* International Journal of Molecular Sciences, 2012. **13**(12): p. 6639-6650.
196. Wei, T., et al., *Thermal analysis and non-isothermal kinetics of poly(ethylene glycol) with different molecular weight.* Polymer Engineering & Science, 2014. **54**(12): p. 2872-2876.
197. Pielichowski, K. and K. Flejtuch, *Differential scanning calorimetry studies on poly(ethylene glycol) with different molecular weights for thermal energy storage materials.* Polymers for Advanced Technologies, 2002. **13**(10-12): p. 690-696.
198. Li, S.-L., et al., *Succinic Acid Based Biodegradable Thermoplastic Poly(ester urethane) Elastomers: Effects of Segment Ratios and Lengths on Physical Properties.* Industrial & Engineering Chemistry Research, 2014. **53**(4): p. 1404-1414.
199. Chen, Q.Z., et al., *Characterisation of a soft elastomer poly(glycerol sebacate) designed to match the mechanical properties of myocardial tissue.* Biomaterials, 2008. **29**(1): p. 47-57.
200. Suyatma, N.E., et al., *Effects of hydrophilic plasticizers on mechanical, thermal, and surface properties of chitosan films.* J Agric Food Chem, 2005. **53**(10): p. 3950-7.
201. Holzapfel, G.A. and R.W. Ogden, *Biomechanics of soft tissue in cardiovascular systems*. CISM courses and lectures. 2003, Wien ; New York: Springer. 342 p.
202. Huebsch, N. and D.J. Mooney, *Inspiration and application in the evolution of biomaterials.* Nature, 2009. **462**(7272): p. 426-32.
203. Martina, M. and D.W. Hutmacher, *Biodegradable polymers applied in tissue engineering research: a review.* Polymer International, 2007. **56**(2): p. 145-157.
204. De, S.K., et al., *Equilibrium swelling and kinetics of pH-responsive hydrogels: models, experiments, and simulations.* Journal of Microelectromechanical Systems, 2002. **11**(5): p. 544-555.

205. Chen, Q., X. Yang, and Y. Li, *A comparative study on in vitro enzymatic degradation of poly(glycerol sebacate) and poly(xylitol sebacate).* RSC Advances, 2012. **2**(10): p. 4125.
206. Sun, Z.-J., et al., *The influence of lactic on the properties of Poly (glycerol–sebacate–lactic acid).* Materials Science and Engineering: C, 2009. **29**(1): p. 178-182.
207. Makadia, H.K. and S.J. Siegel, *Poly Lactic-co-Glycolic Acid (PLGA) as Biodegradable Controlled Drug Delivery Carrier.* Polymers, 2011. **3**(4): p. 1377-1397.
208. Mukundan, S., et al., *Nanofibrous composite scaffolds of poly(ester amides) with tunable physicochemical and degradation properties.* European Polymer Journal, 2015. **68**: p. 21-35.
209. Bian, W. and N. Bursac, *Tissue engineering of functional skeletal muscle: challenges and recent advances.* IEEE Eng Med Biol Mag, 2008. **27**(5): p. 109-13.
210. Bat, E., et al., *Biodegradable elastomers for biomedical applications and regenerative medicine.* Regenerative Medicine, 2014. **9**(3): p. 385-398.
211. Liu, Q., et al., *Synthesis, preparation, in vitro degradation, and application of novel degradable bioelastomers—A review.* Progress in Polymer Science, 2012. **37**(5): p. 715-765.
212. Xue, Y., et al., *Semiquantitative FTIR Analysis of the Crosslinking Density of Poly(ester amide)-Based Thermoset Elastomers.* Macromolecular Materials and Engineering, 2015: p. n/a-n/a.
213. Xue, Y., et al., *PEGylated poly(ester amide) elastomers with tunable physico-chemical, mechanical and degradation properties.* European Polymer Journal, 2015.
214. Karrer, L., et al., *PPS-PEG surface coating to reduce thrombogenicity of small diameter ePTFE vascular grafts.* Int J Artif Organs, 2005. **28**(10): p. 993-1002.
215. Bhardwaj, N. and S.C. Kundu, *Electrospinning: A fascinating fiber fabrication technique.* Biotechnology Advances, 2010. **28**(3): p. 325-347.
216. Soliman, S., et al., *Controlling the porosity of fibrous scaffolds by modulating the fiber diameter and packing density.* Journal of Biomedical Materials Research Part A, 2011. **96A**(3): p. 566-574.
217. Sant, S. and A. Khademhosseini, *Fabrication and characterization of tough elastomeric fibrous scaffolds for tissue engineering applications.* 2010: p. 3546-3548.
218. Fu, W., et al., *Electrospun gelatin/PCL and collagen/PLCL scaffolds for vascular tissue engineering.* Int J Nanomedicine, 2014. **9**: p. 2335-44.
219. Kim, E.S., et al., *Emerging nanotechnology approaches in tissue engineering and regenerative medicine.* Int J Nanomedicine, 2014. **9 Suppl 1**: p. 1-5.
220. Parry, D.A.D., G.R.G. Barnes, and A.S. Craig, *A Comparison of the Size Distribution of Collagen Fibrils in Connective Tissues as a Function of Age and a Possible Relation between Fibril Size Distribution and Mechanical Properties.* Proceedings of the Royal Society B: Biological Sciences, 1978. **203**(1152): p. 305-321.
221. Carraher, C.E. and R.B. Seymour, *Seymour/Carraher's polymer chemistry*. 7th edition / ed. 2008, Boca Raton: CRC Press. 738 p.
222. Lyu, S. and D. Untereker, *Degradability of Polymers for Implantable Biomedical Devices.* International Journal of Molecular Sciences, 2009. **10**(9): p. 4033-4065.
223. Ceonzo, K., et al., *Polyglycolic Acid-Induced Inflammation: Role of Hydrolysis and Resulting Complement Activation.* Tissue Engineering, 2006. **12**(2): p. 301-308.
224. Chapman, R.G., et al., *Surveying for Surfaces that Resist the Adsorption of Proteins.* Journal of the American Chemical Society, 2000. **122**(34): p. 8303-8304.

225. Korossis, S.A., et al., *Tissue engineering of cardiac valve prostheses II: biomechanical characterization of decellularized porcine aortic heart valves.* J Heart Valve Dis, 2002. **11**(4): p. 463-71.
226. Mendelson, K. and F.J. Schoen, *Heart Valve Tissue Engineering: Concepts, Approaches, Progress, and Challenges.* Annals of Biomedical Engineering, 2006. **34**(12): p. 1799-1819.
227. Shih, M.F., et al., *Synthesis and Evaluation of Poly(hexamethylene-urethane) and PEG-Poly(hexamethylene-urethane) and Their Cholesteryl Oleyl Carbonate Composites for Human Blood Biocompatibility.* Molecules, 2011. **16**(12): p. 8181-8197.
228. Tze-Man, K., L. Jui-Che, and S.L. Cooper, *Surface characterization and platelet adhesion studies of plasma-sulphonated polyethylene.* Biomaterials, 1993. **14**(9): p. 657-664.
229. Xu, B., et al., *Mechanically tissue-like elastomeric polymers and their potential as a vehicle to deliver functional cardiomyocytes.* Journal of the Mechanical Behavior of Biomedical Materials, 2013. **28**: p. 354-365.
230. Labrosse, M.R., et al., *Planar biaxial testing of heart valve cusp replacement biomaterials: Experiments, theory and material constants.* Acta biomaterialia, 2016. **45**: p. 303-320.
231. Pham, T., et al., *Quantification and comparison of the mechanical properties of four human cardiac valves.* Acta biomaterialia, 2017. **54**: p. 345-355.
232. Sacks, M.S., *Biaxial mechanical evaluation of planar biological materials.* Journal of Elasticity, 2000. **61**(1-3): p. 199-246.
233. Lam, N.T., et al., *Valve interstitial cell contractile strength and metabolic state are dependent on its shape.* Integrative biology : quantitative biosciences from nano to macro, 2016. **8**(10): p. 1079-1089.
234. Tandon, I., et al., *Valve interstitial cell shape modulates cell contractility independent of cell phenotype.* Journal of biomechanics, 2016. **49**(14): p. 3289-3297.
235. Coombs, K.E., et al., *Isolated effect of material stiffness on valvular interstitial cell differentiation.* Journal of Biomedical Materials Research Part A, 2017. **105**(1): p. 51-61.
236. Kural, M.H. and K.L. Billiar, *Mechanoregulation of valvular interstitial cell phenotype in the third dimension.* Biomaterials, 2014. **35**(4): p. 1128-1137.
237. Mabry, K.M., S.Z. Payne, and K.S. Anseth, *Transcriptional profiles of valvular interstitial cells cultured on tissue culture polystyrene, on 2D hydrogels, or within 3D hydrogels.* Data in Brief, 2015. **5**: p. 959-962.
238. Billiar, K.L. and M.S. Sacks, *Biaxial mechanical properties of the natural and glutaraldehyde treated aortic valve cusp--Part I: Experimental results.* Journal of biomechanical engineering, 2000. **122**(1): p. 23-30.
239. Sacks, M.S., W. David Merryman, and D.E. Schmidt, *On the biomechanics of heart valve function.* J Biomech, 2009. **42**(12): p. 1804-24.
240. Duan, B., et al., *Active tissue stiffness modulation controls valve interstitial cell phenotype and osteogenic potential in 3D culture.* Acta Biomaterialia, 2016. **36**: p. 42-54.
241. Sant, S., et al., *Effect of biodegradation and de novo matrix synthesis on the mechanical properties of valvular interstitial cell-seeded polyglycerol sebacate–polycaprolactone scaffolds.* Acta Biomaterialia, 2013. **9**(4): p. 5963-5973.
242. Xue, Y., et al., *PEGylated poly(ester amide) elastomer scaffolds for soft tissue engineering.* Polymers for Advanced Technologies, 2017. **28**(9): p. 1097-1106.

243. Veleirinho, B., M.F. Rei, and J.A. Lopes-Da-Silva, *Solvent and concentration effects on the properties of electrospun poly(ethylene terephthalate) nanofiber mats.* Journal of Polymer Science Part B: Polymer Physics, 2008. **46**(5): p. 460-471.
244. Tarus, B., et al., *Effect of polymer concentration on the morphology and mechanical characteristics of electrospun cellulose acetate and poly (vinyl chloride) nanofiber mats.* Alexandria Engineering Journal, 2016. **55**(3): p. 2975-2984.
245. Shao, H., et al., *Effect of electrospinning parameters and polymer concentrations on mechanical-to-electrical energy conversion of randomly-oriented electrospun poly(vinylidene fluoride) nanofiber mats.* RSC Advances, 2015. **5**(19): p. 14345-14350.
246. Hotaling, N.A., et al., *DiameterJ: A validated open source nanofiber diameter measurement tool.* Biomaterials, 2015. **61**: p. 327-338.
247. Rezakhaniha, R., et al., *Experimental investigation of collagen waviness and orientation in the arterial adventitia using confocal laser scanning microscopy.* Biomechanics and Modeling in Mechanobiology, 2011. **11**(3-4): p. 461-473.
248. Xue, Y., et al., *Shape-Specific Nanoceria Mitigate Oxidative Stress-Induced Calcification in Primary Human Valvular Interstitial Cell Culture.* Cellular and Molecular Bioengineering, 2017. **10**(5): p. 483-500.
249. Li, Z. and C. Wang, *Effects of Working Parameters on Electrospinning*, in *One-Dimensional nanostructures*. 2013. p. 15-28.
250. Courtney, T., et al., *Design and analysis of tissue engineering scaffolds that mimic soft tissue mechanical anisotropy.* Biomaterials, 2006. **27**(19): p. 3631-8.
251. Beachley, V. and X. Wen, *Fabrication of nanofiber reinforced protein structures for tissue engineering.* Materials Science and Engineering: C, 2009. **29**(8): p. 2448-2453.
252. Yin, Y. and J. Xiong, *Finite Element Analysis of Electrospun Nanofibrous Mats under Biaxial Tension.* Nanomaterials, 2018. **8**(5).
253. Yin, Y., D. Pu, and J. Xiong, *Analysis of the Comprehensive Tensile Relationship in Electrospun Silk Fibroin/Polycaprolactone Nanofiber Membranes.* Membranes, 2017. **7**(4).
254. Liang, X.-H., et al., *Crystalline-Amorphous Phase Transition of Poly(ethylene Glycol)/Cellulose Blend.* Macromolecules, 1995. **28**(19): p. 6551-6555.
255. Nezarati, R.M., M.B. Eifert, and E. Cosgriff-Hernandez, *Effects of Humidity and Solution Viscosity on Electrospun Fiber Morphology.* Tissue Engineering Part C: Methods, 2013. **19**(10): p. 810-819.
256. Yao, J., C. Bastiaansen, and T. Peijs, *High Strength and High Modulus Electrospun Nanofibers.* Fibers, 2014. **2**(2): p. 158-186.
257. Hossain, M.F., R.H. Gong, and M. Rigout, *Effect of polymer concentration on electrospinning of hydroxypropyl-β-cyclodextrins/PEO nanofibres.* The Journal of The Textile Institute, 2016. **107**(12): p. 1511-1518.
258. Sanatgar, R.H., et al., *The influence of solvent type and polymer concentration on the physical properties of solid state polymerized PA66 nanofiber yarn.* Journal of Applied Polymer Science, 2012. **126**(3): p. 1112-1120.
259. Cramariuc, B., et al., *Fiber diameter in electrospinning process.* Journal of Electrostatics, 2013. **71**(3): p. 189-198.
260. Rutkovskiy, A., et al., *Valve Interstitial Cells: The Key to Understanding the Pathophysiology of Heart Valve Calcification.* Journal of the American Heart Association, 2017. **6**(9).

261. Liu, A.C., V.R. Joag, and A.I. Gotlieb, *The Emerging Role of Valve Interstitial Cell Phenotypes in Regulating Heart Valve Pathobiology.* The American Journal of Pathology, 2007. **171**(5): p. 1407-1418.
262. Otto, C.M., *Calcific Aortic Stenosis — Time to Look More Closely at the Valve.* New England Journal of Medicine, 2008. **359**(13): p. 1395-1398.
263. Schoen, F.J. and R.J. Levy, *Calcification of Tissue Heart Valve Substitutes: Progress Toward Understanding and Prevention.* The Annals of Thoracic Surgery, 2005. **79**(3): p. 1072-1080.
264. Xue, Y., et al., *Biodegradable and biomimetic elastomeric scaffolds for tissue-engineered heart valves.* Acta Biomaterialia, 2017. **48**: p. 2-19.
265. Hutcheson, J.D., E. Aikawa, and W.D. Merryman, *Potential drug targets for calcific aortic valve disease.* Nature Reviews Cardiology, 2014. **11**(4): p. 218-231.
266. Mathieu, P. and M.-C. Boulanger, *Basic Mechanisms of Calcific Aortic Valve Disease.* Canadian Journal of Cardiology, 2014. **30**(9): p. 982-993.
267. Sverdlov, A.L., et al., *Pathogenesis of aortic stenosis: not just a matter of wear and tear.* Am J Cardiovasc Dis, 2011. **1**(2): p. 185-99.
268. Heistad, D.D., et al., *Novel Aspects of Oxidative Stress in Cardiovascular Diseases.* Circulation Journal, 2009. **73**(2): p. 201-207.
269. Yip, C.Y.Y. and C.A. Simmons, *The aortic valve microenvironment and its role in calcific aortic valve disease.* Cardiovascular Pathology, 2011. **20**(3): p. 177-182.
270. Hutcheson, J.D., M.C. Blaser, and E. Aikawa, *Giving Calcification Its Due: Recognition of a Diverse Disease.* Circulation Research, 2017. **120**(2): p. 270-273.
271. Fernández Esmerats, J., J. Heath, and H. Jo, *Shear-Sensitive Genes in Aortic Valve Endothelium.* Antioxidants & Redox Signaling, 2016. **25**(7): p. 401-414.
272. Bostrom, K.I., N.M. Rajamannan, and D.A. Towler, *The Regulation of Valvular and Vascular Sclerosis by Osteogenic Morphogens.* Circulation Research, 2011. **109**(5): p. 564-577.
273. Branchetti, E., et al., *Antioxidant Enzymes Reduce DNA Damage and Early Activation of Valvular Interstitial Cells in Aortic Valve Sclerosis.* Arteriosclerosis, Thrombosis, and Vascular Biology, 2012. **33**(2): p. e66-e74.
274. Bowler, M.A. and W.D. Merryman, *In vitro models of aortic valve calcification: solidifying a system.* Cardiovascular Pathology, 2015. **24**(1): p. 1-10.
275. Aikawa, E., et al., *Characterization of Porcine Aortic Valvular Interstitial Cell 'Calcified' Nodules.* PLoS ONE, 2012. **7**(10): p. e48154.
276. Mulholland, D.L. and A.I. Gotlieb, *Cell biology of valvular interstitial cells.* Can J Cardiol, 1996. **12**(3): p. 231-6.
277. Liberman, M., et al., *Oxidant Generation Predominates Around Calcifying Foci and Enhances Progression of Aortic Valve Calcification.* Arteriosclerosis, Thrombosis, and Vascular Biology, 2007. **28**(3): p. 463-470.
278. Shao, J.S., *Molecular Mechanisms of Vascular Calcification: Lessons Learned From The Aorta.* Arteriosclerosis, Thrombosis, and Vascular Biology, 2006. **26**(7): p. 1423-1430.
279. Griendling, K.K., *Oxidative Stress and Cardiovascular Injury: Part II: Animal and Human Studies.* Circulation, 2003. **108**(17): p. 2034-2040.
280. Kobayashi, S., et al., *Expressional changes of the vascular antioxidant system in atherosclerotic coronary arteries.* J Atheroscler Thromb, 2002. **9**(4): p. 184-90.

281. Kim, K.M., *Calcification of matrix vesicles in human aortic valve and aortic media.* Fed Proc, 1976. **35**(2): p. 156-62.
282. Walkey, C., et al., *Catalytic properties and biomedical applications of cerium oxide nanoparticles.* Environ. Sci.: Nano, 2015. **2**(1): p. 33-53.
283. Nelson, B., et al., *Antioxidant Cerium Oxide Nanoparticles in Biology and Medicine.* Antioxidants, 2016. **5**(2): p. 15.
284. Rzigalinski, B.A., C.S. Carfagna, and M. Ehrich, *Cerium oxide nanoparticles in neuroprotection and considerations for efficacy and safety.* Wiley Interdisciplinary Reviews: Nanomedicine and Nanobiotechnology, 2016.
285. Xue, Y., et al., *Synthesis, physico-chemical characterization, and antioxidant effect of PEGylated cerium oxide nanoparticles.* Drug Delivery and Translational Research, 2017.
286. Niu, J., K. Wang, and P.E. Kolattukudy, *Cerium Oxide Nanoparticles Inhibits Oxidative Stress and Nuclear Factor- B Activation in H9c2 Cardiomyocytes Exposed to Cigarette Smoke Extract.* Journal of Pharmacology and Experimental Therapeutics, 2011. **338**(1): p. 53-61.
287. Pagliari, F., et al., *Cerium Oxide Nanoparticles Protect Cardiac Progenitor Cells from Oxidative Stress.* ACS Nano, 2012. **6**(5): p. 3767-3775.
288. Kolli, M.B., et al., *Cerium oxide nanoparticles attenuate monocrotaline induced right ventricular hypertrophy following pulmonary arterial hypertension.* Biomaterials, 2014. **35**(37): p. 9951-9962.
289. Mai, H.-X., et al., *Shape-Selective Synthesis and Oxygen Storage Behavior of Ceria Nanopolyhedra, Nanorods, and Nanocubes.* The Journal of Physical Chemistry B, 2005. **109**(51): p. 24380-24385.
290. Zhang, D., et al., *Synthesis of CeO2Nanorods via Ultrasonication Assisted by Polyethylene Glycol.* Inorganic Chemistry, 2007. **46**(7): p. 2446-2451.
291. Gaharwar, A.K., et al., *Bioactive Silicate Nanoplatelets for Osteogenic Differentiation of Human Mesenchymal Stem Cells.* Advanced Materials, 2013. **25**(24): p. 3329-3336.
292. Cox, R.F., et al., *Microcalcifications in breast cancer: novel insights into the molecular mechanism and functional consequence of mammary mineralisation.* British Journal of Cancer, 2012. **106**(3): p. 525-537.
293. Pesce, M., et al., *Modulation of Human Valve Interstitial Cell Phenotype and Function Using a Fibroblast Growth Factor 2 Formulation.* Plos One, 2015. **10**(6): p. e0127844.
294. Monzack, E.L. and K.S. Masters, *Can valvular interstitial cells become true osteoblasts? A side-by-side comparison.* J Heart Valve Dis, 2011. **20**(4): p. 449-63.
295. Hjortnaes, J., et al., *Simulation of early calcific aortic valve disease in a 3D platform: A role for myofibroblast differentiation.* Journal of Molecular and Cellular Cardiology, 2016. **94**: p. 13-20.
296. MatÉs, J.M., C. Pérez-Gómez, and I.N. De Castro, *Antioxidant enzymes and human diseases.* Clinical Biochemistry, 1999. **32**(8): p. 595-603.
297. Gough, D.R. and T.G. Cotter, *Hydrogen peroxide: a Jekyll and Hyde signalling molecule.* Cell Death and Disease, 2011. **2**(10): p. e213.
298. Byon, C.H., et al., *Oxidative Stress Induces Vascular Calcification through Modulation of the Osteogenic Transcription Factor Runx2 by AKT Signaling.* Journal of Biological Chemistry, 2008. **283**(22): p. 15319-15327.

299. Lai, C.-F., et al., *TNFR1-Activated Reactive Oxidative Species Signals Up-Regulate OsteogenicMsx2Programs in Aortic Myofibroblasts.* Endocrinology, 2012. **153**(8): p. 3897-3910.
300. Pulido-Reyes, G., et al., *Untangling the biological effects of cerium oxide nanoparticles: the role of surface valence states.* Scientific Reports, 2015. **5**: p. 15613.
301. Sakthivel, T., et al., *Morphological Phase Diagram of Biocatalytically Active Ceria Nanostructures as a Function of Processing Variables and Their Properties.* ChemPlusChem, 2013. **78**(12): p. 1446-1455.
302. Pirmohamed, T., et al., *Nanoceria exhibit redox state-dependent catalase mimetic activity.* Chemical Communications, 2010. **46**(16): p. 2736.
303. Popov, A.L., et al., *Cerium oxide nanoparticles stimulate proliferation of primary mouse embryonic fibroblasts in vitro.* Materials Science and Engineering: C, 2016. **68**: p. 406-413.
304. Giachelli, C.M., *The emerging role of phosphate in vascular calcification.* Kidney International, 2009. **75**(9): p. 890-897.
305. Mazière, C., et al., *Oxidized low density lipoprotein inhibits phosphate signaling and phosphate-induced mineralization in osteoblasts. Involvement of oxidative stress.* Biochimica et Biophysica Acta (BBA) - Molecular Basis of Disease, 2010. **1802**(11): p. 1013-1019.
306. Zhang, Q., et al., *Effects of Cerium Oxide Nanoparticles on the Proliferation, Osteogenic Differentiation and Adipogenic Differentiation of Primary Mouse Bone Marrow Stromal Cells <I>In Vitro</I>*. Journal of Nanoscience and Nanotechnology, 2015. **15**(9): p. 6444-6451.
307. Mason, D., et al., *Cardiac gene therapy: Recent advances and future directions.* Journal of Controlled Release, 2015. **215**: p. 101-111.
308. Sacks, M.S., F.J. Schoen, and J.E. Mayer, *Bioengineering challenges for heart valve tissue engineering.* Annu Rev Biomed Eng, 2009. **11**: p. 289-313.
309. Wissing, T.B., et al., *Biomaterial-driven in situ cardiovascular tissue engineering—a multi-disciplinary perspective.* npj Regenerative Medicine, 2017. **2**(1).
310. Ibrahim, D.M., A. Kakarougkas, and N.K. Allam, *Recent advances on electrospun scaffolds as matrices for tissue-engineered heart valves.* Materials Today Chemistry, 2017. **5**: p. 11-23.
311. Nachlas, A.L.Y., S. Li, and M.E. Davis, *Developing a Clinically Relevant Tissue Engineered Heart Valve-A Review of Current Approaches.* Advanced Healthcare Materials, 2017. **6**(24).
312. Stassen, O.M.J.A., et al., *Current Challenges in Translating Tissue-Engineered Heart Valves.* Current Treatment Options in Cardiovascular Medicine, 2017. **19**(9).
313. Rajamannan, N.M., et al., *Calcific Aortic Valve Disease: Not Simply a Degenerative Process: A Review and Agenda for Research From the National Heart and Lung and Blood Institute Aortic Stenosis Working Group * Executive Summary: Calcific Aortic Valve Disease - 2011 Update.* Circulation, 2011. **124**(16): p. 1783-1791.
314. Gaharwar, A.K., N.A. Peppas, and A. Khademhosseini, *Nanocomposite hydrogels for biomedical applications.* Biotechnology and Bioengineering, 2014. **111**(3): p. 441-453.
315. Pyrzynska, K. and A. Pękal, *Application of free radical diphenylpicrylhydrazyl (DPPH) to estimate the antioxidant capacity of food samples.* Analytical Methods, 2013. **5**(17): p. 4288.

316. Annabi, N., et al., *Highly Elastic and Conductive Human-Based Protein Hybrid Hydrogels.* Advanced Materials, 2016. **28**(1): p. 40-49.